The modelling of electromagnetic methods for the nondestructive testing of fatigue cracks

Adam Miles Lewis
University College London
Department of Mechanical Engineering

Submitted to the
Faculty of Engineering of the
University of London
for the degree of
Doctor of Philosophy

1991

Paginated

blank pages are scanned as found in original thesis

No information is missing

Abstract

This thesis describes a theoretical and experimental investigation of electromagnetic methods for the detection and measurement of metal fatigue cracks. The available methods are reviewed, with particular attention being paid to mathematical models, and a new model of the electromagnetic field near a metal fatigue crack for small skin-depths is presented which uses a surface impedance boundary condition with the addition of a line source to represent the crack. This leads to a coupled system of two magnetic scalar potentials, one on the crack face which obeys the two-dimensional Laplace equation and one outside the test-piece which obeys the three-dimensional Laplace equation. The behaviour of the field is governed by a parameter $m = l/(\mu_r\delta)$, where l is the size of the field perturbation, μ_r is the relative permeability and δ is the skin-depth. When m is small, almost all the flux is concentrated inside the metal and the exterior potential also obeys the two-dimensional Laplace equation, on the test-piece surface. When m is large, the perturbation part of the exterior field has a negligible effect on the field inside the crack so that the crack-face potential may be found by the Born approximation. The general m problem is solved for rectangular and semi-elliptical cracks in flat plates, interrogated by uniform fields, and the solution is verified experimentally. A method for calculating the crack depth from the magnetic field is given, with descriptions of industrial applications. The theory is further developed to find the impedance change in an air-cored circular coil caused by a crack, to find the field near overlapping cracks and to find the field near a crack in an interior corner. Finally, a semi-empirical analysis is presented for a ferrite-cored measuring coil.

To my parents,

with gratitude and love

Acknowledgements

I would like to thank my supervisor, Dr Roy Collins, whose suggestion of investigating the magnetic field during an ACPD test led to the work described here and who has helped me and advised me throughout. Professor Hugh Michael realised that the the parameter *m* was important before its full significance was known and suggested that the the Born approximation might be valid in the large *m* limit. The simplification of the summation in section 3.7 is also his, as is the small *m* solution for the corner crack described in section 7.3. Dr Martin Lugg noticed that the integral in Appendix A was listed in standard tables. Discussions with Professor Bert Auld of Stanford University, Dr Maureen McIver, now at Loughborough University, Dr John Moulder of Ames Laboratory, Iowa State University and Dr John Bowler of Surrey University were also very helpful. The test-pieces were made by the Mechanical Engineering workshop and funding was provided by the Wolfson Foundation and by the SERC under contract GR/E/82019. Thanks are also due to Professor Bill Dover and the staff of the NDE Centre and, of course, to my parents to whom this work is dedicated.

Figures

Tables

Table of principal symbols

E,D	Electric field, electric displacement
H,B	Magnetic field, magnetic flux density
j	Electric current density
x,y,z	Cartesian coordinates
ξ,η	Plane-elliptical coordinates
t, f, ω	Time, frequency, angular frequency
r,θ	Polar cordinates
ρ	Electric charge density
ε	Electric permittivity
ε_r	Relative electric permittivity
ε_0	Electric permittivity of free space
μ,μ_r,μ_0	Magnetic permeabilities
σ	Electric conductivity
ψ	Magnetic scalar potential
ϕ	Conjugate potential of ψ inside crack
a	Half-length of crack
b	Depth of crack
c	Focus of semi-elliptical crack
h	Mouth opening
i	$\sqrt{-1}$
δ	Skin depth
k	$(i+1)/\delta$
γ	$(i+1)/(\mu,\delta)$
Z_s	Surface impedance
m	Parameter governing fields

H_0	Uniform incident field
ϕ_0	Potential on crack mouth
~	Indicates Fourier transform
$\delta(y)$	Dirac delta function
k_x,k_y	Spatial frequencies
k_z	$\sqrt{k_x^2+k_y^2}$
G	Green's function
N (*italic*)	Number of turns on coil
l	Length of ACPD probe
r_0	Radius of eddy-current coil
p,q,s	Parameters of semi-empirical model
V_c,V_r	Probe voltage over crack, away from crack
P_n	Polynomial function
$F(x)$	Boundary condition function (convolution)
$L(x)$	Additional boundary condition function for overlapping cracks
J_n,Y_n (roman)	Bessel functions
K_n,I_n (roman)	Modified Bessel functions
I (*italic*)	Integral

1 Introduction

When a metal object is subject to a cyclic load it is possible for a crack to grow and eventually cause fracture even if the stress in the uncracked region is well below the yield point. This process, known as *metal fatigue*, is one of the commonest reasons for the failure of engineering components and structures and can be the cause of much loss of life, expense and environmental damage. Fatigue is a ubiquitous problem but it is of particular importance in the oil, gas, aerospace, nuclear and electricity industries. When fatigue is expected, it is often the practice to replace the vulnerable parts at regular intervals, but adequate protection can then only be achieved if many sound components are discarded as well as the flawed ones. Moreover, this approach may be unpractical if fatigue is expected in a major structural member. Consequently, much effort is devoted to testing components and structures to see if they have suffered fatigue damage and need to be replaced or repaired. This process is called *non-destructive testing* (NDT). Inspection may be formally defined as non-destructive if the performance of the test-piece is not permanently degraded by the test procedure itself. It may, in addition, be desirable for inspection to be non-destructive in the broader sense of allowing normal operations to continue. The component may even remain in service while it is tested; a form of inspection called *condition monitoring*. In order to assess the danger presented by a crack, it is necessary to know its size and location and to predict how quickly it will grow under service conditions. Quantitative NDT, with a criterion to determine if a component is fit for its purpose, is termed *non-destructive evaluation* (NDE).

There are several ways of inspecting for fatigue cracks, some of the best known of which are the visual, ultrasonic, radiographic and dye-penetrant methods. However, this thesis is concerned only with electromagnetic NDT methods, which offer a potential for quantitative work that has not, as yet, been fully exploited. The first chapter is a review of electromagnetic NDT methods currently in use, with the emphasis on mathematical modelling techniques. A distinction is drawn between purely magnetic methods that rely on the crack being a break in the magnetic permeability of the metal, and eddy-current and potential difference methods that rely on the crack being a break in the electric conductivity.

The remainder of the thesis describes a new model of eddy-current and potential difference NDT, based on the *surface impedance boundary condition*, and valid when the skin-depth is small compared with the length ~~of the crack and interrogating field~~ scale of the problem. Detailed calculations of the field inside the metal are avoided by making use of the fact that the exponential decay profile is unaffected by the presence of the crack except at points immediately adjacent to the crack. It is shown in chapter three how one may allow for the presence of a surface-breaking crack by adding a line-source term to the boundary condition. The field in the exterior space and the field on the faces of the crack are described by two magnetic scalar potentials coupled together by the boundary conditions. The behaviour of the fields is shown to be governed by a dimensionless parameter m which depends on the operating frequency, the electromagnetic properties of the metal and the length-scale of the problem under consideration. This parameter is a measure of the ratio of the magnetic flux in the exterior space in the region of the flaw to the magnetic flux inside the metal in the region of the flaw.

The limiting cases of small and large m are shown to correspond to two existing theories. When m is small, the magnetic flux is concentrated into a thin layer just inside the metal and the potential obeys the two-dimensional Laplace equation both outside the crack and inside it, with continuity of potential and normal derivative on the crack mouth. This behaviour corresponds to the "unfolding" model previously developed at UCL. In contrast, when m is large, the perturbation of the exterior field has no effect on the field inside the crack, which may therefore be found using the Born approximation, as assumed by Auld and his co-workers at Stanford University. Explicit calculations for general m are presented for rectangular and semi-elliptical cracks in flat plates under interrogation by a uniform field. The predicted change in the fields has been confirmed experimentally by measuring the field near a rectangular notch over a range of frequencies.

Some practical applications of the model are given, including examples of fatigue crack length and depth measurements. The new model is used to calculate the impedance change for an air-cored eddy-current coil inspecting a fatigue crack of uniform depth. It is explained briefly how the theory can also be used to find the field when the flaw is a pair of overlapping cracks and when the crack is situated in an interior corner. Finally, the response of a ferrite-cored probe is discussed using a semi-empirical approach.

2 Review of Methods of Electromagnetic NDT

2.1 General Principles

All metals are good electrical conductors in three senses relevant to NDT. Firstly, their charge relaxation times [1] are much smaller than the periods of the signals that are used. Any charges existing in the bulk of the metal decay to zero instantaneously and the internal charge density may therefore be neglected in any calculations. Secondly, conduction currents in metals always dominate displacement currents so that the latter may also be neglected. Thirdly, the conductivity of a metal is much larger than that of air or any other likely surrounding medium. Even sea-water typically has a conductivity about a million times smaller than, for example, carbon steel [2]. An interesting exception to the third rule occurs in some nuclear reactors where a liquid metal coolant surrounds the components to be inspected. Iron and steel are, of course, the most important industrial metals of all and many of the components that require inspection for fatigue are ferromagnetic, having relative permeabilities as high as 10^3. A fatigue crack, therefore, not only constitutes a very large break in conductivity but sometimes also a large break in permeability. Electromagnetic NDT for fatigue crack damage may attempt to detect either of these features. For example, if an electric current is established in the metal, it will be diverted by the crack and the consequent changes in the electromagnetic field may be measured with contacting electrodes or a suitable magnetometer. If a magnetic field is established in a ferromagnetic metal, there may also be a detectable leakage of flux from the crack which can be shown up with magnetic ink or measured with a magnetometer.

Mathematical modelling of the signal obtained from a crack of a particular size and shape is referred to as solving the *forward problem*. However, the ultimate aim of theory is to reveal as much information as possible about the crack's size, shape and position from the signals, which is referred to as solving the *inverse problem.*

The discipline of *fracture mechanics* is concerned with the prediction of crack growth and remaining service life by analysing the stresses in the neighbourhood of a crack [3]. Information obtained from NDT is used in fracture

mechanics assessments of cracks. The crack depth is an especially important quantity to know because it is needed to determine the stress field and also to determine how much uncracked material remains.

Time-varying electromagnetic fields inside metals exhibit the *classical skin-effect* [1]. As the frequency is increased, the fields are confined to a thin layer near the surface of the metal. For a uniform field in an infinite half-space the profile in the thin layer is an exponential decay

$$\mathbf{E} = \mathbf{E}_0 \exp[(i+1)z/\delta], \tag{2.1.1}$$

where z is the coordinate normal to the metal surface. The decay length δ is referred to as the *skin-depth* and is given by

$$\delta = \sqrt{\frac{2}{\mu\sigma\omega}}, \tag{2.1.2}$$

where ω is the (angular) frequency, μ is the permeability and σ is the conductivity. For example, the skin-depth in aluminium [4] is 0.84mm at 10kHz. At the same frequency in another non-magnetic metal, which had a lower conductivity than aluminium, it would be a little higher and in a magnetic metal it might be substantially lower. In mild steel, for example, the skin-depth is about 0.1mm at 10kHz. For more complex shapes of test-piece, the formula 2.1.1 is a reasonable approximation if the depth of metal is much greater than δ and the surface is flat on a length scale comparable with δ.

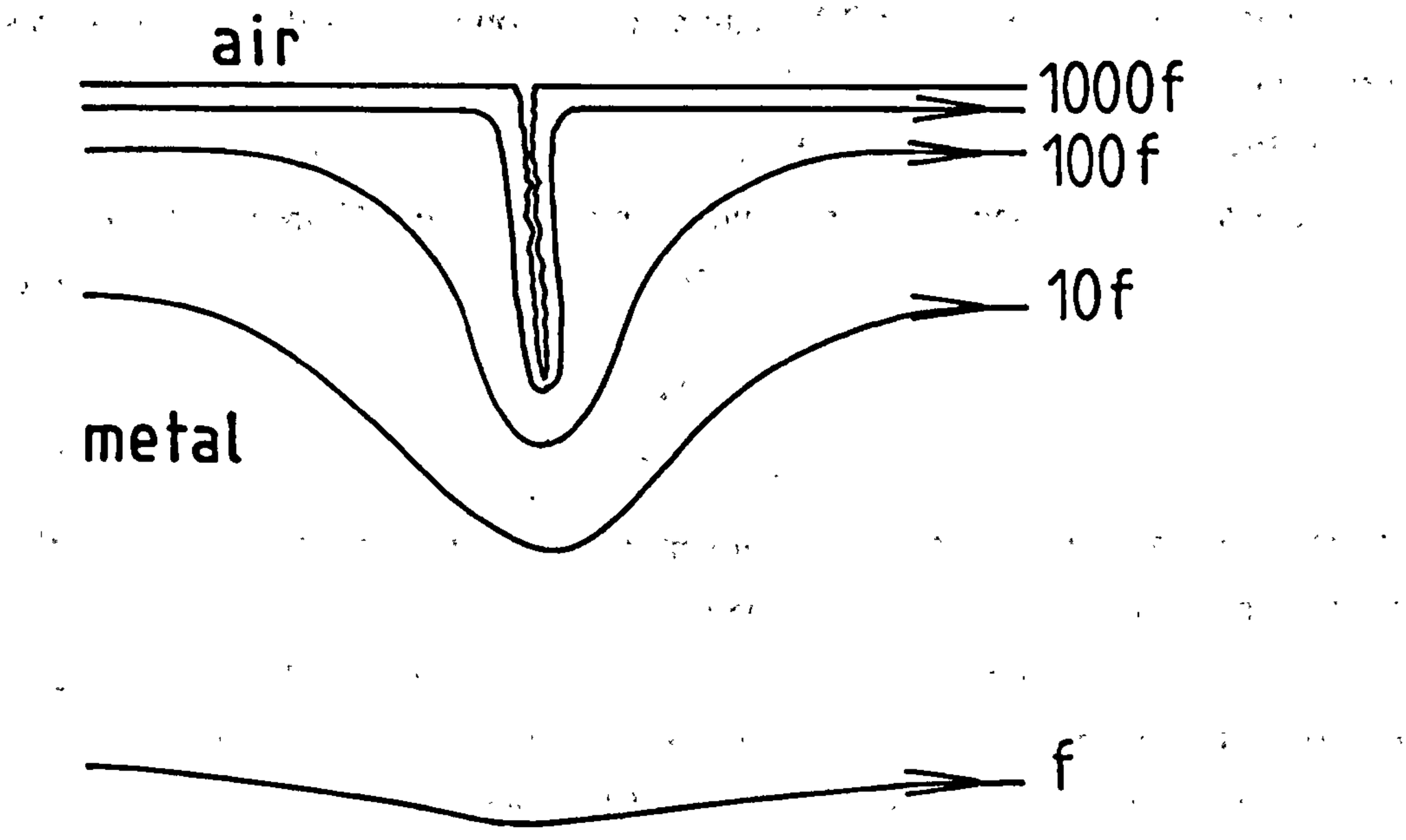

Fig. 2.1 Current flow near a fatigue crack at various frequencies, showing 50% decay contours.

When the test-piece is cracked, the fields are changed significantly from the usual exponential decay pattern, as shown in fig.2.1. If the crack is very small and the frequencies are kept low, the skin-depth may be much larger than the crack depth, this is referred to as the *thick-skin* case. A surface-breaking fatigue crack then perturbs only a small part of the field. At higher frequencies the skin-depth may be much smaller than the crack depth: the *thin-skin* case. Such fields are particularly sensitive to surface breaking defects; they are, however, insensitive to buried defects. Therefore, the best strategy for inspection is to use more than one frequency. In some alloys the permeability is very sensitive to the chemical composition and it may be difficult to distinguish a dangerous flaw from a harmless minor local variation. This problem can be overcome by applying a large d.c. magnetic field which magnetically saturates the material [5]. The metal then behaves like a non-magnetic material in response to the small superimposed a.c. inspection signal. This technique can also be used to increase the skin-depth in order to detect buried flaws.

The skin-depth equation 2.1.1 can also be thought of as describing waves propagating into the material at different speeds. Note that the speeds $\delta\omega$ can be quite slow, for example 53 m s^{-1} for aluminium at 10kHz. For a uniform plane wave, as above, the electric field **E** and the magnetic field **H** are related by

$$E_x = Z_s H_y, \tag{2.1.3}$$

$$E_y = -Z_s H_x, \tag{2.1.4}$$

$$Z_s = \delta/\sigma \quad \frac{(i+1)}{\sigma\delta} \quad . \tag{2.1.5}$$

where x and y are the coordinates tangential to the surface and Z_s is called the characteristic impedance [6] of the metal.

So far it has been implied that the field is sinusoidal. Most commercial equipment is of this type, but it is also possible to excite the test-piece with a pulsed signal, which contains a spectrum of frequencies. The lower frequency components of the pulse travel at slower speeds and penetrate to larger depths.

2.2 Available Electromagnetic NDT Techniques

Perhaps the most widely used electromagnetic NDT method is the *eddy current* method, in which the probe is inductively coupled to the test-piece. Pioneering experiments were undertaken as early as 1879 by Hughes [7] who demonstrated a device which could distinguish between different metal samples and suggested using it to detect counterfeit coins. The technique then developed slowly until the introduction of electronic measurement circuits, such as that described by Vigness, Dinger and Gunn in 1942 [8]. Their electronics relied, of course, on vacuum tube technology. Development then became much more rapid with extensive research conducted for example, by Förster et al. [9]. A thorough description of eddy-current NDT methods was given in a book by Libby [10] in 1971, by which time techniques such as multi-frequency and pulsed excitation had become well established.

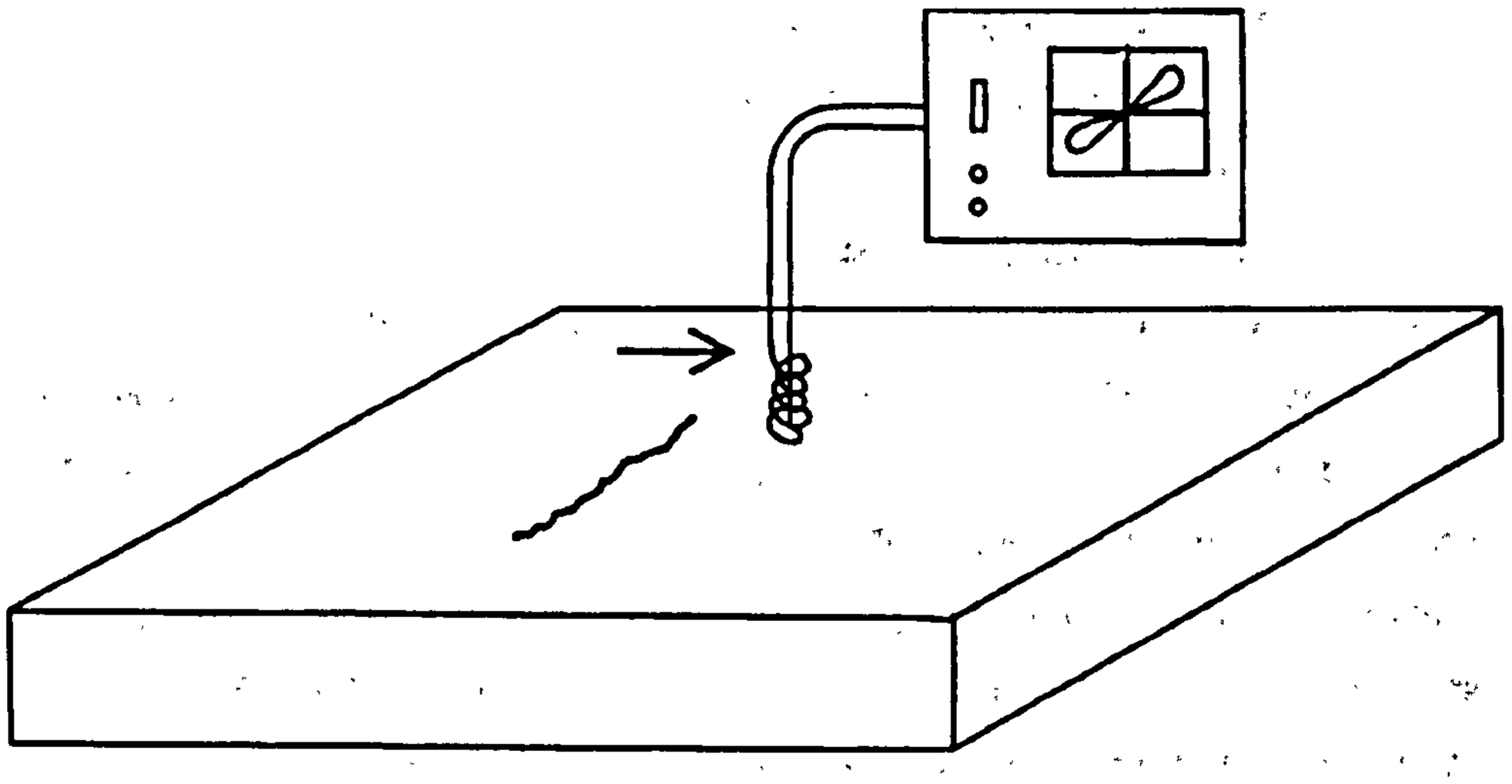

Fig. 2.2 Eddy-current non-destructive testing

In the usual modern variant, shown in fig.2.2, a coil is passed over the test piece and its complex impedance monitored using an a.c. bridge circuit. If a current flows in the coil it induces eddy-currents in the metal which are perturbed by the presence of a flaw. The flux through the coil, the induced voltage across the coil and the measured impedance are also changed. Coils are manufactured for specific applications, for example: they may be wound around the outside of a tubular test-piece, or on a bobbin to go inside a tube, or in the form of a pencil probe to inspect surfaces in general. Ferrite cores may be used to increase the flux coupling with the coil and the probes may also be shielded to concentrate the field in the region immediately beneath the probe. It is conventional to display the complex impedance plane on a storage oscilloscope and to rely on the operator's skill to distinguish the signature of a flaw from spurious signals such as a change caused by a pencil probe being lifted off the surface.

Although the use of one coil has the merit of simplicity, more complex arrangements can improve the sensitivity. For example, two balanced coils, wound in opposite senses, can be connected in series to make a *differential coil eddy current* probe. Separate exciter and receiver coils can be used, each one optimized for its purpose. For this type of probe, the impedance measured is the

mutual inductive reactance. One arrangement, referred to as an *eddy current reflection probe* [11] employs a large exciter coil and a small differential pair of receiver coils.

Eddy current probes are usually placed as close as possible to the region to be inspected and it is generally true that the signals depend only weakly on objects further away. This is a consequence of the fact that the fields are quasistatic rather than radiative. Another way of looking at this is to say that the flaws and probes are much too small to act as efficient antennae at the frequencies used. However, the small signal detected by a receiver coil placed far from an exciter coil may still contain useful information about the region between them. This *remote field* eddy current technique was originally devised by Schmidt [12] to inspect oil-well casings for corrosion and has also been applied to large diameter pipelines [13]. Low frequencies and d.c. magnetic saturation are used so that eddy currents generated on the inside of a piece of tubing penetrate to the outer surface as well.

In some circumstances it is possible to make electrical contact with the test-piece and fatigue cracks can then be measured by *potential difference crack sizing*. An electric current is injected into the metal or induced in it and the potential difference between two points on the surface is monitored. If a crack cuts the surface in the region between the two contacts the p.d. is increased: the deeper the crack the bigger the increase. Both direct current potential difference (DCPD) and alternating current potential difference (ACPD) variants exist.

The idea of using DCPD measurements for crack detection and sizing arose out of work by B M Thornton and W M Thornton [14] on the problem of section thickness measurement, reported in 1938. Another early system was described by Trost [15] six years later. When used on small laboratory samples [16], DCPD can detect incremental crack growth to within 50μm under favourable conditions and often requires only simple electronics. Unfortunately, it is not well-suited for large objects because the current that needs to be supplied to obtain a measurable potential difference is very large. Even a sample of a few centimetres in size might require 50A. Thermal emf's can cause errors in d.c. systems if precautions are not taken to maintain constant temperature [17] which is especially

inconvenient for experiments investigating fatigue over a range of temperatures. Another problem is that the d.c. itself can cause unwanted electrochemical phenomena [18] in corrosion-fatigue experiments.

At high frequencies, the skin-effect causes the effective resistance of a piece of metal to be much higher than its d.c. value. Therefore, the p.d. obtained from a given current is also much higher. Moreover, thermal e.m.f.'s and electrochemical problems are eliminated and it is possible to use frequency and phase discrimination to improve the signal to noise ratio. A number of authors [18],[19],[20] described ACPD systems designed to take advantage of some of these ideas and by 1980 Dover et al. [21],[22],[23] had developed a successful instrument that measured the ACPD with a filtered amplifier and synchronous rectifier, phase-locked to a current source. Recent versions of this device employ a 2A current at 6kHz and have been used for large scale laboratory fatigue tests and also to inspect off-shore structures, pressure vessels and a variety of other industrial plant. The main problems arise from the fact that the potential differences that are measured are still very small, perhaps 10μV. Large common mode interference signals are often encountered but phase discrimination helps to overcome this difficulty because the interference is usually out of phase with the desired voltage. Unwanted signals can also be induced in the probe leads, this problem being especially troublesome with non-magnetic materials. Nevertheless, measurements of crack depth can be found with a precision of about 100μm. Potential difference methods have the advantage of not requiring any measurement of the height of the probe above the surface and often need only relatively simple modelling, as will be discussed in section 2.4.

One of the most important industrial crack detection techniques is *magnetic particle inspection* (MPI), which is a purely magnetic method and suitable only for ferromagnetic metals [4],[24]. A large magnetic field, approaching saturation strength, is applied to the test-piece, which is then sprayed with magnetic ink. Flux leaking from a surface-breaking crack creates a region with a strong local magnetic field which polarises and attracts the ink particles, causing them to accumulate at the crack mouth so that it is revealed as a bright line. Refinements include the use of ink that fluoresces under ultra-violet light to improve contrast,

and the use of Hall probes to measure the applied field to make sure that it is strong enough. No information is obtained about crack depth by the usual MPI test methods but a technique for estimating depth was proposed by Adhikari [25]. He masked the crack with increasing thicknesses of cellulose adhesive tape until no indication remained and took the final tape thickness as his estimate of depth. No justification has been given for the underlying assumption that the leakage field from the crack extends vertically into space to a distance of one crack depth and the technique can also be criticised because the point where the crack indication vanishes is subjective. However, Adhikari obtained some surprisingly good experimental results on shallow cracks.

Hall probe or fluxgate magnetometers can also be used to measure the field near a flaw in a ferromagnetic metal. This technique is used, for example, in the British Gas "pig", an inspection vehicle that travels along the inside of gas pipelines, driven by the pressure of gas [26]. Magnetic particle inspection would be very difficult to apply to such a test-site, because of its inaccessibility.

An unusual magnetic flaw detection system was described by Owston [27] in which an eddy-current coil and d.c. bias coil were used to find changes in incremental permeability of a magnetised tube. Superficially, this resembles an ordinary eddy-current test, but because the d.c. component does not exhibit the skin-effect, deeply buried flaws can be detected.

2.3 Modelling of Eddy Current Systems

Classical electromagnetic fields are described, of course, by the famous set of partial differential equations which were presented by J C Maxwell [28] in 1864, some years before Hughes' experiments on his "induction balance" eddy-current instrument. However, adequate experimental testing of theoretical predictions of probe response only became possible after the introduction of electronic measurement. A review of theoretical models of eddy-current NDT was presented by Lord and Palanisamy [29] in 1981. Early papers gave solutions for probe responses to unflawed samples only. Lord and Palanisamy attributed to Förster and Stambke [30] the calculation of the impedance of a cylindrical coil

concentrically wound around a cylindrical rod and to Waidelich and Renken [31] the equivalent solution for a circular coil over a conducting plane. These axially symmetric problems were solved using analytic methods.

A model of flaw detection was produced by Burrows [32] in which the flaw was approximated as a dipole. He restricted his analysis to low frequencies such that the skin-depth was much greater than the flaw size. As explained above, this is not an appropriate mode in which to inspect for surface-breaking fatigue cracks. Burrows used the Lorentz reciprocity theorem [1] to show that, in two coil systems, it is immaterial which coil is used as the exciter and which as the receiver.

With the advent of high-speed digital computers, evaluation of more complex theories became feasible. Dodd and Deeds [33] generalised the axially symmetric solutions to cover the problem of a coil encircling a conductor with a concentric layer of a different conductor and also the problem of a coil over a two-layer conducting plane. They included a term taken from Burrows' theory to model the effect of a flaw. Kahn, Spal and Feldman [34] found solutions for eddy currents near the lip and tip of a long fatigue crack and by joining these solutions constructed an approximate theory valid for situations where the crack depth was as small as four times the skin-depth. Spal and Kahn [35] produced the first model of the eddy-currents near a fatigue crack which was valid for all skin-depths. In this paper, they considered the case of a tight radial crack in a circular cylinder and found solutions using eigenfunction expansions. In a later paper they used the *boundary integral equation* method (BIE) [36] to generalise their model to cylinders of arbitrary cross-section and opened up the prospect of BIE solutions for a much wider range of geometries.

The BIE method can be most easily understood from the example of its use in solving Laplace's equation

$$\nabla^2\psi = 0. \tag{2.3.1}$$

The Green's function for this equation obeys

$$\nabla^2 G(\underset{\sim}{x},\underset{\sim}{x}') = \delta(\underset{\sim}{x}-\underset{\sim}{x}'), \tag{2.3.2}$$

where δ here denotes the Dirac delta function. Application of the symmetric form of Green's theorem to ψ and G over a volume V, bounded by a surface S, gives

$$\int_V (\psi \nabla^2 G - G \nabla^2 \psi) dV = \int_S \left(\psi \frac{\partial G}{\partial n} - G \frac{\partial \psi}{\partial n} \right) dS, \qquad (2.3.3)$$

where the derivatives with respect to n denote spatial derivatives in the direction normal to S.

Substitution of 2.3.1 and 2.3.2 in 2.3.3, followed by integration over the delta function, gives the *boundary integral equation*

$$\psi(x') = \int_S \left(\psi \frac{\partial G}{\partial n} - G \frac{\partial \psi}{\partial n} \right) dS. \qquad (2.3.4)$$

The BIE method is implemented numerically by dividing the boundary into elements and approximating the potential within each element by a parametric equation so that the field is characterized by a set of unknown parameters. When the BIE, expression 2.3.4, is applied at all points on S, subject to the relevant boundary conditions, a matrix equation for these unknowns is obtained, which is then solved to find the boundary field. This method is referred to as the *boundary element method* (BEM). BIE methods can be applied to other problems, providing that a suitable Green's function is known. The BIE does not give the field at all points inside the volume V but this is not needed to find the probe response in NDT problems.

In ultrasonics it is often the practice to employ the Born approximation of wave scattering theory [37], which involves neglecting the back-scattered wave when calculating the field on the flaw surface. Auld et al. applied this concept to eddy-current modelling of thin-skin fields near surface breaking fatigue cracks [38],[39]. They began by finding a series solution for a rectangular shape and went on to model semi-elliptical cracks using a finite difference method. In this work, the Lorentz reciprocity relationship was used to infer the impedance change directly from the flaw field, without first calculating the flux coupling with the receiver coil. Moulder et al. [40] verified these models experimentally for two cylindrical air-cored probes (quantitatively) and for a ferrite-cored probe (qualitatively). This was the first time that the effect of the two-dimensional shape of a crack on an eddy current system had been taken into account. The Lorentz reciprocity relationship is an exact theorem which can be derived rigorously from

Maxwell's equations and is therefore applicable to all electromagnetic fields whether radiative or not. The Born approximation, however, is a wave scattering result that, at first sight, would not be expected to apply to quasistatic fields such as those encountered in NDT. In chapter 3 it is explained how a general thin-skin model can provide a criterion to determine when the Born approximation is applicable. Auld's model is simplest to evaluate when the eddy-current probe gives a uniform field in the unflawed region. Moulder et al. [41] constructed such a device and were able to invert to find the depth of both electric-discharge machined (EDM) notches and fatigue cracks in titanium alloys.

Palanisamy and Lord [42] first applied the *finite element method* (FEM) to eddy current NDT analysis, solving a problem similar to one treated analytically by Dodd and Deeds. Essentially, FEM is a numerical technique based on the calculus of variations. The region of interest is divided into cells and the fields or potentials are approximated with simple parametric equations within each cell. The governing partial differential equations are then solved by minimizing some suitable functional, such as the energy, with respect to the parameters. Although requiring intensive computation, FEM has the advantage of being able to deal with ferrite-cored probes and, in principle, with inhomogeneous and anisotropic materials. Atherton et al. [43] and Lord [44] et al. have used FEM to model the remote field effect, confirming that it can be understood as a quasistatic phenomenon rather than a radiative one. French and Bond [45] have calculated the eddy currents near slots 0.5, 1 and 2 skin-depths deep using a FEM model of the field inside the metal. However, if the same technique was applied to a thin-skin problem, a prohibitively large number of elements would be needed.

With the exception of the general skin-depth models of Kahn et al., it has also proved difficult to apply the boundary integral equation method to thin-skin problems with cracks. A BIE model of a cuboidal cavity was published by Beissner [46], but, in this work, he restricted his calculations to the thick-skin case. S K Burke [47] used the BIE to calculate the impedance change of an eddy current probe brought near to the edge of a metal block and compared his results with an analytic solution [48] in the thin-skin limit. Very good agreement with experiment was obtained.

Electromagnetic fields are usually described by partial differential equations and boundary conditions. An alternative and equivalent formulation uses the concept of action at a distance. In this description, contributions from all of the charges, currents and electric and magnetic dipoles of media are summed to find the electromagnetic field at each point. For example, the magnetic field due to the currents is given by the Biot-Savart law [1]. In the *volume integral method* of electromagnetic modelling the entire region of interest is discretized and the relationships between the fields, currents, conductivities, permeabilities, charges and dipoles expressed as large matrix equations which are then solved, usually on a supercomputer. A solution to the inverse problem can therefore be found *a priori*, at least in principle. The size of the set of linear equations and, therefore, the time needed to solve them is reduced in certain special cases, for example quasistatic problems and problems not involving magnetic media.

Prompted by its success in modelling geophysical problems, H A Sabbagh and L D Sabbagh [49] applied the volume integral method to flaw shape inversion. Fair agreement was found when their algorithm was used to find the shape of circumferential notches on the interior of a stainless steel pipe [50]. The corners of rectangular notches were poorly reconstructed. Dunbar [51] rederived Burrows' formula for a spherical flaw by the volume integral method and suggested pure volume integral and hybrid finite element/volume integral methods for NDE forward problems, again drawing on previous work in geophysics. McKirdy [52] refined Dunbar's pure volume integral model to give excellent agreement with the experimental measurements of S K Burke [53] for a coil over a cuboidal notch in aluminium. Whilst Dunbar pointed out that the method is sufficiently general to be applied to ferromagnetic test-pieces, all these calculations were restricted to non-magnetic ones. In common with FEM, the volume integral method is computationally intensive but very flexible. Volume integral calculations for advanced problems involving ferrite-cored probes [54],[55] and anisotropic media [56] have been performed more recently by H A Sabbagh, L D Sabbagh and Bowler. Jenkins and Bowler have also used volume integrals to model an air-cored reflection probe [57].

In the thin-skin limit, the tangential variation of the fields takes place on a length scale much greater than the normal variation due to the skin-effect, except at the crack itself. Locally, therefore, the fields resemble uniform plane waves and **E** and **H** are related by equations 2.1.3, 2.1.4 and 2.1.5. Senior [58] attributed to M A Leontovich the idea of using this set of relationships as a boundary condition on the fields outside the conductor. It is usually known as the *surface impedance boundary condition* (SIBC) and is a highly appropriate approximation for NDT calculations because it enables the effort of computation to be put into calculating the fields that couple with the receiver rather than into the irrelevant calculation of the detailed behaviour inside the metal. Fawzi, Ahmed and P E Burke [59] have compared eddy current boundary integral calculations with and without the SIBC and their calculations were refined in a later paper by Ahmed, Lavers and P E Burke [60]. The use of a BIE/SIBC formulation in NDT was proposed by Nicolas [61], and Davey and Turner [62] solved both steady state and transient problems in simple shell structures by this method. Davey and Turner pointed out that the SIBC could also be used in finite element and finite difference calculations. The application of BIE/SIBC methods to flaw detection was developed by Beissner [63],[64],[65] who used reciprocity to write the impedance change in terms of scalar potentials. Beissner and Graves [66] extended this boundary element solution to ferrite cored probes. Unfortunately, the BIE expressions become singular inside a closed crack and numerical evaluations of Beissner's model by Ogilvy et al. [67] had to be restricted to open notches. However, agreement with experimental measurements on an EDM notch was good.

In its usual form, therefore, the SIBC is not applicable to a surface broken by a fatigue crack, which is a major limitation on its use in NDT. The main original work contained in this thesis is an extension of the surface impedance boundary condition to incorporate the presence of a surface breaking fatigue crack. The crack is considered to act as a line source of magnetic flux, with a strength proportional to the cross-crack potential difference. The justification for this approach is given in chapter 3. It is also shown that, under certain conditions, the model reduces to the Born approximation used by Auld et al.

In order to find crack depth, eddy current probes are sometimes calibrated against a set of notches of various depths, cut in a block made of the same material as the test-piece. An objection to this method is that it is not known if an open notch changes the probe impedance in the same way as a closed crack. In chapter 3 it is shown that a correction factor can be included in the extended surface impedance model to take account of finite notch opening. Using calibration against notches, Oaten and Blitz [68] were able to size fatigue cracks in mild steel by the *touch method*. This consists of lowering the eddy current probe vertically onto the metal surface. Their success is consistent with the fact that the correction factor to the SIBC model of chapter 3 is, under some circumstances, negligible in ferromagnetic materials.

Fatigue cracks can occur in thin metal sheets as well as in bulk components. When a.c. fields are used to inspect this type of test piece it is possible for the skin-depth to be thicker that the test-piece. An analytical model of this situation, proposed by S K Burke and Rose [69], is valid for cracks much longer than the coil diameter. More recently, they have developed a general theory [70],[71] in which the crack is represented by a line of vortices in the current field. The plate was shown to be characterised by a length scale δ^2/h where h is the plate thickness and δ the skin-depth. They presented solutions for the limiting cases valid when the crack is long or short compared with this length and gave a numerical solution for the intermediate case. Burke [72] also extended the solution to the problem of two thin conducting plates separated by an insulating layer, one of the plates being cracked. All of these models were verified experimentally. The basic problem of a crack penetrating a thin plate was also treated by Rodger [73] using FEM.

Finally, it should be mentioned that some models of potential difference crack measurement, discussed in the next section, have been applied to eddy current systems. An example is the work of Saddeghi and Mirshekar-Syahkal [74],[75] which uses the unfolding theory of Collins, Dover and Michael, discussed in detail in the next section, to model an eddy-current probe employing a single wire U-shaped inducer. The ACFM probe described in chapter 4 also uses a crack depth inversion scheme based on the unfolding theory.

2.4 Modelling of Potential Difference Methods

Calibration of DCPD measurements traditionally relied on comparison with some analogous electrical system that had an adjustable feature to represent the crack, for example, a thin foil with a razor slit or a tank of electrolyte in which was suspended a sheet of insulating material [76]. Direct currents flowing in a good conductor obey the 3-dimensional Laplace equation for each component,

$$\frac{\partial^2 \mathbf{j}}{\partial x^2}+\frac{\partial^2 \mathbf{j}}{\partial y^2}+\frac{\partial^2 \mathbf{j}}{\partial z^2}=0. \qquad (2.4.1)$$

Since Laplace's equation does not contain any material constants, calibration analogues can be made from any homogeneous conducting material of appropriate geometry. Such calibrations require tedious experimental work which may have to be repeated if there is any change in the DCPD test conditions. Moreover, it is often difficult to achieve the same accuracy in the calibration measurements as can be achieved in the DCPD test itself. Mathematical modelling is used to overcome these difficulties by eliminating the need for calibration.

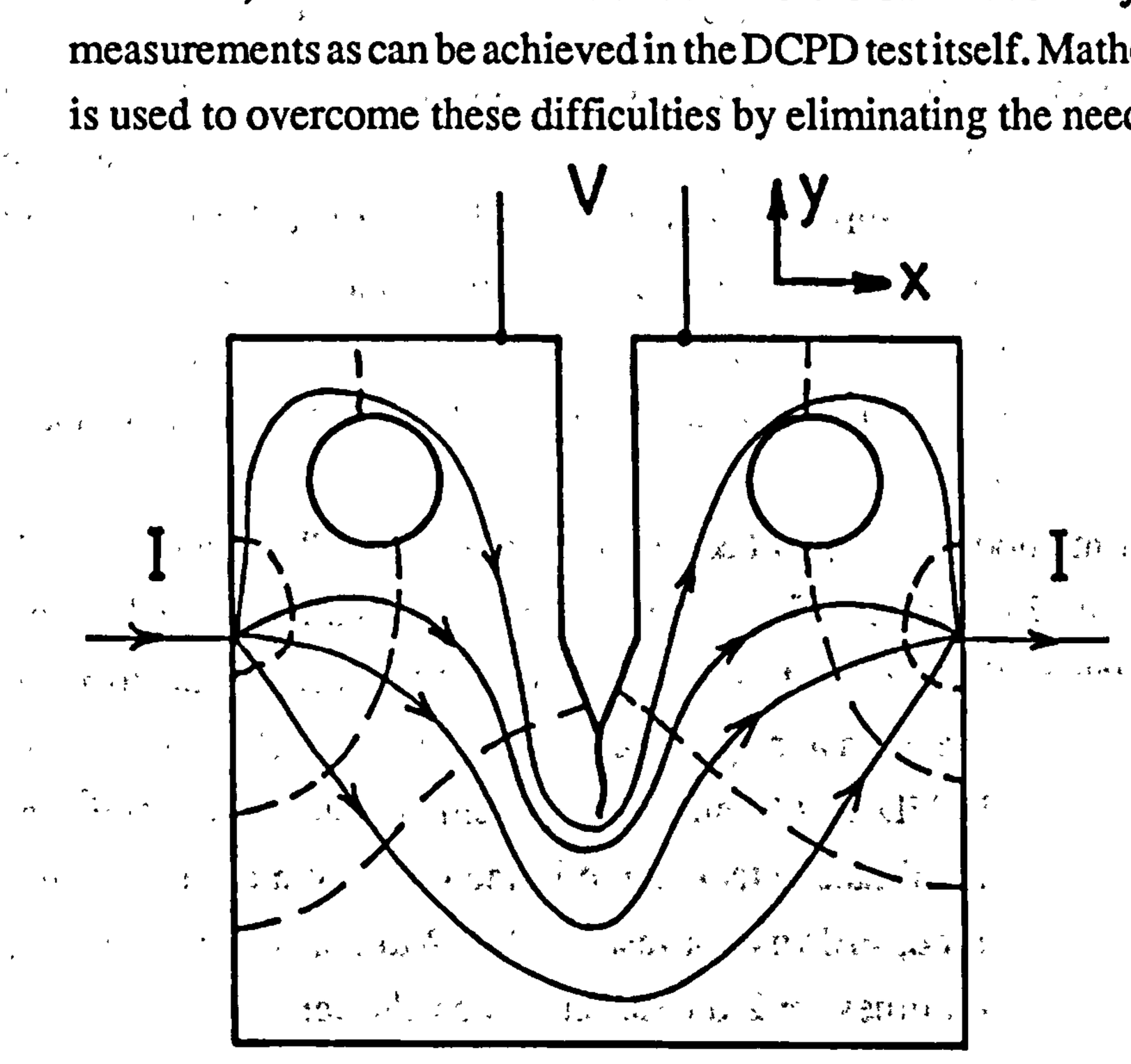

Fig. 2.3 Equipotentials (broken) and streamlines (solid) for a DCPD test.

Translationally symmetric problems, where there is no variation on z, have currents obeying the 2-dimensional Laplace equation which is satisfied if the components of the field **E** are the x and y derivatives of a potential that itself satisfies Laplace's equation or, equivalently, the real and imaginary parts of an analytic function (fig.2.3). Johnson [77] found a suitable function to model DCPD systems using as a boundary condition the requirement that no current can cross the crack. He considered in particular the growth of a fatigue crack from a starter notch, showing that the crack length can be inferred from the ratio of potential differences measured on the specimen in the cracked and uncracked state. It is not necessary to know the conductivity or field strength to evaluate his formula. The estimate of crack length is given in proportion to the specimen width (the meanings of the terms "crack length" and "crack depth" depend on the geometry of the sample and are used in different ways by different authors). Picking a suitable analytic function that satisfies the appropriate boundary conditions is equivalent to finding a conformal mapping that transforms the problem of interest into one for which a solution is known. This analytic approach has the advantage that it often gives the solutions in closed form. Schwalbe and Hellmann [78] pointed out that Johnson's formula gives an approximate model for DCPD measurements on the most common laboratory test geometries: the centre-cracked tension (CCT), single-edge-notched bend (SEN) and compact tension (CT) specimens.

Numerical methods have also been used to model DCPD in more detail. Ritchie and Bathe [79] used the finite element method to calibrate DCPD and Aronson and Ritchie [80] used this type of calculation to optimize the positioning of the contacts in a compact tension specimen. Nath [81] et al. Used both FEM and BIE methods for DCPD in CT and SEN specimens and concluded that Johnson's formula underestimates crack depth in the CT specimen. Unlike the conformal mapping method, FEM is not restricted to 2-dimensional problems, however, the computation times for 2-d cases are much shorter.

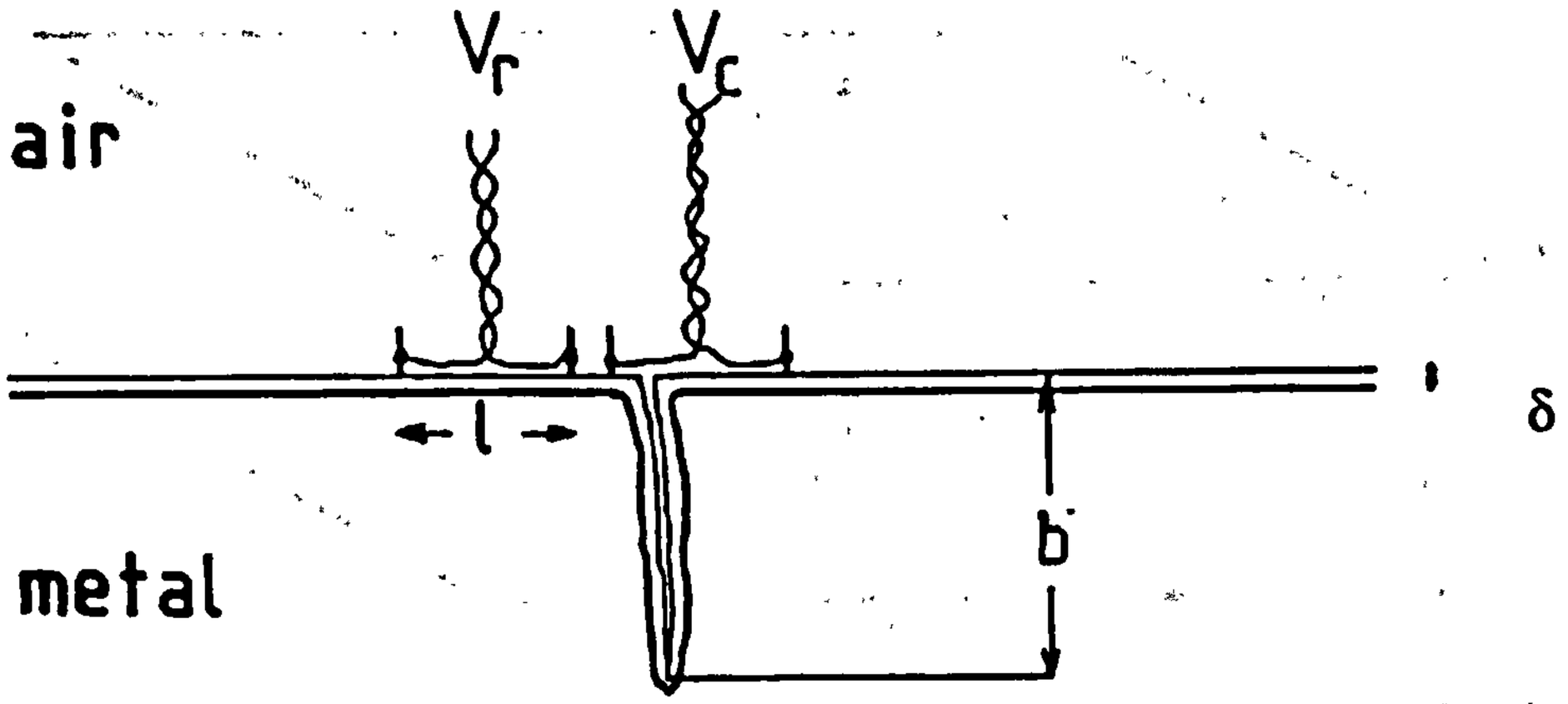

Fig. 2.4 Crack depth measurement using ACPD.

A particularly simple 1-dimensional formula exists for crack depth measurements by the ACPD method (fig.2.4) when the skin-depth is small, if the crack is of uniform depth. The p.d. measured in the uncracked region by a probe of length l is

$$V_r = El, \tag{2.4.2}$$

where E is the field strength. When the probe straddles a crack of depth b, the currents must follow a longer path and the p.d. is therefore increased to

$$V_c = E(l+2b). \tag{2.4.3}$$

Solving the simultaneous equations 2.4.2 and 2.4.3, one obtains the crack depth

$$b = \frac{l}{2}\left(\frac{V_c}{V_r} - 1\right) \quad . \tag{2.4.4}$$

This formula is only applicable ~~if the field~~ if the field is uniform. In particular, if the crack is short (in the direction perpendicular to the plane of the paper in fig.2.4), some of the current will go around the ends, rather than underneath, so that the 1-d formula 2.4.4 underestimates the crack depth. Fig.2.5 shows a section through a test-piece with such a crack; the electric field is applied in the y direction.

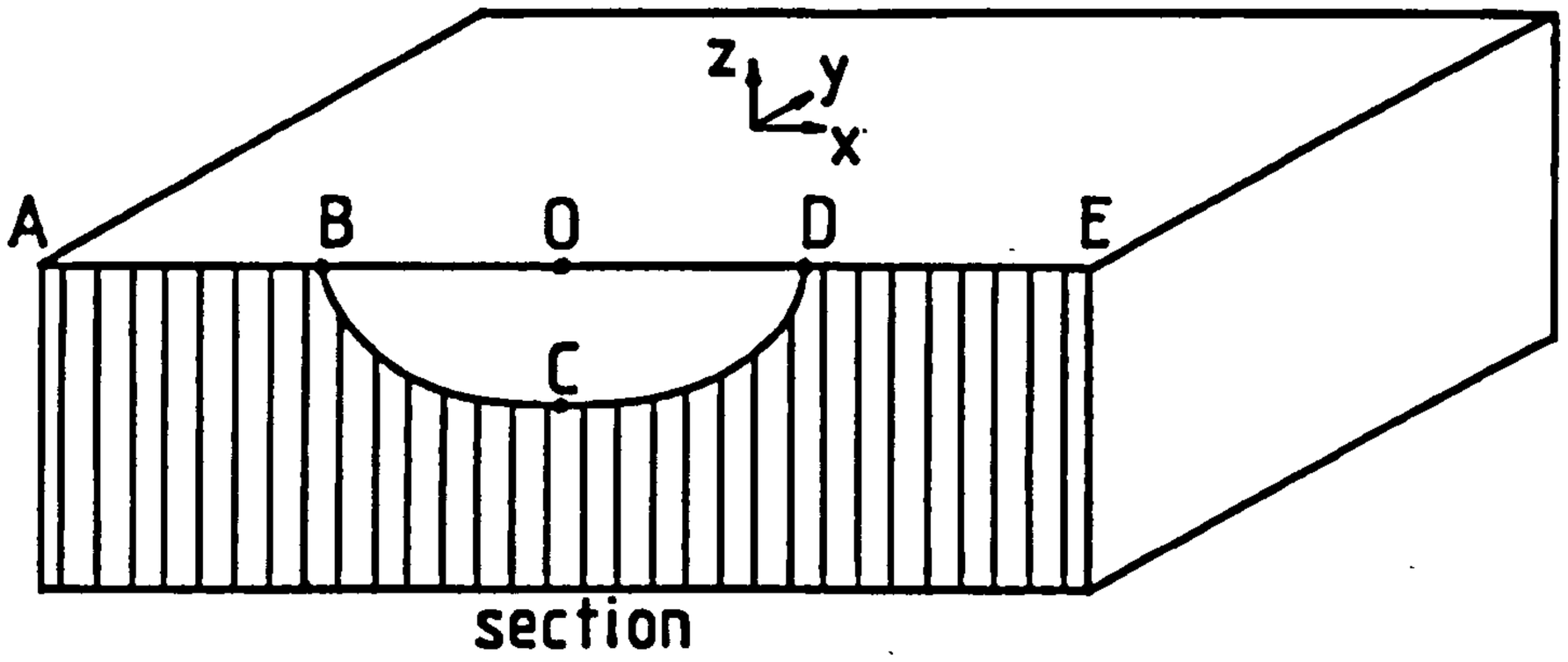

Fig. 2.5 Section through a test-piece with a short crack

A great deal of experimental and theoretical work on ACPD has been performed at University College London by Dover, Collins, Michael and co-workers. This was prompted by the need to measure fatigue crack growth in welded steel tubular joints, of the type used in off-shore structures. The tubes concerned are of the order of 0.5m in diameter and, as explained above, the DCPD technique is unsuitable for use in such large objects. Having developed the technique for this purpose, they also applied it to other types of test-piece, including non-ferromagnetic ones. One of the aims of this thesis is to show that much of the theory of ACPD developed in this programme is relevant to eddy-current testing and vice versa. Most ACPD modelling assumes that the incident field is uniform, so it is most readily applicable to uniform field eddy-current probes.

In their original paper on ACPD, Dover, Charlesworth, Taylor, Collins and Michael [21] derive a correction factor to the one-dimensional formula 2.4.4. Their analysis begins with the eddy-current equation

$$\frac{\partial^2 \mathbf{E}}{\partial x^2}+\frac{\partial^2 \mathbf{E}}{\partial y^2}+\frac{\partial^2 \mathbf{E}}{\partial z^2}=k^2\mathbf{E} \qquad (2.4.5)$$

for the field inside the metal. In this equation $k^2 = i\mu\sigma\omega$ is assumed to be constant. In order to describe the thin layer of current they took a Laplace transform on z, that is to say, they assumed a z dependency of the form $\exp(sz)$, so that

$$\frac{\partial^2 \mathbf{E}}{\partial x^2}+\frac{\partial^2 \mathbf{E}}{\partial y^2}=(k^2-s^2)\mathbf{E}(x,y). \qquad (2.4.6)$$

They then observed that for a uniform field $s=k$ and, since s and k are independent of x and y, infer that $s=k$ also for a uniform field perturbed by the presence of a crack. This is not strictly correct, because the field in general will include contributions from modes with different values of s, including modes that are zero in the unperturbed region but have s not equal to k. When s is taken to be equal to k everywhere, 2.4.6 reduces to the two-dimensional Laplace equation.

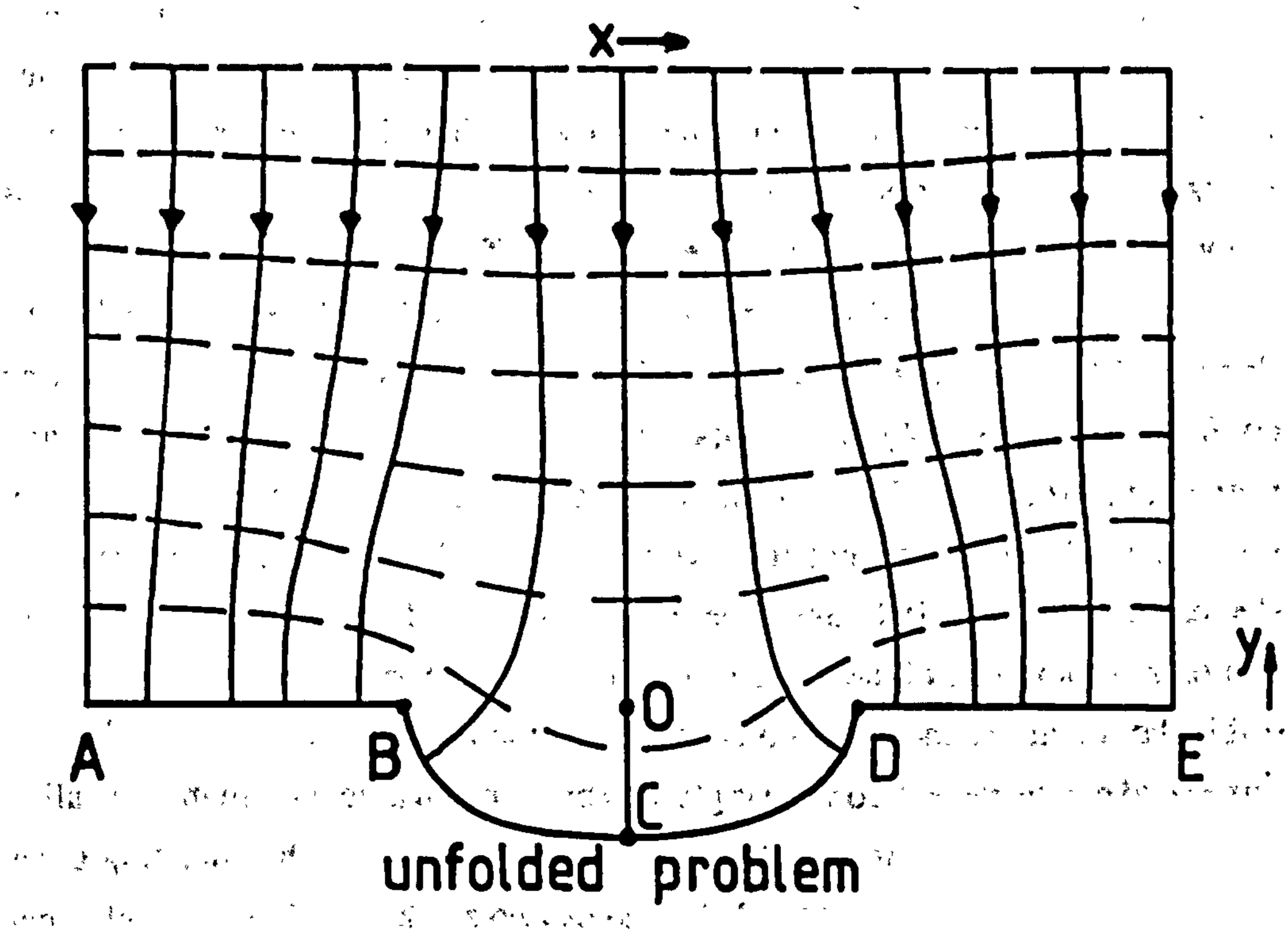

Fig. 2.6 The unfolding model

Dover et al. considered the two-dimensional Laplace equation to apply to the fields on the surface of the test-piece and also on the two faces of the crack, with the field components continuous at the crack mouth (BOD in fig.2.5) and the crack bottom-edge (BCD in fig.2.5). The field was found by solving a two-dimensional potential problem over the top surface and crack faces subject to the boundary condition of a uniform incident field. Continuity of the field components on BOD is ensured automatically and continuity across BCD is

imposed by making the electric potential zero on ABCDE so that the bottom edge is a line of symmetry. Fig.2.6 shows the resulting field on one side of ABCDE; the broken lines are electric equipotentials and the solid lines are currents. They referred to their solution as the "unfolding" model because the surface of fig.2.6 is produced by unfolding the surface of fig.2.5 along the line ABODE. Using this unfolding model and conformal mapping, Dover et al. calculated correction factors to the ACPD one-dimensional formula for a crack of circular-arc form. In chapter 3, it is shown that the unfolding model can be derived as a limiting case of the extended surface impedance model. The relevant limit occurs for short cracks in strongly ferromagnetic metals, which explains why Dover et al. reported good agreement with experimental measurements in mild steel plates. It must be stressed that Laplace's equation in ACPD is not applied in the same way as it is in DCPD and the rationale for its use is quite different.

Different conformal maps provide models of other shapes of crack. The *Schwarz-Christoffel transformation* [82] is a well known algorithm for generating conformal maps of polygonal shapes and was used to model rectangular and triangular [83] cracks. Whilst these shapes are not encountered in practice, they give potential differences that differ very little from those given by more realistic shapes. Shang et al. [84] used the Schwarz-Christoffel transformation in an approximate analysis of the fields near a crack in the corner of a specimen. In the original circular-arc model a two-stage trigonometric mapping was used, but the same field can be generated in a single step by using an algebraic mapping called the *Kármán-Trefftz transformation*. A second application of this mapping gives the field near the bow-shaped crack formed by two cracks running into each other [85], which is of common occurrence in practice. Sometimes, especially on tubular welded joints, cracks occur with a thin line of metal bridging the two faces. Michael and Collins [86] gave a simple algebraic transformation that can be used to find the fields near such a line contact on a uniformly deep crack. It is also possible to combine this map with, for example, the Kármán-Trefftz to give a circular arc with a line contact. Two other useful mappings were given in the same paper. The first transforms fields that are zero at infinity to fields with periodic boundary conditions, which occur on the surface of cylindrical

test-pieces. The second is applicable to a crack that penetrates right through a plate. Such through-crack problems were discussed in detail in a more recent paper [87].

It is, of course, possible to use other methods of solving the two-dimensional Laplace equation in the unfolding model. In particular, a Fourier series solution was derived by Collins et al. [88],[89] for semi-elliptical cracks, which yields potentials that are slightly different from those of a circular arc of the same aspect ratio. Using finite differences, Haq et al. [90] solved the unfolded problem for overlapping rectangular cracks. Whatever method is used, the advantage of the unfolding model is that the surface field distributions can be found by solving a two-dimensional problem only.

Given sufficiently detailed and accurate measurements of the cross- crack potential difference, it is possible to infer the complete profile of the crack. An iterative algorithm, which relies in part on the intuition of the user, was developed by Connolly et al. [85] to invert in this way. He used the boundary element method to solve the unfolded problem at each stage of the iteration. Bipolar coordinates were used to handle singularities at the crack ends. More recently, a single-step inversion algorithm was published by McIver [91], which requires the user to give only one parameter. Both of these algorithms use the unfolding concept and so are valid only for short cracks in ferromagnetic metals. Shape inversion seems to be numerically unstable in principle, so it is always necessary to include some artificial smoothing. It is shown in chapter 3 that the potential difference across a semi-elliptical crack differs by, at most, about 5% from the p.d. across a rectangular crack.* Very accurate measurements are therefore needed if inversion routines are to show the bottom corners of a rectangle. This conclusion is also true of the volume integral inversion routine of Sabbagh and Sabbagh [50] for circumferential notches, described above.

* For the same aspect ratio.

When an a.c. field is of sufficiently low frequency that the skin-depth is much greater than the crack depth, the right-hand side of 2.4.5 is negligible and the field may be regarded as a d.c. field for theoretical purposes. This can happen even at kHz frequencies in a poorly conducting non-magnetic metal. Michael et al. [92] modelled ACPD tests on threaded bolts made of titanium and Inconel in

this way, mapping the thread shape onto a straight line. Thin-skin ACPD gives a depth measurement according to the one (or two) dimensional path only and is therefore insensitive to the angle θ which the crack face makes with the metal surface. In situations where this is likely to differ significantly from 90°, it is thus not possible to say, from the thin-skin data alone, whether the crack is close to penetrating through the test-piece. Lugg et al. [93] investigated the use of thicker-skin fields to measure crack inclination. An important practical conclusion from this work was that an inclined crack could be immediately recognized by the asymmetric shape of the ACPD signal as the probe traverses the crack.

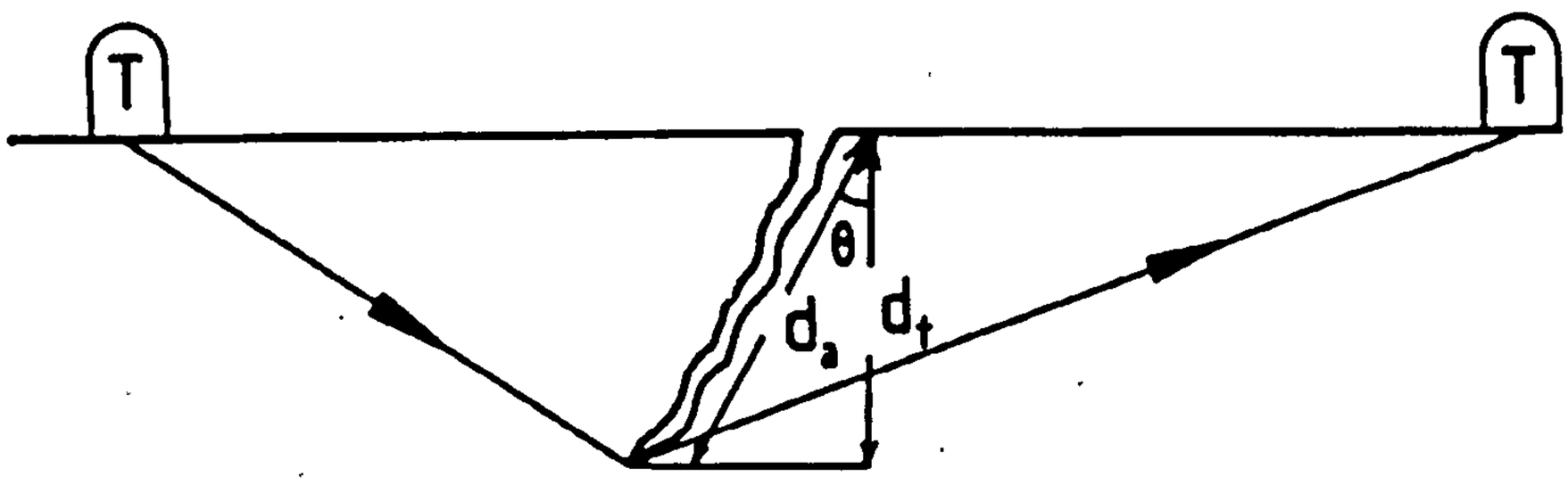

Fig. 2.7 Comparison of the crack depth estimates given by ACPD and TOFD.

This inability of thin-skin ACPD to determine crack inclination is a limitation that applies to all high frequency techniques, as will be shown from the SIBC model in chapter 3. Although a detailed comparison of the various NDT methods for measuring crack depth is beyond the scope of this thesis, it is worthwhile contrasting the depth estimates of ACPD and ultrasonic time of flight diffraction (TOFD) [94]. The former gives the distance in the plane of the crack face from the surface to the crack tip whilst TOFD gives the vertical distance from the surface to the crack tip. The TOFD depth estimate (fig.2.7) is found by measuring the time taken for an ultrasonic wave to propagate between two transducers T via the crack tip. The transducers are moved, keeping their separation constant, until the time of flight is a minimum, which indicates that

they are symmetrically positioned about the crack tip, and the depth d_t is then inferred by triangulation. Crack inclination could be deduced by making an ACPD depth measurement d_a and using the formula

$$\theta = \cos^{-1}(d_t/d_a). \tag{2.4.7}$$

The two techniques are also complementary in the sense of relying on different material properties. A discrepancy between the two depths should not, therefore, be interpreted as an indication of crack inclination until the possibility of local changes in material properties has been eliminated.

It is impossible in practice to construct a probe that only measures the surface electric potential difference. Inevitably there is always some inductive coupling as well, although it can be minimized by careful probe design. This effect is especially strong in non-magnetic materials where the flux density outside the metal is of the same order of magnitude as it is inside the metal. When ACPD measurements are made on open notches, rather than closed cracks, a finite inductance arises just from the geometry of the test-piece. Mirshekar-Syahkal et al. [95] derived a correction to the one- dimensional formula which allows for the voltage induced by the magnetic field in a notch or because of probe design. The notch correction factor is incorporated into the extended SIBC model in chapter 3.

2.5 Modelling of Flux Leakage Methods

Flux leakage methods are discussed here rather briefly because they are less relevant to the remainder of the thesis and because the literature has been reviewed recently by Jiles [96].

Calculations of leakage fields from cracks in ferromagnetic metals were made by Zatsepin, Shcherbinin [97],[98],[99] and other workers in the Soviet Union from 1966. At this time, computers powerful enough to solve complex magnetostatic problems numerically were unavailable so they used approximate analytical solutions in which the flaws were modelled as point, line or strip dipoles. Verifying experiments were also conducted.

Hwang and Lord [100] applied finite element analysis to leakage field calculations and this method has been further developed by Lord et al. [101] and Atherton et al. [102],[103] . An important advantage of FEM for this application is that it is potentially possible to allow for the non-linear and hysteretic behaviour of strongly magnetised materials. Flux leakage is quite different in this respect from eddy-current NDT, where the magnetisation is always much smaller than that required for saturation and it is reasonable to neglect these effects. Förster [104] reported poor agreement between Hall probe field mapping experiments and FEM calculations.

It might have been imagined from the development of the subject that the possibility of finding analytic solutions had by now been completely exhausted. However, in 1986 Edwards and Palmer [105] used the method of images to find the surface polarity inside a long semi-elliptical notch and showed that the polarity inside a narrow notch or crack is nearly constant, as assumed by Zatsepin and Scherbinin [97]. They also calculated the magnitude of the polarity in terms of the applied field and predicted the field outside the notch by substituting this dipole strength into the expressions of Zatsepin and Scherbinin. This prediction was confirmed by Hall probe measurements. Edwards and Palmer also discussed the significance of their results for practical MPI testing and concluded that an applied field strength of the order of hundreds or thousands of Am^{-1} is needed to detect a crack. For comparison, the British Standard [24] in most circumstances recommends that the field exceed $2400Am^{-1}$.

Magnetic particle inspection is a quantitative technique only insofar as it shows the crack length on the surface - only a crude estimate can be made of the crack depth. Modelling studies are therefore conducted with the aim of optimizing sensitivity and reliability [106] rather than of determining crack profiles. McCoy and Tanner [107] used the magnetic field of Edwards and Palmer to find the equations of motion of small magnetic particles in a viscous fluid. From a computer simulation of the MPI process, based on these equations, they concluded that 20μm particles gave better contrast then 10μm particles and that the optimum viscosity of the carrier fluid was around 0.7 mPa s, close to that of the light oils used in practice.

3 Theory of the Extended Surface Impedance Model

3.1 Introduction

Beginning from Maxwell's equations, this chapter explains how the field near a crack in the surface of a metal object may be derived from a scalar potential and how the field inside the metal may be accounted for by using the surface impedance. The effect of the crack itself is modelled by considering it to act as a line source, described mathematically using a Dirac delta function. A boundary condition on the scalar potential is derived ~~from these prineiples.~~ by these methods. It is also shown that on the crack face itself, the field obeys Laplace's equation in two dimensions.

Two important limiting cases are then discussed, governed by the dimensionless parameter $m = a/(\mu,\delta)$ where a is the length scale of the problem. When m is large, the new boundary condition is shown to reduce to the simple requirement that the component of magnetic flux normal to the metal surface is zero. This is the condition that was used by Auld et al. in their Born approximation model. Conversely, when m is small, it is shown that the new boundary condition implies that the field on the metal surface obeys Laplace's equation in two dimensions, just as it does on the crack face. Therefore, if the scalar potential is symmetric about the crack line, the unfolding model of Collins, Dover and Michael is correct.

The model is further developed for the specific example of a crack in a half space, interrogated by a uniform field. It is shown by symmetry that a uniform field parallel to the crack is not perturbed at all, so only the component of the uniform field perpendicular to the crack is considered. A Fourier transform solution is obtained which enables the scalar potential to be written in terms of the cross-crack potential difference. In the limiting cases, it is shown that the field at any point in the three-dimensional space outside the crack can then be found immediately by using the existing solutions, the conditions for their validity now being known. For the intermediate case, new solutions, using series methods, are given for rectangular and semi-elliptical cracks, and they are shown to be in agreement with the earlier models in the limiting cases. A brief description of a boundary element solution, due to McIver, is also given.

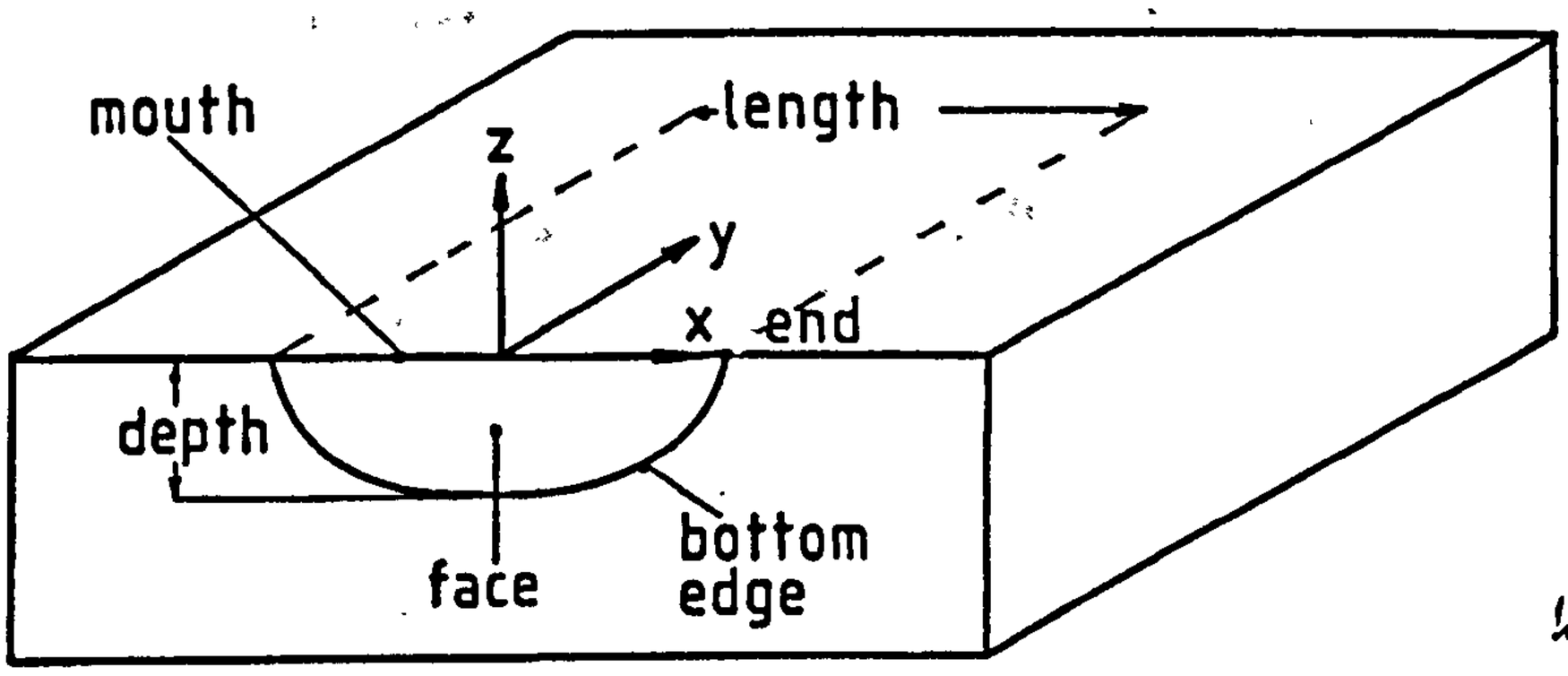

Fig. 3.1 Coordinate system and terminology.

The coordinate system and terminology for the different parts of the crack shown in fig. 3.1 will be used throughout the thesis, except where stated otherwise.

3.2 Derivation of the Surface Impedance Boundary Condition

Classical electromagnetic fields obey Maxwell's equations

$$\mathbf{div}\ \mathbf{D} = \rho, \tag{3.2.1}$$

$$\mathbf{div}\ \mathbf{B} = 0, \tag{3.2.2}$$

$$\mathbf{curl}\ \mathbf{E} = -\frac{\partial \mathbf{B}}{\partial t}, \tag{3.2.3}$$

$$\mathbf{curl}\ \mathbf{H} = \mathbf{j} + \frac{\partial \mathbf{D}}{\partial t}, \tag{3.2.4}$$

together with the relationships

$$\mathbf{B} = \mu \mathbf{H}, \tag{3.2.5}$$

$$\mathbf{D} = \varepsilon \mathbf{E}, \tag{3.2.6}$$

which are used to account for the effects of the dipoles of media. In this thesis, only isotropic media will be considered, so the permeability μ and conductivity σ are scalars. It will also be assumed that the media are homogeneous, so μ and σ are constants. As discussed in chapter 2, it is usually the practice to work with individual frequency components when making NDT measurements, so a time dependence of the form $\exp(i\omega t)$ will be assumed. Assuming the test-piece is surrounded by air, or some other medium whose electromagnetic properties

closely resemble those of free-space, the charge and current densities are zero and Maxwell's equations in the external region, for each frequency component, are

$$\mathbf{div}\ \mathbf{E} = 0, \tag{3.2.7}$$

$$\mathbf{div}\ \mathbf{B} = 0, \tag{3.2.8}$$

$$\mathbf{curl}\ \mathbf{E} = -i\omega\mathbf{B}, \tag{3.2.9}$$

$$\mathbf{curl}\ \mathbf{B} = i\omega\mu_0\varepsilon_0\mathbf{E}. \tag{3.2.10}$$

It is well-known that solutions to these equations may be written in terms of travelling electromagnetic waves with speed $c = (\mu_0\varepsilon_0)^{-1/2}$, the speed of light. However, in NDT problems the free-space wavelengths are always much larger than the scale of the problem, so the time taken for a wave to propagate over the region of interest is negligible compared with $1/\omega$. For example, the minimum free-space wavelength likely to be encountered is about 10m, corresponding to a frequency of 30MHz and the fatigue cracks must usually be detected when they are no more than a few millimetres long and sometimes less than 1mm long, depending on the metal in question. For NDT purposes, therefore, the propagation speed may be regarded as infinite and the right-hand side of 3.2.10 taken to be zero. Such fields are said to be *quasistatic* and are distinguished from truly static fields because Faraday's law, equation 3.2.3, maintains time dependence. The term that is neglected originates from the second term on the right-hand side of 3.2.4, known as the *displacement current.*

Quasistatic magnetic fields are irrotational, that is to say, they obey

$$\mathbf{curl}\ \mathbf{H} = 0, \tag{3.2.11}$$

and may therefore be described, without loss of generality, by a scalar potential ψ where

$$\mathbf{H} = \nabla\psi. \tag{3.2.12}$$

Substitution of 3.2.12 and 3.2.5 into 3.2.8 shows that ψ obeys Laplace's equation

$$\nabla^2\psi = 0 \tag{3.2.13}$$

in the external region.

Next, consider the region inside the test-piece. The metal will be assumed to be isotropic and homogeneous as far as its conductivity σ and relative permeability μ_r are concerned. Ohm's law

$$\mathbf{j} = \sigma \mathbf{E} \tag{3.2.14}$$

is obeyed, if the magnetic field is never strong enough to deflect the conduction electrons significantly. The internal charge density ρ will be assumed to be zero, since metals are good conductors. For the same reason, the conduction current density $\mathbf{j}$ will always far exceed the displacement current density, which can again be ignored. Maxwell's equations inside the test-piece are therefore

$$\text{div } \mathbf{E} = 0, \tag{3.2.15}$$

$$\text{div } \mathbf{B} = 0, \tag{3.2.16}$$

$$\text{curl } \mathbf{E} = -i\omega \mathbf{B}, \tag{3.2.17}$$

$$\text{curl } \mathbf{B} = \mu\sigma \mathbf{E}. \tag{3.2.18}$$

Taking the curl of 3.2.18

$$\text{curl curl } \mathbf{B} = \mu\sigma \text{ curl } \mathbf{E} \tag{3.2.19}$$

and substituting in 3.2.17, one obtains

$$\text{curl curl } \mathbf{B} = -i\omega\mu\sigma \mathbf{B}. \tag{3.2.20}$$

A vector identity is

$$\text{curl curl } \mathbf{B} \equiv \text{grad (div } \mathbf{B} \text{)} - \nabla^2 \mathbf{B}. \tag{3.2.21}$$

From 3.2.20, 3.2.21 and 3.2.16, it follows that $\mathbf{B}$ inside the metal obeys the Helmholtz equation

$$\nabla^2 \mathbf{B} = k^2 \mathbf{B}, \tag{3.2.22}$$

where

$$k^2 = i\omega\mu\sigma. \tag{3.2.23}$$

Note that the assumption of zero charge density implicit in 3.2.15 is not actually required in deriving 3.2.22. However, by taking the curl of 3.2.17 in a similar way and using 3.2.18 and 3.2.15, it may be shown that $\mathbf{E}$ and hence, from 3.2.14, $\mathbf{j}$ also obey the Helmholtz equation.

A field that is uniform in the x and y directions satisfies 3.2.22 if

$$\mathbf{B} = \mathbf{B}_0 e^{kz}, \tag{3.2.24}$$

where $\mathbf{B}_0$ is the value of $\mathbf{B}$ at $z = 0$ (the surface) and it is understood that the sign of the real part of k is positive, in order to keep $\mathbf{B}$ bounded as $z \to -\infty$ deep inside the metal. If the frequency is high, the exponential decay length $\delta = 1/\mathrm{Re}(k)$, known as the skin depth, is small and the field is effectively confined to a layer near the surface - the skin effect mentioned in the previous chapter. These statements also apply to the fields $\mathbf{E}$ and $\mathbf{j}$, since they obey the same differential equations and boundary conditions. The flux contained in the thin layer, per unit transverse length, is

$$\int_{-\infty}^{0} \underset{\sim}{B}_0 e^{kz} \mathrm{d}z = \frac{\underset{\sim}{B}_0}{k}. \tag{3.2.25}$$

Considering the surface of the test-piece near the crack, but not actually on the crack line itself, one may expect the perturbation of the field to occupy a length comparable with the crack length. When the skin depth is much smaller than this, contributions to $\nabla^2\mathbf{B}$ from changes in the tangential direction are negligible compared with contributions from the changes in the normal direction caused by the skin-effect. Therefore, the exponential decay profile of the fields inside the metal is essentially unaffected by the presence of the crack, except in the region within a distance δ of the crack line.

On the interface between the metal and the space above, the standard boundary conditions [1] apply: tangential components of $\mathbf{H}$ and normal components of $\mathbf{B}$ are continuous. The $\mathbf{B}$ field inside the metal can therefore be written in terms of the derivative of the scalar potential ψ on $z = +0$ as

$$\mathbf{B} = \mu_0 e^{kz}\left(\mu_r \frac{\partial\psi}{\partial x}, \mu_r \frac{\partial\psi}{\partial y}, \frac{\partial\psi}{\partial z}\right) \tag{3.2.26}$$

so that 3.2.16 implies that

$$\frac{\partial^2\psi}{\partial x^2} + \frac{\partial^2\psi}{\partial y^2} + \frac{k}{\mu_r}\frac{\partial\psi}{\partial z} = 0. \tag{3.2.27}$$

This is the usual surface impedance boundary condition, written in terms of the scalar potential ψ.

For an alternative approach to this condition one may ~~In order to obtain the alternative form of the SIBC, it is simply necessary to~~ consider the x and y components of 3.2.18 inside the test-piece

$$\frac{\partial B_z}{\partial y}-\frac{\partial B_y}{\partial z}=\mu\sigma E_x, \tag{3.2.28}$$

$$\frac{\partial B_x}{\partial z}-\frac{\partial B_z}{\partial x}=\mu\sigma E_y. \tag{3.2.29}$$

If the tangential derivatives are neglected as before then

$$E_x=-Z_s H_y, \tag{3.2.30}$$

$$E_y=+Z_s H_x, \tag{3.2.31}$$

where

$$Z_s=\frac{k}{\sigma}=\frac{\mathrm{i}+1}{\sigma\delta}. \tag{3.2.32}$$

Since the parallel components of **E** are also continuous at the interface [1], 3.2.30 and 3.2.31 apply to the fields immediately outside the test-piece as well.

3.3 Extension to Cracked Test-Pieces

In the thin-skin limit, the fields decay exponentially from the crack faces in the same manner as they decay from the top surface, except for small regions near the mouth and near the bottom edge (this point is made clearer by reference to figure 2.1 which shows schematically how the fields inside the test-piece vary with frequency as the thin-skin limit is approached). The SIBC therefore applies on the crack faces, the appropriate equations being

$$\frac{\partial^2\psi}{\partial x^2}+\frac{\partial^2\psi}{\partial z^2}+\frac{k}{\mu_r}\frac{\partial\psi}{\partial y}=0 \tag{3.3.1}$$

on $y = -0$ and

$$\frac{\partial^2\psi}{\partial x^2}+\frac{\partial^2\psi}{\partial z^2}-\frac{k}{\mu_r}\frac{\partial\psi}{\partial y}=0 \tag{3.3.2}$$

on $y = +0$. For a closed crack, continuity of B_y implies that 3.3.1 and 3.3.2 can only be consistent if ψ obeys the two-dimensional Laplace equation

$$\frac{\partial^2\psi}{\partial x^2}+\frac{\partial^2\psi}{\partial z^2}=0. \tag{3.3.3}$$

On the crack faces, 3.2.30 and 3.2.31 still hold, it being understood that $\pm z$ must be substituted for y on $y = \pm 0$. Therefore, from 3.3.3

$$\frac{\partial E_z}{\partial x} - \frac{\partial E_x}{\partial z} = 0. \tag{3.3.4}$$

This is a sufficient condition to enable (E_x, E_z) to be written in terms of a potential ϕ,

$$E_x = -Z_s \frac{\partial \phi}{\partial x}, \tag{3.3.5}$$

$$E_z = -Z_s \frac{\partial \phi}{\partial z}. \tag{3.3.6}$$

The magnetic flux lines and electric field lines on the two faces are shown in fig. 3.2.

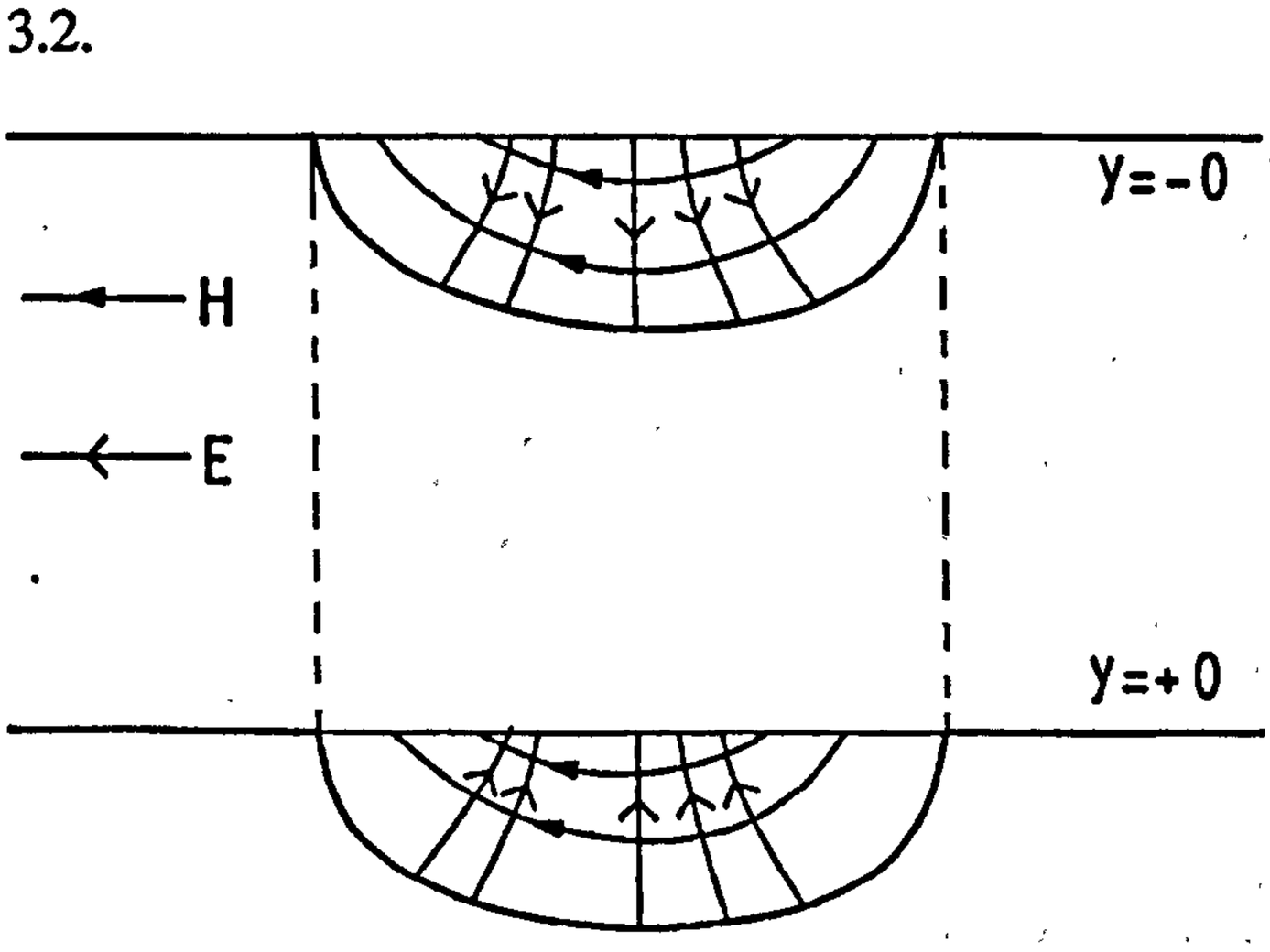

Fig. 3.2 Fields on opposite crack faces.

The potential ϕ is related to the potential ψ by the Cauchy-Riemann equations

$$\frac{\partial \phi}{\partial x} = \frac{\partial \psi}{\partial z}, \tag{3.3.7}$$

$$\frac{\partial \phi}{\partial z} = -\frac{\partial \psi}{\partial x}, \tag{3.3.8}$$

which, in this context, follow immediately from 3.2.30, 3.2.31 and the definitions of the potentials. For a closed crack, the measured a.c. potential difference is equal to the line integral of **E** between the probe points, and the contribution from the crack is equal to the difference in the potential ϕ across the crack, multiplied by Z_s. The electric fields on the two faces are antisymmetric, so the arbitrary constant in the definition of ϕ can most conveniently be chosen to give ϕ antisymmetric also. The value of ϕ on the line $z=0$ will be denoted by ϕ_0 so, the cross-crack potential difference is $2\phi_0 Z_s$.

The field on the faces, which obeys the two-dimensional Laplace equation, couples with the field outside the metal, which obeys the three-dimensional Laplace equation. This coupling can be modelled by thinking of the crack as a line source. Begin by considering a small element of the thin-skin layer of area $\Delta x \Delta y$ and centred on the point (x,y). The net flux leaving this region in the x direction is, from 3.2.25,

$$\frac{1}{k}\Delta y\left[B_x\left(x+\frac{\Delta x}{2}\right)-B_x\left(x-\frac{\Delta x}{2}\right)\right]=\frac{\mu}{k}\frac{\partial^2\psi}{\partial x^2}\Delta x\Delta y. \qquad (3.3.9)$$

Similarly, the net flux leaving in the y direction is

$$\frac{1}{k}\Delta x\left[B_y\left(y+\frac{\Delta y}{2}\right)-B_y\left(y-\frac{\Delta y}{2}\right)\right]=\frac{\mu}{k}\frac{\partial^2\psi}{\partial y^2}\Delta x\Delta y. \qquad (3.3.10)$$

The flux leaving in the z direction is

$$\mu_0\frac{\partial\psi}{\partial z}\Delta x\Delta y. \qquad (3.3.11)$$

The total flux leaving a region of the surface away from the crack is the sum of 3.3.9, 3.3.10 and 3.3.11

$$\left\{\frac{\mu}{k}\left(\frac{\partial^2\psi}{\partial x^2}+\frac{\partial^2\psi}{\partial y^2}\right)+\mu_0\frac{\partial\psi}{\partial z}\right\}\Delta x\Delta y. \qquad (3.3.12)$$

The effect of the crack can be included simply by adding to 3.3.12 the contribution of the flux from the two crack faces, which is

$$-\frac{2}{k}B_z(x,0)\Delta x=-\frac{2\mu}{k}H_z(x,0)\Delta x \qquad (3.3.13)$$

where $H_z(x,z)$ is the field on the crack face. Therefore, conservation of flux implies that

$$\left\{\frac{\mu}{k}\left(\frac{\partial^2\psi}{\partial x^2}+\frac{\partial^2\psi}{\partial y^2}\right)+\mu_0\frac{\partial\psi}{\partial z}\right\}\Delta x\Delta y=0. \tag{3.3.14}$$

for all points on the test-piece surface except on the crack mouth where

$$\left\{\frac{\mu}{k}\left(\frac{\partial^2\psi}{\partial x^2}+\frac{\partial^2\psi}{\partial y^2}\right)+\mu_0\frac{\partial\psi}{\partial z}\right\}\Delta x\Delta y-\frac{2\mu}{k}H_z(x,0)\Delta x=0. \tag{3.3.15}$$

Let

$$\gamma=k/\mu, \tag{3.3.16}$$

then, in the limit as Δy goes to zero,

$$\frac{\partial^2\psi}{\partial x^2}+\frac{\partial^2\psi}{\partial y^2}+\gamma\frac{\partial\psi}{\partial z}=2H_z(x,0)\delta(y), \tag{3.3.17}$$

where $\delta(y)$ is the Dirac delta function (*not* skin-depth in this equation). The perturbation due to the crack depends on the normal component of the field in the crack mouth or, equivalently, on the derivative parallel to the crack line of $2\phi_0$,

$$\frac{\partial^2\psi}{\partial x^2}+\frac{\partial^2\psi}{\partial y^2}+\gamma\frac{\partial\psi}{\partial z}=2\frac{\partial\phi_0}{\partial x}\delta(y). \tag{3.3.18}$$

Equation 3.3.18 is the extended surface impedance boundary condition which can be used to find the flux coupling with a receiver coil in terms of the cross-crack potential difference. It constitutes a fundamental connection between the eddy-current and ACPD methods of NDT. An important feature of the analysis given above is that the coupling between the two-dimensional and three-dimensional fields is independent of the angle at which the crack meets the surface. Consequently, thin-skin field methods give no information about crack inclination, as stated in the previous chapter.

3.4 The parameter *m*

The relationship of the new model to the existing Born approximation and unfolding models can best be understood with reference to the parameter

$$m=\frac{a}{\mu_r\delta}=\frac{|k|a}{\mu_r\sqrt{2}} \qquad (3.4.1)$$

In this equation, a is a parameter giving the length-scale of the crack and it can be given a more precise definition for a particular problem. For example, $2a$ will be used in sections 3.7 and 3.8 to mean the surface length of rectangular and semi-elliptical cracks respectively. In equation 3.3.18, the orders of magnitude of the terms on the left-hand side are

$$\frac{\partial^2\psi}{\partial x^2}+\frac{\partial^2\psi}{\partial y^2}\sim\psi/a^2, \qquad (3.4.2)$$

$$\frac{k}{\mu_r}\frac{\partial\psi}{\partial z}\sim\frac{k}{\mu_r}\psi/a. \qquad (3.4.3)$$

The ratio of these two orders of magnitude is $1/m$. As explained in the previous section, 3.4.2 originates from the flux in the thin surface layer and 3.4.3 originates from the flux that leaves the surface layer and goes into the exterior space. The parameter m is therefore a measure of the ratio of the exterior flux to the interior flux. In the limit as m becomes infinite, the boundary condition 3.3.18 becomes

$$\frac{\partial\psi}{\partial z}=\frac{(1-\mathrm{i})a}{m}\frac{\partial\phi_0}{\partial x}\delta(y). \qquad (3.4.4)$$

The perturbation part of the field caused by the line source is of order $1/m$ and may be neglected when solving for the potential on the crack face. This is exactly the algorithm of the Born approximation. Therefore, when m is very large the Born approximation is always valid. Conversely, when m is small 3.3.18 becomes

$$\frac{\partial^2\psi}{\partial x^2}+\frac{\partial^2\psi}{\partial y^2}=2\frac{\partial\phi_0}{\partial x}\delta(y). \qquad (3.4.5)$$

which is exactly the equation that would have been obtained if the crack had been coupled to a field obeying the two-dimensional Laplace equation, as in the unfolding model. In non-magnetic metals, for any field of high enough frequency to be in the thin-skin limit, m is large and the Born approximation is valid. In

ferromagnetic metals, when the frequency is only just high enough for the thin-skin condition $\delta << a$ to be true, m is small and the unfolding theory is valid. At rather higher frequencies, when m is of order 1, the full three-dimensional model must be used and at still higher frequencies the Born approximation is applicable.

An important feature of the unfolding limit is that the parameters μ and σ do not appear in the boundary condition 3.4.5. In a magnetic metal for which approximate values of these quantities are known, the operating frequency may be chosen so that m is small and one may then calculate the fields without knowing precise values for these material constants. It is therefore possible, in principle, to measure the crack depth without calibration. The practical implementation of this idea is described in chapter 5.

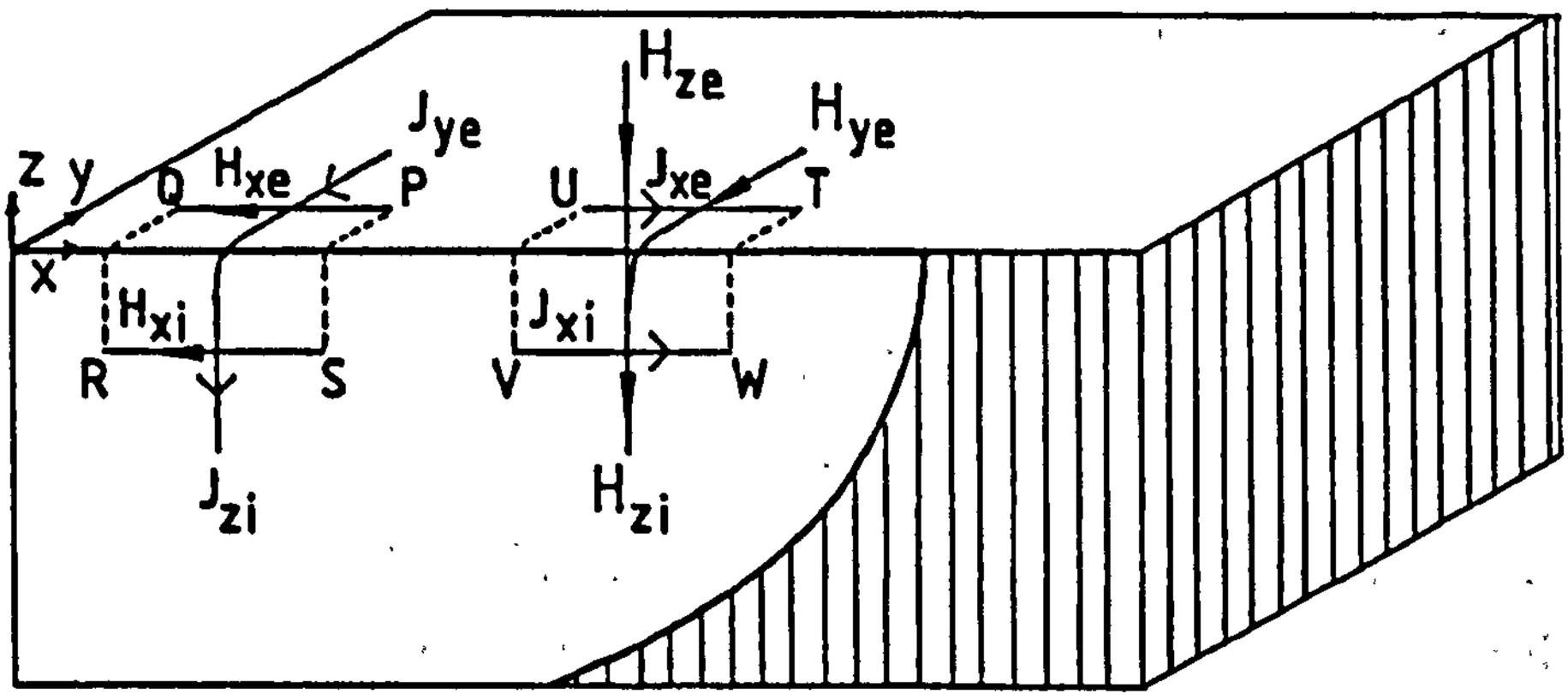

Fig. 3.3 Detail of the fields near the crack mouth.

To further clarify the significance of 3.3.18, it is helpful to examine the joining conditions linking the fields on the crack faces, on the top surface and in the exterior. Equation 3.2.11 implies that the **H** field integrated around the loop PQRS in fig. 3.3 should be zero, regardless of the value of m. If the loop is drawn very near to the crack mouth $y=z=0$ then the contributions to the integral around PQRS from the portions along QR and SP are small and the x component of the exterior magnetic field H_{xe} must be continuous with the x component of the magnetic field inside the crack H_{xi}. From the surface impedance equations (3.2.30 and 3.2.31 on the top surface and the analogous expressions in x and z on the

crack face) this corresponds to saying that the y component of the exterior electric field E_{ye} and the z component of the electric field inside the crack E_{zi} are continuous. Equivalently, continuity of E_{ye} and E_{zi} may be inferred from the fact that the corresponding current densities j_{ye} and j_{zi} must be continuous because the conductivity is too high to allow charges to build up on the crack lip.

However, the *magnetic* flux that comes out of the two thin-layers just behind the crack faces is, in general, channelled partly into the thin-layer just below the top surface and partly into the exterior space, so that H_{ye} is not continuous with H_{zi}. From 3.2.25, the flux that leaks into the exterior per unit transverse length is

$$\frac{1}{k}(B_{zi}-B_{ye})=\frac{\mu}{k}(H_{zi}-H_{ye}). \tag{3.4.6}$$

The e.m.f. induced around the loop TUVW by this leaking flux is given by Faraday's Law 3.2.3 as

$$-\frac{i\omega\mu}{k}(H_{zi}-H_{ye}). \tag{3.4.7}$$

From 3.2.23, 3.2.30 (and the analogous equation in x and z) and 3.2.32, this is exactly equal to the discontinuity in the x components of E.

$$-Z_s(H_{zi}-H_{ye})=E_{xe}-E_{xi}. \tag{3.4.8}$$

In the limit as m approaches zero, the term in 3.3.18 which originates from the flux that goes into the exterior space is negligible. Consequently, it may be inferred that all the flux that comes out of the crack is channelled into the top surface layer and that H_{ye} and H_{zi} are then continuous. To summarise, whilst continuity of H_{xe} and H_{xi} must always be imposed, continuity of H_{ye} and H_{zi} is only imposed in the small m limit when the unfolding model is valid.

3.5 Modifications for Open Notches

For the purpose of experimental testing and calibration, it is common practice to make measurements on narrow saw-cut or electric discharge machined (EDM) notches, which are used as simulated cracks. The theory developed above for cracks may be applied to this type of artificial flaw, providing that the notch opening h is small enough, as may be seen from the following argument.

The crack theory will only be applicable if the field distribution on the notch faces obeys the two-dimensional Laplace equation. From 3.3.1 and 3.3.2, a non-Laplacian field on the face implies a sharp change in the y component across the notch,

$$\frac{\partial^2\psi}{\partial x^2}+\frac{\partial^2\psi}{\partial z^2}=\frac{\gamma}{2}\left[\frac{\partial\psi}{\partial y}(y=+0)-\frac{\partial\psi}{\partial y}(y=-0)\right]. \qquad (3.5.1)$$

To first order, this difference is (assuming ψ varies on a length scale of order a)

$$\frac{1}{2}\left(\frac{\partial\psi}{\partial y}(y=+0)-\frac{\partial\psi}{\partial y}(y=-0)\right)\sim\frac{\partial^2\psi}{\partial y^2}h/2. \qquad (3.5.2)$$

However, since ψ obeys the three-dimensional form of Laplace's equation inside the gap between the faces,

$$-\frac{\partial^2\psi}{\partial y^2}=\frac{\partial^2\psi}{\partial z^2}+\frac{\partial^2\psi}{\partial x^2} \qquad (3.5.3)$$

so that, from 3.5.1, 3.5.2 and 3.5.3

$$\frac{\partial^2\psi}{\partial z^2}+\frac{\partial^2\psi}{\partial x^2}\sim-\frac{h\gamma}{2}\left(\frac{\partial^2\psi}{\partial z^2}+\frac{\partial^2\psi}{\partial x^2}\right). \qquad (3.5.4)$$

This relationship is self-consistent if the dimensionless ratio $h\gamma/2$ is of the order of 1. However, if $h\gamma/2$ is much less than 1, then 3.5.4 is only self-consistent if ψ obeys the two-dimensional Laplace equation. It is therefore reasonable to assume that if h is small enough to make $h\gamma/2$ small, then open notches behave like cracks in the sense that the two-dimensional Laplace equation is obeyed over the flaw faces. In other circumstances, the notch opening will probably be wide enough to enable BIE methods to be applied over the whole of the test-piece surface, including the interior of the notch, as in the calculations of Beissner [66] and Ogilvy et al. [67] mentioned in chapter 2.

Notches also differ from cracks because the volume between the notch faces contains magnetic flux which contributes to the strength of the line source representing the flaw. Even when the notch is narrow enough for the crack model to be applicable, it is still necessary to include a correction factor to take account of this. Assuming that H_z is continuous across the notch mouth, the extra contribution to 3.3.13 is

$$H_z(x,0)h\mu_0\Delta x. \tag{3.5.4}$$

Consequently, 3.3.18 should be modified to

$$\frac{\partial^2\psi}{\partial x^2}+\frac{\partial^2\psi}{\partial y^2}+\gamma\frac{\partial\psi}{\partial z}=2\frac{\partial\phi_0}{\partial x}(1+h\gamma/2). \tag{3.5.5}$$

The correction term $h\gamma/2$ is exactly the quantity required above to be small in order for the crack model to be valid. Therefore, in circumstances where the crack model is applicable, the correction for notch opening will always be small.

The notch correction factor given here was originally derived by Mirshekar-Syakhal et al. [95] for ACPD, but it is clearly applicable to eddy current testing as well. Finally, it must be emphasised that fatigue cracks may also behave differently from ~~notches if a line contact is present.~~

ideally narrow notches because, in fatigue cracks, it is possible for the faces to be in electrical contact due to the presence of small bridges, known as line contacts.

3.6 A Crack in a Thick Flat Plate with a Uniform Incident Field

The new model is relatively easy to solve for the example of a crack in a half-space interrogated by a uniform field. This should be a good model of a crack in a flat plate that is much thicker than the skin-depth and much larger than the crack length, with an applied field that is uniform in the uncracked region. Since non-linear magnetic effects have been ignored, the field may be considered as a superposition of the unperturbed uniform field and a disturbance caused by the flaw. Similarly, the total incident field may be thought of as the sum of a uniform field in the x direction and a uniform field in the y direction. By symmetry, the component of the uniform electric field that is parallel to x causes no potential difference across the crack. The basic equation of the model, 3.3.18, then implies that there is no perturbation of this field by the crack. Therefore, there is no loss of generality in considering only the effect of a uniform electric field parallel to y, corresponding to a uniform magnetic field parallel to x.

The total scalar potential is written

$$\psi = \psi_c + H_0 x. \tag{3.6.1}$$

The unperturbed potential $H_0 x$ trivially satisfies Laplace's equation 3.2.13, therefore the perturbed part ψ_c must also satisfy it. Consider the two-dimensional Fourier transform of ψ_c on a plane of constant z

$$\tilde{\psi}_c(k_x, k_y, z) = \int_{-\infty}^{\infty}\int_{-\infty}^{\infty} \psi_c(x, y, z) e^{-ik_x x} e^{-ik_y y} dx dy. \tag{3.6.2}$$

Consider also the transform of Laplace's equation

$$\int_{-\infty}^{\infty}\int_{-\infty}^{\infty}\left(\frac{\partial^2\psi_c}{\partial x^2}+\frac{\partial^2\psi_c}{\partial y^2}+\frac{\partial^2\psi_c}{\partial z^2}\right)e^{-ik_x x} e^{-ik_y y} dx dy = 0. \tag{3.6.3}$$

By integrating twice by parts on both x and y one obtains

$$\int_{-\infty}^{\infty}\int_{-\infty}^{\infty}\left\{(-k_x^2-k_y^2)\psi_c+\frac{\partial^2\psi_c}{\partial z^2}\right\}e^{-ik_x x} e^{-ik_y y} dx dy = 0. \tag{3.6.5}$$

If the differentiation on z is taken outside the integral; 3.6.5 may be rewritten in terms of the transform as

$$\frac{\partial^2 \tilde{\psi}_c}{\partial z^2} = k_z^2 \tilde{\psi}_c, \tag{3.6.6}$$

where

$$k_z^2 = k_x^2 + k_y^2 \quad . \tag{3.6.7}$$

The general solution to this differential equation is a linear combination of growing and decaying exponentials but in this problem the growing solutions are forbidden, because the field must be bounded as $z \rightarrow \infty$. In terms of the transform on z=0, the transform at arbitrary positive z is therefore

$$\tilde{\psi}_c(k_x, k_y, z) = \tilde{\psi}_c(k_x, k_y, 0) \exp(-|k_z| z), \tag{3.6.7}$$

so, by the Fourier inversion theorem, the total scalar potential at any point in space is

$$\psi(x, y, z) = \frac{1}{4\pi^2} \int_{-\infty}^{\infty} \int_{-\infty}^{\infty} \tilde{\psi}_c(k_x, k_y, 0) e^{ik_x x} e^{ik_y y} e^{-|k_z| z} dk_x dk_y + H_0 x \quad . \tag{3.6.8}$$

The equations 3.6.2-3.6.8 are true for any bounded quasistatic fields above a flat plate. The new boundary condition for a cracked flat plate may be incorporated by taking the transform of both sides of 3.3.18,

$$\int_{-\infty}^{\infty} \int_{-\infty}^{\infty} \left(\frac{\partial^2 \psi_c}{\partial x^2} + \frac{\partial^2 \psi_c}{\partial y^2} + \gamma \frac{\partial \psi_c}{\partial z} \right) e^{-ik_x x} e^{-ik_y y} dx dy =$$

$$\int_{-\infty}^{\infty} \int_{-\infty}^{\infty} 2 \frac{\partial \phi_0}{\partial x} \delta(y) e^{-ik_x x} e^{-ik_y y} dx dy \quad . \tag{3.6.9}$$

and the delta function may be integrated directly to give

$$\int_{-\infty}^{\infty} \int_{-\infty}^{\infty} \left(\frac{\partial^2 \psi_c}{\partial x^2} + \frac{\partial^2 \psi_c}{\partial y^2} + \gamma \frac{\partial \psi_c}{\partial z} \right) e^{-ik_x x} e^{-ik_y y} dx dy =$$

$$\int_{-\infty}^{\infty} 2 \frac{\partial \phi_0}{\partial x} e^{-ik_x x} dx. \tag{3.6.10}$$

If the z derivative is taken outside the integral and both sides are integrated by parts, 3.6.10 becomes

$$\left[-k_x^2-k_y^2+\gamma\frac{\partial}{\partial z}\right]\int_{-\infty}^{\infty}\int_{-\infty}^{\infty}\psi_c e^{-ik_x x}e^{-ik_y y}\mathrm{d}x\mathrm{d}y = ik_x\int_{-\infty}^{\infty}2\phi_0 e^{-ik_x x}\mathrm{d}x. \quad (3.6.11)$$

From 3.6.5 and 3.6.2, the left-hand side may be written in terms of $\tilde{\psi}_c$ so that

$$[-k_x^2-k_y^2-\gamma|k_z|]\tilde{\psi}_c = ik_x\int_{-\infty}^{\infty}2\phi_0 e^{-ik_x x}\mathrm{d}x. \quad (3.6.12)$$

On rearranging 3.6.12, one obtains $\tilde{\psi}_c$ in the form

$$\tilde{\psi}_c = -ik_x\frac{2\tilde{\phi}_0}{k_z^2+\gamma|k_z|} \quad (3.6.13)$$

where

$$\tilde{\phi}_0 = \int_{-\infty}^{\infty}\phi_0 e^{-ik_x x}\mathrm{d}x. \quad (3.6.14)$$

The formula 3.6.13 may then be substituted into 3.6.8 in order to find the magnetic scalar potential in terms of the cross-crack electric potential difference. The magnetic field can then be found by differentiation. Numerically, 3.6.8 may be evaluated using a Fast Fourier Transform (FFT) [108]. The whole field can be generated with a two-dimensional FFT or the field values on a line of constant x or y at a particular height z can be found using a one-dimensional FFT.

Magnetic fields can be calculated for the limiting cases by using the Born approximation and the unfolding model to calculate ϕ_0. In the general m case, the function ϕ_0 is determined by the crack shape and the requirement that H_x on the line $y=z=0$ be consistent with the three-dimensional solution. That is to say, a two-dimensional potential problem must be solved on the crack face subject to the condition that when ϕ_0 is substituted into 3.6.14 and used in 3.6.13 and 3.6.8, the same function $H_x(x,0,0)$ is given by the two-dimensional and three-dimensional solutions. Without loss of generality, continuity of H_x may be ensured by imposing continuity of the scalar potential ψ. The presence of the exterior three-dimensional space can therefore be allowed for by imposing the following boundary condition on the potentials inside the crack:

$$\psi(x,0)=\frac{1}{2\pi}\int_{-\infty}^{\infty} ik_x\tilde{F}(k_x)\tilde{\phi}_0(k_x)e^{ik_x x}\,dk_x + H_0 x \qquad (3.6.15)$$

where

$$\tilde{F}(k_x)=-\frac{1}{\pi}\int_{-\infty}^{\infty}\frac{dk_y}{k_z^2+\gamma|k_z|} \quad . \qquad (3.6.16)$$

In Appendix A this expression is integrated analytically. The function $ik_x\tilde{F}(k_x)$ is plotted in fig. 3.4.

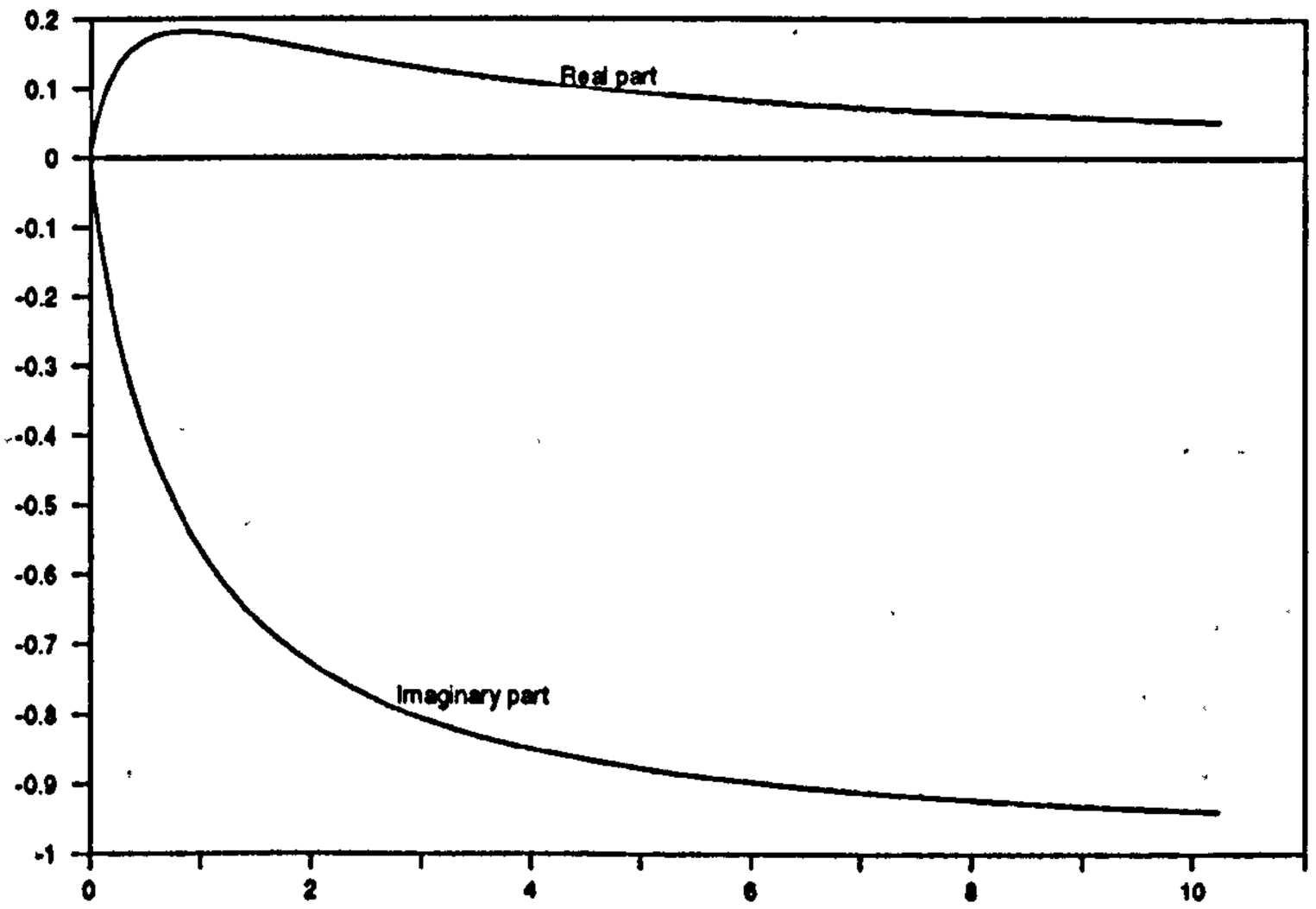

Fig. 3.4 Boundary condition function.

To get a better understanding of 3.6.15 it may be rewritten using the convolution theorem as

$$\psi(x,0,\emptyset)=\int_{-\infty}^{\infty} H_z(x-x',0)F(x')dx' + H_0 x. \qquad (3.6.17)$$

Equation 3.6.17 is a relationship between ψ and its derivative H_z on the crack lip which is a boundary condition for the two-dimensional problem. It has the unusual feature of being *non-local*, since it relates ψ at a particular point to H_z at all points

on the lip. For numerical purposes, it is better to work with the potential ϕ_0 than the field H_z, because the latter is discontinuous at the crack ends. The boundary condition is then a relationship between the potentials

$$\psi(x,0,0) = \int_{-\infty}^{\infty} \phi_0(x-x') \frac{\partial F(x')}{\partial x'} dx' + H_0 x. \qquad (3.6.18)$$

For closed cracks, the magnetic fields on the two crack faces must be equal, as shown in figure 3.2, or 3.2.11 would be violated. Consequently, on the bottom edge of the crack, the component of flux normal to the edge must be zero or else there would a net divergence in flux density, which is forbidden by 3.2.2. In terms of the potentials, the normal derivative of ψ and the tangential derivative of ϕ are zero on the bottom edge. This means, in particular, that the bottom edge is a line of constant ϕ. In section 3.3 the arbitrary constant in the definition of ϕ was chosen so that ϕ was antisymmetric across the faces, which implies that, on the bottom edge, $\phi = 0$.

3.7 Series Solution for a Rectangular Crack

Solutions already exist for the limiting cases when m is very small [83] or very large [38]. In this section, a series solution is presented for a rectangular crack shape, as shown in fig. 3.5, that is valid for general m. The more realistic example of a semi-elliptical crack is treated in the next section.

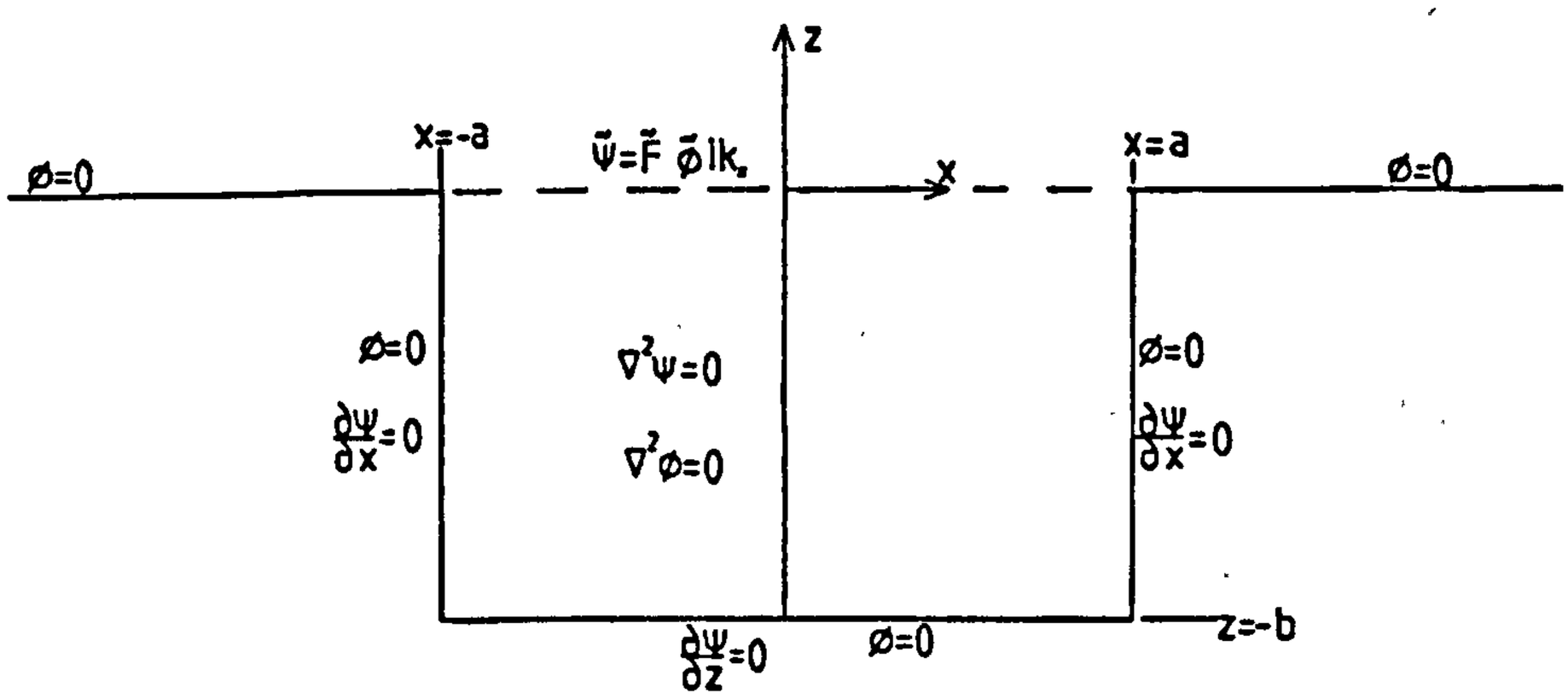

Fig. 3.5 Potential problem on a rectangular crack face.

Without loss of generality, the scalar potential ψ can be written as a Fourier series inside the crack. For a uniform incident field, ψ is antisymmetric in x so the appropriate series is

$$\psi = \sum_{n=1}^{\infty} \frac{B_n \sin[(2n-1)\pi x/2a] \cosh[(2n-1)\pi(z+b)/2a]}{(2n-1)\sinh[(2n-1)\pi b/2a]} \qquad (3.7.1)$$

and the conjugate potential is

$$\phi = \sum_{n=1}^{\infty} \frac{-B_n \cos[(2n-1)\pi x/2a] \sinh[(2n-1)\pi(z+b)/2a]}{(2n-1)\sinh[(2n-1)\pi b/2a]} \quad . \qquad (3.7.2)$$

It is straightforward to verify that the Cauchy-Riemann equations and bottom edge boundary conditions are satisfied. The factors in the denominators have been included to make all of the coefficients B_n of the same order of magnitude. If this precaution is not taken, small errors in the numerical evaluation of the lower order coefficients can cause large errors in the higher terms.

In order to apply the general m model, one must first take the Fourier *transform* 3.6.14 of the crack potential ϕ on the line z=0. This function is given by the Fourier *series* 3.7.2 for $|x| \le a$ but is zero by definition when $|x| > a$. The required transform is therefore

$$\tilde{\phi}(k_x) = \sum_{n=1}^{\infty} \frac{-B_n I_n(k_x)}{2n-1}, \tag{3.7.3}$$

where

$$I_n(k_x) = \int_{-a}^{a} \cos[(2n-1)\pi x/2a] \exp(-ik_x x)dx$$

$$= \frac{(-1)^n a(2n-1)\pi\cos(k_x a)}{k_x^2 a^2 - \left(n-\frac{1}{2}\right)^2\pi^2} \qquad \text{for } k_x a \neq \left(n-\frac{1}{2}\right)\pi$$

$$= a \qquad \text{for } k_x a = \left(n-\frac{1}{2}\right)\pi. \tag{3.7.4}$$

Substituting 3.7.3 and 3.7.1 into 3.6.15, one obtains

$$\sum_{n=1}^{\infty} \frac{B_n \sin[(2n-1)\pi x/2a]\coth[(2n-1)\pi b/2a]}{2n-1} = H_0 x - \frac{1}{2\pi}\int_{-\infty}^{\infty} \sum_{n=1}^{\infty} \frac{B_n I_n(k_x)}{2n-1} ik_x \tilde{F}(k_x) e^{ik_x x} dk_x. \tag{3.7.5}$$

Multiplication by $\sin\frac{(2l-1)\pi x}{2a}$ and integration over [$-a$, a] gives

(where $l = 1, 2, 3, \ldots$)

$$\frac{aB_l}{2l-1}\coth[(2l-1)\pi b/2a]+\frac{1}{2\pi}\int_{-\infty}^{\infty}\sum_{n=1}^{\infty}B_nI_n(k_x)I'_l(k_x)\frac{ik_x}{2n-1}\bar{F}(k_x)dk_x$$

$$=-\frac{2a^2(-1)^lH_0}{\left(l-\frac{1}{2}\right)^2\pi^2},$$

(3.7.6)

where

$$I'_l(k_x)=\int_{-a}^{a}\sin\frac{(2l-1)\pi x}{2a}e^{ik_xx}dx. \tag{3.7.7}$$

Integration of 3.7.7 shows that

$$I'_l(k_x)=I_l(k_x)\frac{ik_xa}{\left(l-\frac{1}{2}\right)\pi} \tag{3.7.8}$$

so 3.7.6 can be rewritten in terms of the I'_l alone as

$$\frac{aB_l\coth\frac{(2l-1)\pi b}{2a}}{2l-1}+\sum_{n=1}^{\infty}\frac{B_n}{4a}\int_{-\infty}^{\infty}I'_n(k_x)I'_l(k_x)\bar{F}(k_x)dk_x=-\frac{2a^2(-1)^lH_0}{\left(l-\frac{1}{2}\right)^2\pi^2}. \tag{3.7.9}$$

The coefficients B_n are determined by the infinite set of linear simultaneous equations given in 3.7.9. In order to solve numerically for the B_n, the following approximations were made:

$$B_n=0 \quad \text{for } n>N, \tag{3.7.10}$$

$$\int_{-\infty}^{\infty}I'_n(k_x)I'_l(k_x)\bar{F}(k_x)dk_x\approx\frac{\pi}{2a}\sum_{j=1}^{J}I'_n\left(\frac{j\pi}{4a}\right)I'_l\left(\frac{j\pi}{4a}\right)\bar{F}\left(\frac{j\pi}{4a}\right). \tag{3.7.11}$$

That is to say, the linear set was truncated at $n=N$ and the integral was discretized. The choice of $k_x=j\pi/(4a)$ is equivalent to imposing the condition $\psi=0$ at $x=4a$ and neglecting the influence of that part of the field that lies beyond this distance.

In discrete form, the simultaneous equations are

$$\frac{aB_l \coth\frac{(2l-1)\pi b}{2a}}{2l-1} - \frac{\pi}{8}B_l\tilde{F}\left[\left(l-\frac{1}{2}\right)\pi/a\right]$$

$$-\frac{8}{\pi}\sum_{n=1}^{N}B_n\sum_{j=1}^{J}\frac{(-1)^{l+n}j^2\cos^2\frac{j\pi}{4}\tilde{F}\left(\frac{j\pi}{4a}\right)}{[j^2-(4n-2)^2]\,[j^2-(4l-2)^2]} = \frac{-2a^2(-1)^l H_0}{\left(l-\frac{1}{2}\right)^2\pi^2} \qquad (3.7.12)$$

where it is understood that the summation on j is taken for all j in the indicated range except

$$j = 4n-2 \quad \text{and} \quad j = 4l-2 \qquad (3.7.13)$$

Because $\cos(j\pi/4) = 0$, these values of j give zero contribution to the sum except when $n = l$, when their contribution is taken account of by the inclusion of the second term on the left-hand side.

One of the most time-consuming steps in evaluating the model is the calculation of the N^2 summations on j. Fortunately, it is only actually necessary to calculate $2N$ independent sums because of the relationship

$$\sum_{j=1}^{J}\frac{j^2\cos^2\frac{j\pi}{4}\tilde{F}\left(\frac{j\pi}{4a}\right)}{[j^2-(4n-2)^2]\,[j^2-(4l-2)^2]} = \frac{(4n-2)^2S_n-(4l-2)^2S_l}{(4n-2)^2-(4l-2)^2} \qquad (3.7.14)$$

where

$$S_r = \sum_{j=1}^{J}\frac{\cos^2\frac{j\pi}{4}\tilde{F}\left(\frac{j\pi}{4a}\right)}{j^2-(4r-2)^2} \qquad (3.7.15)$$

which is true for all $n \neq l$. All the necessary sums can be found by evaluating the N sums S_r and the N sums for which $n=l$.

To get a good representation of the field outside the crack, it is necessary to consider values of k_x large enough to make the $I'(k_x)$ small. On examination of 3.7.4, it is apparent that this happens when

$$k_x a >> \left(l-\frac{1}{2}\right)\pi \qquad (3.7.16)$$

or in the discrete implementation when

$$J >> 4N-2. \qquad (3.7.17)$$

A Microvax II computer takes less than 30 seconds to find the crack-lip potential ϕ_0 with J=512 and N=64, using LU decomposition [108] to solve the simultaneous equations. The accuracy was assessed by comparing the general solution, evaluated at m=0, with a Schwarz-Christoffel solution of the unfolded two-dimensional Laplace equation problem. The two solutions agreed to within 1%. A description of the method used to evaluate the Schwarz-Christoffel mapping is given in Appendix B together with a detailed comparison of the results. In the limit as $m \rightarrow \infty$ the model reduces to the Born approximation as expected because $\tilde{F}(k_x)$ is very small for all k_x relevant to the problem and the integrals on the left-hand side of 3.7.9 vanish.

Results from this evaluation of the general m model are shown in fig. 3.6 for a rectangle with aspect ratio b/a=1 . The functional form of the crack-lip potential is essentially the same, regardless of the value of m, but its magnitude increases as m is varied between the two limits, the most rapid change occurring when m is of the order of 1.

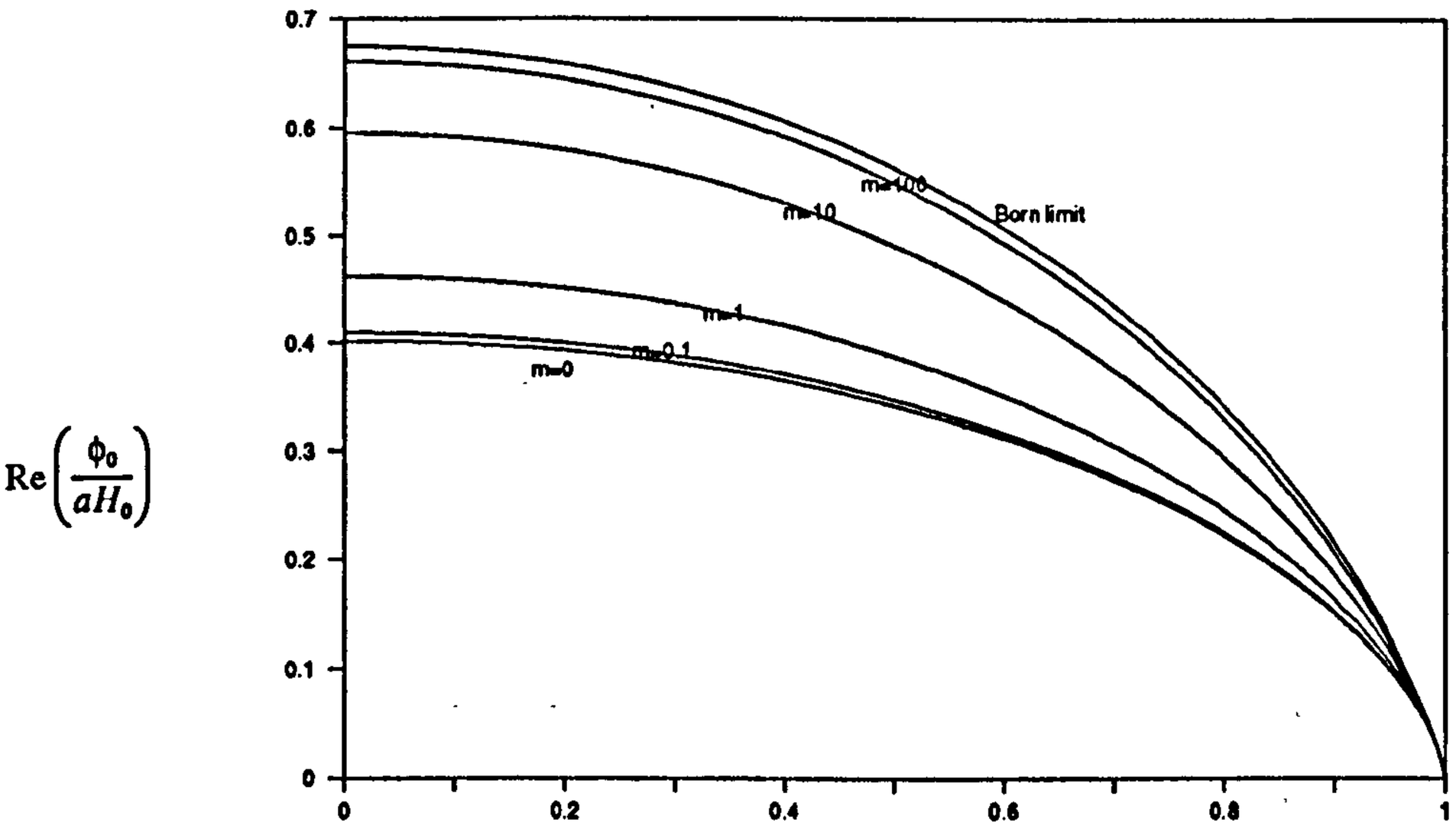

Fig. 3.6 Potential ϕ_0 for a rectangle a=b=1.

When the model is evaluated at other aspect ratios, the dependence on m is seen to become weaker as b/a falls, so that when b/a=0 the one-dimensional solution $\phi_0 = H_0 b$ is recovered for all values of m. This limit can also be confirmed directly from 3.7.9 because as b/a falls to zero, the hyperbolic cotangents approach

$$\frac{2a}{(2l-1)\pi b} \tag{3.7.18}$$

and the terms in $\bar{F}(k_x)$ become negligible by comparison. The solution of 3.7.9 is then

$$B_l = -(-1)^l 4b \frac{H_0}{\pi} \tag{3.7.19}$$

and the series 3.7.2 becomes

$$\phi = \frac{4H_0 b}{\pi} \sum_{n=1}^{\infty} \frac{(-1)^n \cos[(2n-1)\pi x/2a]}{2n-1} \tag{3.7.20}$$

which is just the standard Fourier series representation of

$$\begin{aligned} \phi &= H_0 b && |x| < a, \\ &= 0 && |x| = a. \end{aligned} \tag{3.7.21}$$

Values of the real part of ϕ_0 at x=0 for various aspect ratios are given in table 3.1, for the two limiting cases and for m=1. The general trend is for ϕ_0 at x=0 to increase as the crack gets deeper, but the rate of increase falls off.

Table 3.1 Crack Lip Centre Potentials for a Rectangle

b/a	ϕ_0 at x=0 m=0	ϕ_0 at x=0 m=1	ϕ_0 at x=0 m=10^{10}
0.1	0.093168400	0.096218064	0.099975243
0.2	0.1712335	0.1818736	0.1998494
0.3	0.2339059	0.2539705	0.2973872
0.4	0.2826807	0.3120656	0.3872032
0.5	0.3198386	0.3574695	0.4650054
0.6	0.3477511	0.3922271	0.5293525
0.7	0.3685275	0.4184639	0.5808350
0.8	0.3838997	0.4380792	0.6210479
0.9	0.3952284	0.4526467	0.6519101
1.0	0.4035550	0.4634146	0.6752898

The m dependent behaviour described here has been observed experimentally, as will be described in chapter 4.

3.8 Series Solution for a Semi-Elliptical Crack

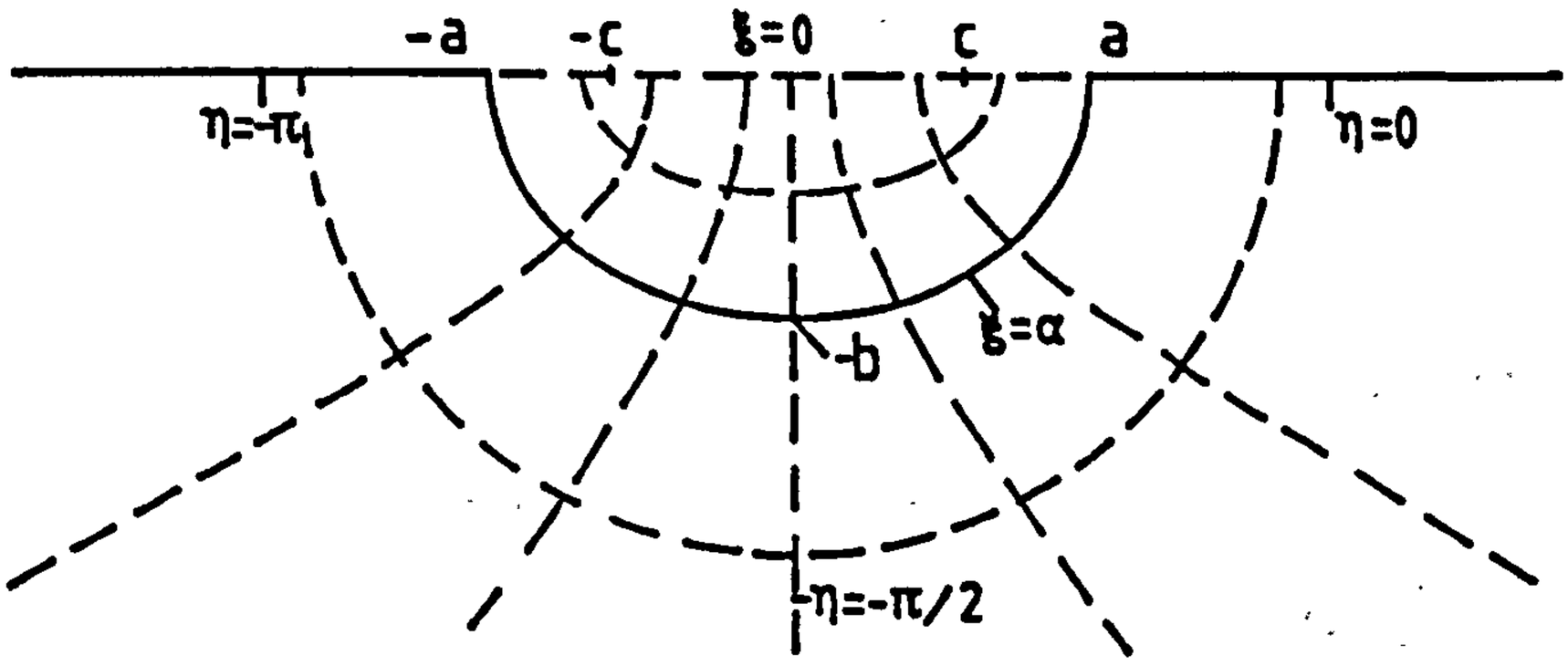

Fig. 3.7 Plane elliptical coordinate system.

A semi-elliptical shape is a much better representation of a typical fatigue crack then a rectangular shape. Plane elliptical coordinates as shown in fig. 3.7

$$x = c\cosh\xi\cos\eta, \tag{3.8.1}$$

$$z = c\sinh\xi\sin\eta, \tag{3.8.2}$$

are used here to develop a series solution for this shape for arbitrary m. The foci of the ellipse are at the points

$$x = \pm c; \quad z = 0 \tag{3.8.3}$$

which correspond to

$$\xi = 0; \quad \eta = -\pi, 0. \tag{3.8.4}$$

The semi-major and semi-minor axes are of lengths

$$a = c\cosh\alpha \tag{3.8.5}$$

and

$$b = c\sinh\alpha \tag{3.8.6}$$

respectively and the bottom edge of the crack is at

$$\xi = \alpha, -\pi < \eta < 0. \tag{3.8.7}$$

Now if ϕ,ψ satisfy the Cauchy-Riemann equations in x,y coordinates then they must also satisfy them in ξ,η coordinates. In order to prove this, consider first

$$\frac{\partial\psi}{\partial\xi}=\frac{\partial x}{\partial\xi}\frac{\partial\psi}{\partial x}+\frac{\partial z}{\partial\xi}\frac{\partial\psi}{\partial z} \tag{3.8.8}$$

so that from 3.8.1 and 3.8.2

$$\frac{\partial\psi}{\partial\xi}=c\sinh\xi\cos\eta\frac{\partial\psi}{\partial x}+c\cosh\xi\sin\eta\frac{\partial\psi}{\partial z}. \tag{3.8.9}$$

Similar relationships apply for the other derivatives,

$$\frac{\partial\psi}{\partial\eta}=-c\cosh\xi\sin\eta\frac{\partial\psi}{\partial x}+c\sinh\xi\cos\eta\frac{\partial\psi}{\partial z}, \tag{3.8.10}$$

$$\frac{\partial\phi}{\partial\xi}=c\sinh\xi\cos\eta\frac{\partial\phi}{\partial x}+c\cosh\xi\sin\eta\frac{\partial\phi}{\partial z}, \tag{3.8.11}$$

$$\frac{\partial\phi}{\partial\eta}=-c\cosh\xi\sin\eta\frac{\partial\phi}{\partial x}+c\sinh\xi\cos\eta\frac{\partial\phi}{\partial z}. \tag{3.8.12}$$

By the Cauchy-Riemann equations in Cartesian coordinates, 3.3.7 and 3.3.8, it follows from 3.8.9-3.8.12 that

$$\frac{\partial\phi}{\partial\xi}=\frac{\partial\psi}{\partial\eta}, \tag{3.8.13}$$

$$\frac{\partial\phi}{\partial\eta}=-\frac{\partial\psi}{\partial\xi}, \tag{3.8.14}$$

which are the Cauchy-Riemann equations in elliptical coordinates. The general m problem can therefore be solved by finding solutions of 3.8.13 and 3.8.14 which satisfy all the boundary conditions.

Solutions of the form $\cosh n\xi\sin n\eta$ and $\sinh n\xi\cos n\eta$ are forbidden in this problem because they give infinite fields at the foci, as may be seen from 3.8.9-3.8.12, but solutions of the form $\sinh n\xi\sin n\eta$ and $\cosh n\xi\cos n\eta$ are allowed. Since η lies in the interval $[-\pi,0]$ the solutions can be restricted to integer n without loss of generality. For a uniform incident field, ϕ is symmetric about $\eta=-\pi/2$ and ψ is antisymmetric, so the correct series are

$$\phi = \sum_{n=1}^{\infty} A_n \frac{\cosh(2n-2)\xi \cos(2n-2)\eta}{\cosh(2n-2)\alpha} - \sum_{n=1}^{\infty} B_n \frac{\sinh(2n-1)\xi \sin(2n-1)\eta}{\sinh(2n-1)\alpha},$$

(3.8.15)

$$\psi = \sum_{n=2}^{\infty} A_n \frac{\sinh(2n-2)\xi \sin(2n-2)\eta}{\cosh(2n-2)\alpha} + \sum_{n=1}^{\infty} B_n \frac{\cosh(2n-1)\xi \cos(2n-1)\eta}{\sinh(2n-1)\alpha}.$$

(3.8.16)

For the rectangle, the boundary condition $\phi = 0$ on the crack bottom edge was imposed by the choice of functions in the series expansion. Unfortunately, it is not possible to do this in the semi-elliptical case because some of the forbidden solutions mentioned above would have to be included. Instead, the boundary condition is imposed by finding a relationship between the two sets of coefficients A_n and B_n. Substituting $\phi = 0$ on $\xi = \alpha$ into 3.8.15, one obtains

$$\sum_{n=1}^{\infty} A_n \cos(2n-2)\eta = \sum_{n=1}^{\infty} B_n \sin(2n-1)\eta. \qquad (3.8.17)$$

Multiplication by $\sin(2l-1)\eta$ and integration over $[-\pi,0]$ yield the required relationship

$$\frac{\pi}{4} B_l = \sum_{n=1}^{\infty} \frac{2l-1}{(2n-2)^2 - (2l-1)^2} A_n. \qquad (3.8.18)$$

The remaining boundary condition has been written as a convolution on the x coordinate in equation 3.6.18 or as a relationship between Fourier transforms on x in equation 3.6.15, but in either form it is awkward to write in the plane elliptical coordinates. It is therefore appropriate to rewrite the series for the potentials in terms of x on the line z=0. In Appendix C it is shown that they become power series

$$\phi = \sum_{l=1}^{\infty} P_{2l-2}(x) A_l, \qquad (3.8.19)$$

$$\psi = \sum_{l=1}^{\infty} P_{2l-1}(x) B_l, \qquad (3.8.20)$$

where the P_l are polynomial functions defined by

$$P_r = \frac{(x+\sqrt{x^2-c^2})^r + (x-\sqrt{x^2-c^2})^r}{(a+b)^r + (-1)^r (a-b)^r} \tag{3.8.21}$$

The formula 3.8.21 is valid for $|x| \geq c$ and also for $|x| < c$ where the square roots are imaginary. The boundary condition 3.6.18 becomes

$$\sum_{l=1}^{\infty} P_{2l-1}(x) B_l = H_0 x + \sum_{n=1}^{\infty} \int_{-\infty}^{\infty} P_{2l-2}(x-x') \frac{\partial F(x')}{\partial x'} A_l dx'. \tag{3.8.22}$$

The coefficients A_n and B_n are determined by the simultaneous equations 3.8.18 and 3.8.22. As in the rectangular case, the equations were solved by numerical approximation and truncation of the set at $n=N$. The polynomials were evaluated at the points

$$x_s = s\Delta - 4a \tag{3.8.23}$$

where

$$s = 1, 2, 3 \ldots\ldots S \tag{3.8.24}$$

and

$$\Delta = \frac{8a}{S}. \tag{3.8.25}$$

The discrete form of 3.8.22 is therefore

$$\sum_{l=1}^{N} P_{2l-1}(x_s) B_l = \sum_{n=1}^{N} D_{sn} A_n + H_0 x_s. \tag{3.8.26}$$

where D_{sn} is a matrix of discrete convolutions defined by

$$D_{sn} = \Delta \sum_{s'=-S}^{S} P_{2n-2}(x_s - x_{s'}) \frac{\partial F}{\partial x}(x_{s'}). \tag{3.8.27}$$

Since the transform of F is already known, it is convenient to evaluate the convolutions by the Fast Fourier Transform (FFT) method [108] so that the boundary condition was, in effect, applied as a discrete form of 3.6.15. Combining 3.8.18 and 3.8.26, one obtains the linear set

$$\sum_{n=1}^{N} A_n \left\{ \sum_{l=1}^{N} \frac{4}{\pi} P_{2l-1}(x_s) \frac{2l-1}{(2n-2)^2 - (2l-1)^2} - D_{sn} \right\} = H_0 x_s \tag{3.8.28}$$

in which there is one equation for each point on the crack lip. By analogy with the rectangle, it was assumed that the fields were best represented by taking a much larger number of terms S in the discrete convolutions than the number of coefficients N, so that the simultaneous equations 3.8.28 form an overdetermined linear problem from which the coefficients A_n may be found; the potential ϕ can then be obtained by direct evaluation of 3.8.15. For S=512, N=32 a Microvax II computer took about one minute to find the cross-crack potential. NAG routine C06FRF was used for the FFT calculations and NAG routine F04JGF was used to solve the overdetermined linear problem by the least-squares method [109]. Results for the semi-circle are shown in fig. 3.8.

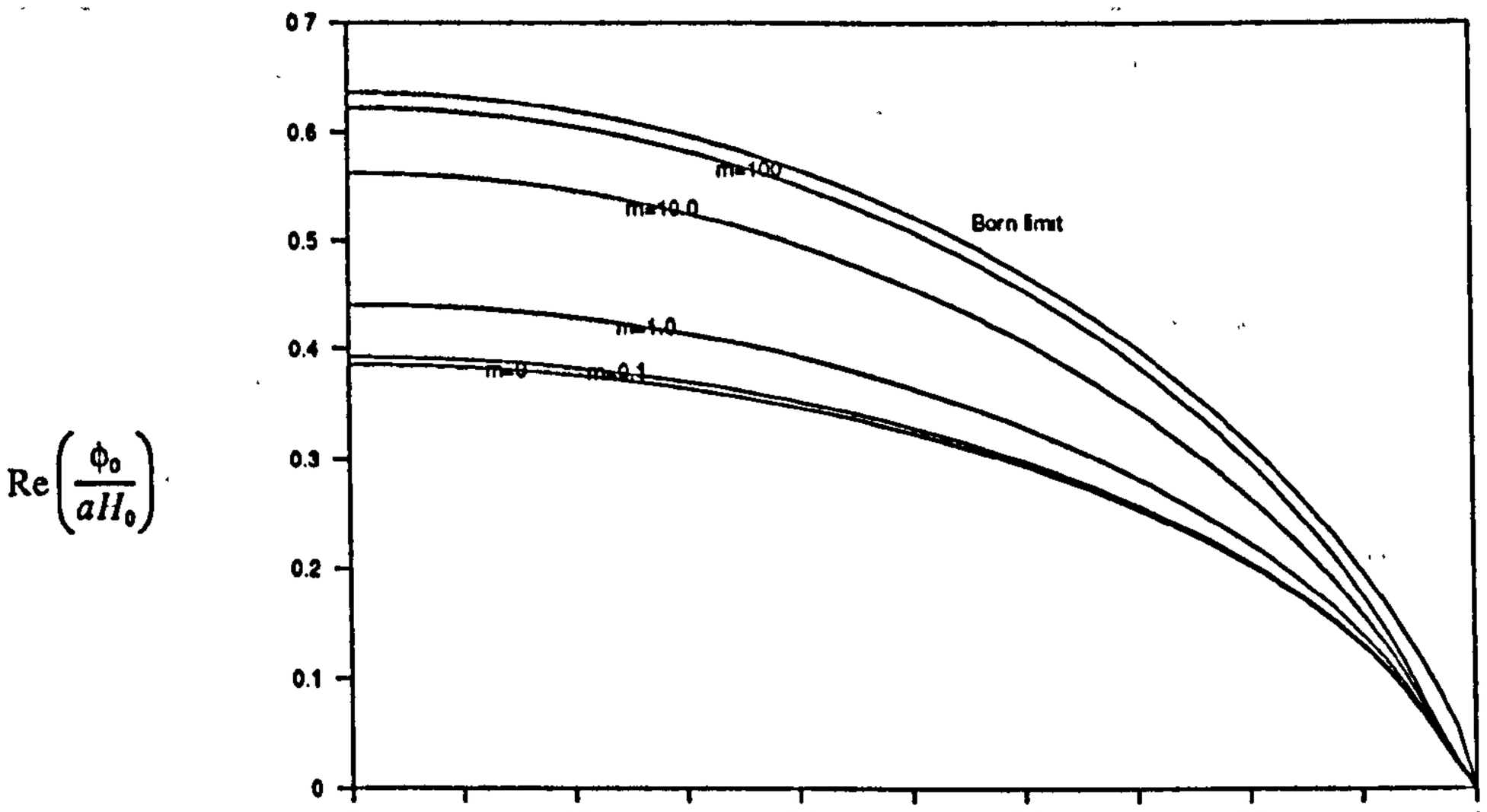

Fig. 3.8 Potential ϕ_0 for a semi-ellipse a=b=1.

In the limiting cases, the general m solution agreed with the existing Born approximation [89] and unfolding solutions [88] to order 1%; detailed figures are given in Appendix D. There is very little difference between the solutions for the rectangular and semi-elliptical cracks as can be seen in fig. 3.9 which shows the real and imaginary parts of the potentials for a=2b and m=1. The rectangle gives the larger signal, as might be expected from the fact that its area is greater, but the difference between the potentials for the two shapes is only of the order of 5% whilst the ratio of the areas is $4/\pi$, which suggests that the bottom corners of the rectangle have very little effect on the field (Muennemann et al. [38] drew the same conclusion, for non-uniform fields in the Born limit).

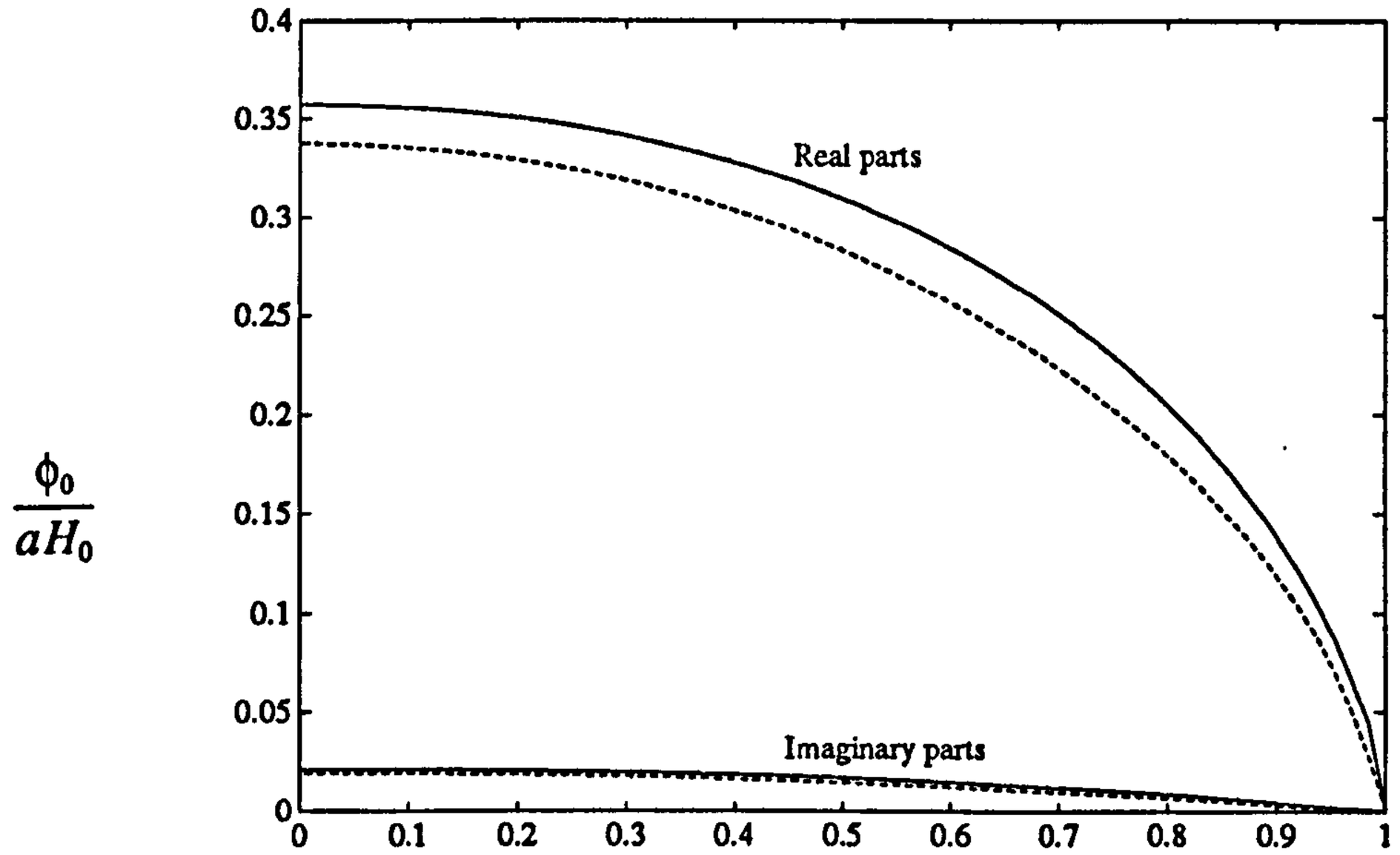

Fig 3.9 Crack lip potential calculated from series solutions for m=1.
Rectangle a/b=2 (solid line)
Semi-ellipse a/b=2 (broken line)

The real part of ϕ_0 at x=0 is given in table 3.2 for the same aspect ratios and m values as in table 3.1.

Table 3.2 Crack Lip Centre Potentials for a Semi-Ellipse

b/a	ϕ_0 at x=0 m=0	ϕ_0 at x=0 m=1	ϕ_0 at x=0 m=10^{10}
0.1	0.090675339	0.093721680	0.099498749
0.2	0.1641954	0.1741654	0.1959595
0.3	0.2227121	0.2410264	0.2862321
0.4	0.2684473	0.2950294	0.3673674
0.5	0.3036140	0.3376096	0.4374709
0.6	0.3304173	0.3706823	0.4960952
0.7	0.3507092	0.3960856	0.5439311
0.8	0.3660512	0.4155043	0.5823002
0.9	0.3774944	0.4301321	0.6127397
1.0	0.3863492	0.4415018	0.6367425

3.9 Boundary Element Solution

McIver [110] has also solved the general m problem for arbitrary crack shape by the boundary element method. The two-dimensional Green's function

$$G = \frac{1}{2\pi}\ln[(x-x')^2+(z-z')^2] \tag{3.9.1}$$

is used, which has the property

$$\frac{\partial G}{\partial z} = 0 \quad \text{at } z = 0, z' = 0. \tag{3.9.2}$$

The boundary integral equation, 2.3.4, is applied to the potential ϕ with this Green's function to give

$$\phi(x',0) = -\int G(x,z,x',0)\frac{\partial \phi(x,z)}{\partial n}\mathrm{d}s, \tag{3.9.3}$$

which may be rewritten as

$$\phi(x',0) = -\int \psi(x,z)\frac{\partial G(x,z,x',0)}{\partial s}\mathrm{d}s. \tag{3.9.4}$$

A second Green's function

$$G_1 = G(x,z,x',z') - G(x,z,x',-z') \tag{3.9.5}$$

is then constructed which has the property

$$G_1(x,0,x',z') = 0. \tag{3.9.6}$$

The conjugate function to G_1 is

$$H_1 = \frac{1}{\pi}\tan^{-1}\frac{z-z'}{x-x'} - \frac{1}{\pi}\tan^{-1}\frac{z+z'}{x-x'} \tag{3.9.7}$$

so that G_1 and H_1 obey the Cauchy-Riemann equations in x and z. The boundary integral equation, applied to ψ and G_1 takes the form,

$$\psi(x',z') = \int \psi\frac{\partial G}{\partial n}\mathrm{d}s \tag{3.9.8}$$

and may be rewritten as

$$\psi(x',z') = \int \psi\frac{\partial H_1}{\partial s}\mathrm{d}s. \tag{3.9.9}$$

Equations 3.9.4 and 3.9.9 can be very conveniently discretized because, if the potentials are approximated with simple constants over each element, the integrals become finite series. Together with the convolution boundary condition 3.6.18, they give a complete set of linear algebraic equations from which the potentials can be found. This boundary element solution was tested against the semi-elliptical and rectangular solutions and found to give very good agreement. Fig. 3.10 is a reproduction of fig. 3.9, with data points from McIver's program superimposed.

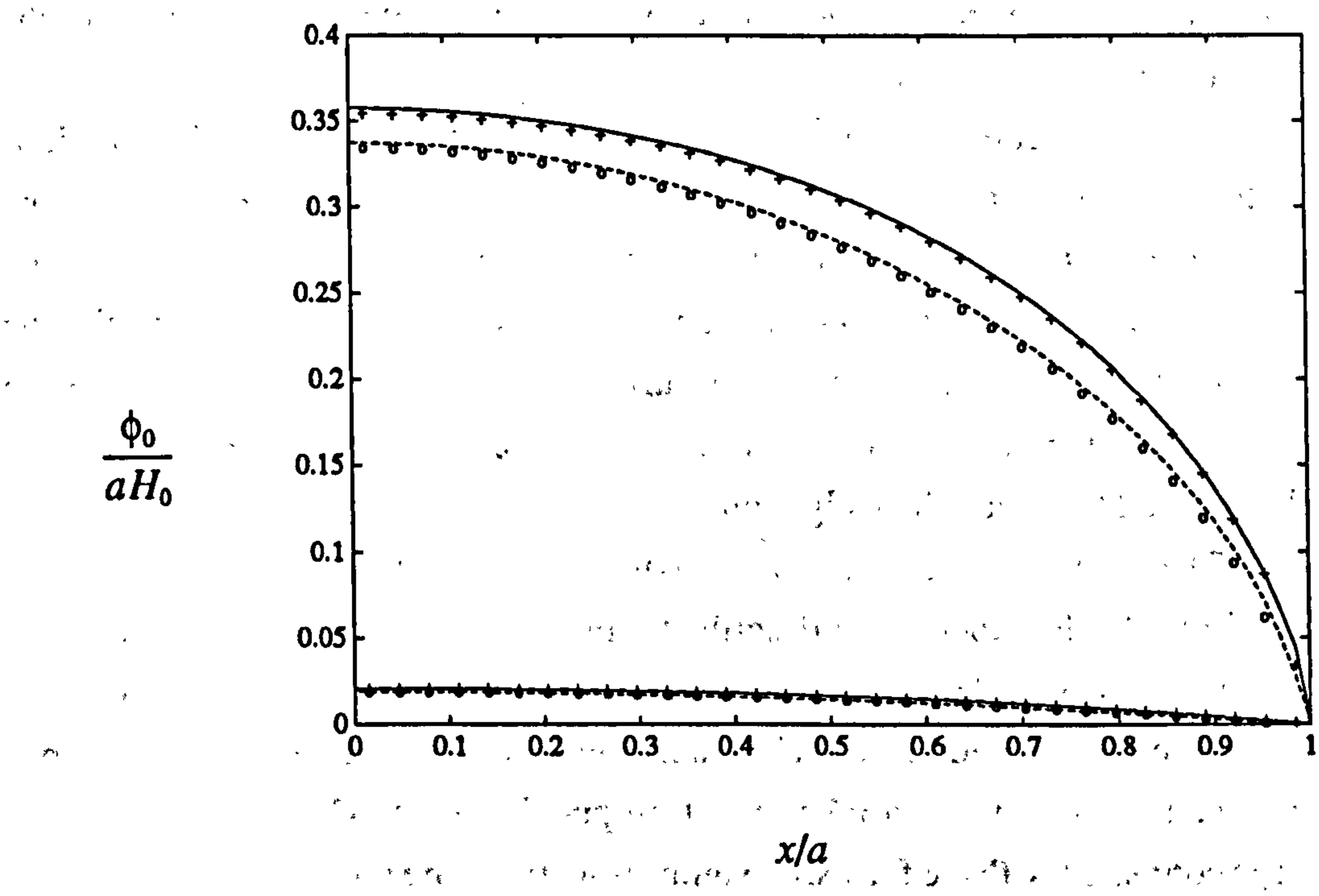

Fig 3.10 Comparison of series and boundary element solutions for m=1.

Rectangle a/b=2 Series solution (solid line)

Boundary element solution (crosses)

Semi-ellipse a/b=2 Series solution (broken line)

Boundary element solution (circles)

4 Experiments

4.1 Introduction

This chapter describes experimental work undertaken to verify the general m theory described in the last chapter. Thin-skin magnetic fields near surface-breaking cracks and notches were investigated in different materials and over a wide range of frequencies using search coils. A computer-controlled x-y table, driven by stepping motors and lead-screws was used to scan over flat-plate specimens at fixed height. New computer programs were written to control the measuring instrument, to synchronise measurements with the movements of the x-y table and to acquire data.

In order to compare the experimental results with the theoretical predictions of the previous chapter, it is necessary to know the value of the parameter m, which depends on the frequency, crack length and material properties. It is shown that the relevant material constant can be inferred from the ratio of the electric and magnetic fields on the test-piece surface. This ratio was measured over the required frequency range for a number of test-pieces, including the ones used for the detailed flaw-field investigations.

The m-dependent behaviour predicted by the theory is quantitatively confirmed by the experiments described in this chapter. Not only are the principal features of the signal observed, but some quite subtle features of the signal shape are correctly predicted as well. The main limitation of the theory is that it assumes that the test-piece is of infinite extent. In practice, even when the test-piece is large compared with the flaw size, significant effects are observed because of the edges of the test-piece. Likewise, the signals are also sensitive to non-uniformities in the applied field.

4.2 Apparatus

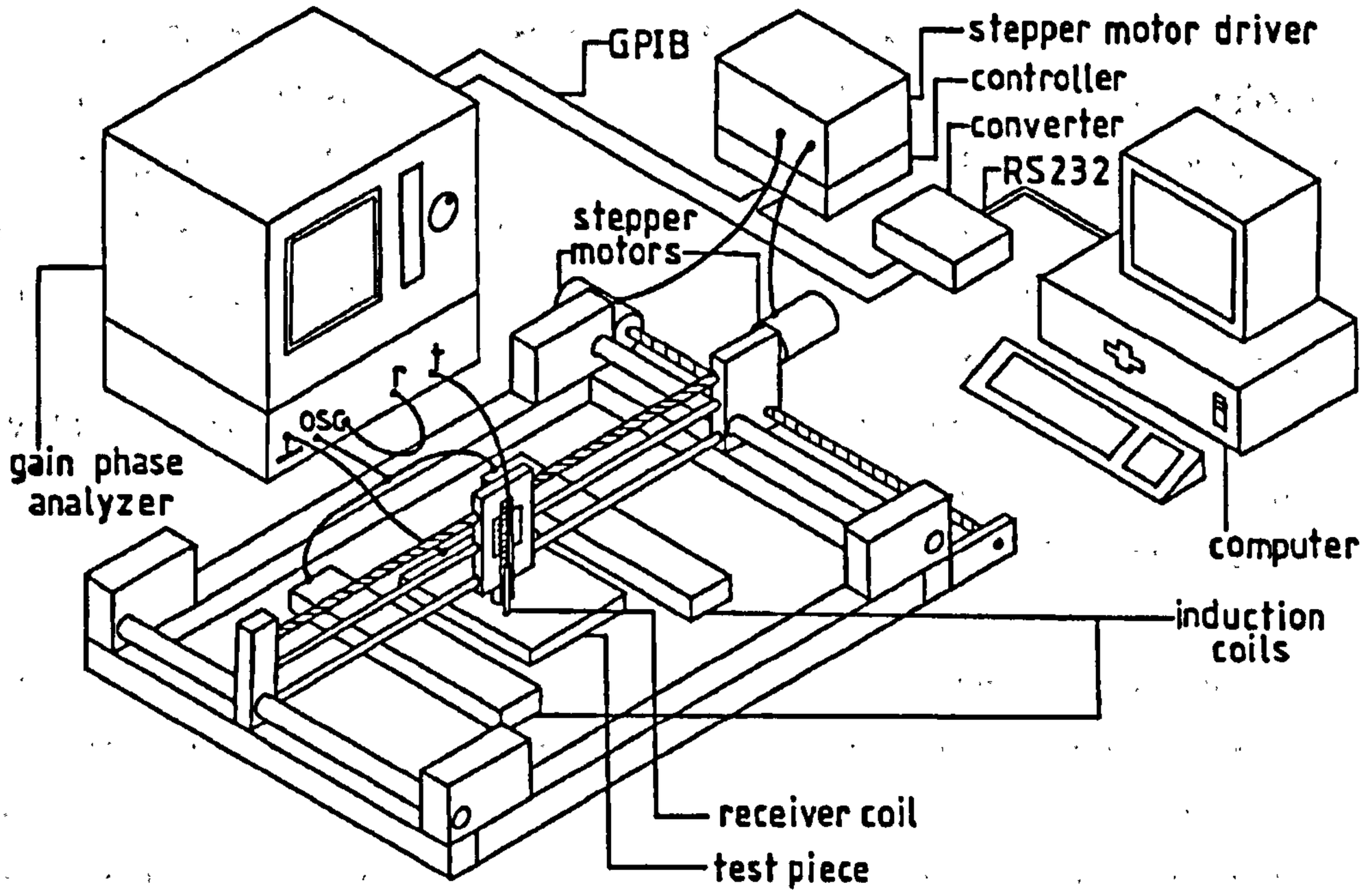

Fig. 4.1 Principal Experimental Apparatus.

The basic experimental arrangement is shown in fig. 4.1; modifications for specific experiments are explained individually below. The system is based on a Hewlett-Packard 4194A Impedance/Gain-Phase Analyzer, used both to provide the exciting current and to measure the voltage across the search coils. In fig.4.1, the receiver coil is shown as being connected to the test channel of the analyzer, marked "t", and one side of the dual output oscillator is connected to the reference channel, marked "r" ; the other side of the oscillator is connected to the induction coils. The analyzer was configured to measure the gain and phase between the test and reference channels. A direct connection is also shown between the test-piece and the instrument case, this is a precaution against interference and is discussed below. The search coils were made very much smaller that the flaw lengths and were designed so that, as far as possible, they did not change the fields in which they were placed. The use of small coils eliminates the need to average the theoretical predictions over the sampling volume and gives spatially

detailed maps of the fields. However, the signals obtained from the coils are in proportion to their area and their number of turns, so the price of using small coils is that the voltages that need to be measured are also small and very careful precautions have to be taken to eliminate interference. The search coils were wound from very thin wire, in order to get as many turns as possible in a given volume. The signal strength could also have been increased by using ferrite-cored receiver coils, but the magnetic field distribution would have been altered by the presence of the ferromagnetic cores and the signals would not have been directly proportional to the theoretical field values as calculated in the previous chapter. For this reason, the coils were constructed with cores of nylon or perspex. The presence of a thick coaxial cable near the test-piece might also conceivably alter the field, so each coil was connected to its cable via a few centimetres of unscreened twisted wire pair.

The theoretical models to be tested assume that the unperturbed field is uniform, so an important requirement of the apparatus is the production of such a field. It is well-known that a pair of Helmholtz Coils, coaxial circular coils separated by one radius length, give a highly uniform field in the free-space region near the centre. Unfortunately, no such simple arrangement is known that gives a uniform field in the presence of a metal test-piece at all frequencies. Therefore, an empirical approach was adopted in which two long rectangular coils were placed along the specimen sides and moved around until the field was reasonably uniform, in the absence of a flaw.

Strictly speaking, the reference channel should be connected to a reading of the applied field strength, for example from a second search coil. It could be argued that movements of the x-y table would alter the impedance of the induction coils and thus change the applied field strength achieved for a given oscillator voltage. However, in practice the impedance of the coils was not measurably affected by table movement and the arrangement of fig. 4.1 was satisfactory.

The coils were energized by connecting them directly to the analyzer's own oscillator, which is designed to supply up to 4.4V to a load matched with the oscillator's 50Ω output impedance. The purpose of matching the impedance of the load to the impedance of the oscillator is to couple as much power as possible into the load, but this is not necessarily a critical factor in very low voltage measurement. It is much more important to ensure that the energizing currents

do not cause the instrument ground to deviate excessively as the oscillator output is changed [111], because all the measured signals are referred to this ground. In the experiments described here, the typical signals were of the order of 20μV, or five orders of magnitude below the oscillator voltage, so very great care was needed to avoid interference. Fortunately, ground errors cause large common-mode interference which can be detected easily when using phase sensitive instruments because the signal does not reverse sign when the measuring coil is reversed.

To overcome the ground fluctuation problem, it was necessary to find a way to couple a relatively high current into the test-piece whilst drawing as low a current as possible from the instrument. In order to do this, energizing coils with a large number of turns were used. (Another method would have been to use a buffer output stage, drawing current from a power supply with a separate ground, e.g. a battery). For the lower frequencies, below 150kHz, a set of coils with about 400 turns each were found to give acceptable common-mode errors. In order to obtain a wide range of m values it was necessary to go to frequencies well above the resonant point of this coil set. At these frequencies, hardly any signal is coupled into the specimen by the 400 turn coils because stray capacitances short them out. A second set of coils with only 20 turns were made for the higher frequencies, up to about 1.5MHz. Ground errors did not occur on these higher frequency measurements because the inductive reactance of the 20 turn coils was sufficient to keep the output current low and the measured voltages across the search coils were higher.

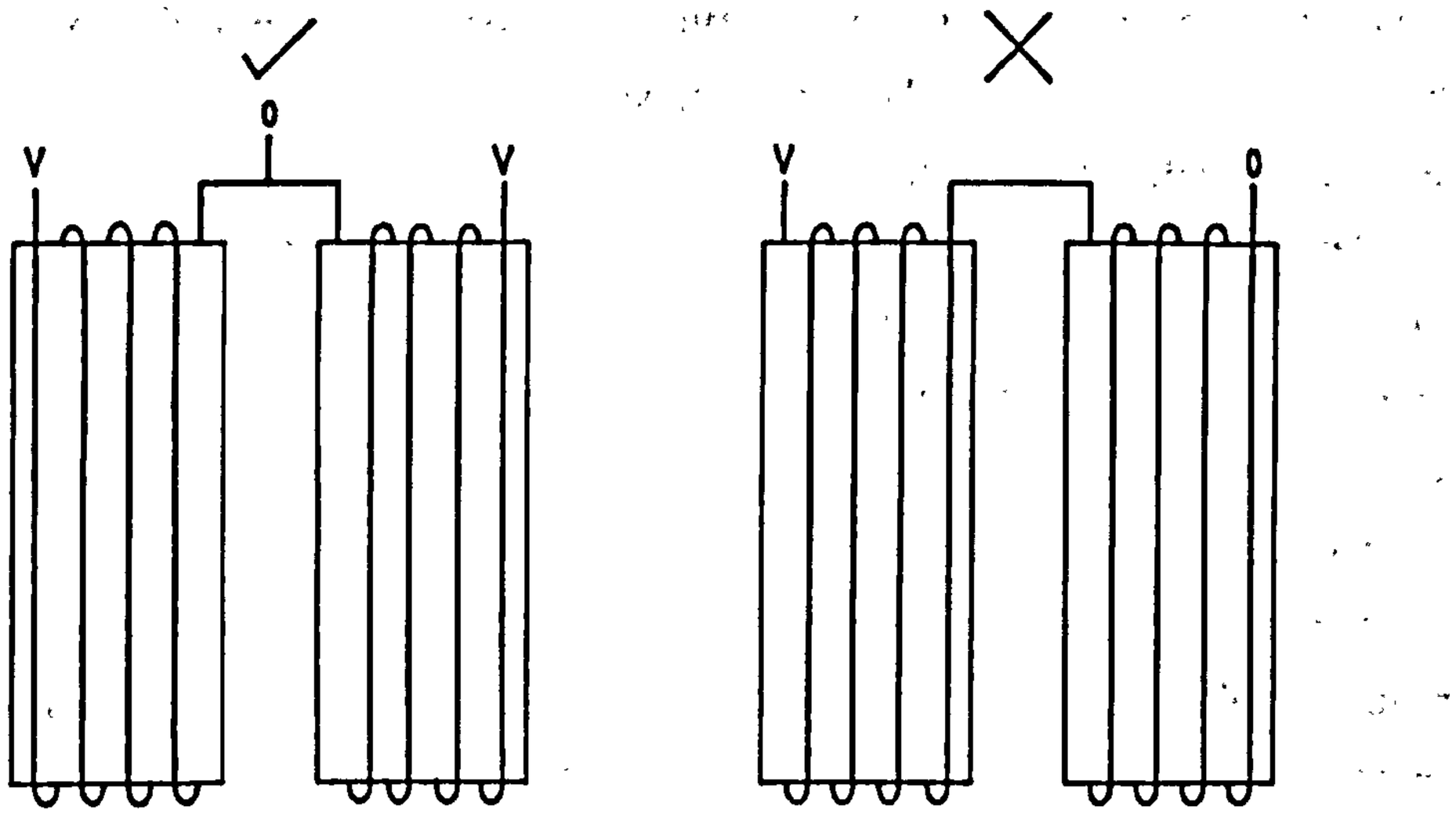

Fig. 4.2 Correct and incorrect wiring of induction coils

Another source of common-mode errors in low voltage measurements is the finite common-mode rejection ratio of the measuring amplifier. As mentioned above, the signals to be measured were much smaller than the oscillator output voltage so this type of common-mode error was a serious problem, especially when the probes made electrical contact with the test-piece. For the higher frequencies, where capacitive coupling between the search coils and the test-piece was large, common-mode errors occurred even without electrical contact. The energizing coil sets were originally made with both coils wound with the same chirality and connected in series. This arrangement was found to be unsatisfactory because the test-piece was then in a plane at about half the oscillator voltage. A much better arrangement was adopted (fig. 4.2) with the two coils wound with opposite chirality (one right-handed and one left-handed) and connected in parallel so that the test-piece was in a plane at about ground voltage, greatly decreasing the common-mode errors. In the experiments where only non-contacting probes were used, additional protection was obtained by connecting the test-piece directly to instrument ground. It was not possible to do this when a probe made contact with the test-piece because a ground-loop [111] would have been formed.

At the time the experiments were began, in March 1989, a stepper motor driven x-y table was in existence in the Mechanical Engineering Department which had been set up by Dr Darius Mirshekar-Syahkal for the purpose of verifying ACPD models with a fixed frequency instrument. Computer control was effected using a PDP-11 computer and a digital to analogue converter which produced clock pulses to trigger the stepper motor drive circuitry. Some of the control programs were written in assembler code. It would have been possible to incorporate the HP-4194A analyzer into this system, but it was decided instead to modernize the computer control arrangement in order to eliminate the need for assembler programming, to guard against failure of the old hardware and to allow for the addition of other equipment in the future.

The basis of the system is a GPIB interface across which both the x-y table and the analyzer are controlled and data is transmitted. Other instruments can be connected to the interface if necessary, without changes to the hardware. A Tastronics TAS016 GPIB to RS232 converter is used to connect the system to a computer with a standard RS232 serial port. An IBM PS/2 model 50 was used for the measurements reported here, because it happened to be available, but almost any personal computer would suffice. All the software was written in interpreted BASIC. The GPIB is a parallel bus which allows data to be transmitted at a higher rate than the serial line. However, in these low voltage measurements it is necessary to allow a fairly long time for the analyzer to acquire the primary data, in order to eliminate random noise, so the transmission speed on the serial line makes a negligible contribution to the total time taken. For example, a single complex number data point is typically measured in about 7s, stored as eight bytes of eight bits each and takes only 0.013s to transmit at 4800 baud. Use of the RS232 serial port to connect the system enables it to be controlled from many metres away if necessary, eliminates the need to install additional circuit boards in the computer and allows the computer to be replaced easily. However, by far the greatest advantage of the system is the simplicity of the control programs. The 4194A analyzer can measure up to 401 points in each sweep, which gives a data set that is small enough to be accommodated directly by the computer's input buffer without the need for handshaking, providing that the interpreter is invoked with a qualifier instructing the computer to enlarge the buffer.

The stepper motors are driven from a 24V supply by two Parker Digiplan LD2 drive boards via 44Ω current-limiting resistors. Manual controls are provided for initial positioning when setting up experiments. This part of the system is essentially unchanged from Mirshekar-Syahkal's original apparatus. In the new system, a Parker Digiplan 1185A control board is used to connect the stepper drive boards to the GPIB. This circuit has the ability to control a third stepper motor if needed. The LD2 drive boards are operated in the half-step mode in which the currents are of full and half strengths alternately, giving 400 steps per revolution. Lead screws with a pitch of 4mm converted the rotations of the stepper motors into translational motion with a resolution of 0.01mm. No errors were detected when the table was instructed to move repeatedly through prescribed lengths alongside a rule. The speed of the x-y table was in the range $8mms^{-1}$ to $12mms^{-1}$, but it was not a critical factor in maintaining precision.

Movement of the probes in a vertical direction was not controlled automatically, so scans were restricted to constant lift-off. A non-conducting, non-magnetic Vernier caliper was screwed to the head of the x-y table and the receiver coil attached with putty, allowing the lift-off to be controlled with a resolution of 0.05mm. In the most careful series of experiments, described in section 4.5, the test-piece was ground flat and paper shims were used to level it so that the same lift-off was measured at all points over the surface. Lift-off was taken to be the distance from the plate surface to the centre of the receiver coil.

4.3 Measurement of the Material Constants

In order to test the model it is necessary know the value of m. From 3.4.1, m can be calculated given the crack length and the quantity μ,δ, which, from 2.1.2, depends on the material constant μ_r/σ and the operating frequency. The surface tangential electric field **E** and magnetic field **H**, apart from at the crack line itself, obey the usual equations of the surface impedance boundary condition,

$$E_y = +Z_s H_x, \tag{4.3.1}$$

$$E_x = -Z_s H_y, \tag{4.3.2}$$

where x,y are the coordinates tangential to the metal surface and

$$Z_s = \frac{i+1}{\sigma\delta} = (i+1)\sqrt{\frac{\pi f \mu_0 \mu_r}{\sigma}} \tag{4.3.3}$$

is the surface impedance. Therefore, by measuring E and H on the surface for a given frequency it is possible to infer the value of the constant μ_r/σ.

This technique has the advantage that it may be used on any shape of test-piece, providing that it has a small flat area to which the necessary probes can be attached. It is important that the field strength is kept small, as in the flaw measurements themselves, so that the correct incremental permeability is measured. The values obtained apply on the surface of the metal only and are not necessarily valid deep inside the test-piece.

A field with a region of high uniformity was induced in the test piece with a pair of rectangular induction coils, as explained above. The analyzer was configured to measure the gain and phase between two input channels V_E and V_H. The head of the x-y table was not moved during the material constant measurements, but it provided a convenient support for the probes.

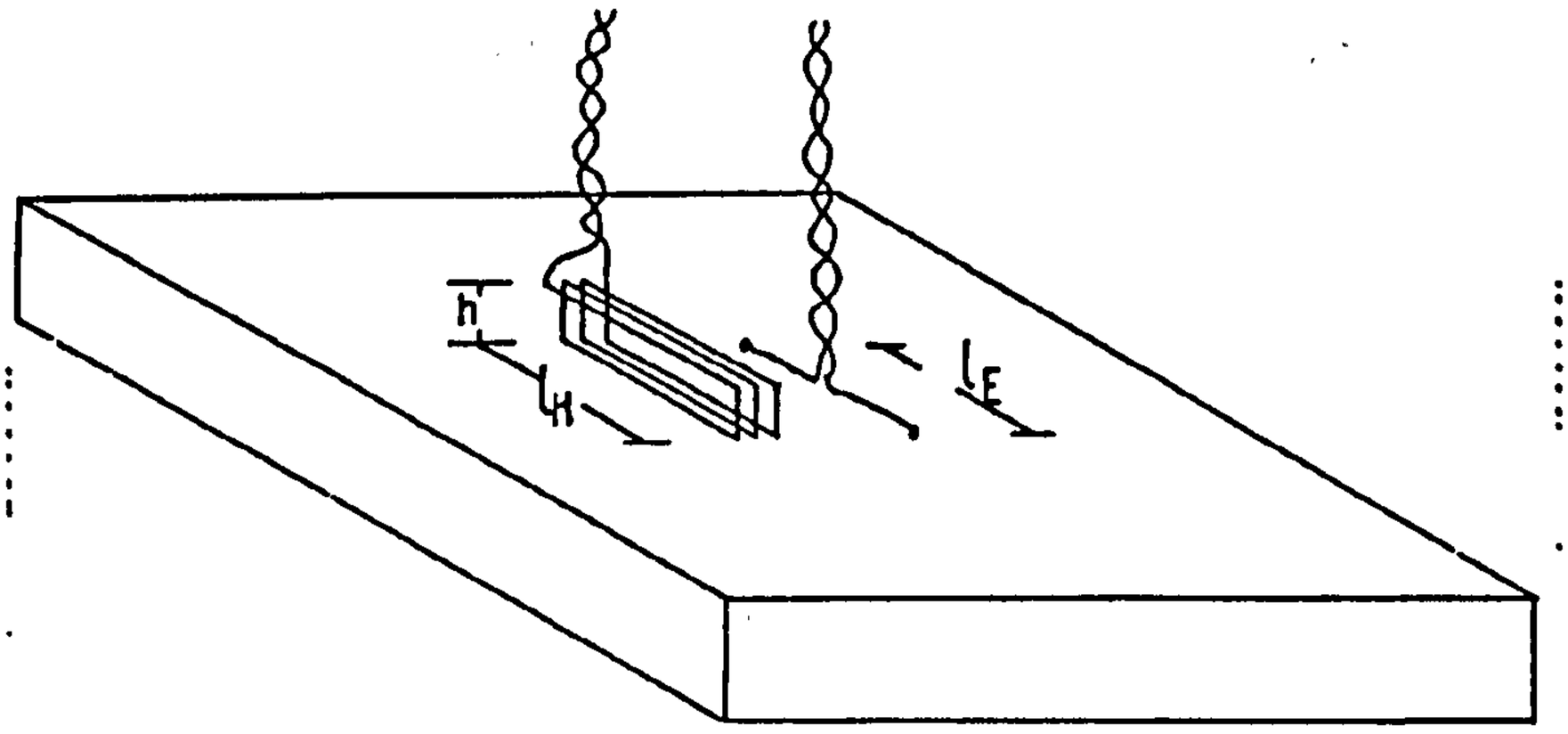

Fig. 4.3 Experimental apparatus for material constant measurement.

Two contacts placed a distance l_E apart on the test-piece surface in the uniform-field region, well away from any flaws, were connected to the first channel as in fig.4.3 so that

$$V_E = l_E E_y - 2\pi i f \mu_0 H_x A \tag{4.3.4}$$

where A is the area of the loop formed by the probe leads and the test piece. No connection was made to instrument-ground, in order to avoid forming a ground-loop. The probe was designed to keep A as small as possible. A coil of width l_H, height h with N turns, placed immediately adjacent to the contacting probe was connected to the second channel so that

$$V_H = -2\pi i f \mu_0 H_x N l_H h. \tag{4.3.5}$$

From 4.3.1, 4.3.4 and 4.3.5, the gain/phase measured between the two channels was therefore

$$V_E/V_H = \frac{A}{l_H h N} + \frac{i l_E}{l_H h N}\frac{Z_s}{2\pi f \mu_0} = \frac{A}{l_H h N} + \frac{(i-1) l_E}{2 l_H h N}\mu_r \delta. \tag{4.3.6}$$

The coaxial cable connecting the probes to the analyzer was kept as short as possible (about 300mm) to reduce electrostatic interference. After one sweep through the desired frequency range, the induction coils were interchanged, to reverse the sign of the field with respect to the phase of the oscillator and the

sweep was then repeated. The final value for V_E/V_H was taken as the average of the two complex numbers representing the readings for the two senses, so that any remaining common-mode errors were eliminated.

The real and imaginary parts of V_E/V_H were plotted against $f^{-1/2}$ over a range of frequencies in a variety of materials. If the permeability and conductivity are simple constants, independent of field strength, direction and frequency, the gradients should be equal and opposite and of magnitude

$$\frac{l_E}{2l_H Nh}\mu_r\delta\sqrt{f}=\frac{l_E}{2l_H Nh}\sqrt{\frac{\mu_r}{\pi\mu_0\sigma}} \quad . \tag{4.3.7}$$

In all the samples tested, the plots were close to straight lines as expected; some examples are shown in figs.4.4-4.7. Values for the constant μ_r/σ were found from the data by least squares fitting. The line for the imaginary part was constrained to pass through the origin but the line for the real part was offset, in order to allow for the term in A. Probe dimensions are given in table 4.1.

Table 4.1 Dimensions of probes

l_H	19.15 ± 0.02mm
l_E	20.0 ± 0.5mm
N	28
h	2.89 ± 0.01mm

In the following figures, the solid lines are the experimental data and the broken lines are the least-squares straight line fits.

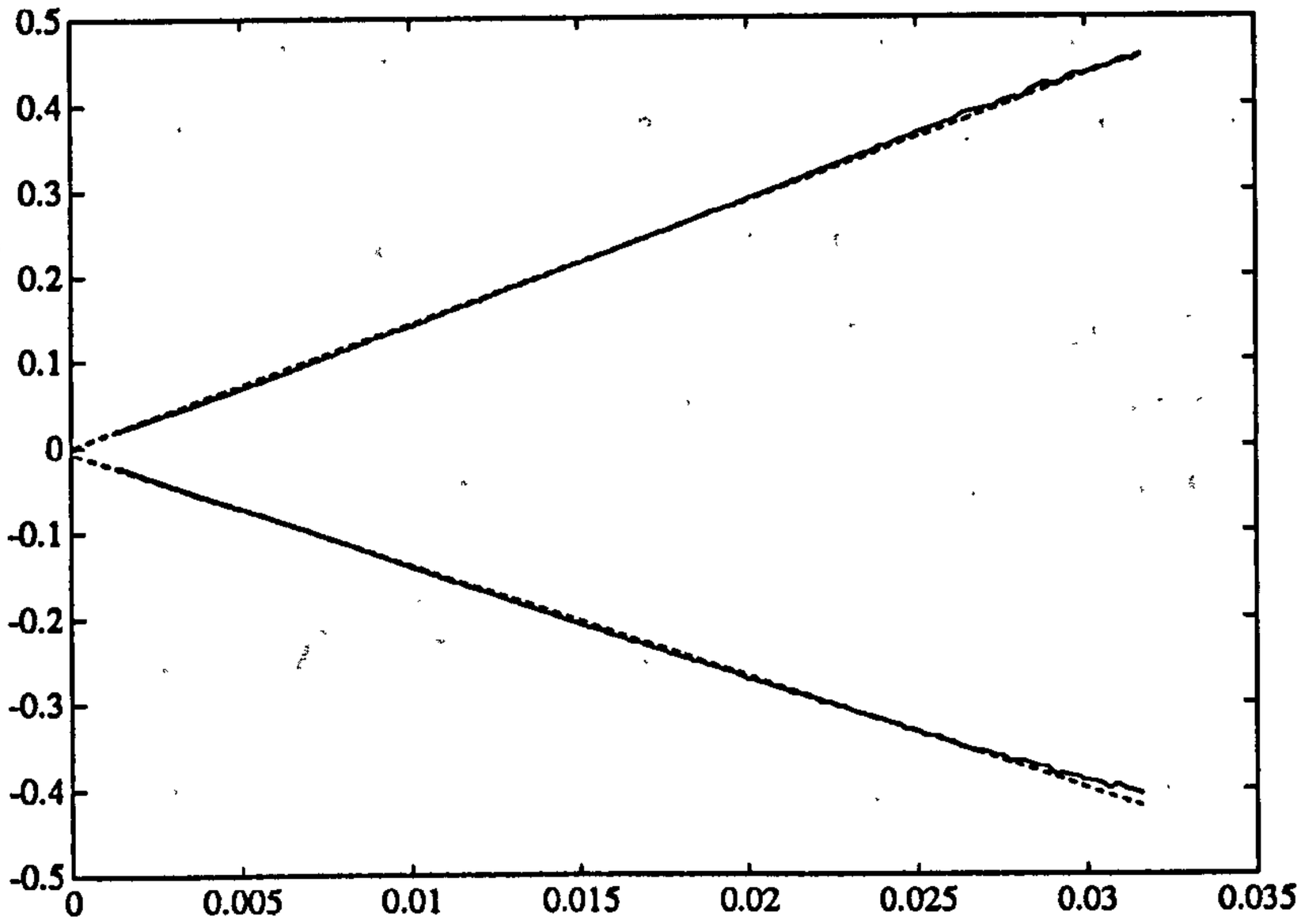

Fig. 4.4 V_E/V_H for mild steel
Frequency band: 1kHz-500kHz

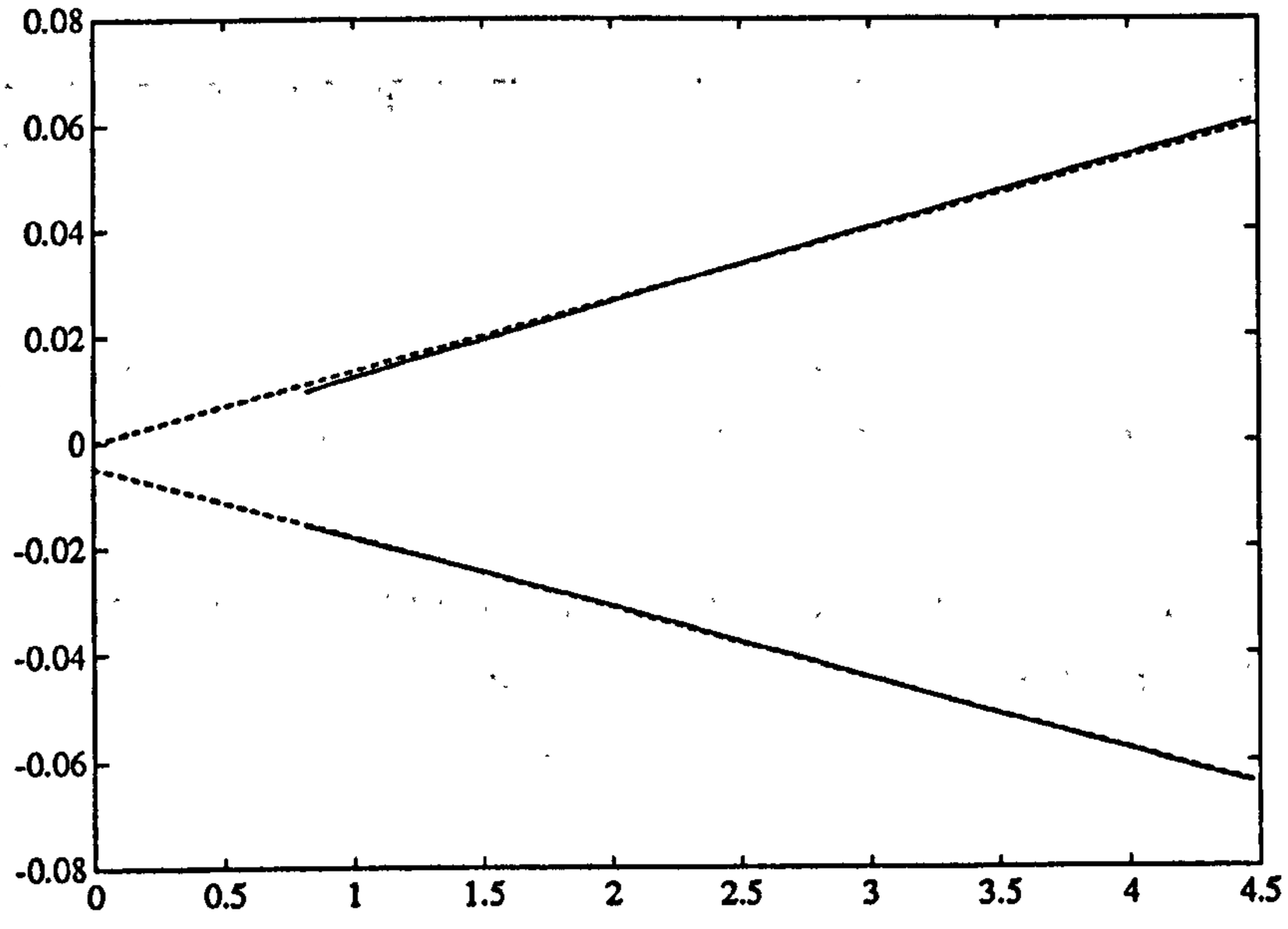

Fig. 4.5 V_E/V_H for mild steel
Frequency band: 50kHz-1.5MHz

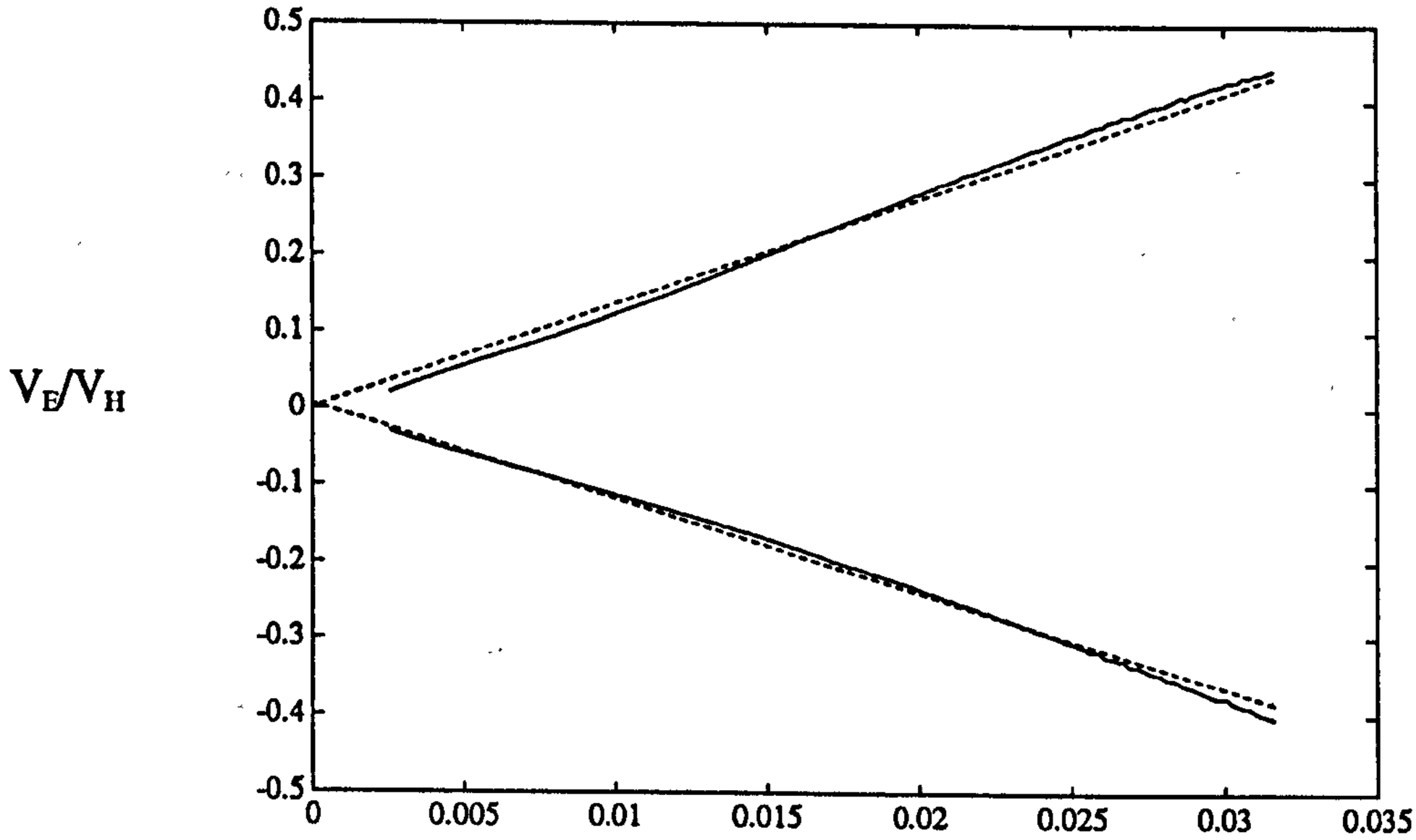

Fig. 4.6 V_E/V_H for high-strength steel AISI-4145

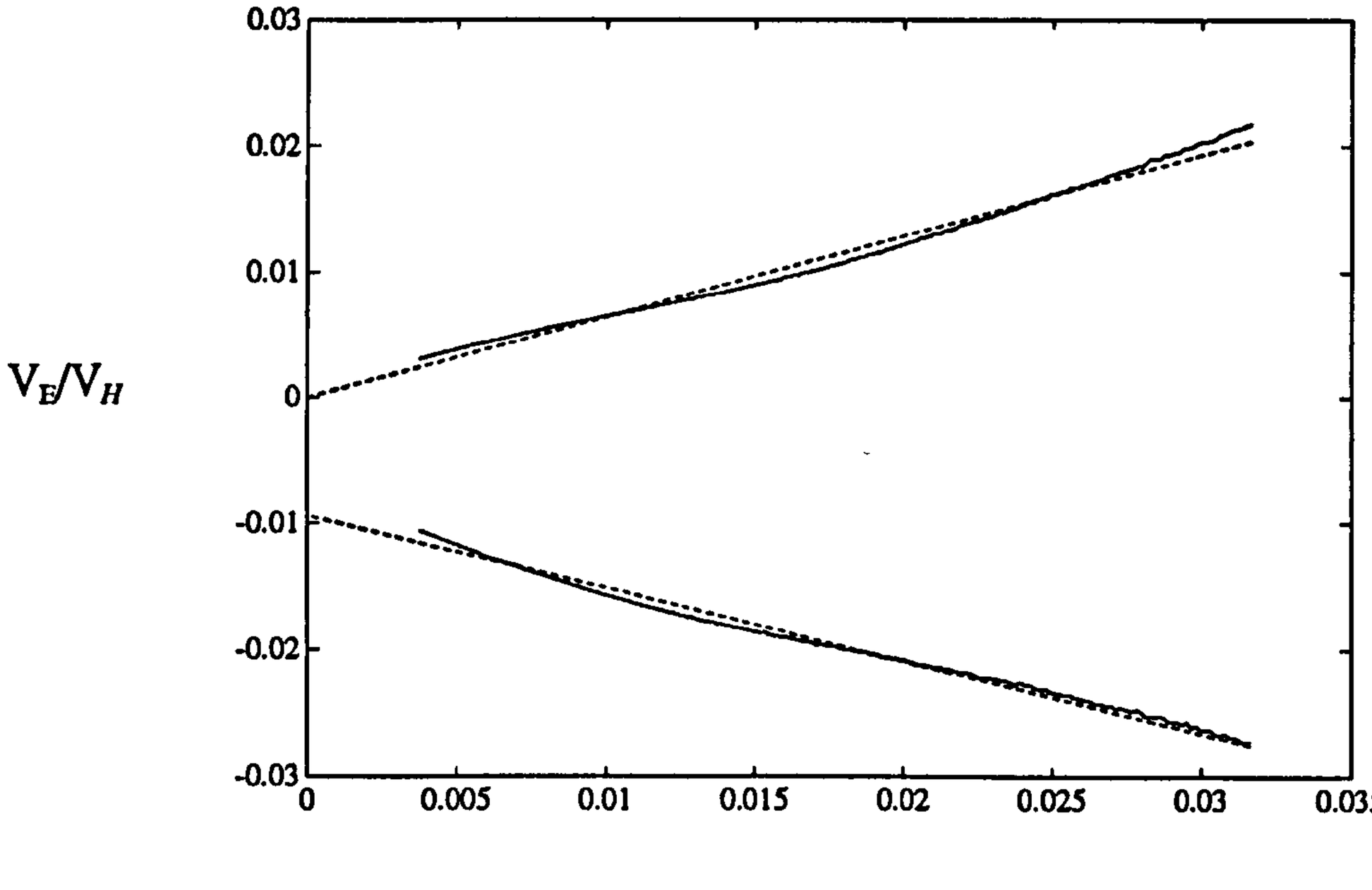

Fig. 4.7 V_E/V_H for Dural NS8

The probe lengths l_E and l_H were made nearly equal so that the two fields were being measured over the same region. Random noise, as indicated by the standard deviation associated with fitting the straight lines, was negligible. The gain/phase was measured with the exciting coils in both orientations and the mean values of the two senses, for each of the real and imaginary parts, were used for line fitting. A lower bound on the experimental accuracy is 2.5%, the error in the measurement of the probe length l_E.

Results for several materials are shown in table 4.2. Structural steel 50D is a material used for making large welded-steel structures, such as oil-rigs. High-strength steel AISI-4145 is another material used in the oil industry, for making drilling equipment. Dural NS8 is an aluminium-based alloy of a type common in the aerospace industry. Austenitic stainless steel is a common metal, of interest because it is ferrous but not ferromagnetic.

The values of $\mu_r\delta$ for the ferromagnetic metals 50D, mild-steel and AISI-4145 are much greater than for the other two materials, as one would expect. All the phase values are close to 135° which is the theoretical phase for isotropic, homogeneous and non-hysteretic materials. The value of μ_r/σ for the Dural is

effectively just the resistivity $1/\sigma$ because the material is non-magnetic. For comparison, the resistivity of pure Al is $2.55 \times 10^{-8}\Omega$m [2]. The bandwidth over which measurements in Dural were practicable was low because the voltages on the contacting probe were very small. In general, the technique works better on ferromagnetic metals in which it is easier to induce a field. The low frequency μ_r/σ of 50D is lower in the heat affected zone than in the parent material. This effect it probably caused by a reduction of the permeability by the heating process, since Thompson, Allen and Turner [112] found a similar reduction for the d.c. permeability. However, the high frequency μ_r/σ is higher in the heat affected zone than in the parent metal.

A useful conclusion from these experiments is the approximate rule that $\mu_r \delta f^{1/2}$ in ferromagnetic steels is typically about 2000mm$\sqrt{\text{Hz}}$. For a given expected size of fatigue crack, it is therefore possible to pick an operating frequency such that the unfolding model applies.

Table 4.2 Results of Material Constant Measurements

Material	f/kHz	$\frac{\mu_r\delta\sqrt{f}}{mm\sqrt{Hz}}$	phase	$\frac{\mu_r/\sigma}{10^{-6}\Omega m}$
Structural steel 50D	1-150	2181	131.1°	18.78
	100-1500	1859	134.2°	13.64
High strength steel AISI-4145	1-150	2078	137.9°	17.05
Heat affected zone of weld in 50D	1-150	1785	136.7°	12.58
	100-1500	2155	137.6°	18.33
Dural NS8	1-70	97.29	131.8°	0.03737
Austenitic stainless steel	1-150	378.6	135.8°	0.5659
Mild steel plate (used in section 4.5)	1-500	2124	134.6°	17.82
	50-1500	2196	132.1°	19.04

4.4 Experiments to Verify the Asymptotic Limits

Before the general m solutions had been found, experiments were conducted with Mirshekar-Syahkal's apparatus to verify the limiting cases. The measuring instrument was a "Crack Microgauge" (an ACPD device of the type developed by Dover et al. and mentioned in section 2.2) with a search coil substituted for the contacting probe. The Microgauge is designed to inject a 2A current directly into the test-piece, so it was not necessary to use induction coils. The phase control was adjusted to maximise the response to the upstream field. This means that the measured fields signals were proportional to the part of the fields in phase with the upstream field (the real part). Data were acquired by the PDP-11 computer with an analogue to digital converter connected to the analogue output of the Microgauge. No modifications were made to the original software at this stage. A mild steel plate with a fatigue crack was used as an example of a flaw in the small m limit and a Dural plate with a semi-circular spark eroded notch of 0.8mm opening was used as an example of a flaw in the large m limit. The fatigue crack length was measured by magnetic particle inspection and its depth by conventional ACPD, using the one-dimensional formula 2.4.4.

Table 4.3 Flaws used in the Limiting Case Studies

Material	Block Size (mm)	Crack length $2a$ (mm)	Crack depth b (mm)	μ,δ (mm)	m
Mild steel	354×85×12.5	37	3.0	31.4	0.588
Dural NS8	310×201×25.6	40.35	20.0	1.26	16.0

(The value of m for the Dural block is based on the more accurate material constant measurements made with the new apparatus). Experimental measurements of H_z for the two flawed blocks are shown as crosses in fig.4.8 and 4.9. The Born approximation model is shown as a broken line and the unfolding model is shown as a solid line. Clearly, the field over the steel block follows the unfolding model and the field over the Dural block follows the Born approximation model, as expected. Fig. 4.10 and 4.11 show similar data for the

y component and, once again, the behaviour is as expected. Note that in all four plots the physically observed field corresponds to the model which gives the smaller perturbation. The theoretical data in the figures are more accurate than the theoretical data as published in reference [89] because these older calculations used the discontinuous function $H_z(x,0)$ rather than the continuous function ϕ_0 to generate the fields. However, the essential features are unaffected.

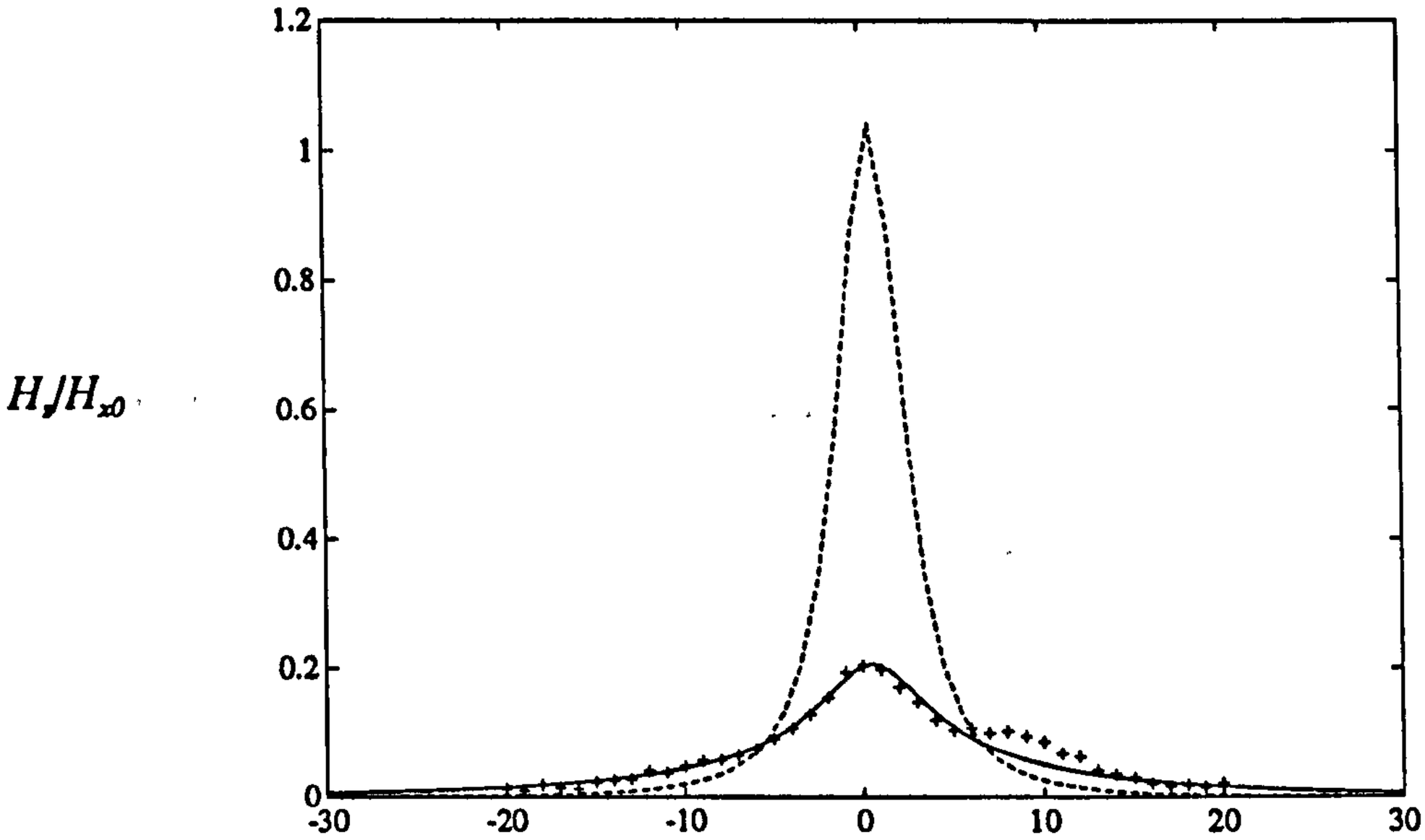

Fig.4.8 Magnetic field near a fatigue crack in a mild steel block
a=18.5mm, b=3.0mm H_z at x=14mm, z=2.0mm

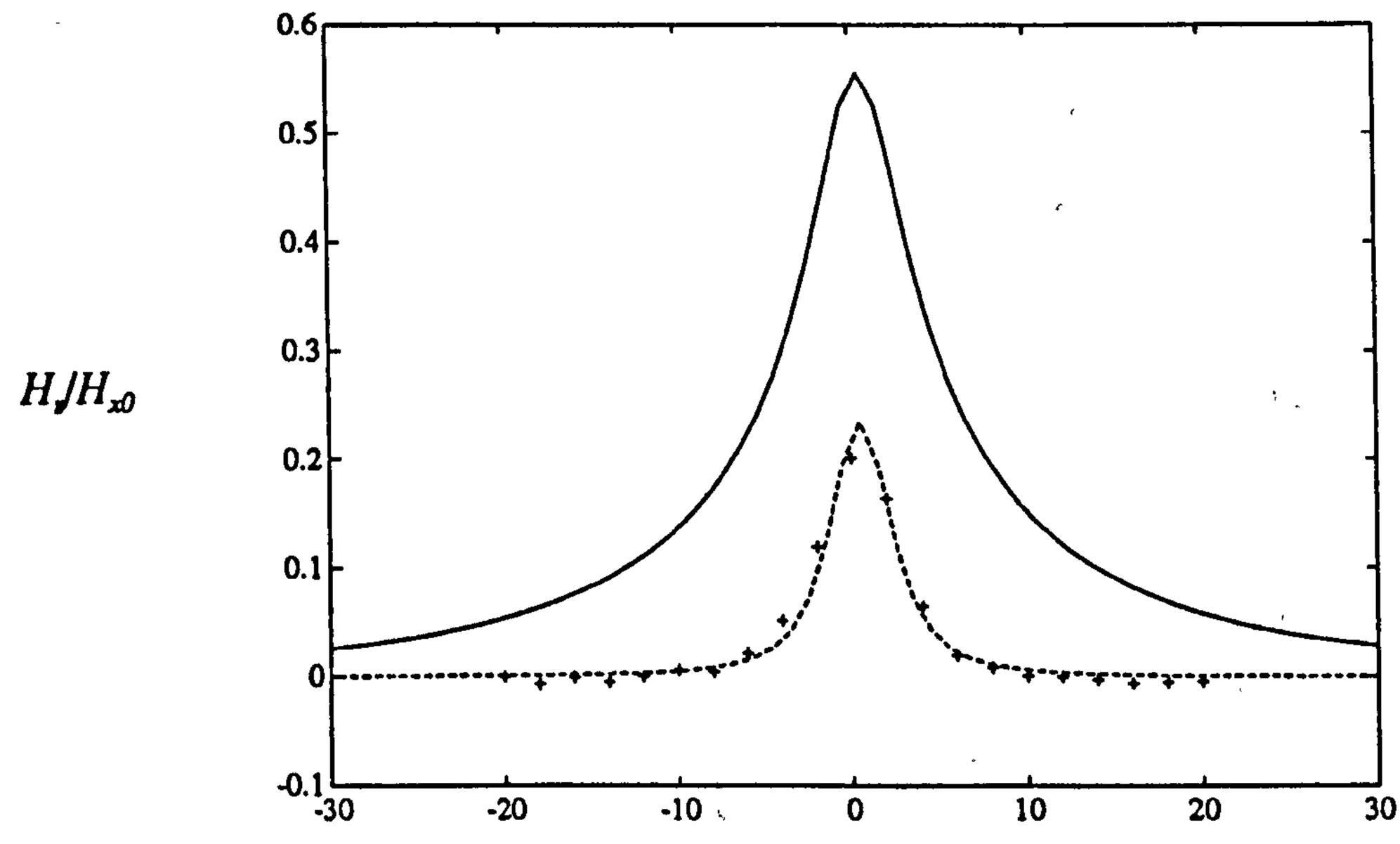

Fig.4.9 Magnetic field near an EDM notch in a Dural block
a=20.175mm, b=20.0mm H_z at x=20.175mm, z=2.0mm

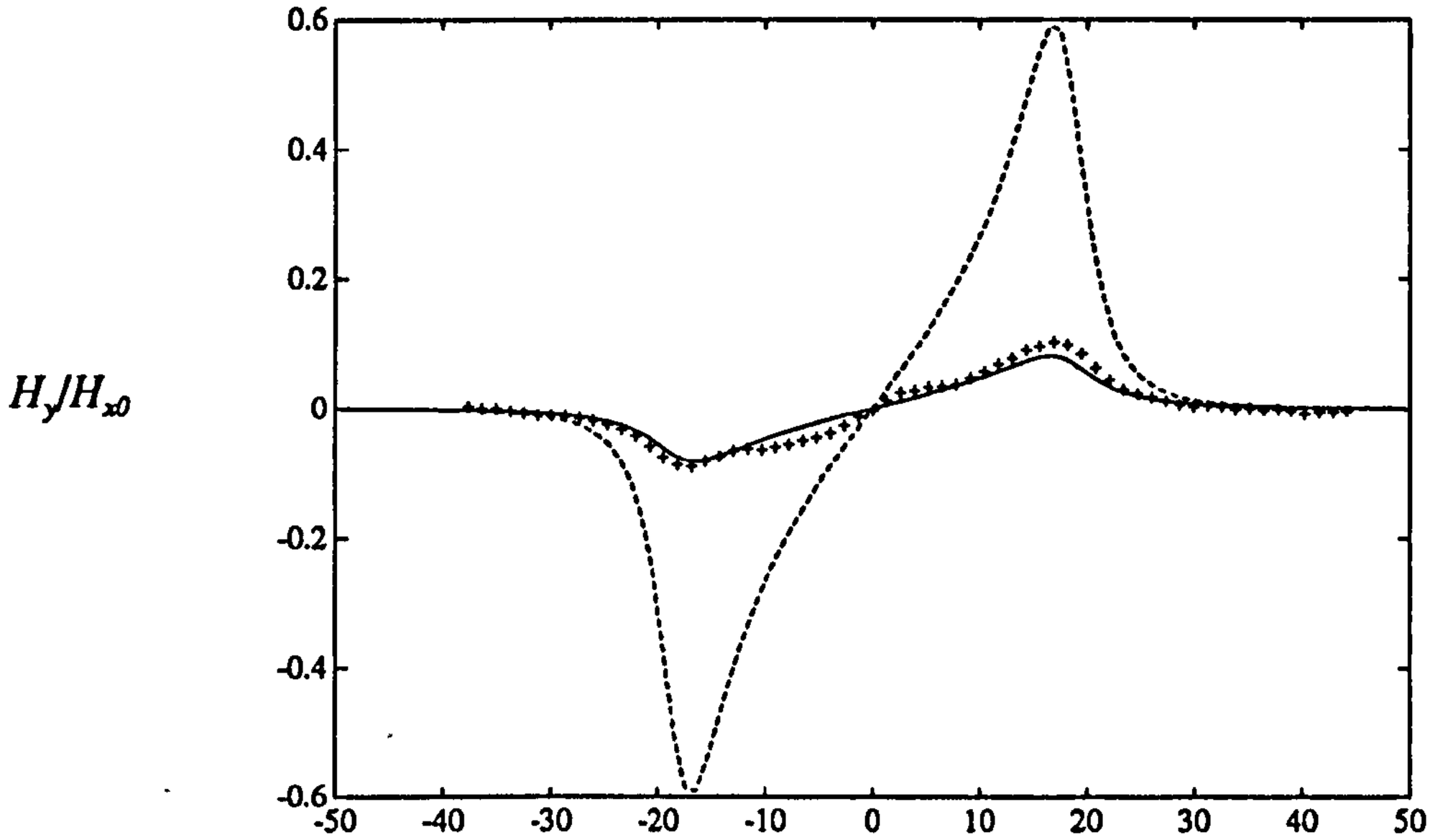

Fig.4.10 Magnetic field near a fatigue crack in a mild steel block
a=18.5mm, b=3.0mm H_y at y=3mm, z=2.0mm

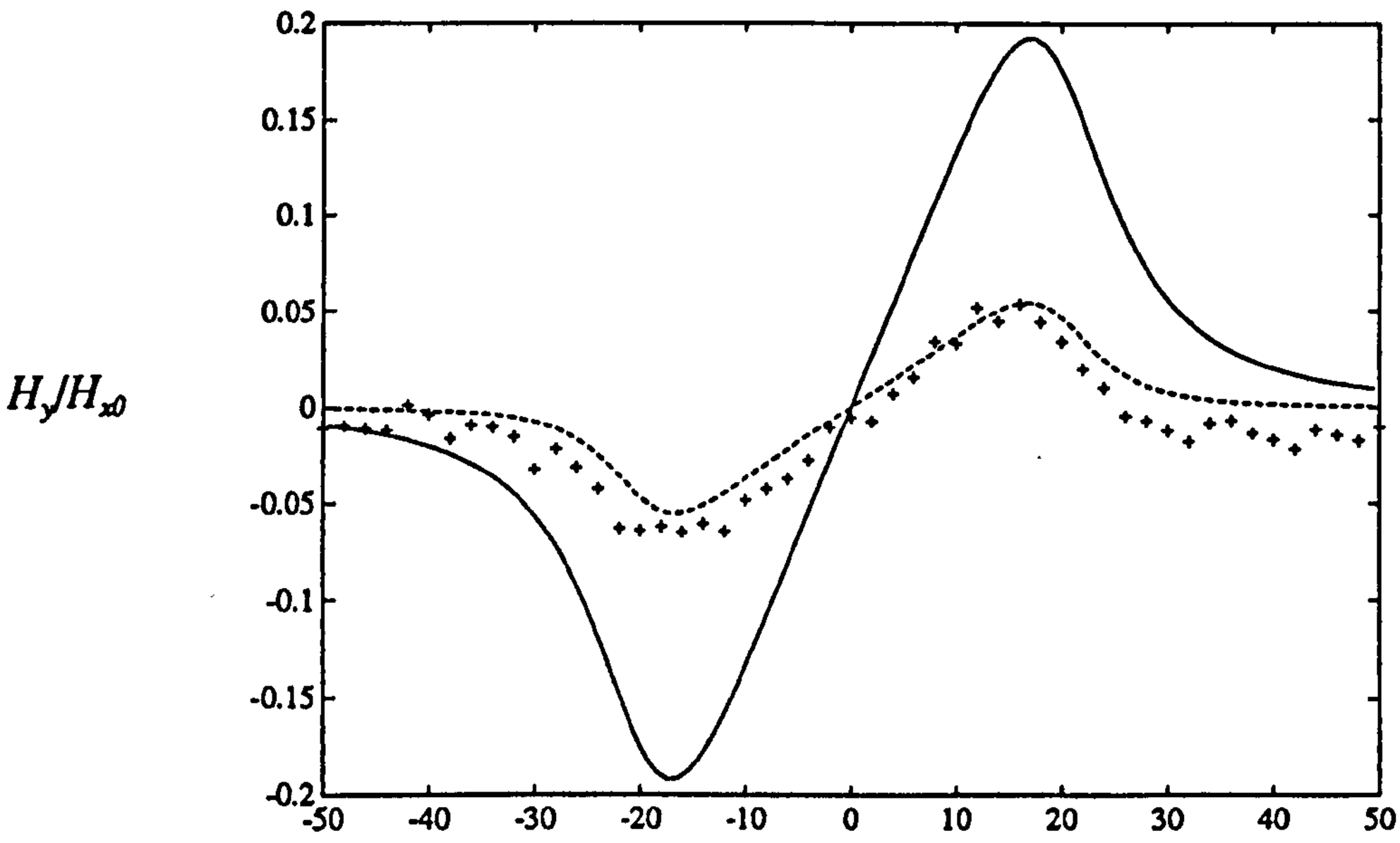

Fig.4.11 Magnetic field near an EDM notch in a Dural block
a=20.175mm, b=20.0mm H_y at y=7.0mm, z=2.0mm

4.5 Measurements of the Field Near a Rectangular Notch at General *m*

Once the general *m* solutions of the previous chapter had been obtained, it became desirable to verify the predicted behaviour for intermediate values of *m*. A rectangular electric discharge machined notch of length $2a$=30mm, depth b=15mm and opening h=0.75mm was made in a mild steel plate of dimensions 152×202×19mm in the x, y and z directions respectively and the plate was ground flat.

The material constant μ/σ was measured by the method of section 4.3, on part of the surface well removed from the notch. Using the average value for the two frequency ranges in table 4.2, $\mu\delta$=2160mm, frequencies were selected to give the values of *m* shown in table 4.4.

Table 4.4 Test frequencies and *m* values

f/kHz	*m*	Line style in figures
5.184	0.5	solid
20.736	1	broken
82.944	2	dotted
331.776	4	dot-dashed
1 327.104	8	dot-dot-dashed

Search coils were wound on perspex formers with overall coil dimensions in mm shown in table 4.5. (The y coil is just the x coil reorientated). Measurements of all three field components were made at the frequencies given in table 4.4, at a lift-off of 2.0mm, with the coils traversed through 120 steps of 0.5mm in the x direction. Similar scans were then conducted in the y direction. Once again, the final data are averages of readings conducted in both senses, to eliminate any residual common-mode errors. The theoretical predictions are given in terms of the applied field, so all the measurements were referred to the average field at y=2a, where the perturbation due to the flaw was small enough to be ignored.

Table 4.5 Dimensions of measuring coils

orientation	x dimension	y dimension	z dimension	Number of turns
x	3	2	2	200
y	2	3	2	200
z	4	2	1.5	100

Plots of the real parts of the x, y and z components of the field as calculated from the theory are given in figs.4.12a, 4.13a and 4.14a, for varying x at fixed y. The corresponding experimental measurements are shown in figs.4.12b, 4.13b and 4.14b. The line-styles for the various frequencies are listed in table 4.4. There is general agreement between theory and experiment to within about 5% of the applied field strength and the signals are correctly ranked with m. Fig. 4.15, 4.16 and 4.17 show the three components at fixed x, as y is varied. Once again, the observed field is as predicted by the theory.

Some subtle features of the fields are also correctly predicted. In fig.4.12a, the plot of H_x against x, the signal is flatter in the centre for large m, where the Born approximation is valid, and the flattening is seen in the experimental plot 4.12b. In fig. 4.13b, the gradient $\partial H_y/\partial x$ is slightly smaller at x=0 than at x=0.5a, as expected from the theoretical signal 4.13a. A similar change is seen in fig. 4.14a and 4.14b. An important feature of the fields is the quadrupole symmetry of the y component, that is to say, it is antisymmetric in both y and x, In particular, there is an abrupt change in sign on crossing the crack line near each of the crack ends, as shown in fig. 4.16a and 4.16b.

The theoretical field values also have a small imaginary part, so there ought to be a signal in quadrature with the applied field. Although it was too small to measure accurately, the quadrature signal was observed and the readings are shown in fig.4.18b, with theoretical values in fig.4.18a. The order of magnitude is correct and the maximum signal occurs for intermediate m, as predicted by theory.

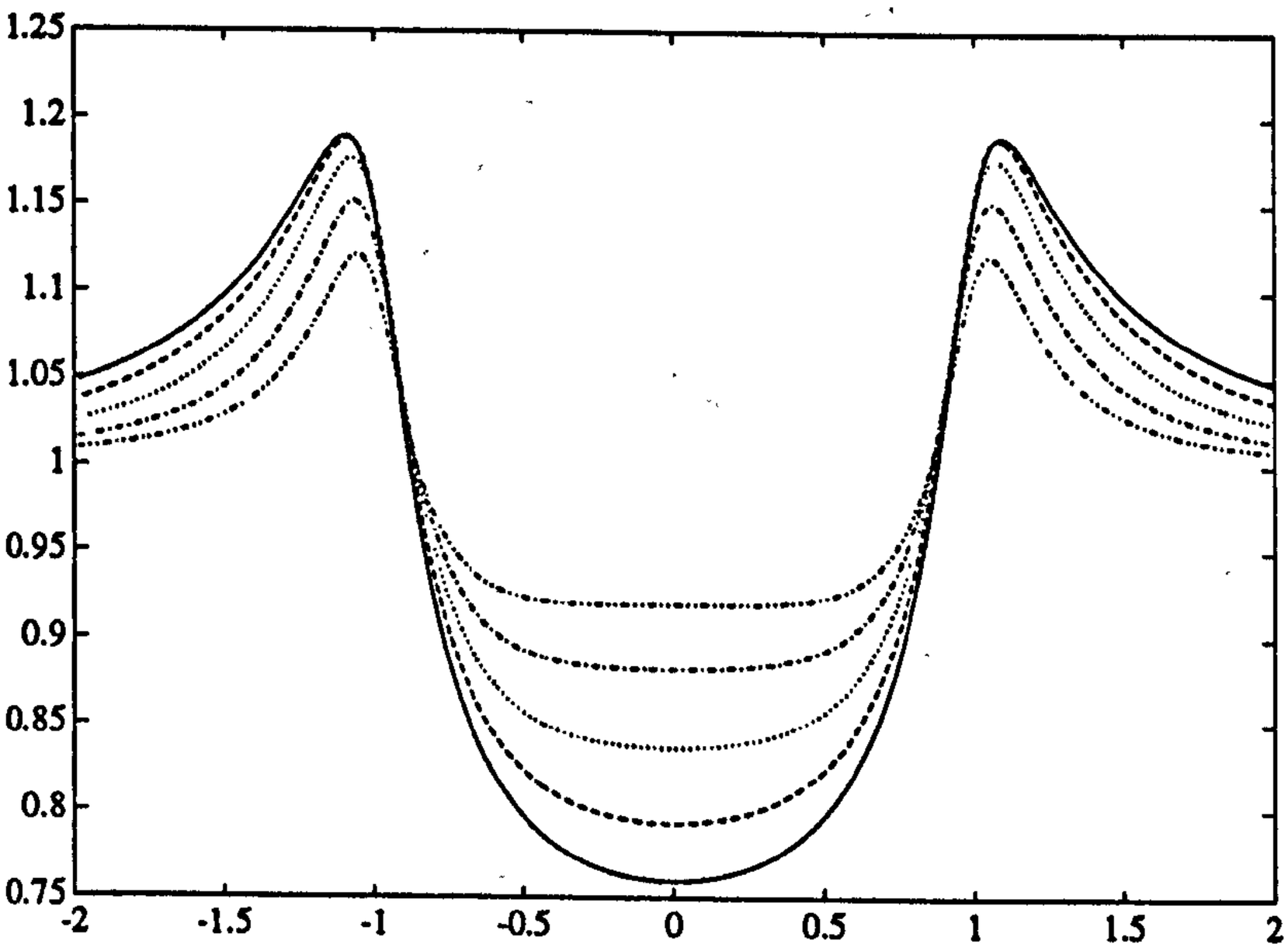

Fig.4.12a H_x at y=0 Theoretical

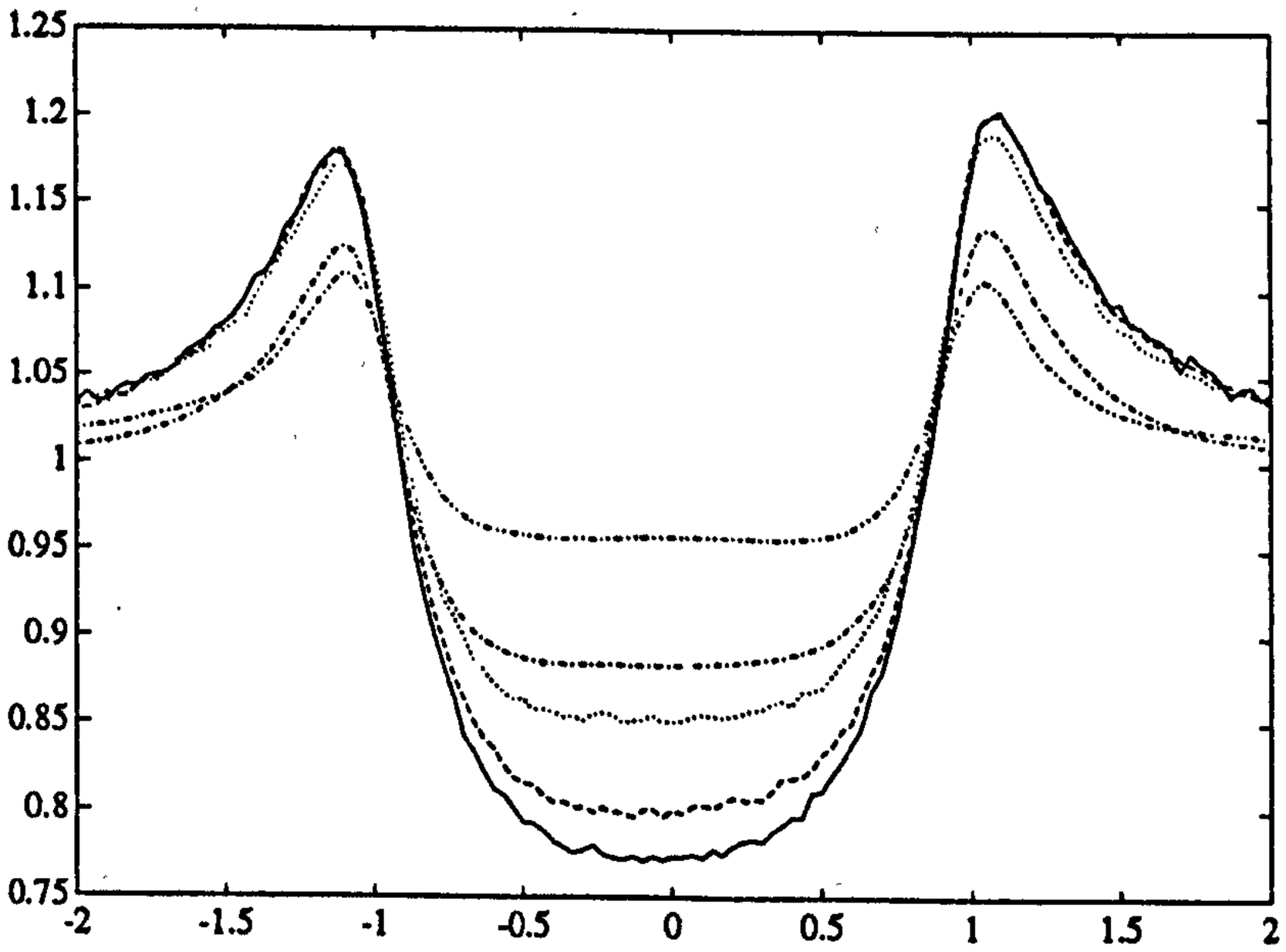

Fig. 4.12b H_x at y=0 Experimental

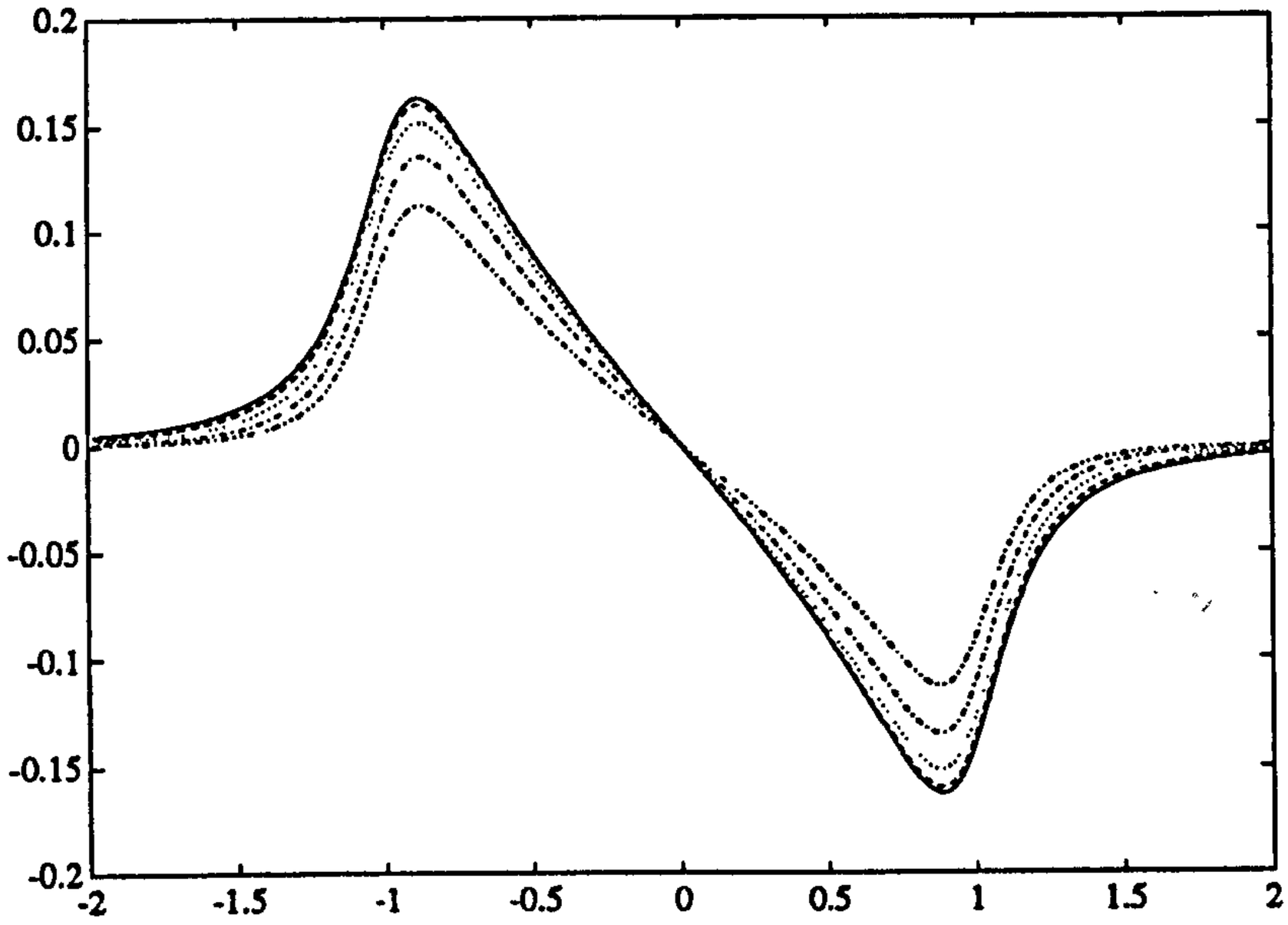

Fig. 4.13a H_y at y=0.1a Theoretical

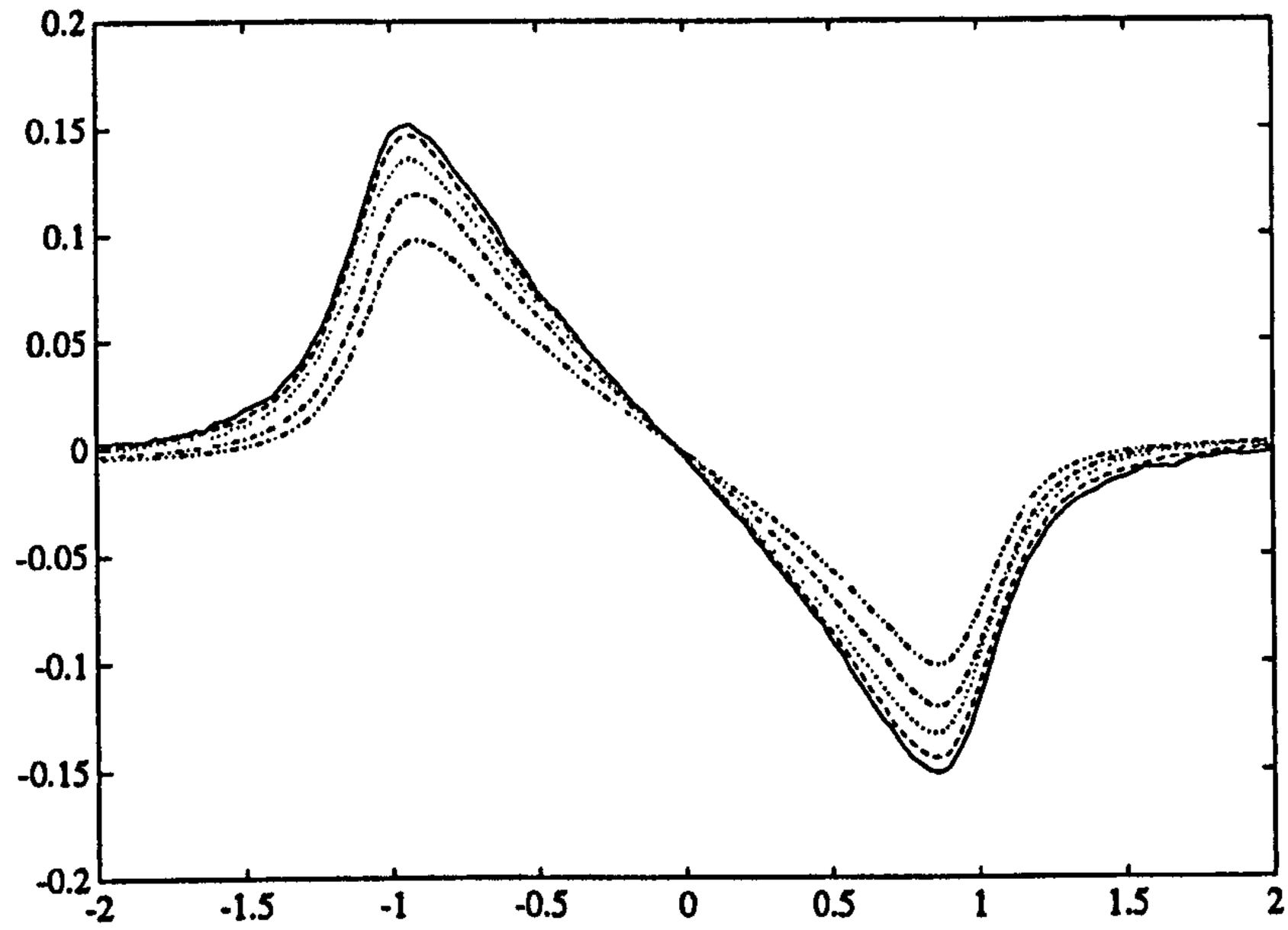

Fig. 4.13b H_y at y=0.1a Experimental

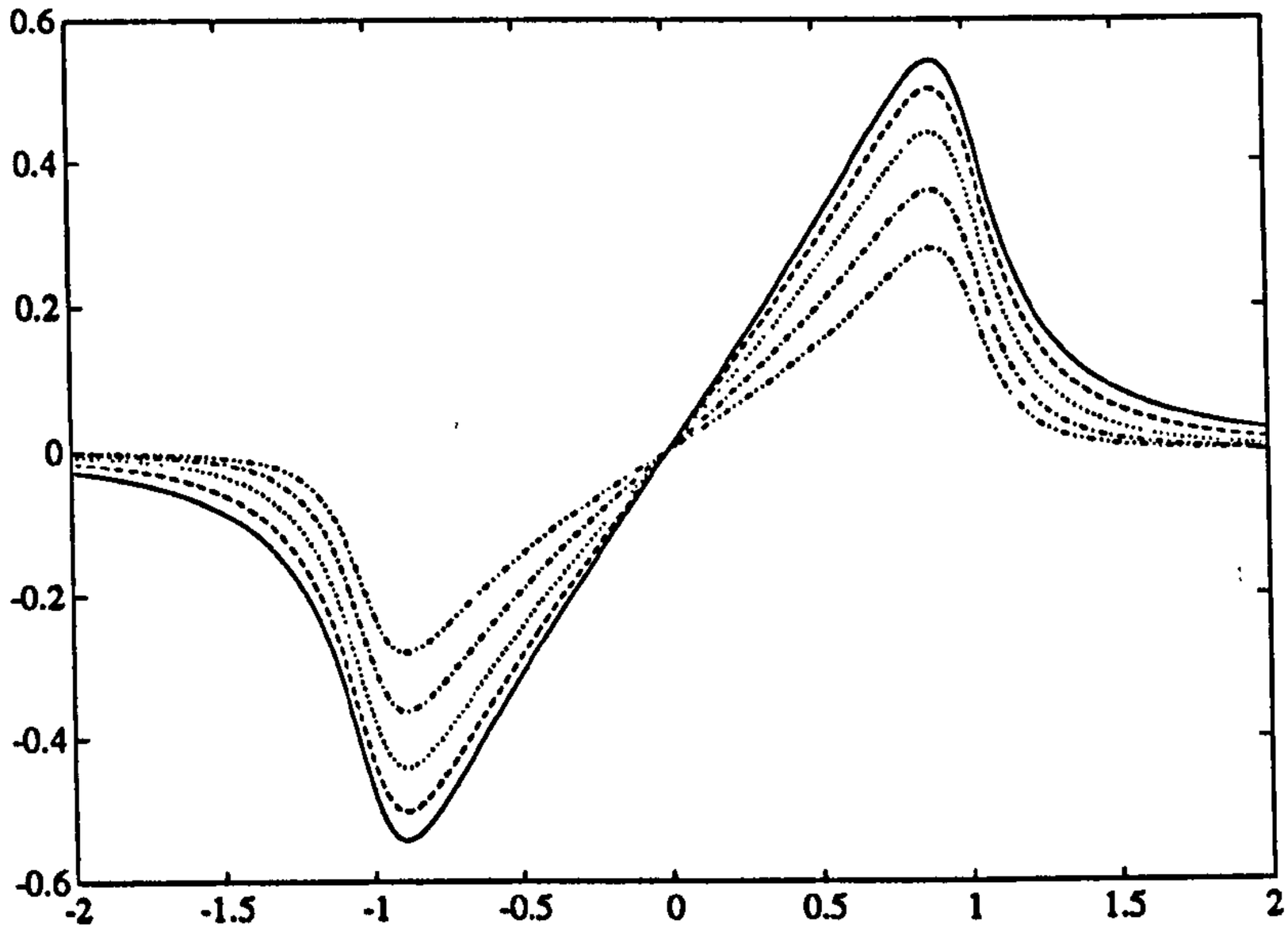

Fig. 4.14a H_z at y=0 Theoretical

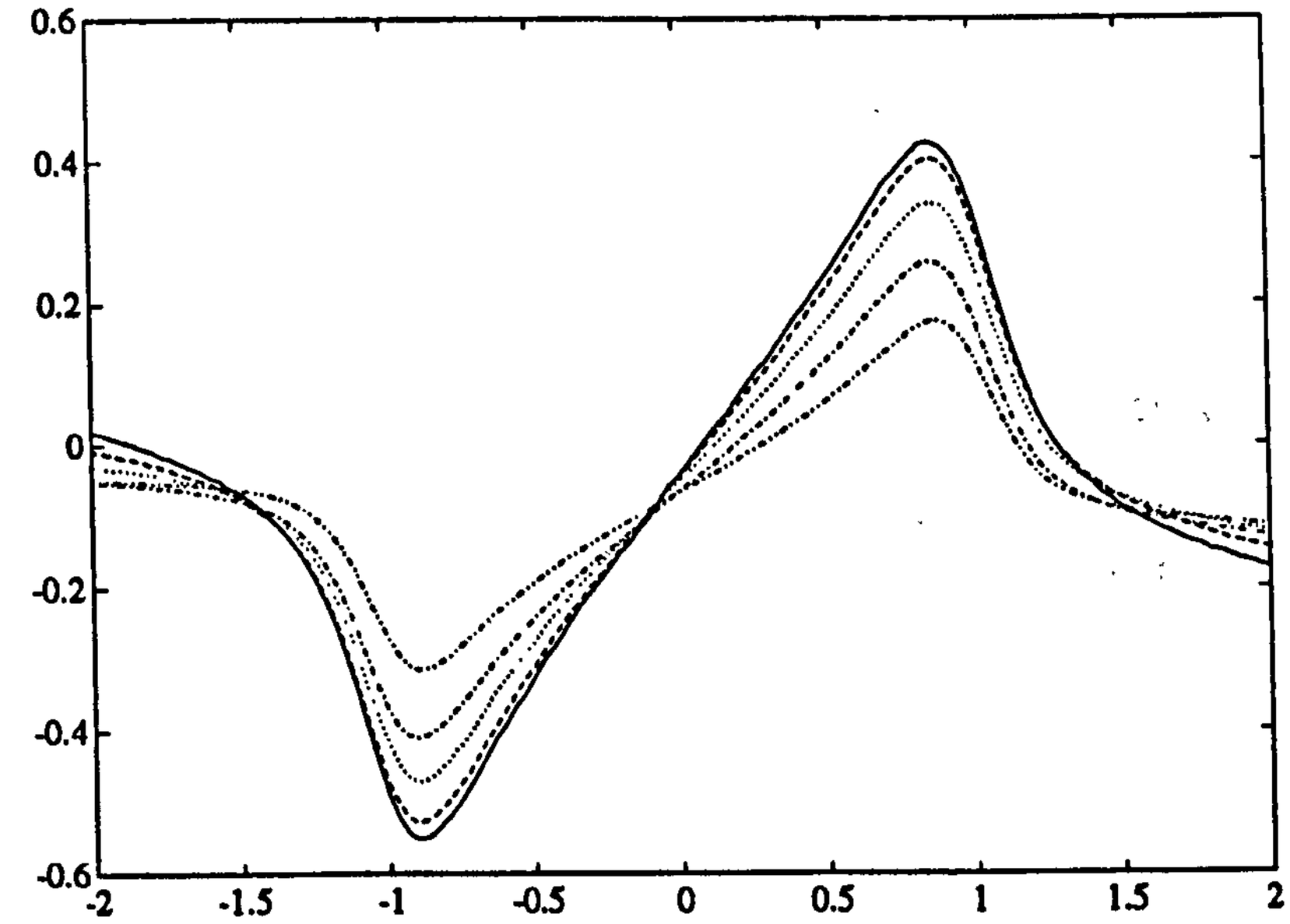

Fig. 4.14b H_z at y=0 Experimental

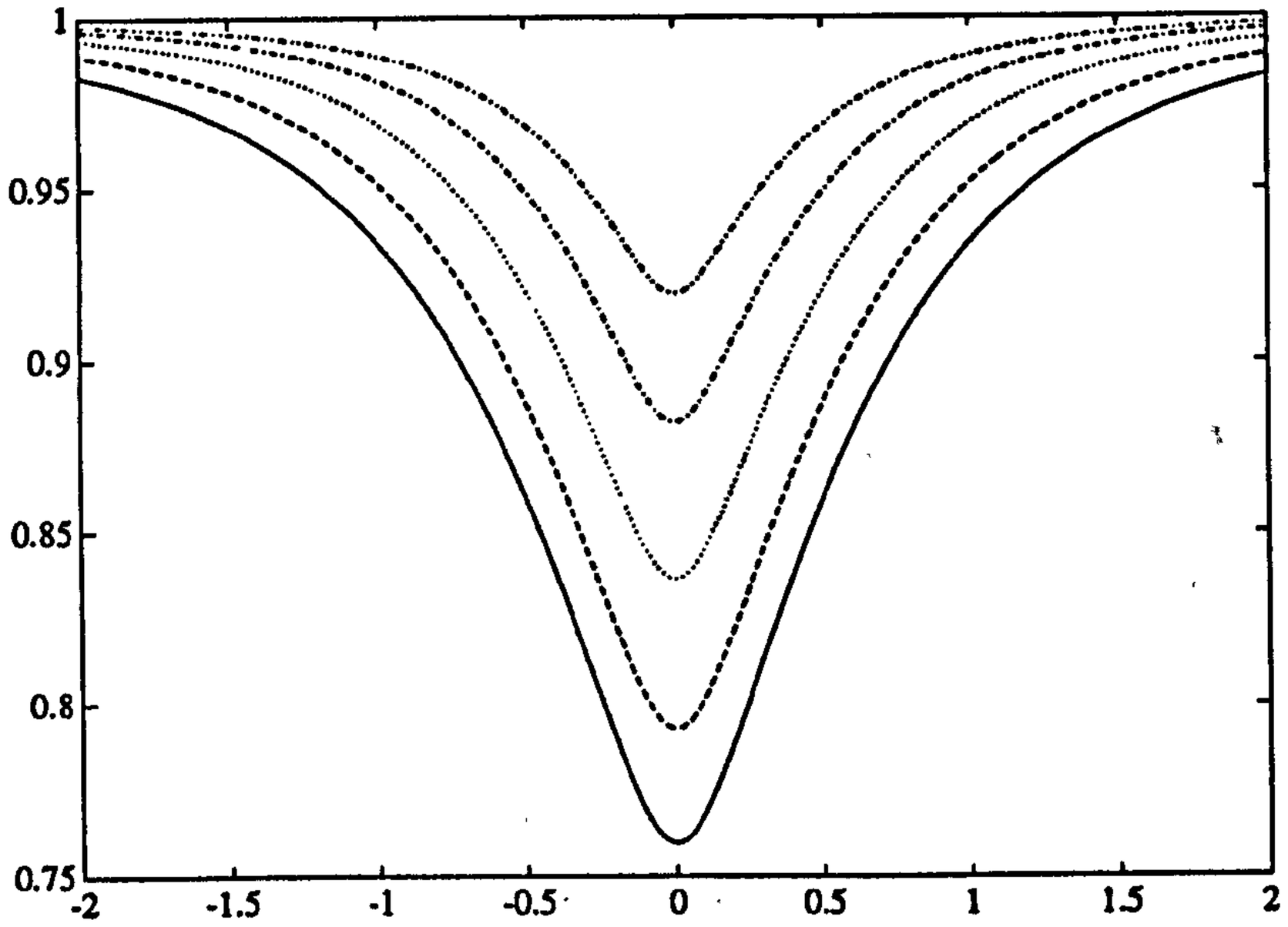

Fig. 4.15a H_x at x=0 Theoretical

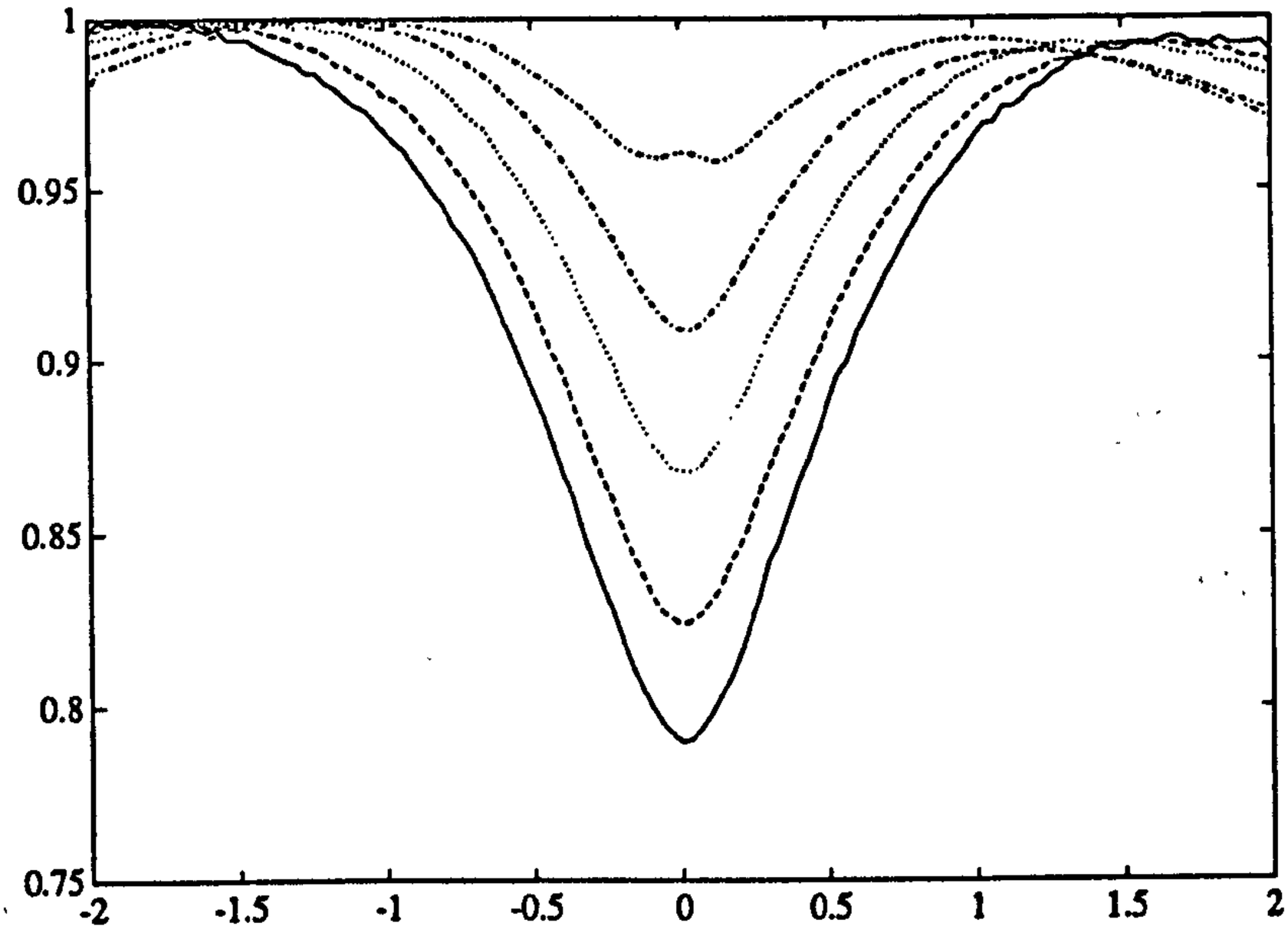

Fig. 4.15b H_x at x=0 Experimental

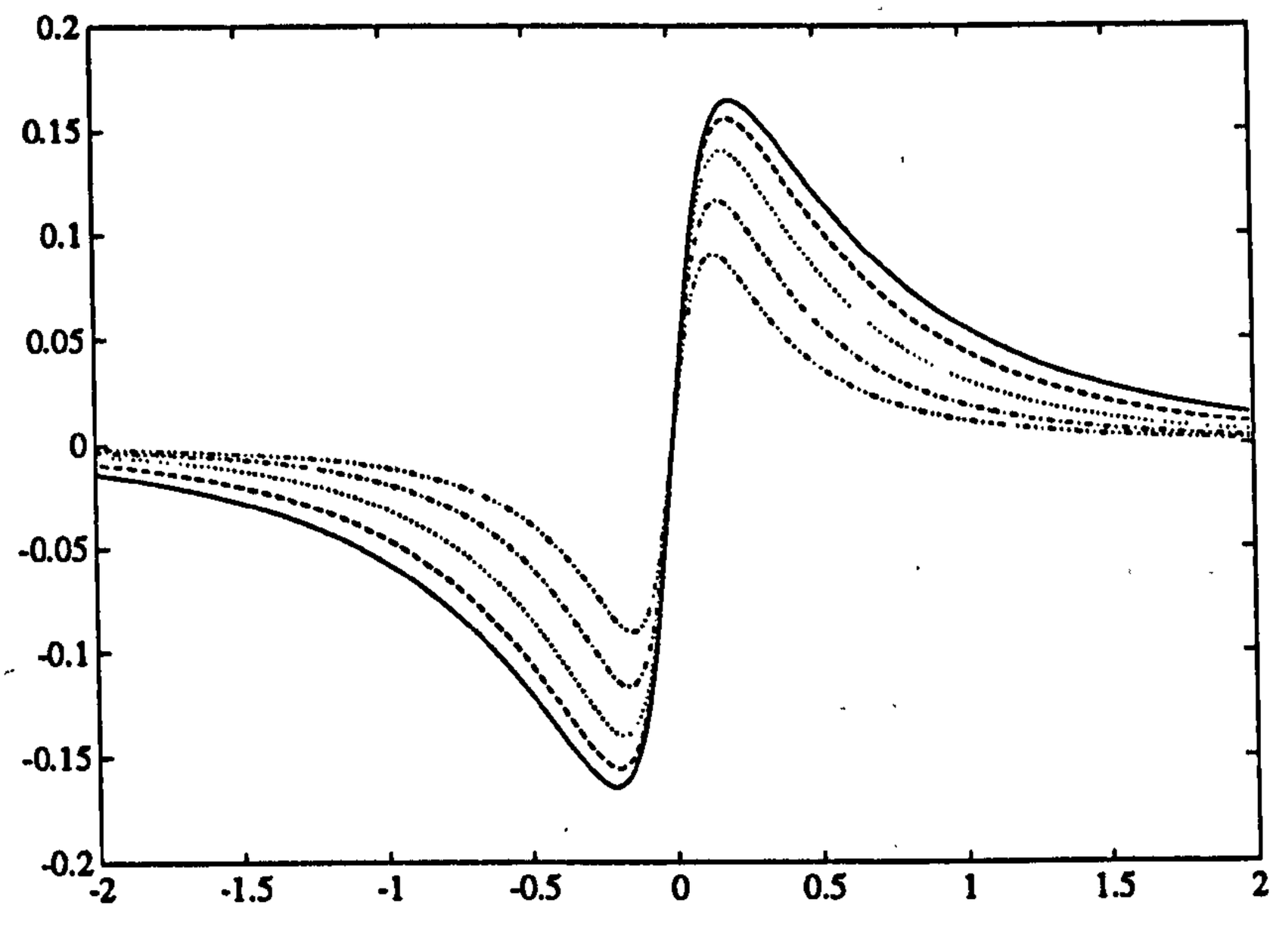

Fig. 4.16a H_y at $x=a$ Theoretical

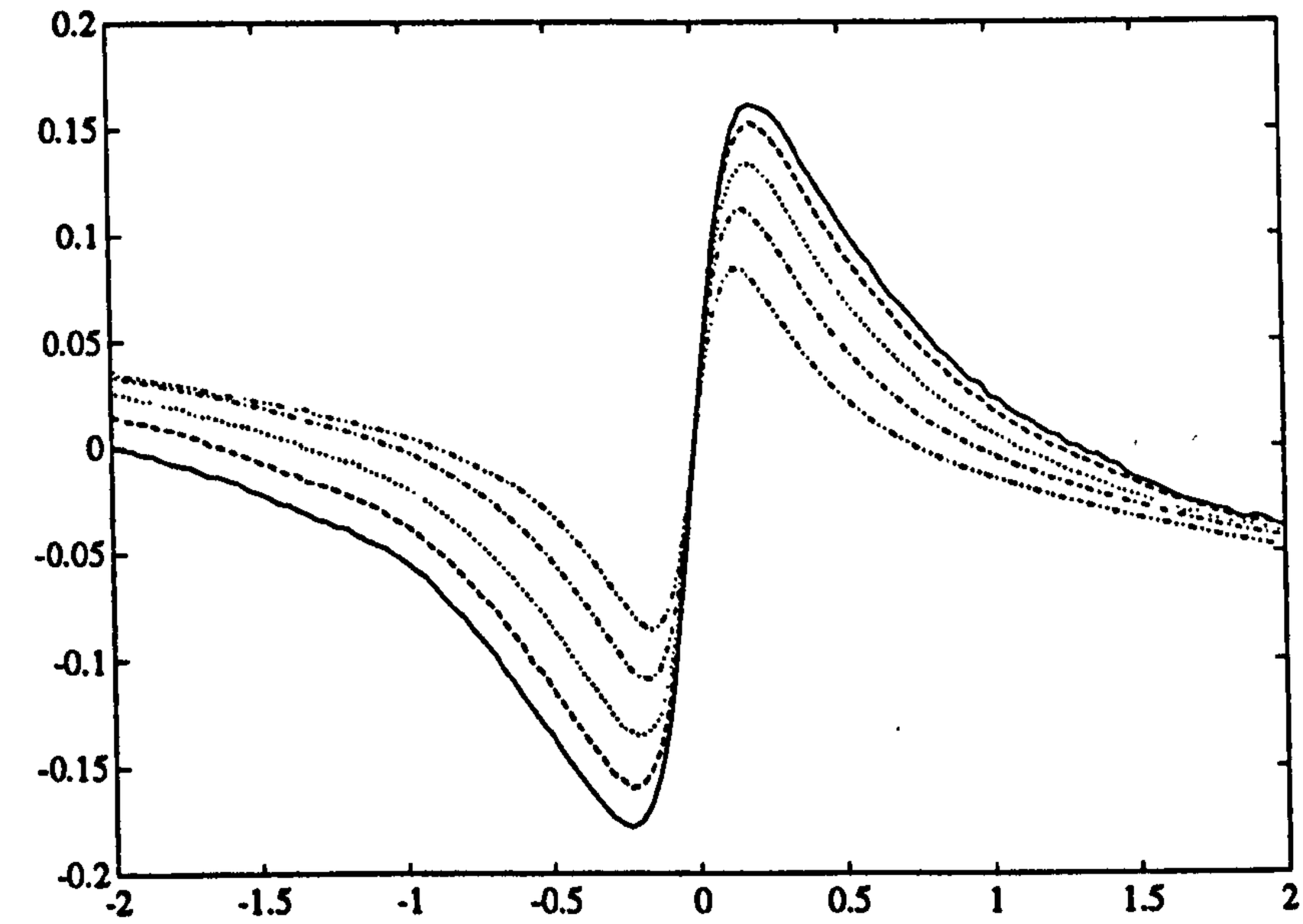

Fig. 4.16b H_y at $x=a$ Experimental

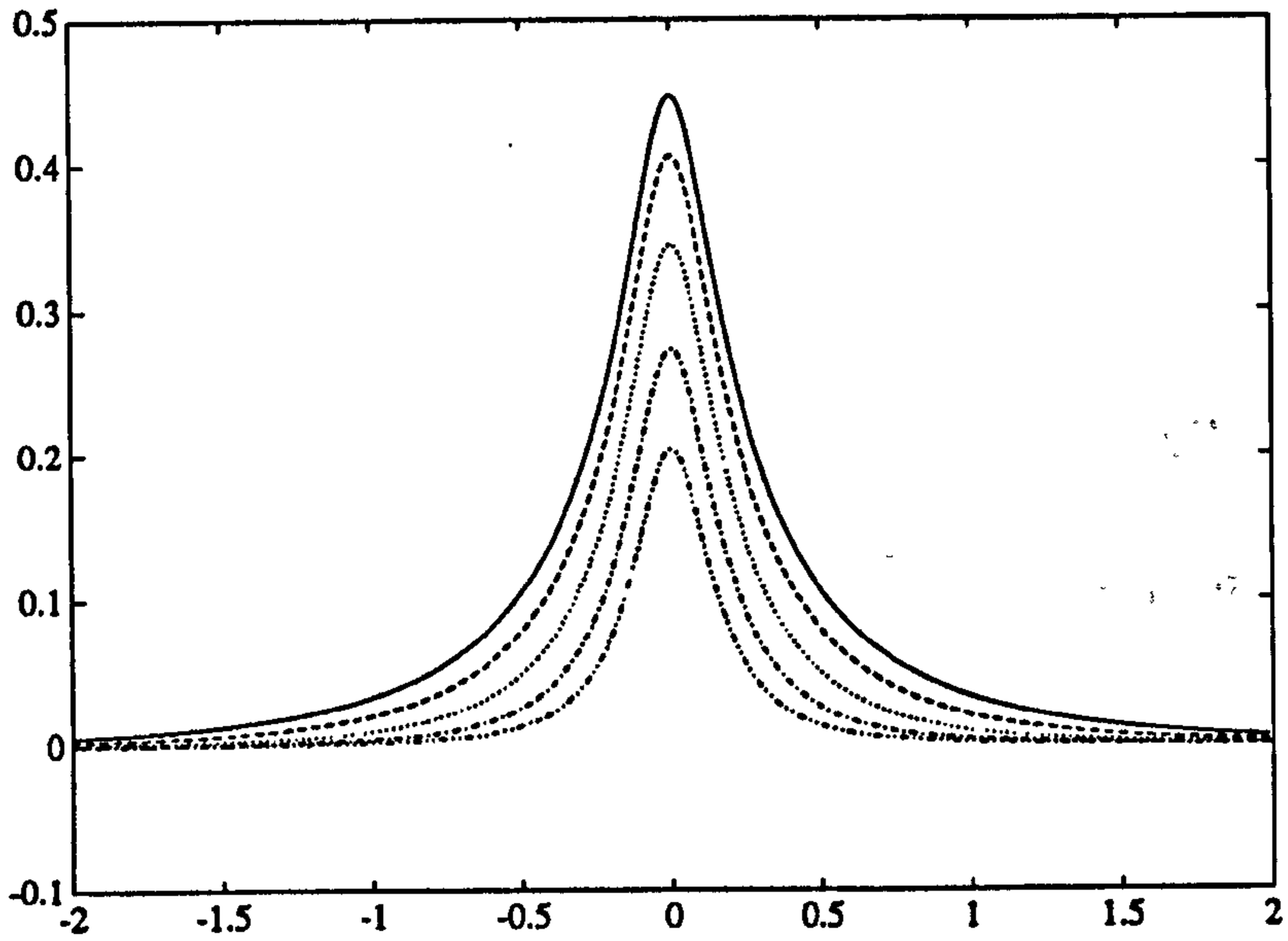

Fig. 4.17a H_z at $x=a$ Theoretical

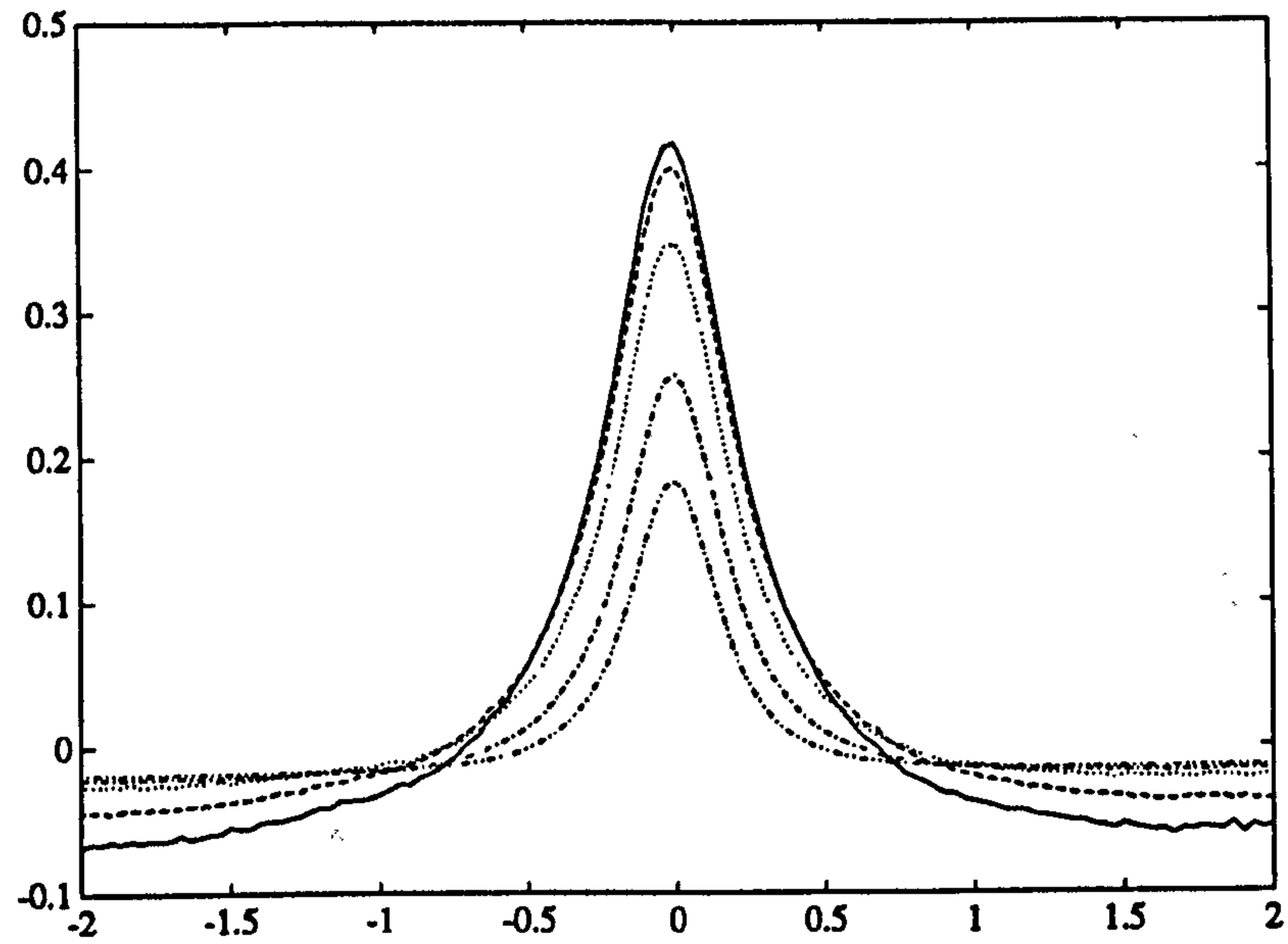

Fig. 4.17b H_z at $x=a$ Experimental

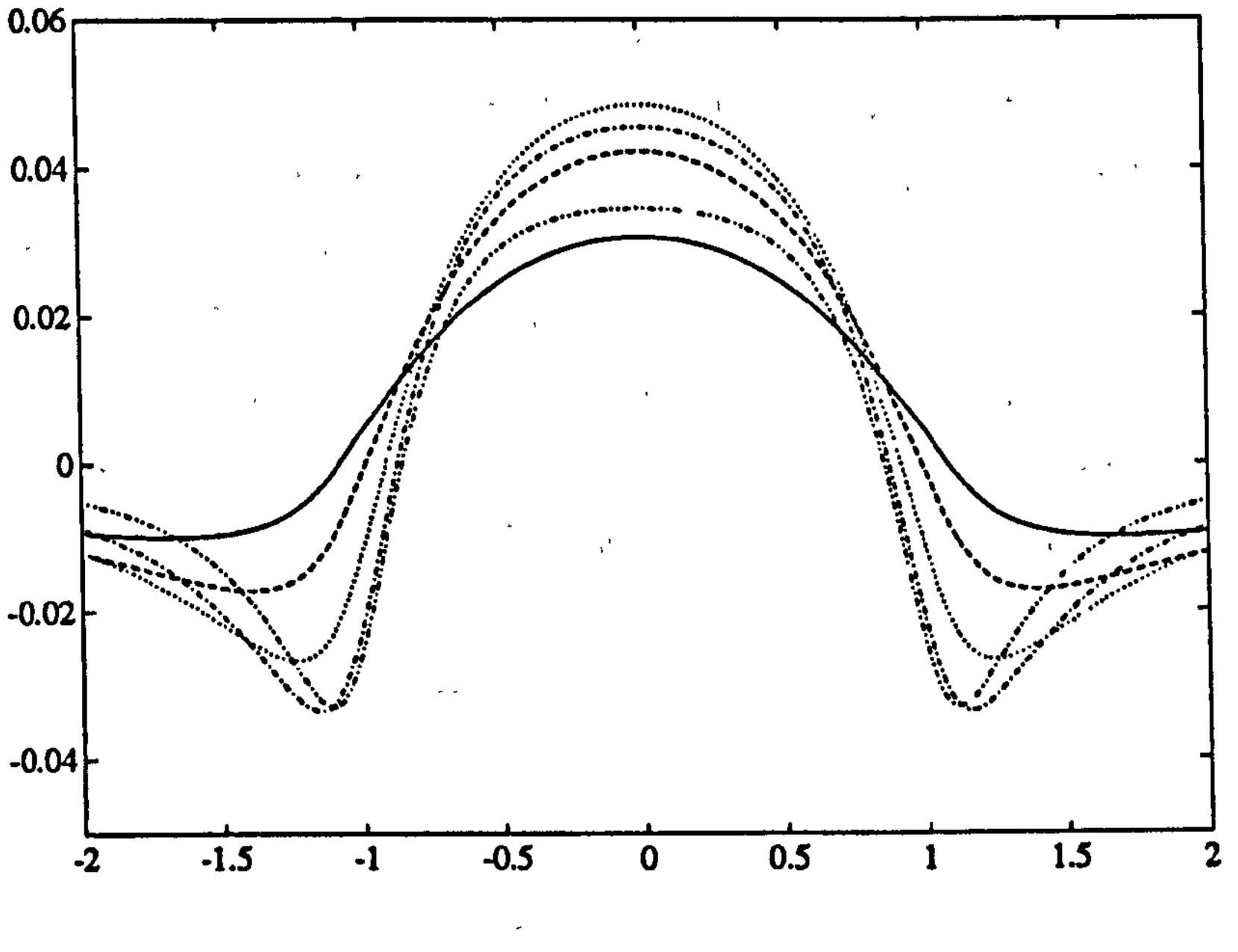

Fig. 4.18a H_x at y=0 Theoretical

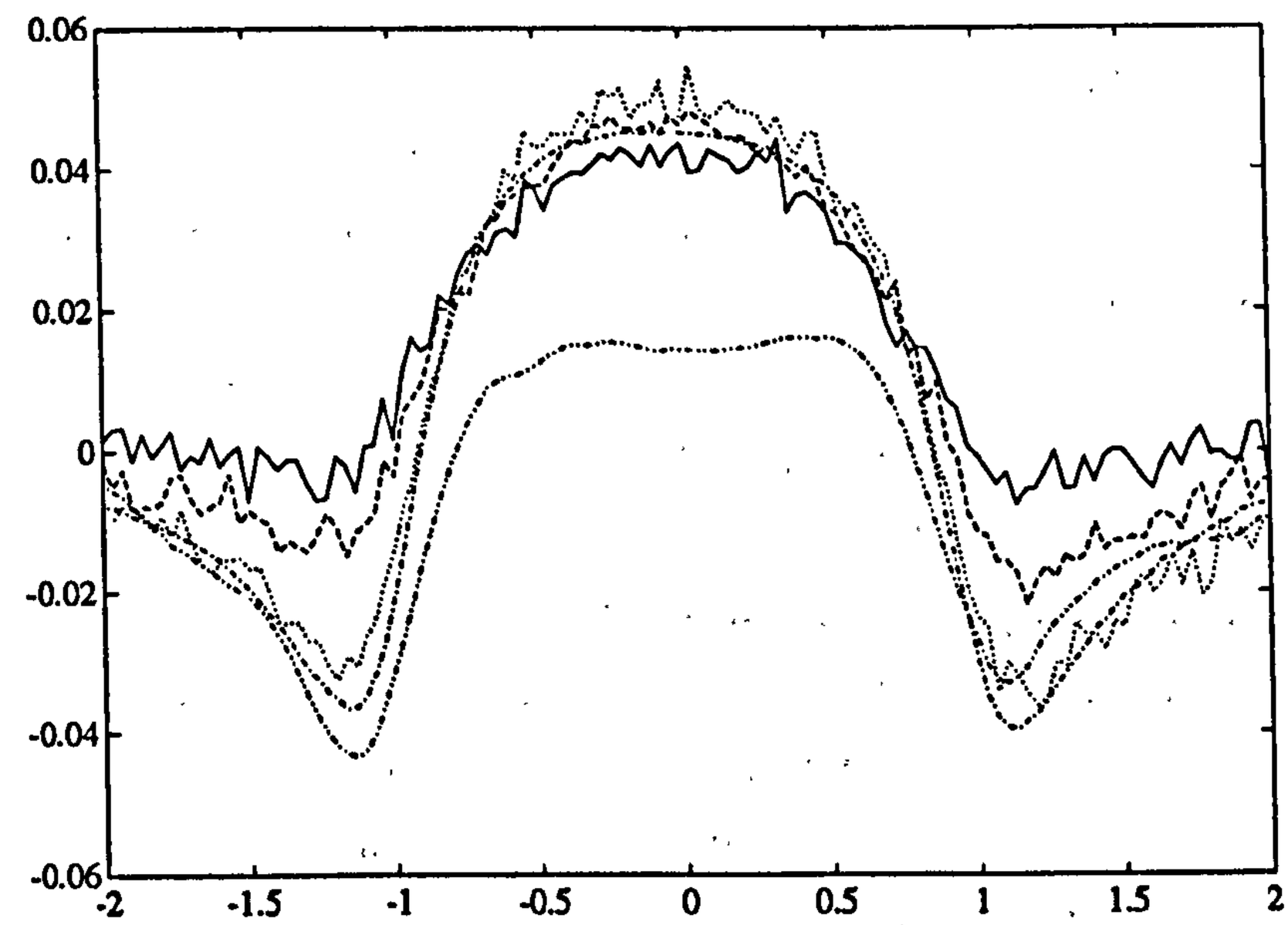

Fig. 4.18b H_x at y=0 Experimental

The main departures from the calculated fields occur near the edges of the plots and may be attributed to non-uniformity in the applied field near the test-piece edges. These effects were found to be sensitive to the position of the induction coils. If the coils were brought up close to the sides of the test-piece, the non-uniformities were more severe. However, if the induction coils were moved too far away, the applied field strength became too weak to give an accurately measurable signal. Positioning the induction coils at about 25mm from the test-piece gave an acceptable compromise. In order to discriminate the flaw signal from the non-uniformity in the applied field, the exact quantity plotted in fig. 4.12b is

$$1 \quad + \quad \frac{H_x(y=0) - H_x(y=2a)}{\langle H_x(y=2a) \rangle} \tag{4.5.1}$$

and in fig. 4.13b it is

$$\frac{H_y(y=0.1a) - H_y(y=-0.1a)}{2H_x(y=2a,\ \alpha=0)} \quad . \tag{4.5.2}$$

In figs. 4.12b and 4.15b, the H_x signal from the crack at large m is less than that expected from the theory and examining fig.4.15b in particular, one may discern a local perturbation in the signal at y=0. In section 3.5, it was shown that the first order correction for notch opening was valid providing that $h\gamma/2$ is small. For the rectangular notch under consideration, the magnitude of this quantity is about $0.035m$, so that is equal to 0.28 at m=8. It is therefore reasonable to expect some second-order perturbations to be observed and the discrepancies in figs.4.12b and 4.15b are probably effects of this kind.

In addition to the spatial scans plotted above, experiments were conducted in which the parameter m was varied, for fixed position, by varying the frequency. In fig. 4.19 experimental values of the real part of H_x at x=0, y=0 for varying values of m are shown as circles and the corresponding theoretically predicted field is shown as a solid line. The imaginary part is shown in fig. 4.20. This experiment was conducted before computer control had been implemented, so there are fewer data points. The search coil was also rather less sensitive than those of table 4.5 and only the two lowest frequency measurements were conducted in both senses. For these reasons, the data are not quite as good as the data in figs.4.12-4.18.

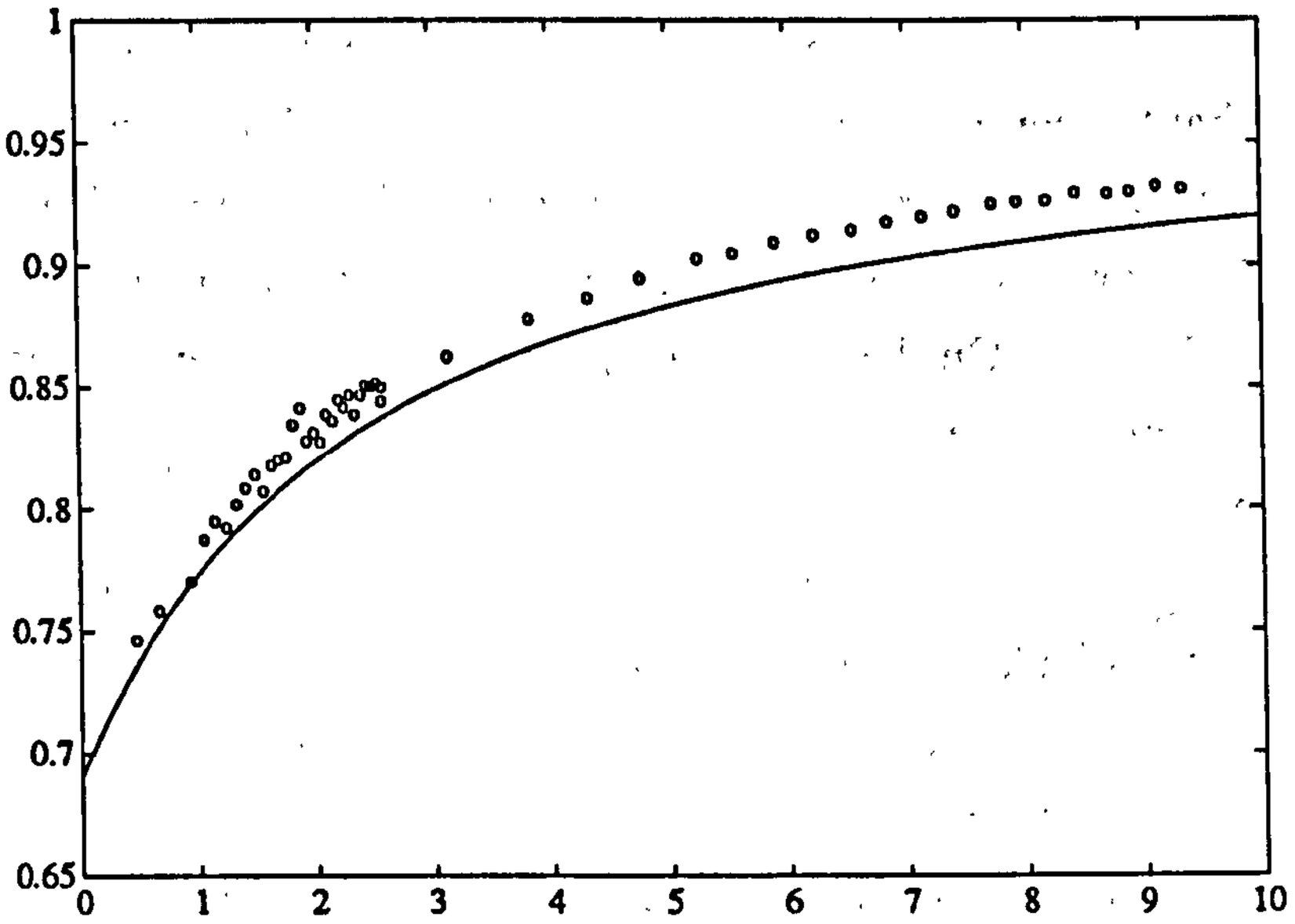

Fig. 4.19 H_x at x=y=0.0 z=1.5mm

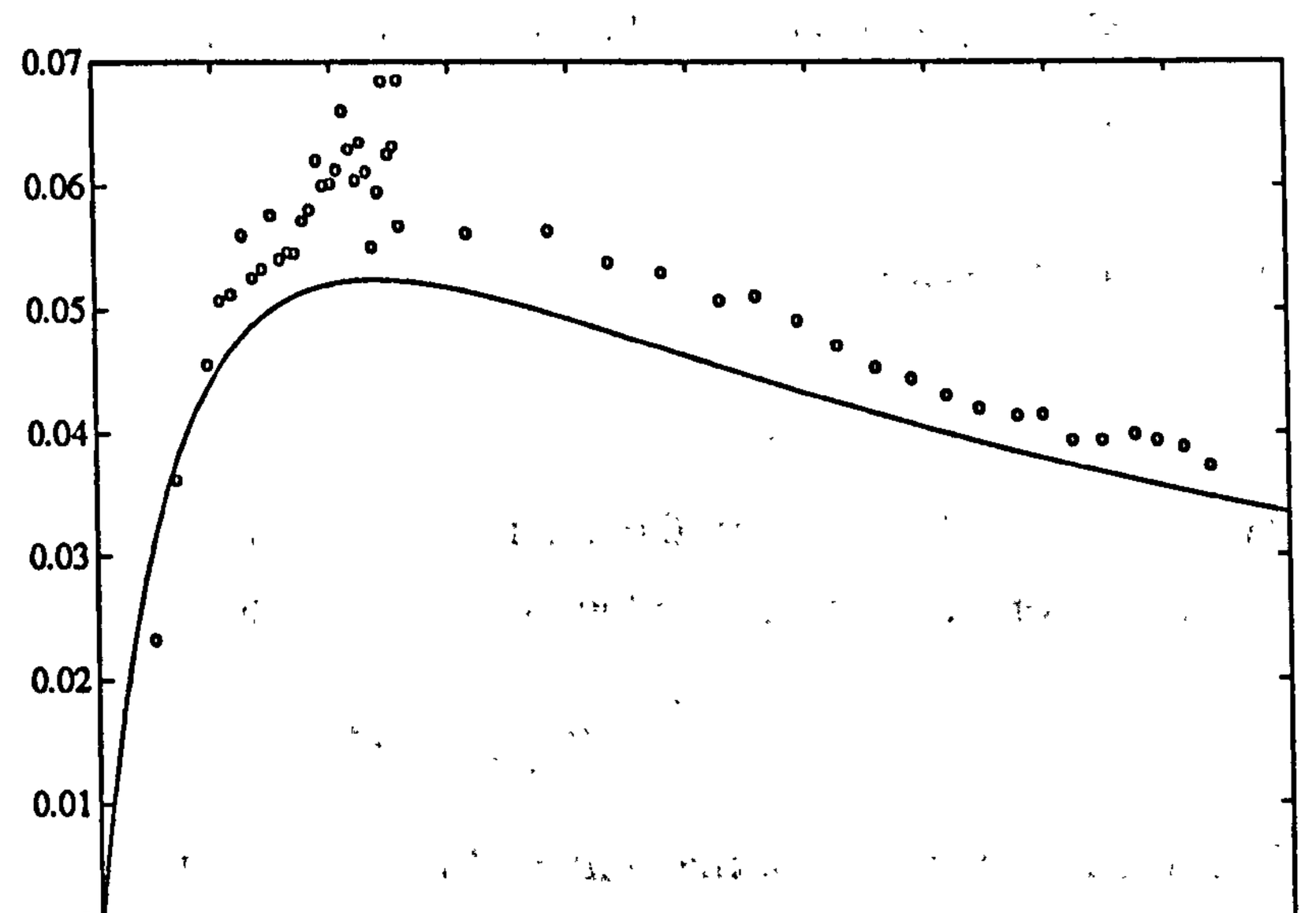

Fig. 4.20 H_x at x=y=0.0 z=1.5mm

4.6 Parallel Currents

One of the main predictions of chapter 3 is that a uniform field applied so that the currents are in the x direction (parallel to the crack) is not perturbed at all, providing the crack is tightly closed. This implies that for parallel currents interrogating a closed crack, the unfolding theorem does not apply, even when m is small. On the other hand, for notches that are sufficiently wide to allow different values of the magnetic scalar potential on the two faces, one would expect the unfolding theory to be valid in the small m limit. The equipotentials and streamlines are simply interchanged from their positions for the perpendicular interrogating current. In section 3.5, it was shown that the theory for closed cracks interrogated by a perpendicular current is only valid for open notches if the parameter $h\gamma/2$ is small. In a similar fashion, it is possible to deduce how wide a notch must be to perturb parallel currents.

From 3.2.11, we have

$$\frac{\partial H_x}{\partial y}=\frac{\partial H_y}{\partial x} \quad . \tag{4.6.1}$$

For parallel currents, H_x should be antisymmetric in y so that

$$\frac{\partial H_x}{\partial y}\sim\frac{2H_x}{h} \quad . \tag{4.6.2}$$

Therefore, from 4.6.1,

$$\frac{2H_x}{h}\sim\frac{H_y}{a}. \tag{4.6.3}$$

Whatever the direction of the interrogating current, the surface impedance boundary condition applies on the faces of the crack,

$$\frac{\partial^2\psi}{\partial x^2}+\frac{\partial^2\psi}{\partial z^2}\pm\frac{k}{\mu_r}H_y=0. \tag{4.6.4}$$

Considering the orders of magnitude of the terms in this equation, one may see that

$$\frac{H_x}{a}\sim\frac{k}{\mu_r}H_y. \tag{4.6.5}$$

If the field components H_x and H_y are non-zero, 4.6.3 and 4.6.5 are only self-consistent if

$$\frac{h}{2a} \sim \frac{ka}{\mu_r}, \tag{4.6.6}$$

that is to say

$$\frac{h}{2a} \sim m. \tag{4.6.7}$$

For cracks, and narrow notches for which $h \ll a$, criterion 4.6.7 cannot be satisfied unless m is much less than 1. The minimum possible value of m which can occur in practice is of the order of 0.01, because the relative permeability of a metal is never much greater than 1000 and m is only meaningful when $\delta \ll a$. For a crack longer than 10mm, equation 4.6.7 can only be satisfied if h is of the order of 0.1mm, but fatigue cracks are usually closed much more tightly, especially if a compressive load is applied. Therefore, it is not possible for a closed crack to perturb parallel currents. To summarise, parallel currents are not perturbed by cracks and narrow notches in non-magnetic metals or by tightly closed cracks in magnetic metals but they may be perturbed by open cracks or notches in magnetic metals.

This phenomenon was investigated experimentally with a 10mm contacting probe aligned along the x axis. Current was induced in the specimens from a second plate placed underneath the test-piece and insulated from it, energized by injection of 2A from a Crack Microgauge ACPD instrument. The HP-4194A analyzer and x-y table were used to plot the signal as before. This method of induction is more suitable for non-magnetic test-pieces where it is difficult to couple in a strong field from coils. The experiment was conducted on three test-pieces with flaw dimensions given in table 4.6.

Table 4.6 Flaw dimensions for parallel current experiment

Material	Flaw type	Length $2a$/mm	Depth b/mm	Opening h/mm	$2ma$/mm (approx.)
Mild steel	crack	50	3.3	<0.1	50
Mild steel	notch	50	5.0	0.71	50
Dural	notch	20	3.0	0.27	160

In these scans it was particularly important to subtract the field away from the crack, because the aim was to detect whether there was any small perturbation of this field. Results are shown in figs. 4.21, 4.22 and 4.23. Of the three flaws, the notch in the mild steel is the nearest to satisfying criterion 4.6.7 and it is the only one that appreciably perturbs the parallel currents, as expected from the theory.

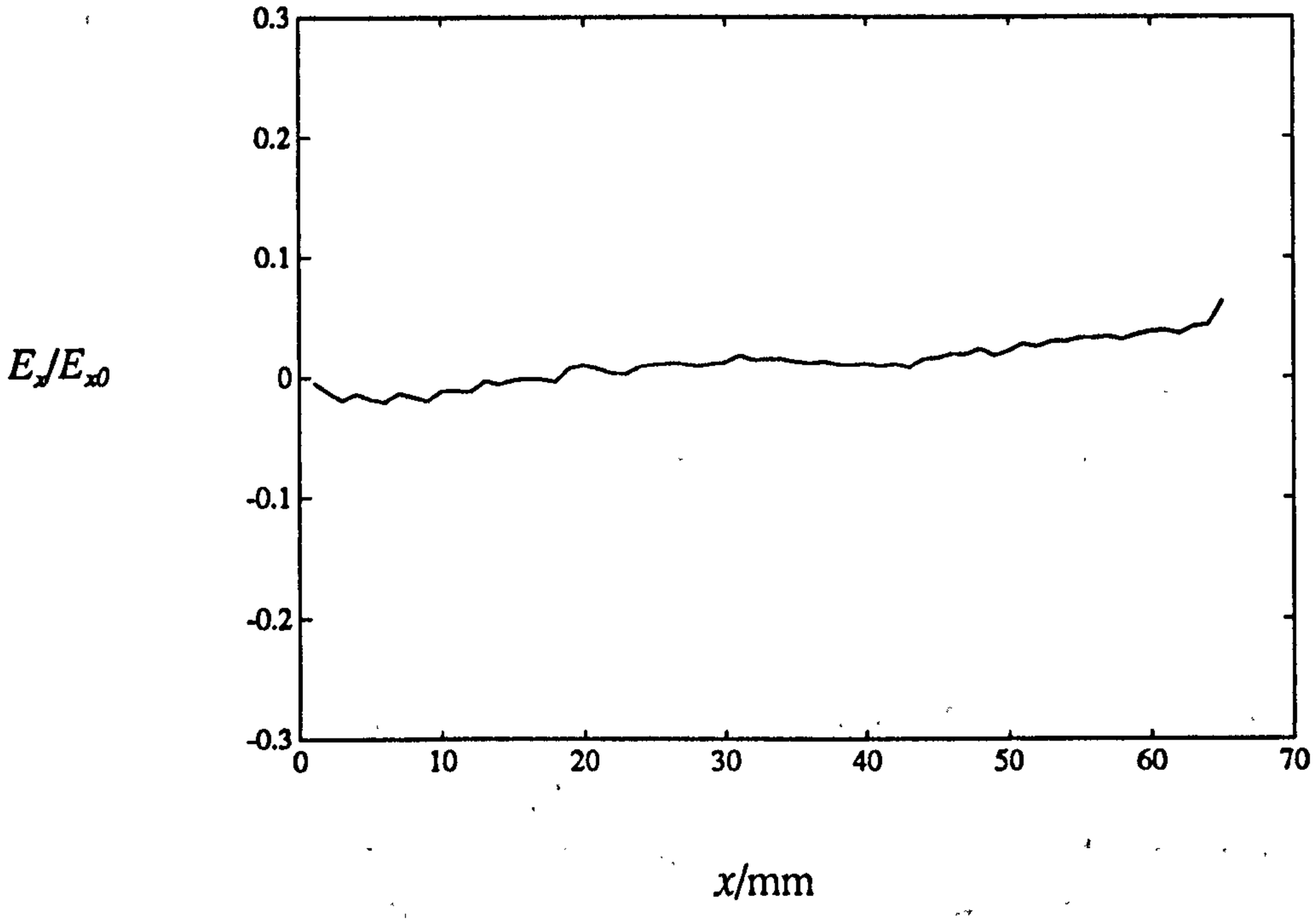

Fig 4.21 E_x caused by a parallel current interrogating a crack in mild steel

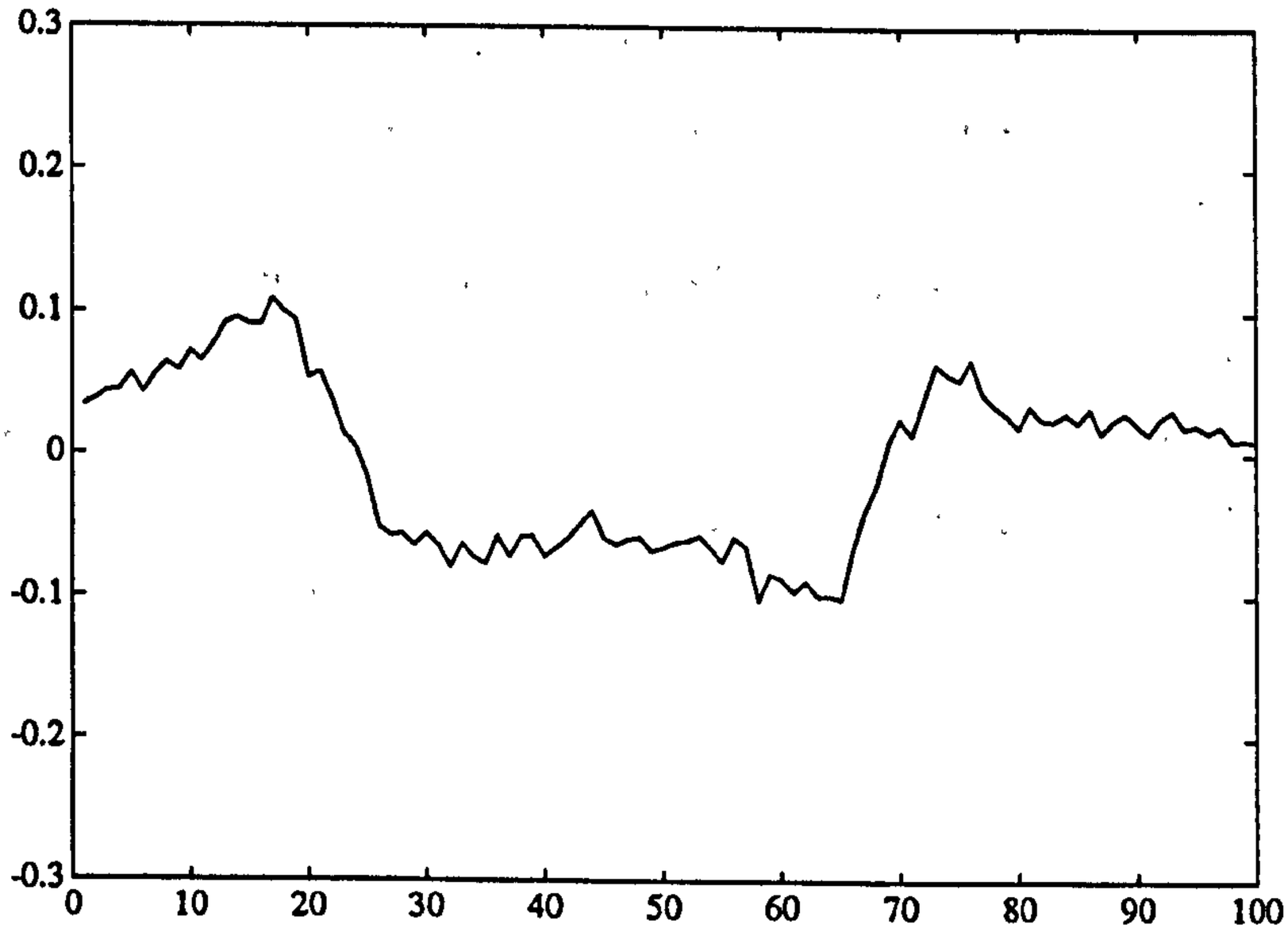

Fig 4.22 E_x caused by a parallel current interrogating a notch in mild steel

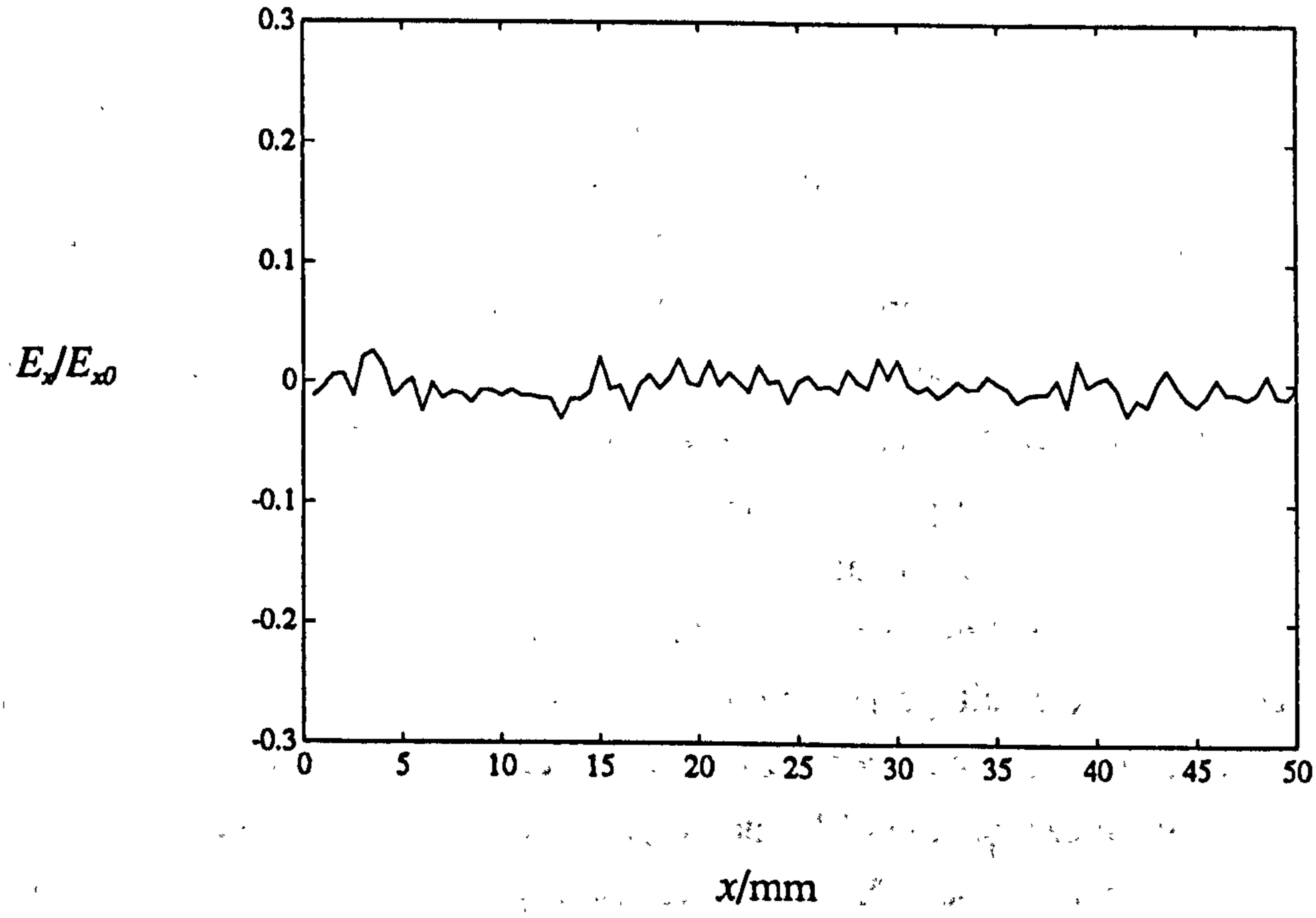

Fig 4.23 E_x caused by a parallel current interrogating a notch in Dural

4.7 Accuracy and Precision

For the purpose of this discussion, accuracy means the extent to which the measurements are free from systematic error and precision means the extent to which they are free from random error.

Non-uniformity in the applied field is a cause of loss of accuracy. The field will be truly uniform if all the flux that enters the top surface of the block from one induction coil passes straight across and goes into the induction coil on the far side. In practice, some of the flux leaves the top surface and returns around the back of the first coil, so that the field is stronger at the edges of the block than in the centre. By careful positioning of the coils, it was possible to reduce this non-uniformity so that the field at x=0 was only about 15% lower than the field at x=2a, in an unflawed part of the test-piece. The departure of the flaw fields from theory at the edges of plots 4.12b-4.17b is typically about 3% of the applied field strength, so that it seems reasonable to interpret it as being caused by the edges as well.

A second possible cause of loss of accuracy is non-linearity in the measuring instrument. The manufacturer's estimated accuracy (and precision) for the HP-4194A at 20μV is only about 45% in gain readings and 16° in phase. If taken at face value, these figures would imply that search coil measurements made at these signal levels are virtually meaningless. However, the manufacturer's figures are not necessarily a good estimate of the accuracy in the experiments described above, where careful precautions were taken to eliminate interference. Moreover, the apparent agreement between theory and experiment suggests that the actual instrument performance was much better. Clearly, it is essential to get a realistic estimate of the instrumental accuracy in order to know if the experiments constitute a valid verification of the theory.

All the readings were referred to the upstream field value, so the absolute accuracy of the voltage measurements is immaterial, providing that the instrument is linear over the required range. An indication of the linearity was found by making a measurement of B_x and varying the oscillator voltage V from 0.05V to the operating value. This procedure was performed for the minimum and maximum frequencies used: f=5184Hz with an operating voltage of 1.0V and

f=1327104Hz with an operating voltage of 0.5V. If the instrument was perfectly linear, the gain g should be a constant. The non-linearity was estimated by fitting a quadratic

$$g = g_2 V^2 + g_1 V + g_0 \tag{4.7.1}$$

to the results, by the method of least-squares. Results are shown in table 4.7.

Table 4.7 Linearity of measuring instrument

f/kHz	Part	g_2/V^{-2}	g_1/V^{-1}	g_0
5.184	Real	-7.8946×10^{-10}	1.1611×10^{-7}	1.4550×10^{-5}
5.184	Imaginary	-3.8724×10^{-7}	4.6677×10^{-7}	2.0536×10^{-5}
1327.104	Real	1.6328×10^{-6}	2.2831×10^{-6}	1.3299×10^{-3}
1327.104	Imaginary	2.1708×10^{-5}	-1.9447×10^{5}	1.4321×10^{-3}

Note that the imaginary part is the part in quadrature with the oscillator voltage. It should not be confused with the part in quadrature with the applied field, plotted in figs.4.18 and 4.20. The maximum error caused by the non-linearity over the range of the results will be of the order $(g_2 + g_1)/g_0$. For both frequencies, it is the imaginary part which is worst affected, the maximum error being 4.2% at the lower frequency and 2.9% at the higher frequency.

In figs.4.12b-4.18b, there appears to be some random noise on the low frequency data, but much less on the high frequency data. The low frequency noise is about 0.5% of the applied field. A measurement of B_x upstream was repeated 50 times without moving the probe and the standard deviation was found to be 0.066% of the mean, for the real part, and 0.039% of the mean, for the imaginary part, which is too small to explain the noise on the low frequency plots. The noise cannot be attributed to errors in the positioning system, because these would affect the high frequency data as well. Movement of the connecting cables did not seem to produce significant noise either. A scan of the upstream field was performed twice, without otherwise altering the apparatus, in order to see if the apparently random variations on the signal were reproducible, which would indicate that they were due to variations in the test-piece. It was difficult to interpret the data, but most of the local variations were not reproduced.

To summarise, the accuracy of the measurements is limited to 3 or 4% by the linearity of the instrument at the low signal strengths used, and by the difficulty of obtaining a uniform field. The precision of the measurements at low frequencies is limited to about 0.5%, but the precise cause of the noise is not known.

5 Applications

5.1 Introduction

The previous two chapters described the calculation and measurement of the magnetic field near a crack in the presence of a uniform applied field. In this chapter, it is explained how the theoretical model has been used to develop an algorithm for the estimation of crack length and crack depth from the high-frequency magnetic field measurements. The technique is referred to as a.c. field measurement (ACFM), to distinguish it from the d.c. flux leakage method and from the contacting a.c. potential difference method.

Two examples of the application of ACFM in the petroleum industry are given. The first example is a system to detect and size cracks in the screw-threaded joints of a "drill-string". This is the technical term for the train of strong steel pipes which are used to provide power to the drill-bit. The second example is a probe, for use underwater, to detect and size fatigue cracks at the welded joints of tubular steel off-shore structures.

5.2 Drill-string threaded connections

Fracture of drill-strings due to fatigue is a persistent and expensive problem in the oil industry. Drill-string failure increases equipment cost, wastes rig time and, in some circumstances, can even lead to the abandonment of a well. At present, magnetic particle inspection is used to examine the drill pipe, but its performance has been disappointing. For example, Dale and Moyer [113] presented results of field evaluations of MPI for drill pipe in which the probability of detecting a 25mm long crack was as low as 50%. Fig. 5.1 is a diagram of a typical threaded connection, the outer diameter is typically about 150mm.

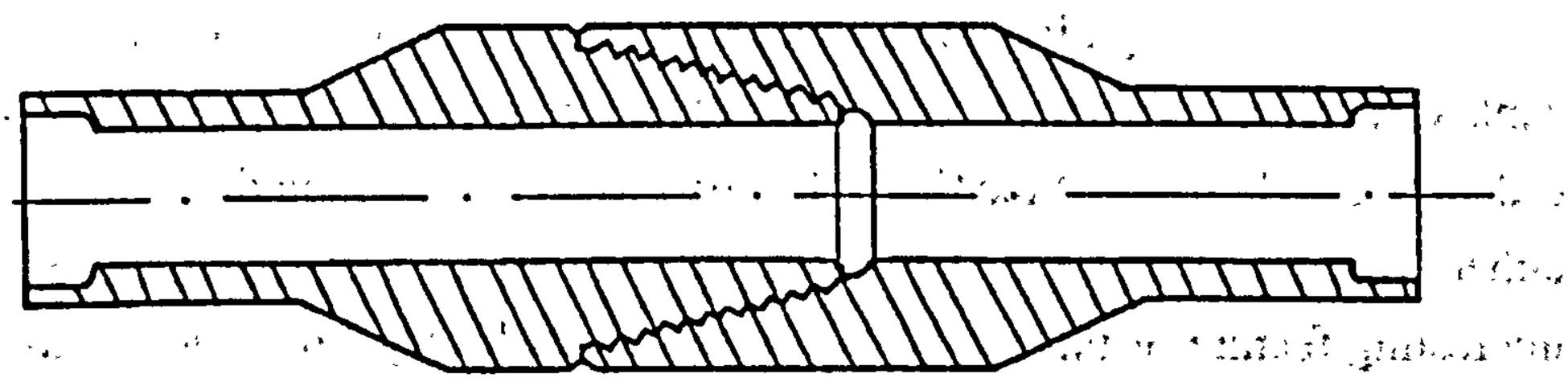

5.1 Drill-String Threaded Connection.

An extensive programme of work was undertaken by UCL in collaboration with several industrial companies to address the drill-string fatigue problem. In addition to fatigue crack growth studies and stress analysis studies, measurement of the a.c. magnetic field was proposed as a means of detecting and sizing cracks. A dedicated inspection machine was made by Hunting Offshore Services Ltd. with a probe, containing search coils and an induction coil, which engages with the thread and is driven around the pipe by pneumatic actuators. The whole of the thread length is thus scanned and the tangential and radial magnetic field components measured using suitably orientated search coils (fig. 5.2). Separate machines were built to inspect both the "pin" or male part of the joint and the "box" or female part. The ACFM circuitry was originally made by Inspectorate Unit Inspection Ltd. and subsequently developed by Technical Software Consultants Ltd. using a crack sizing algorithm described in section 5.4.

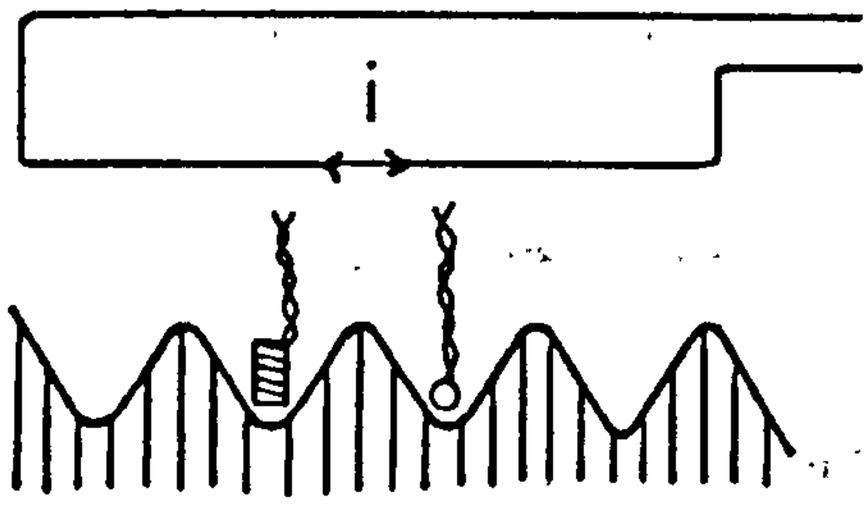

Fig. 5.2 Search coils measuring tangential and radial field components near a drill-string thread.

Most drill pipe is manufactured from ferromagnetic high tensile-strength steel, such as the AISI-4145 material mentioned in the previous chapter. Special non-magnetic steel pipes are used at certain points on the drill-string where instruments have been placed to take readings of the earth's magnetic field for use in steering during directional drilling operations. (Oil wells are not always sunk vertically but are often made to follow oblique or even curved paths, in order to make best use of the field). The ACFM technique should be suitable for either magnetic or non-magnetic pipes; MPI is restricted to magnetic ones. An interesting feature of this application is that both the high and low m limiting cases are likely to occur in practice. For the magnetic drill-pipe, it is best to operate in the low m limit so that no material constant measurements are necessary. For the non-magnetic drill-pipe, if the skin-depth is small, the values of m will always be high.

The drill-string inspection instrument produces estimates of crack length and depth from the flaw signal using the flat plate model for a semi-elliptical crack as an approximate model of the fields near the cracked thread. The sizing algorithm may be used for either limiting case, details are given in section 5.4. At the time of writing, trials have only been conducted with magnetic drill-pipe but work on non-magnetic drill-pipe is planned. Details of the construction of the inspection system and examples of results may be found in reference [114]. Reliable detection has been achieved for cracks as small as 8mm long and 0.5mm deep.

5.3 Welded steel tubular joints

Since sea-water, by comparison with steel, is effectively an insulator, electromagnetic methods can also be applied under the sea. One important application is to the detection of fatigue cracks in off-shore structures made from welded steel tubes. In this case, the fatigue cracks grow because of the cyclic load caused by sea-waves. The usual site of crack formation is at the "toe" of a weld, that is, at the line joining the weld metal with the parent metal. As a rule, it is more common for the crack to propagate into the parent metal rather than into the weld. Fig.5.3 shows some typical geometries of joint, named after the letters of the alphabet T,Y and K that they resemble. The tube diameter D is of the order of 0.5m or greater.

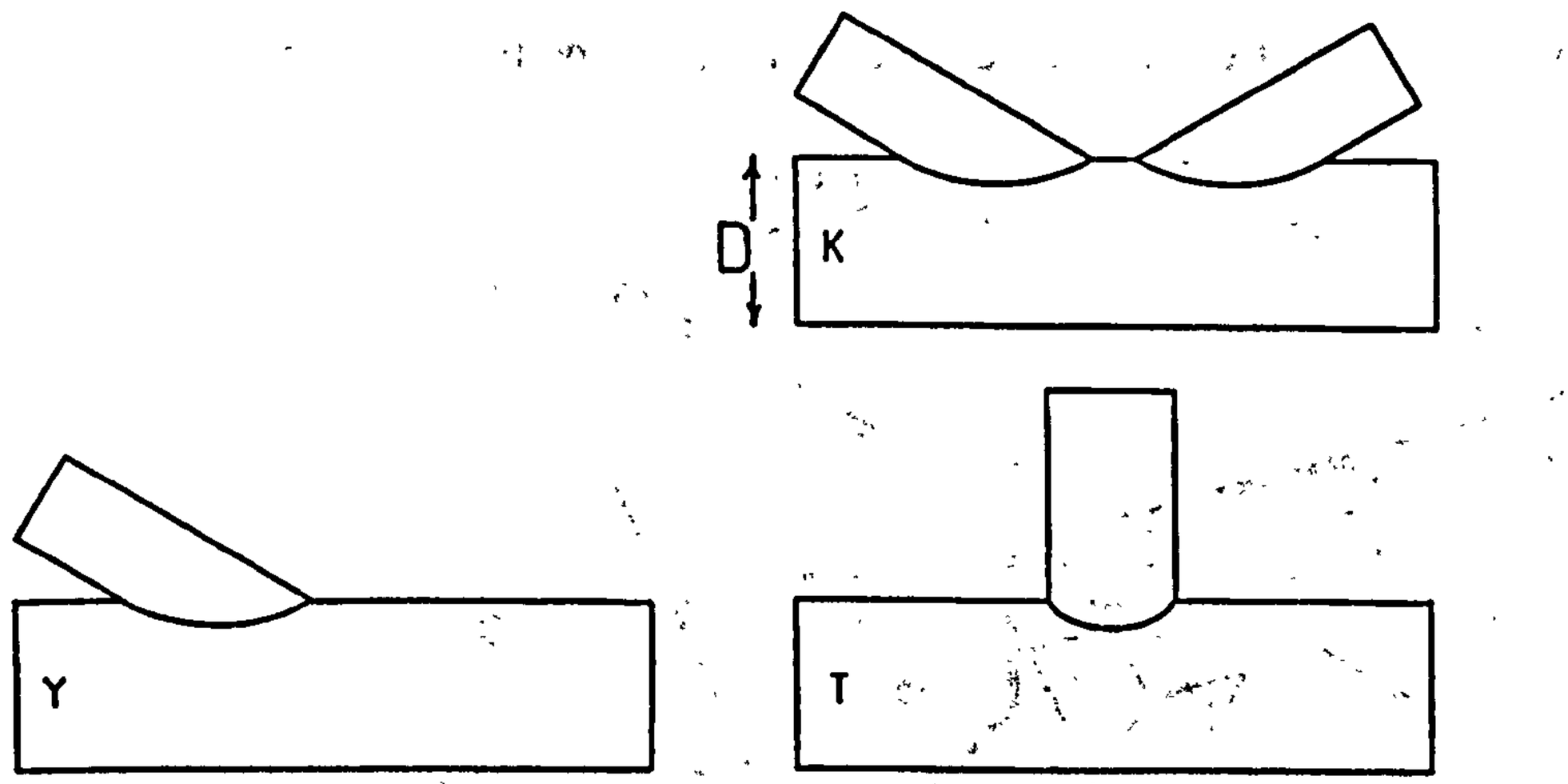

Fig. 5.3 Some typical tubular joints.

Conventional practice is to use a team of divers to inspect the weld toes using MPI. If a crack is found, it may be sized with contacting ACPD or by ultrasonic means. This sort of inspection is both laborious and expensive, since

oil-rigs may be very large indeed; for example, greater than 250m in height. It is necessary to remove marine growth and clean down to bare metal to obtain reliable MPI results and the divers may also have to spend a considerable amount of time in decompression, all of which adds to the expense. There is therefore a strong incentive to develop a faster inspection method and to eliminate tasks that can only be performed by hand, so that eventually the entire inspection can be carried out using a remotely operated vehicle.

One serious problem in using ACFM for tubular joints is that the cracks encountered may be as long as 200mm. It is virtually impossible to design a probe to generate a near-uniform field over this length in a wide variety of tubular joint geometries. Furthermore, for reasonable operating frequencies, the cracks will tend to fall in the intermediate range of m values.

It was initially decided to proceed in the same manner as for the drill-string project, in spite of these difficulties. A probe was constructed to fit onto the tubular joints in such a way that the coils were stationed just above the weld toe (fig.5.4). The field was induced by a magnetising yoke of mild steel, carrying 2A from an ACPD Crack Microgauge. One receiver coil was orientated parallel to the weld line (referred to as the x coil) and one was orientated to be roughly normal to the weld metal surface (referred to as the z coil). The width of the inducing yoke is about 50mm. There is no reason to believe that the signal measured by the z coil will be proportional to the z component as calculated in the flat plate model. The probe was built so that the receiver coils could be removed and replaced.

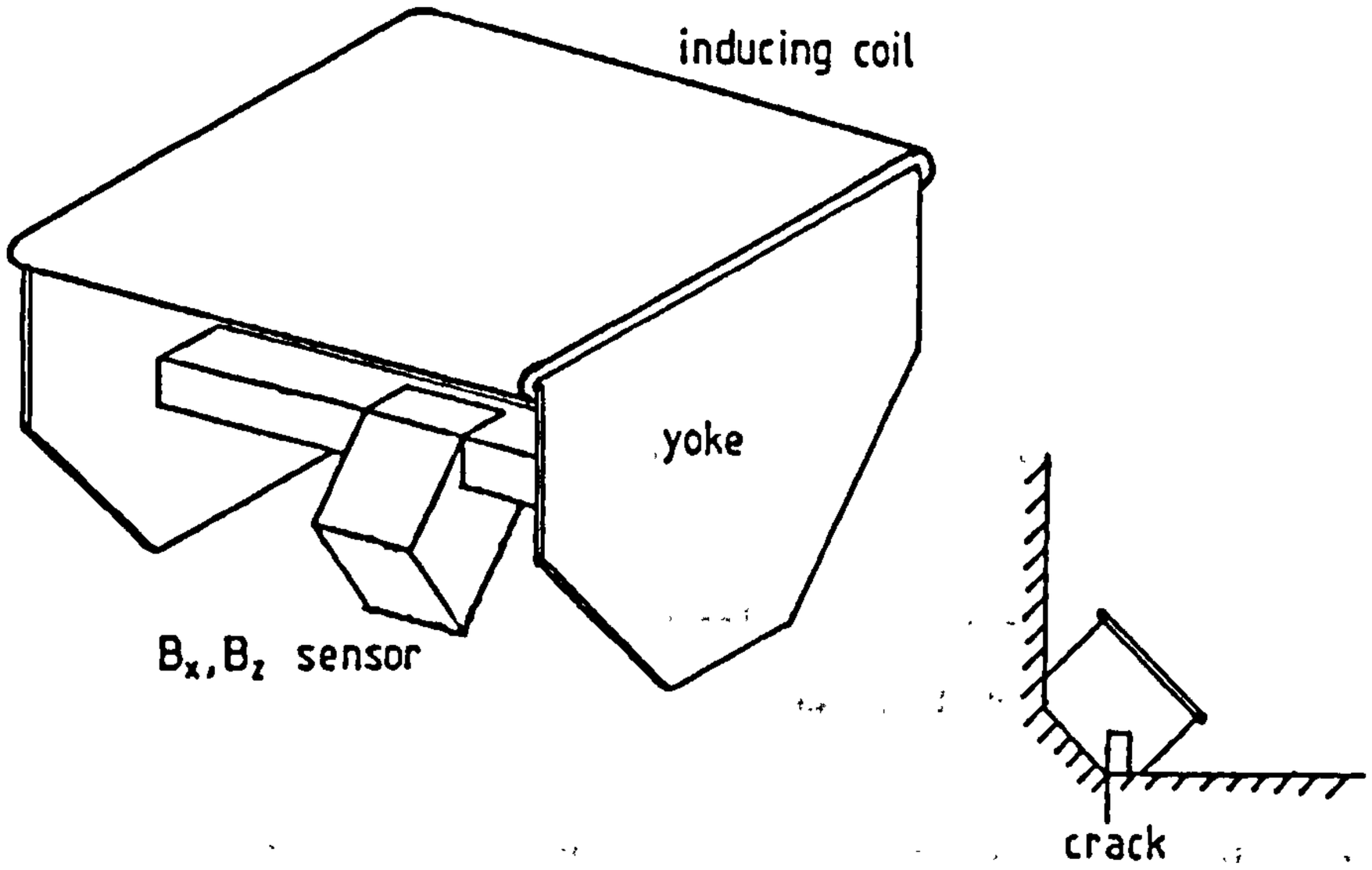

Fig.5.4 Tubular joint inspection probe.

The probe was used to inspect eight cracked tubular joints in the UCL "library" of specimens situated at The City University. The welds in question were not permanently labelled, in order to preserve the integrity of the library for blind inspection tests. Readings from both the *z* and *x* coils were taken at 10mm intervals using receiver coils of 2mm diameter. The measurements were then repeated with receiver coils of 3mm and 5mm diameters. The probe was insufficiently robust and had to be repaired and reinforced several times. The 2mm diameter coil did not survive.

A second set of readings was taken from five of the eight cracks, with measurements made at 5mm intervals with the 5mm diameter coil only. One extra set of readings was also taken with the 3mm coil. In these more detailed measurements, the region beyond the crack ends was also inspected, in order to assess how clearly the crack signal could be seen above the background noise. Finally, the ratio of the sensitivities of the *z* and *x* coils was measured, by comparing their responses to a roughly uniform field above a flat plate, when each coil was orientated to give its maximum signal.

Fig.5.5 shows the *x* signal and fig.5.6 the *z* signal from one of the shorter cracks. The signals display the characteristic shapes expected from the flat plate theory (figs.4.12 and 4.14) so that the presence of a crack can be inferred. Fig.5.7 and fig.5.8 are plots of the same signals for one of the longer cracks and they show that the system is much less effective for such flaws. This may well be a serious disadvantage, because the longer flaws will, in general, be the most dangerous ones.

Table 5.1 shows crack length and depth measurements by ACFM using the *x* coil, as compared with contacting ACPD, for the tubular joints. The ACFM figures were calculated by the method described in section 5.4, assuming the flaws were in the unfolding limit. The length measurements are all reasonably good and a useful estimate of depth is also obtained from the *x* signal. Table 5.2 shows size estimates made with the *z* coil alone- the depths are all too small. On the basis of these results, a more robust version of the ACFM probe was built and is undergoing off-shore trials.

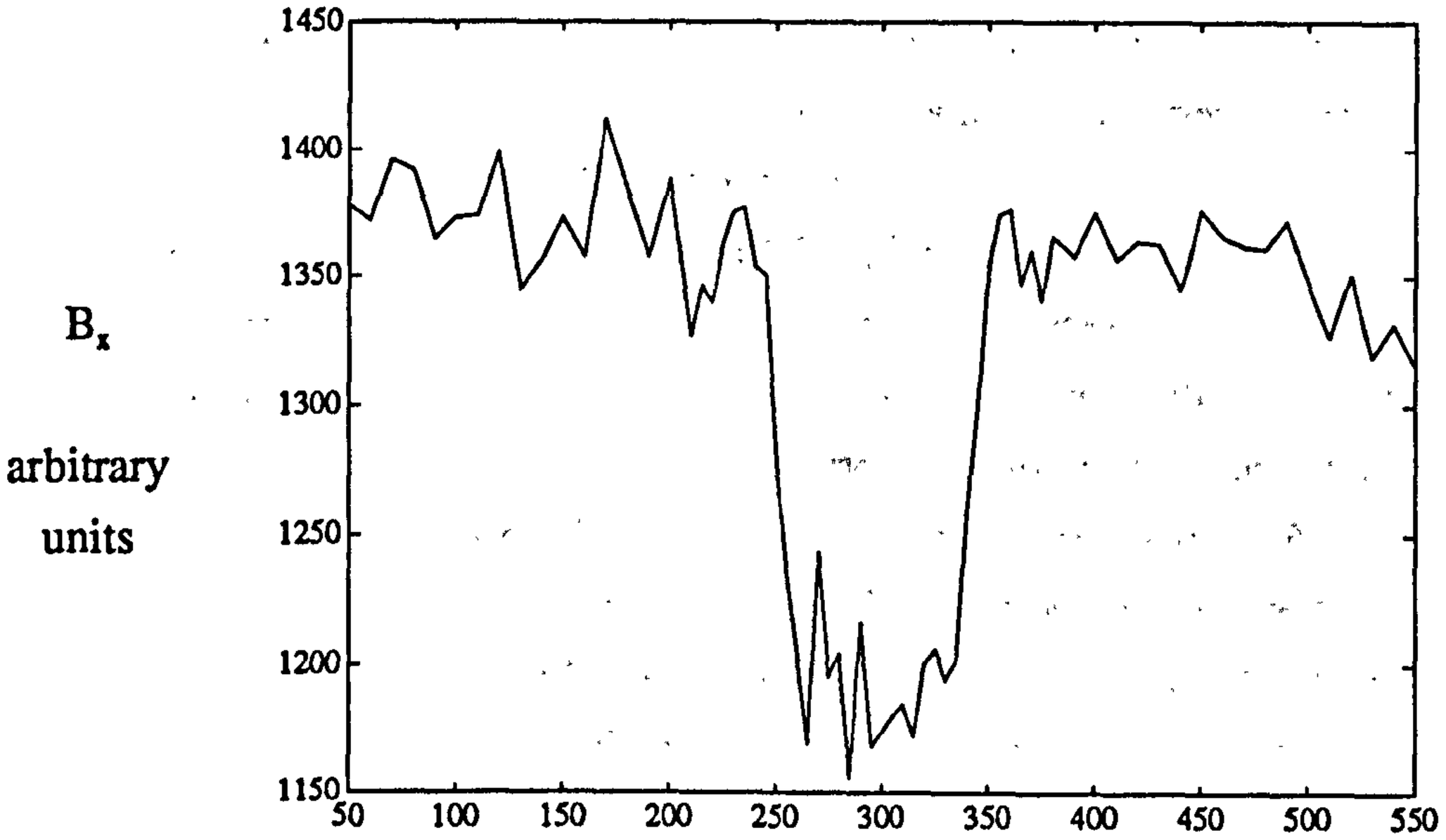

Fig. 5.5 ACFM probe *x* coil response from a tubular joint crack
Length 2*a*=65mm depth *b*=5.2mm

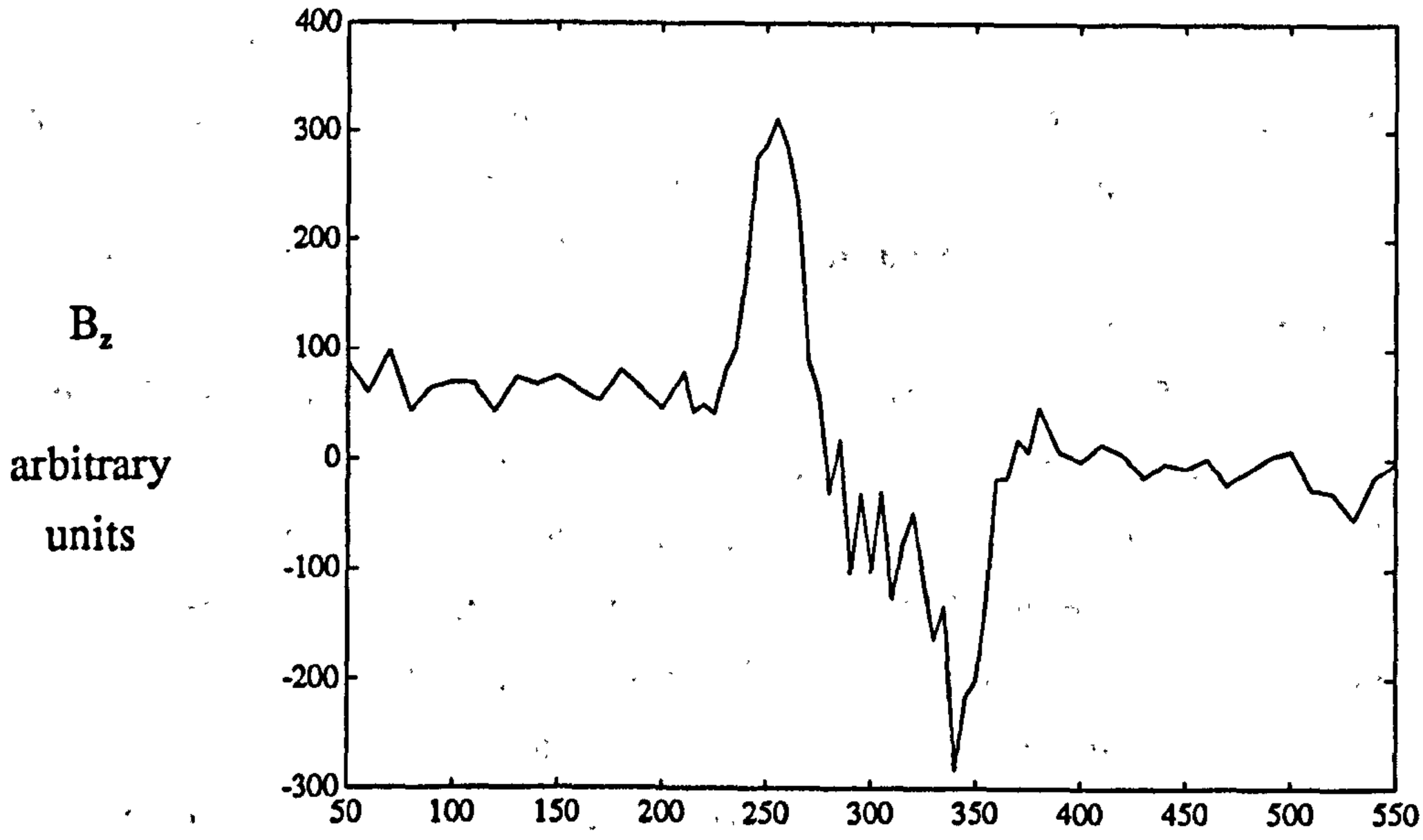

Fig. 5.6 ACFM probe *z* coil response from a tubular joint crack
Length 2*a*=65mm depth *b*=5.2mm

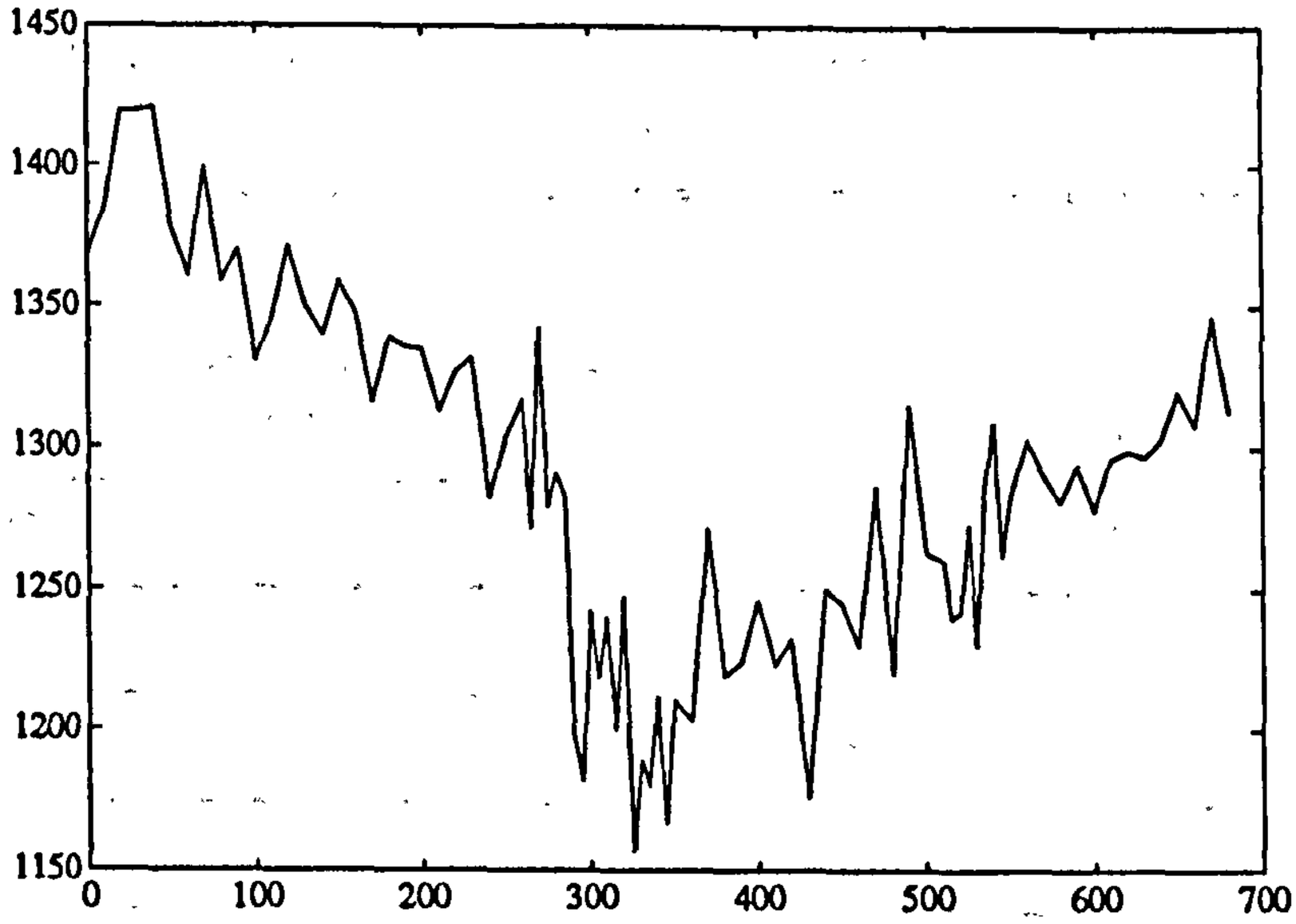

Fig. 5.7 ACFM probe *x* coil response from a tubular joint crack
Length 2*a*=190mm depth *b*=4.3mm

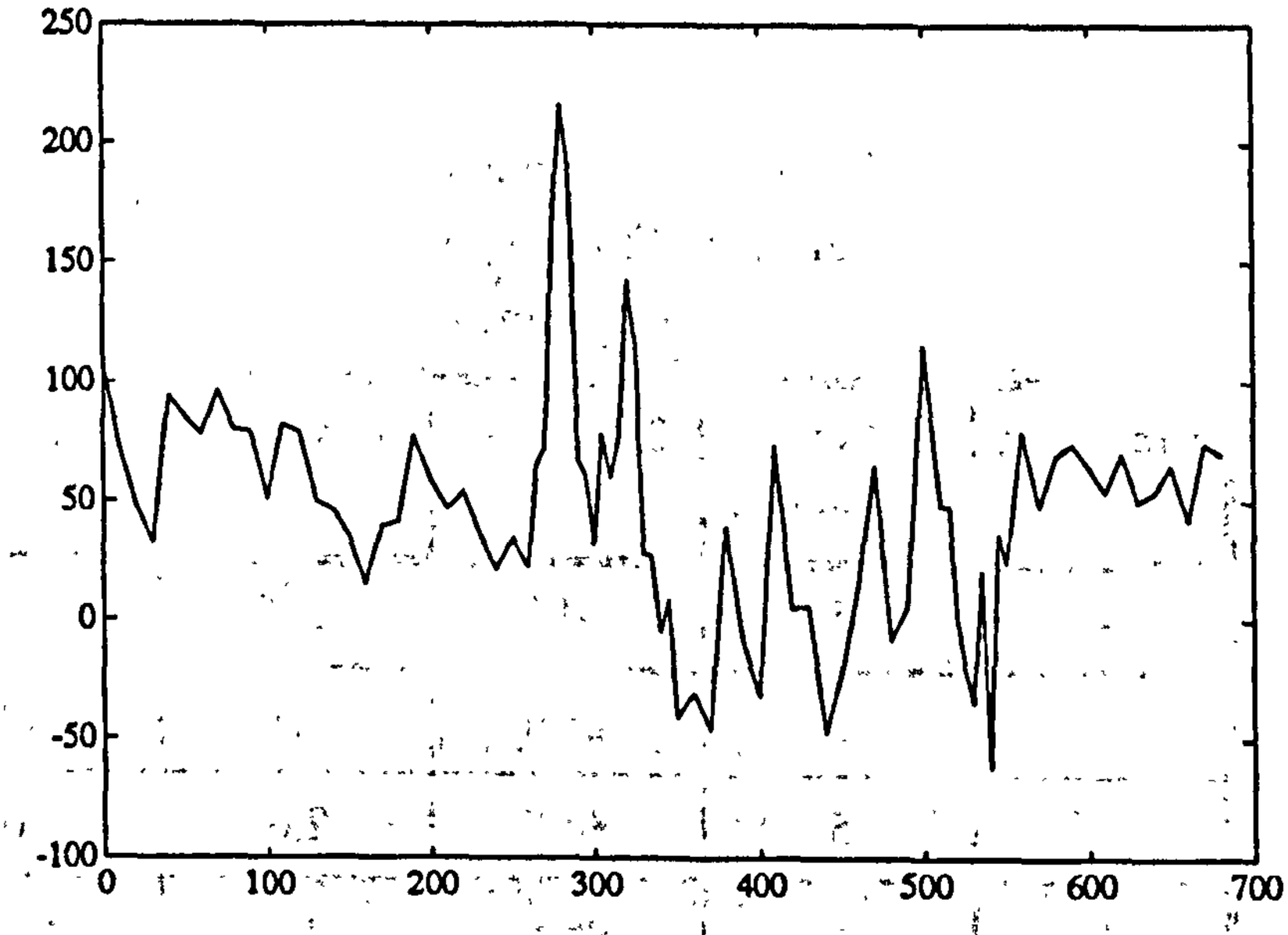

Fig. 5.8 ACFM probe *z* coil response from a tubular joint crack
Length 2*a*=190mm depth *b*=4.3mm

Table 5.1 Crack sizing in tubular joints by ACPD
and by ACFM using B_x for depth and B_z for length.
(All dimensions in mm)

Crack No.	Coil diameter	2*a* ACFM	*b* ACFM	2*a* ACPD	*b* ACPD
4	5	60.7	4.4	65	5.2
6	5	28.6	2.4	30	1.9
7	5	34.1	3.1	50	4.4
8	5	96.8	9.8	125	8.7
5	5	62.8	5.6	65	5.8
7	3	33.9	3.2	50	4.4
7	2	42.0	3.4	50	4.4
8	3	100.8	10.2	125	8.7
8	2	110	13.5	125	8.7

Table 5.2 Crack sizing in tubular joints by ACPD
and by ACFM using B_z for depth and length.
(All dimensions in mm)

Crack No.	Coil diameter	2*a* ACFM	*b* ACFM	2*a* ACPD	*b* ACPD
4	5	60.7	2.3	65	5.2
6	5	28.6	2.1	30	1.9
7	5	34.1	2.6	50	4.4
8	5	96.8	2.1	125	8.7
7	3	33.9	2.0	50	4.4
8	3	100.8	2.6	125	8.7

5.4 Method of crack sizing

Evaluation of the theoretical models for different depths of crack showed that the signals were always of the general forms plotted in figs. 4.12-4.18, but that the magnitude of the peaks and troughs increased monotonically with crack depth, without exception. This implies that the depth is uniquely determined by the signal magnitude, when all of the other parameters are fixed. Fatigue crack measurement is not, of course, only conducted in flat plates. It is important to know if the flat-plate model will give a reasonable approximation for the geometry of test-piece used in each application. As explained in chapter 3, in the unfolding limit the fields are independent of the material constants, so in magnetic metals it is highly desirable to select a frequency that puts the flaws in this limit. The data below are all evaluated for the unfolding limit, except where stated otherwise.

It is not immediately obvious how to orientate the sense-coil in order to get the most reliable estimate of crack depth and length or whether different orientations should be used for detection and for sizing. Since a measurement must be made of the applied field in the x direction, an advantage of using the magnitude of the x component is that the same coil may be used for readings in both the flawed and unflawed parts. There is then no need to measure the relative sensitivities of two separate coils. However, a possible disadvantage of this method is that the crack signal is a small perturbation of a large signal, so the signal to noise ratio must be good if the measurement is to be reliable. The central trough of the plot of B_x against x (fig. 4.12) spreads over most of the crack length, so that smoothing by the measuring coil should not significantly alter the reading. Moreover, because it consists mainly of contributions from the low spatial frequencies in the transform, the depth of the central trough varies only slowly with lift-off. The y component has the important feature of changing sign on crossing the crack. If the component geometry allows measurement on both side of the crack, it may be possible to take advantage of this anti-symmetry by measuring the difference in the y component across the crack, possibly reducing the effects of field non-uniformities. On the other hand, a small error in coil position might cause a gross error in the depth estimate, because the field strength changes rapidly with y. The perturbation magnitude of the z component is larger than that for the other components. This suggests that the z component is the most suitable for detection purposes.

The first step in developing an inversion procedure was to run the theoretical model, for m=0, for a variety of relative lift-off values and aspect ratios. No simple equation could be found that accurately fitted the data, so it was decided instead to store the results and interpolate. A crude estimate of crack length can be obtained immediately by measuring the distance between peak and trough of B_z that occur at the crack ends. This distance will be referred to as $2a^*$. The crack-end peaks of the x signal could also be used for this purpose, but it was found experimentally that they tended to be less well-marked than the z signal crack-end features. The y component has not so-far been used for sizing, because both for the welded tubular joints and for the drill-string threads it was impractical to make measurements on either side of the crack.

The crack depth is a function of peak magnitude, aspect ratio b/a and lift-off ratio z/a. However, initially all that is known is the peak magnitude and the ratio of the lift-off to the approximate crack length $2a^*$. In general, one would expect the interpolation to be quite complicated, because the ratio a/a^* may be dependent on the aspect ratio, which is initially unknown. Fortunately, according to the theoretical model, a/a^* is almost independent of aspect ratio, varying by only about 3% over the whole range of aspect ratios from 0 to 1, so the interpolation process can be made relatively simple by ignoring this slight variation and working with the mean a/a^* value.

The unfolding solution for a semi-elliptical crack was evaluated for b/a=0.05,0.1,.....1 and z/a=0.05,0.125,.....0.725. The peak value of B_z and the central trough value of B_x were calculated, giving 400 tabulated values overall. The position of the peak of B_z was selected as the clearest indication of the crack ends and 10 values of a/a^* were found for each aspect ratio. The 10 mean values of a/a^* over the aspect ratios were tabulated against the measurable quantity z/a^*. The sizing algorithm begins by finding the half-length a from z/a^*, by using linear interpolation, and then infers the lift-off ratio z/a. Beginning from the smallest tabulated aspect-ratio, the predicted peak magnitude for the relevant field component is found by linear interpolation between the two z/a values that bound the one that has just been calculated. This process is repeated for increasing b/a until a peak magnitude is found that is greater than the observed peak magnitude. The correct aspect ratio b/a for the crack being measured is then found by a final linear interpolation. Fig. 5.9 shows plots of the perturbation part of B_x, normalised to the incident field strength, against b/a for the z/a values given above. The higher

field values correspond to smaller lift-offs, so that the sensitivity is better for smaller lift-offs, as one might expect. The dependence on aspect ratio *b/a* is close to linear for shallow cracks and becomes weaker as the aspect ratio rises.

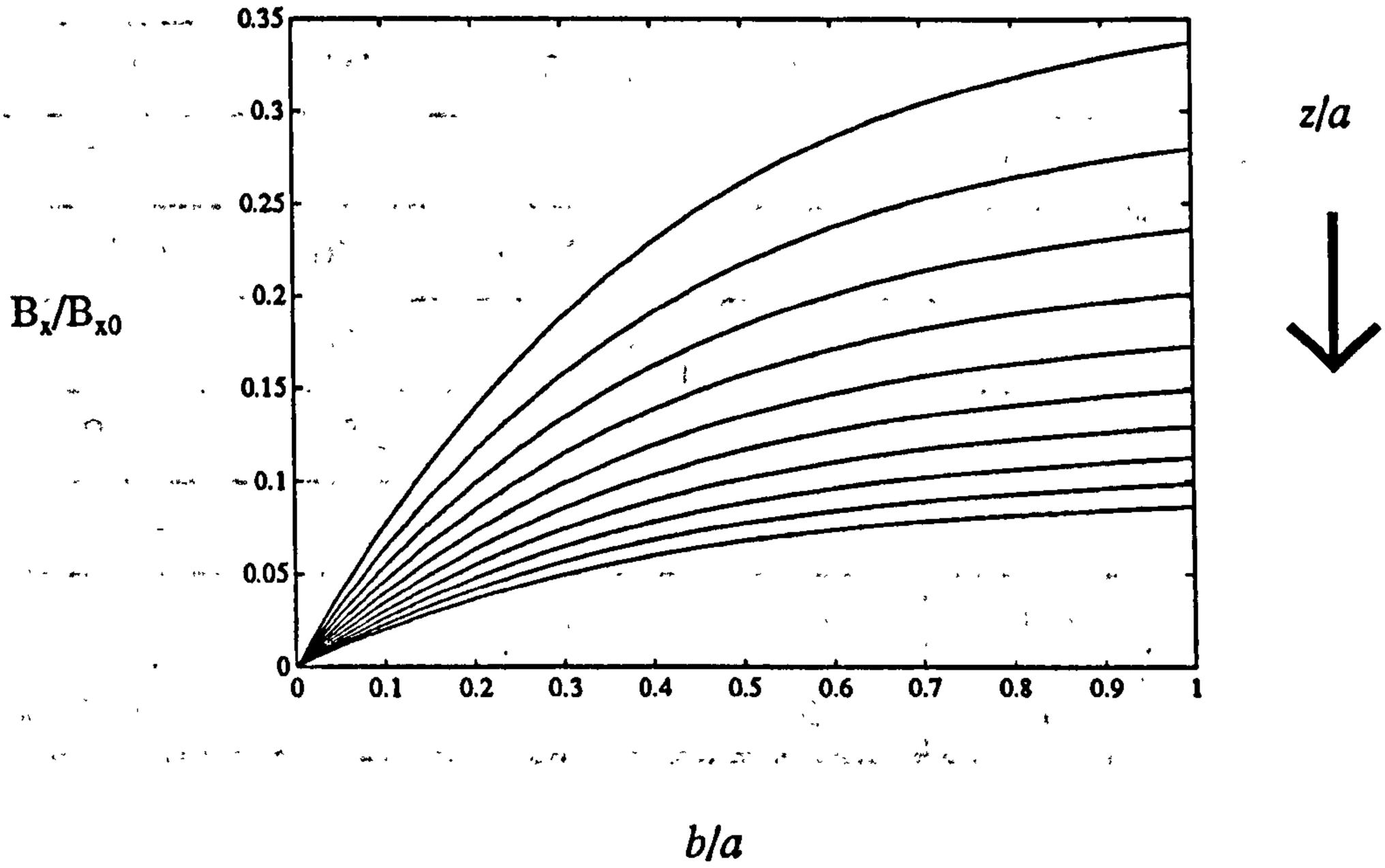

Fig. 5.9 Variation of signal strength with aspect ratio for 10 values of lift-off ratio
z/a = 0.05,0.125,.....0.725
Unfolding limit

A self-consistency test was conducted on this interpolation scheme in which peak values and positions predicted by the model were used as input data for the sizing program. The length estimates from the peaks of the *z* signal were found to be consistent with the input lengths to within 2.25% as shown in table 5.3. The depths from the central trough of the *x* signal were consistent with the input depths to within 1.5% (table 5.4). Depth estimates from the *z* signal were not quite as good, one value being in error by 5.2% (table 5.5), because of the greater sensitivity to lift-off.

Table 5.3 Self-consistency check on length estimate

depth b	length $2a$	$2a^*$	estimated length	% error
0.5	8	7.125	8.169	+2.11
1.0	8	7.125	8.169	+2.11
2.0	8	6.875	7.852	-1.85
1.0	16	14.25	16.36	+2.25
2.0	16	14.25	16.36	+2.25
3.0	16	13.75	15.81	-1.19
1.0	24	21.375	24.10	+0.42
2.0	24	21.375	24.10	+0.42
3.0	24	21.375	24.10	+0.42

Table 5.4 Self consistency check on depth estimate by x component

depth b	length $2a$	B_x (peak)	$2a^*$	estimated depth	% error
0.5	8	0.9630802	7.125	0.5014	+0.28
1.0	8	0.9349023	7.125	0.9946	-0.54
2.0	8	0.8988158	6.875	2.030	+1.5
1.0	16	0.9403898	14.25	1.011	+1.1
2.0	16	0.8944303	14.25	2.007	+0.35
3.0	16	0.8599268	13.75	2.983	-0.57
1.0	24	0.9508463	21.375	1.004	+0.40
2.0	24	0.9092289	21.375	2.001	+0.05
3.0	24	0.8742926	21.375	2.989	-0.37

Table 5.5 Self consistency check on depth estimate by z component

depth b	length $2a$	B_z (peak)	$2a^*$	estimated depth	% error
0.5	8	0.043983899	7.125	0.4956	-0.88
1.0	8	0.077089399	7.125	0.9813	-1.9
2.0	8	0.1186514	6.875	2.050	+2.5
1.0	16	0.094825536	14.25	0.9778	-2.2
2.0	16	0.1659807	14.25	1.932	-3.4
3.0	16	0.2178786	13.75	2.931	-2.3
1.0	24	0.095024139	21.375	0.9614	-3.9
2.0	24	0.1741818	21.375	1.904	-4.8
3.0	24	0.2388117	21.375	2.843	-5.2

A robustness check was carried out in which the peak position a^* was deliberately made 5% too big or too small, to see the effect on sizing. For both length and depth estimates, the error in sizing was first order in the error in input data, the z signal being more sensitive than the x signal. Results are in table 5.6 and 5.7.

Table 5.6 Sensitivity of z size estimates to small errors

depth b	length $2a$	$2a^*$	estimated depth (using $1.05a^*$)	estimated length (using $1.05a^*$)	estimated depth (using $0.95a^*$)	estimated length (using $0.95a^*$)
0.5	8	7.125	0.4824	8.600	0.5084	7.710
1	8	7.125	0.9455	8.600	1.058	7.395
2	8	6.875	1.878	8.282	2.288	7.395
1	16	14.25	0.9726	17.14	1.017	15.57
2	16	14.25	1.909	17.14	1.971	15.57
3	16	13.75	2.841	16.57	3.062	15.05
1	24	21.375	0.9657	25.25	0.9607	22.95
2	24	21.375	1.899	25.25	1.917	22.95
3	24	21.375	2.830	25.25	2.868	22.95

Table 5.7 Sensitivity of x depth estimates to small errors

depth b	length $2a$	$2a^*$	estimated depth (using $1.05a^*$)	estimated depth (using $0.95a^*$)
0.5	8	7.125	0.4824	0.5084
1	8	7.125	0.9455	1.058
2	8	6.875	1.878	2.288
1	16	14.25	0.9726	1.017
2	16	14.25	1.909	1.971
3	16	13.75	2.841	3.062
1	24	21.375	0.9657	0.9607
2	24	21.375	1.899	1.917
3	24	21.375	2.830	2.868

From all these tests, it was concluded that the sizing algorithm was self-consistent and robust to within the accuracy required for engineering purposes and that it was not necessary to use a higher order interpolation scheme. The first versions of the software for the ferromagnetic drill-strings and for the tubular joints used the algorithm exactly as described here.

An improved program was written for the second prototype tubular joint probe, incorporating a correction for the finite size of the measuring coil (as discussed in section 6.5), so that small cracks can be sized with the 5mm diameter probe. Since the coil size defines an absolute length scale, it was necessary to evaluate the model for various absolute lengths, instead of working with the dimensionless ratio z/a. The x coil was taken to be approximately cuboidal and the coil-size correction factor was of the form

$$\operatorname{sinc}\frac{p_x k_x}{2}\operatorname{sinc}\frac{p_y k_y}{2}\operatorname{sinch}\frac{p_z k_z}{2} \qquad (5.4.1)$$

for each spatial frequency k_x,k_y where the coil dimensions are p_x,p_y and p_z. The function sinch is just the hyperbolic analogue of sinc. The correction factor for a cylindrical coil of diameter p_d orientated in the z direction is

$$2\frac{J_1(p_d k_z/2)}{p_d k_z/2}\operatorname{sinch}(p_z k_z/2). \qquad (5.4.2)$$

where J_1 is the first order Bessel function. Note that both these coil-size correction factors reduce to 1 for an ideally small coil. The look-up table was generated by running the unfolding model for semi-elliptical cracks with aspect ratios b/a=0.02,0.04,....0.98 and lengths $2a$=4,6,8,.....100 mm giving 2401 values of B_z(peak) and B_x(peak), with 49 values of a^*.

When the sizing algorithm is used in the Born limit, there is the slight additional complication that the predicted signal strength depends on the length $\mu_r\delta$ and also on the notch width, where applicable. It is necessary to be more careful about defining the phase of the signals because the perturbation is not in phase with the applied field. Fig. 5.10 shows plots of the normalised perturbation part of B_x against aspect ratio, for the same lift-off ratios as fig. 5.9. The normalised B_x, which is always purely real, is calculated by dividing by the upstream B_x and also by a factor

$$(\mu_r/k + h/2)/a = \frac{\mu_r\delta + h - i\mu_r\delta}{2a}. \qquad (5.4.3)$$

The sizing program first infers a from the peak positions, as in the small m case. Given the value of $\mu_r\delta$, the normalised B_x (or B_z) is inferred from the real part of the signal using 5.4.3. The program then proceeds to size the crack by interpolation in the same way as the program for the small m limit. It is also possible to work with the imaginary part of the signal if desired, providing the notch width h is known. In the large m limit, the real and imaginary parts of the field are equal if the crack is closed, i.e. if h=0.

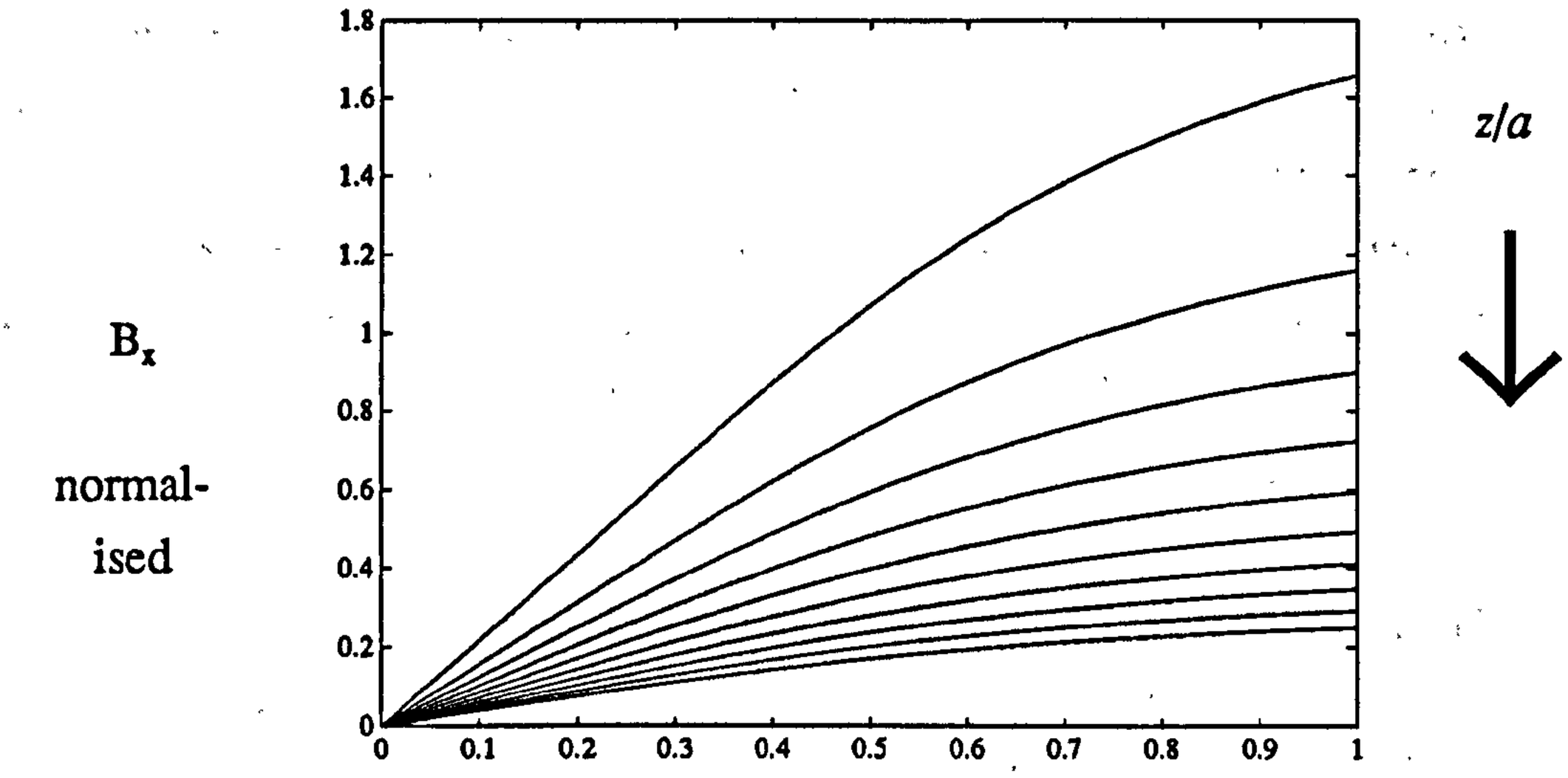

Fig. 5.10 Variation of signal strength with aspect ratio
for 10 values of lift-off ratio
$z/a = 0.05, 0.125, ...0.725$
Born limit

Finally, in the large m limit, if both real and imaginary parts of any component of the magnetic field are known it is possible to infer h using 5.4.3,

$$h = \mu,\delta[\,|Re(B)|\,/\,|Im(B)|\,-1]. \qquad (5.4.4)$$

At the time of writing, no experimental data is available for the nonmagnetic materials.

The main advantage of the interpolation method described in this chapter is that very little arithmetic is required to obtain the crack size once the data has been tabulated over the required range, so that a personal computer can give size estimates almost instantaneously. Calculation of the data tables usually requires several hours processing on a minicomputer. A general m depth inversion program based on the same method would need data tables with an additional degree of freedom, which are likely to take a prohibitive length of time to compute. However, it may be possible to devise a general m depth calculation, based on an iterative use of the rectangular solution of chapter 3, which would take longer to run than the interpolation algorithm but which would not require a lengthy preliminary calculation.

6 Impedance of a Circular Coil Near a Crack

6.1 Introduction

In chapter 3, solutions were presented for the field near a flat plate with a uniform incident field but the same concepts can also be used to model more conventional eddy-current tests. In this chapter, the new model is used to calculate the impedance change for a circular air-cored coil with its axis perpendicular to a flat plate with a uniformly deep, infinitely long fatigue crack. The final expression for the impedance change is evaluated using numerical integration and the results are expressed in terms of the parameter $m=r_0/\mu_r\delta$ where r_0 is the coil radius. The analysis for a single-coil system is generalised to treat a two-coil system with an exciter coil and a receiver coil.

6.2 Solution for the Fourier transform of the scalar potential

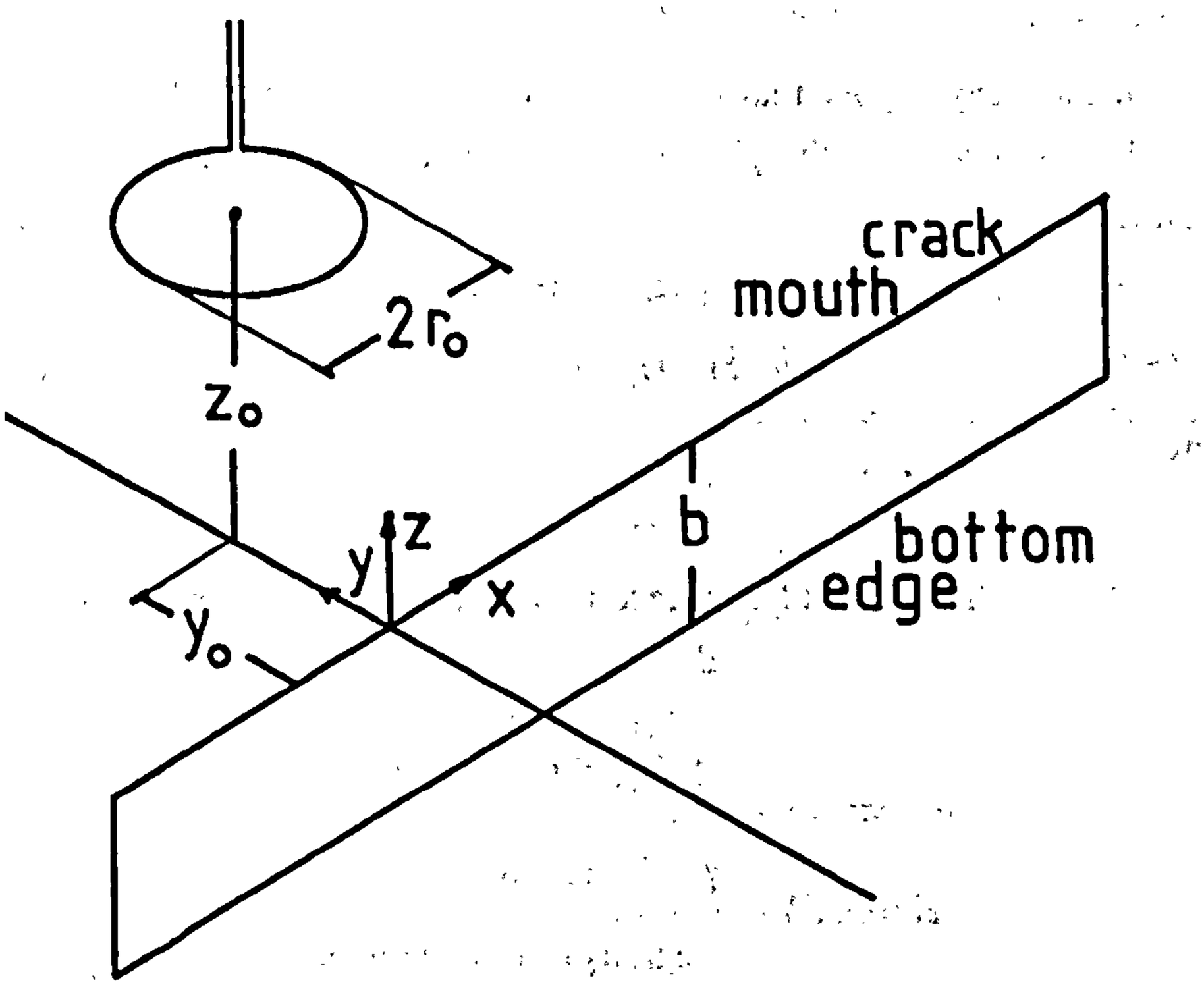

Fig. 6.1 Circular coil near a uniform crack

The Fourier transform method was used in chapter 3 to solve the uniform-field problem for a flat plate but it is equally applicable to non-uniform

fields. Auld's student Riaziat [115] has discussed in detail how the behaviour of an arbitrary coil near a flat plate may be understood using spatial Fourier transforms and the analysis given here combines his method with the surface impedance method of chapter 3.

Let the coil radius be r_0, let the lift-off be z_0, the horizontal offset be y_0, let there be N turns and let the crack depth be b, as shown in fig.6.1. It will be assumed that the coil wire is thin compared to the coil diameter. The impedance change for a coil with windings of finite cross-section can be found by integrating the field of the thin-coil over the cross-section.

The scalar potential ψ may be considered in two parts: ψ_f, the potential that would exist if the coil were situated in free space and ψ_p, the perturbation caused by the cracked plate,

$$\psi = \psi_p + \psi_f \quad . \tag{6.2.1}$$

As usual, each component of the two-dimensional Fourier transforms, $\tilde{\psi}_f$ and $\tilde{\psi}_p$ must decay exponentially, $\tilde{\psi}_f$ as the distance from the coil increases and $\tilde{\psi}_p$ as the distance from the plate increases. At a height z, the potentials are therefore

$$\tilde{\psi}_f(z) = \tilde{\psi}_f(z_0)\exp(-k_z|\, z - z_0|\,), \tag{6.2.2}$$

$$\tilde{\psi}_p(z) = \tilde{\psi}_p(0)\exp(-k_z z), \tag{6.2.3}$$

where

$$k_z^2 = k_x^2 + k_y^2. \tag{6.2.4}$$

On the plane z=0, the extended surface impedance boundary condition, 3.3.17, applies to the total scalar potential,

$$\frac{\partial^2\psi}{\partial x^2} + \frac{\partial^2\psi}{\partial y^2} + \gamma\frac{\partial\psi}{\partial z} = 2H_z(x,0)\delta(y), \tag{6.2.5}$$

$$\gamma = (\mathrm{i}+1)/\mu,\delta. \tag{6.2.6}$$

Writing this equation in terms of the transforms and remembering that $\tilde{\psi}_f$ and $\tilde{\psi}_p$ decay in opposite directions, one obtains

$$(-k_z^2 - k_z\gamma)\tilde{\psi}_p + (-k_z^2 + k_z\gamma)\tilde{\psi}_f = 2\tilde{H}_z(k_x,0) = 2\int_{-\infty}^{\infty} H_z(x,0)e^{-ik_x x}\,\mathrm{d}x. \tag{6.2.7}$$

In 6.2.7, $\tilde{H}_z(k_x,0)$ is the one-dimensional transform of the vertical component of magnetic field inside the crack. Equation 6.2.1 can be used to eliminate $\tilde{\psi}_p$ from 6.2.7 so that the transform of the total potential is

$$\tilde{\psi}=\frac{2\gamma k_z\tilde{\psi}_f-2\tilde{H}_z(k_x,0)}{k_z^2+\gamma k_z}. \tag{6.2.8}$$

This equation can be usefully arranged in a slightly different form with the exponential factors made explicit,

$$\tilde{\psi}(0)=\tilde{\psi}_f(z_0)\exp(-k_z z_0)+\frac{\gamma-k_z}{\gamma+k_z}\tilde{\psi}_f(z_0)\exp(-k_z z_0)-\frac{2\tilde{H}_z(k_x,0)}{k_z^2+\gamma k_z}. \tag{6.2.9}$$

The second term on the right-hand side of 6.2.9 has the typical form of a reflection coefficient and is the perturbation caused by the uncracked plate. The third term is the additional perturbation due to the crack. The potential at coil height can be inferred by multiplying each term in 6.2.9 by its appropriate exponential factor,

$$\tilde{\psi}(z_0)=\tilde{\psi}_f(z_0)+\frac{\gamma-k_z}{\gamma+k_z}\tilde{\psi}_f(z_0)\exp(-2k_z z_0)-\frac{2\tilde{H}_z(k_x,0)}{k_z^2+\gamma k_z}\exp(-k_z z_0). \tag{6.2.10}$$

6.3 Effect of the crack

On the crack faces, the conditions of chapter 3 apply: the potential ψ must satisfy the two-dimensional Laplace equation, it must be continuous with the exterior potential on the line z=0 and it must have zero normal derivative on the crack bottom edge. A suitable form that satisfies these conditions is

$$\psi=\frac{1}{4\pi^2}\int_{-\infty}^{\infty}\int_{-\infty}^{\infty}\tilde{\psi}\frac{\cosh[k_x(z+b)]}{\cosh(k_x b)}e^{ik_x x}\,dk_x dk_y. \tag{6.3.1}$$

Differentiating with respect to z on the line z=0, one obtains

$$H_z(x,0)=\frac{1}{4\pi^2}\int_{-\infty}^{\infty}\int_{-\infty}^{\infty}k_x\tilde{\psi}\tanh(k_x b)e^{ik_x x}\,dk_y dk_x, \tag{6.3.2}$$

so that the one-dimensional transform on x of $H_z(x,0)$ is

$$\tilde{H}_z(k_x,0)=\frac{1}{2\pi}\int_{-\infty}^{\infty}k_x\tilde{\psi}\tanh(k_x b)\,dk_y. \tag{6.3.3}$$

If 6.2.8 is substituted into 6.3.3, it may be seen that

$$\tilde{H}_z(k_x,0) = k_x \tanh k_x b\,[\tilde{I}(k_x) + \tilde{F}(k_x)\tilde{H}_z(k_x,0)], \tag{6.3.4}$$

where

$$\tilde{I}(k_x) = \frac{1}{2\pi}\int_{-\infty}^{\infty} \frac{2\gamma\tilde{\psi}_f \exp(-k_z z_0)}{k_z+\gamma}\,dk_y \tag{6.3.5}$$

and

$$\tilde{F}(k_x) = -\frac{1}{2\pi}\int_{-\infty}^{\infty} \frac{2dk_y}{k_z^2+\gamma k_z} \tag{6.3.6}$$

is the boundary condition function of chapter 3, discussed in Appendix A. Equation 6.3.4 can be rearranged to give

$$\tilde{H}_z(k_x,0) = \frac{k_x \tanh(k_x b)\tilde{I}(k_x)}{1-\tilde{F}(k_x)k_x \tanh(k_x b)}. \tag{6.3.7}$$

In 6.2.9, the part of the scalar potential caused by the crack is proportional to $H_z(x,0)$ and the impedance change caused by the crack will therefore depend on $H_z(x,0)$ also. The free-space part of the potential ψ_f drives the solution via the integral $\tilde{I}(k_x)$ of equation 6.3.5.

6.4 Free-space field of the coil

The field of an air-cored coil of arbitrary shape can be expressed as an integral of elementary dipole fields. Each dipole corresponds to a infinitesimal current loop and the coil is built up by combining the loops edge to edge so that the currents cancel along all the edges except the outer edge of the coil.

The scalar potential distance r from a unit dipole orientated in the z direction is

$$\psi_d = \frac{z-z_0}{4\pi[r^2+(z-z_0)^2]^{3/2}}. \tag{6.4.1}$$

The transform of this potential is

$$\tilde{\psi}_d = \int_{-\infty}^{\infty}\int_{-\infty}^{\infty} \frac{z-z_0}{4\pi[r^2+(z-z_0)^2]^{3/2}} e^{-ik_x x} e^{-ik_y y}\,dx\,dy, \tag{6.4.2}$$

which expressed in polar coordinates, centred on the point (x',y'), is

$$\tilde{\psi}_d = e^{-i(k_x x'+k_y y')} \int_0^{2\pi}\int_0^{\infty} \frac{z-z_0}{4\pi[r^2+(z-z_0)^2]^{3/2}} e^{-irk_z\cos\theta} r\,dr\,d\theta. \tag{6.4.3}$$

The integral on θ is a definition of the Bessel function J_0 and the integral on r is given in standard tables (formula 6.554.4 in reference [116]),

$$\tilde{\psi}_d = \frac{1}{2} e^{-i(k_x x' + k_y y')} \int_0^\infty \frac{(z - z_0) J_0(k_z r)}{[r^2 + (z - z_0)^2]^{3/2}} r \, dr = \frac{1}{2} e^{-k_z |z - z_0| - i(k_x x' + k_y y')}. \quad (6.4.4)$$

The transform of the potential due to the whole coil is the integral of 6.4.4 over the area of the coil

$$\tilde{\psi}_f = \frac{1}{2} N I_c e^{-k_z |z - z_0|} \int_{coil\,area} e^{-ik_x x'} e^{-ik_y y'} \, dx' dy', \quad (6.4.5)$$

For the particular case of a circular coil of N turns, radius r_0, centre $(0, y_0)$, carrying a current I_c, the transform of the field is

$$\tilde{\psi}_f(z) = \frac{1}{2} N I_c e^{-ik_y y_0 - k_z |z - z_0|} \int_0^{r_0} \int_0^{2\pi} e^{ik_z r \cos\theta} r \, dr \, d\theta, \quad (6.4.6)$$

$$\tilde{\psi}_f(z) = \pi N I_c e^{-ik_y y_0 - k_z |z - z_0|} \int_0^{r_0} r J_0(k_z r) dr, \quad (6.4.7)$$

which is another standard integral (5.52.2 in [116]), so that

$$\tilde{\psi}_f(z) = \pi r_0^2 N I_c e^{-ik_y y_0 - k_z |z - z_0|} \frac{J_1(k_z r_0)}{k_z r_0}. \quad (6.4.8)$$

In optics textbooks, for example [117], the same integral appears in the calculation of the diffraction pattern of a circular aperture, which is a related problem.

6.5 Voltage measured across the coil

The measured voltage is given by Faraday's Law

$$V = \mu_0 N i\omega \int_{coil\,area} \frac{\partial \psi}{\partial z} ds. \qquad (6.5.1)$$

Each spatial frequency (k_x,k_y) makes a contribution

$$\tilde{V}(k_x,k_y) = \mu_0 N i\omega k_z \tilde{\psi}(z_0) \int_{coil\,area} e^{ik_x x} e^{ik_y y} dx dy, \qquad (6.5.2)$$

which is the complex conjugate of the integral that appears in 6.4.5, so that for a circular coil

$$\tilde{V}(k_x,k_y) = N\pi r_0^2 i\omega\mu_0 e^{ik_y y_0} \frac{2J_1(k_z r_0)}{k_z r_0} k_z \tilde{\psi}(z_0). \qquad (6.5.6)$$

The formal resemblance between the behaviour of the coil as an exciter and its behaviour as a receiver does not depend on the shape of the coil. For example, it is well-known that the mutual inductance of a transformer is the same regardless of which coil is regarded as the primary. Burrows [32] gave a derivation of this theorem, with initial assumptions applicable to eddy-current NDE, based on the Lorentz reciprocity relationship

$$\nabla \cdot (\mathbf{E}_1 \times \mathbf{H}_2 - \mathbf{E}_2 \times \mathbf{H}_1) = 0. \qquad (6.5.7)$$

Auld [38],[39] has shown that it is possible to use 6.5.7 to calculate the impedance change from the fields in the region of the flaw only, without working out explicitly how the magnetic field induces a voltage in the receiver coil. However, in the case under consideration here, the direct calculation was straightforward.

Equation 6.5.6 can also be used to correct for the finite size of a cylindrical measuring coil, perpendicular to the test-piece surface, when the inducing field is uniform. This correction was incorporated into the tubular joint program described in the previous chapter. A correction factor for a coil with its axis perpendicular to the test-piece was also mentioned, which was derived in a similar way, except that the coil shape was assumed to be cuboidal to simplify the integration.

6.6 Impedance change due to the crack

To summarise the calculation so far, the general interaction of a coil with a cracked flat plate was modelled using the surface impedance boundary condition and Fourier transforms, the specific fields for a uniform crack and a circular inducing coil were calculated, finally the voltage measured across a circular receiver coil was calculated for each Fourier component. It is now possible to find the impedance change of the coil caused by the crack.

In 6.2.9, the contribution to the transform of the scalar potential from the crack, which will be denoted $\tilde{\psi}_{pc}$, was

$$\tilde{\psi}_{pc} = \frac{2\tilde{H}_z(k_x,0)}{k_z^2+\gamma k_z}. \qquad (6.6.1)$$

This formula applies to the potential on the test-piece surface. At measuring coil height,

$$\tilde{\psi}_{pc} = \frac{2\tilde{H}_z(k_x,0)e^{-k_z z_0}}{k_z^2+\gamma k_z}. \qquad (6.6.2)$$

Substitution of 6.6.2 into 6.5.6 gives the voltage $\tilde{V}_{pc}$ induced in the measuring coil by each component of the field due to the flaw,

$$\tilde{V}_{pc} = N\pi r_0^2 i\omega\mu_0 \frac{2J_1(k_z r_0)}{k_z r_0}\frac{2\tilde{H}_z(k_x,0)e^{-k_z z_0+ik_y y_0}}{k_z+\gamma}. \qquad (6.6.3)$$

The mouth field $\tilde{H}_z(k_x,0)$ is given by 6.3.7, so that

$$\tilde{V}_{pc} = N\pi r_0^2 i\omega\mu_0 \frac{2J_1(k_z r_0)}{k_z r_0}\frac{2e^{-k_z z_0+ik_y y_0}}{(k_z+\gamma)}\frac{k_x\tanh(k_x b)\tilde{I}(k_x)}{[1-k_x\tilde{F}(k_x)\tanh(k_x b)]}. \qquad (6.6.4)$$

For a circular coil, the integral $\tilde{I}(k_x)$ is obtained by substituting 6.4.8 into 6.3.5 to give

$$\tilde{I}(k_x) = r_0^2 N I_c \gamma \int_{-\infty}^{\infty} \frac{e^{-k_z z_0}\cos k_y y_0}{(k_z+\gamma)}\frac{J_1(k_z r_0)}{k_z r_0}dk_y. \qquad (6.6.5)$$

The measured voltage across the coil is given by inverting 6.6.4, i.e. dividing it by $4\pi^2$ and integrating it over all (k_x,k_y). Because of the reciprocity relationship, the integral on k_y turns out to be exactly the same as the integral in 6.6.5. The impedance change in a single coil system is

$$\Delta Z_{pc} = V_{pc}/I_c, \tag{6.6.6}$$

so that in this case

$$\Delta Z_{pc} = \frac{2i\omega\mu_0}{\pi\gamma I_c^2}\int_0^\infty \frac{\tilde{I}^2(k_x)k_x\tanh(k_x b)}{1-k_x\tilde{F}(k_x)\tanh(k_x b)}dk_x. \tag{6.6.7}$$

Similarly, for a system of two concentric coils, the mutual inductive reactance would be

$$\Delta X_{pc} = \frac{2i\omega\mu_0}{\pi\gamma}\int_0^\infty \frac{\tilde{I}_1(k_x)\tilde{I}_2(k_x)k_x\tanh(k_x b)}{1-k_x\tilde{F}(k_x)\tanh(k_x b)}dk_x. \tag{6.6.8}$$

where $\tilde{I}_1$ and $\tilde{I}_2$ are calculated from 6.6.5 for each of the two coils and for unit current. It is immediately clear that the mutual inductance is unaffected by interchanging the exciter and receiver coils, as expected from the reciprocity theorem.

In order to show more clearly the dependence on the various different parameters it is helpful to write 6.6.7 and 6.6.8 in terms of the following dimensionless functions and variables

$$m = r_0\gamma/(\mathrm{i}+1), \tag{6.6.9}$$

$$l = k_x r_0, \tag{6.6.10}$$

$$n = k_y r_0, \tag{6.6.11}$$

$$p = k_z r_0 = (l^2+n^2)^{1/2}, \tag{6.6.12}$$

$$s = z_0/r_0, \tag{6.6.13}$$

$$t = b/r_0, \tag{6.6.14}$$

$$w = y_0/r_0, \tag{6.6.15}$$

$$\mathrm{j}(l,m,s,w) = \int_0^\infty \frac{e^{-sp}\cos(nw)}{[p+(\mathrm{i}+1)m]}\frac{2\mathrm{J}_1(p)}{p}\mathrm{d}n \quad , \tag{6.6.16}$$

$$f(m/l) = k_x \bar{F}(k_x). \tag{6.6.17}$$

The expressions 6.6.7 and 6.6.8 for the impedance change, in terms of these dimensionless quantities, are

$$\Delta Z_{pc} = 4(\mathrm{i}-1)r_0 f\mu_0 N^2 m \int_0^\infty \frac{j^2(l,m,s,w)l\tanh(lt)}{1-f(m/l)\tanh(lt)}\mathrm{d}l, \tag{6.6.18}$$

$$\Delta X_{pc} = 4(\mathrm{i}-1)r_0 f\mu_0 N_1 N_2 m \int_0^\infty \frac{j_1 j_2 l\tanh(lt)}{1-f(m/l)\tanh(lt)}\mathrm{d}l \quad , \tag{6.6.19}$$

where

$$j_1 = j(lr_1/r_0, mr_1/r_0, z_1/r_1, y_1/r_1) \tag{6.6.20}$$

and

$$j_2 = j(lr_2/r_0, mr_2/r_0, z_2/r_2, y_2/r_2) \tag{6.6.20}$$

In these equations r_1 and r_2 are the radii of the two coils and N_1 and N_2 are their numbers of turns. Any arbitrary length scale can be used for r_0, providing that it is used consistently, but it is natural to pick one representative of the problem, such as the mean of the two coil radii, so that m has its usual significance.

In 6.6.7, the dependence on crack depth is expressed by the hyperbolic tangents. The sensitivity of the impedance to depth becomes weak as the crack depth becomes large compared with the coil size because $\tanh(k_r b)$ asymptotically approaches 1. The variation of impedance change with crack depth for m=1, is shown in fig.6.2, the form of the signal seen on crossing the crack is shown in fig.6.3, and the variation with m is shown in fig.6.4. These results were calculated by using Simpson's rule to evaluate 6.6.16 and 6.6.18 and are given in terms of $Z_0 = 4fr_0\mu_0N^2$ with the real parts shown solid and the imaginary parts shown broken.

On examination of 6.6.16-6.6.18, it is apparent that, in the large m limit, the crack signal becomes proportional to $1/m$ in the same way as it did in the uniform field problem. However, in contrast to the uniform field case, in the small m limit the signal becomes proportional to m instead of independent of it. The maximum impedance change occurs near m=1.

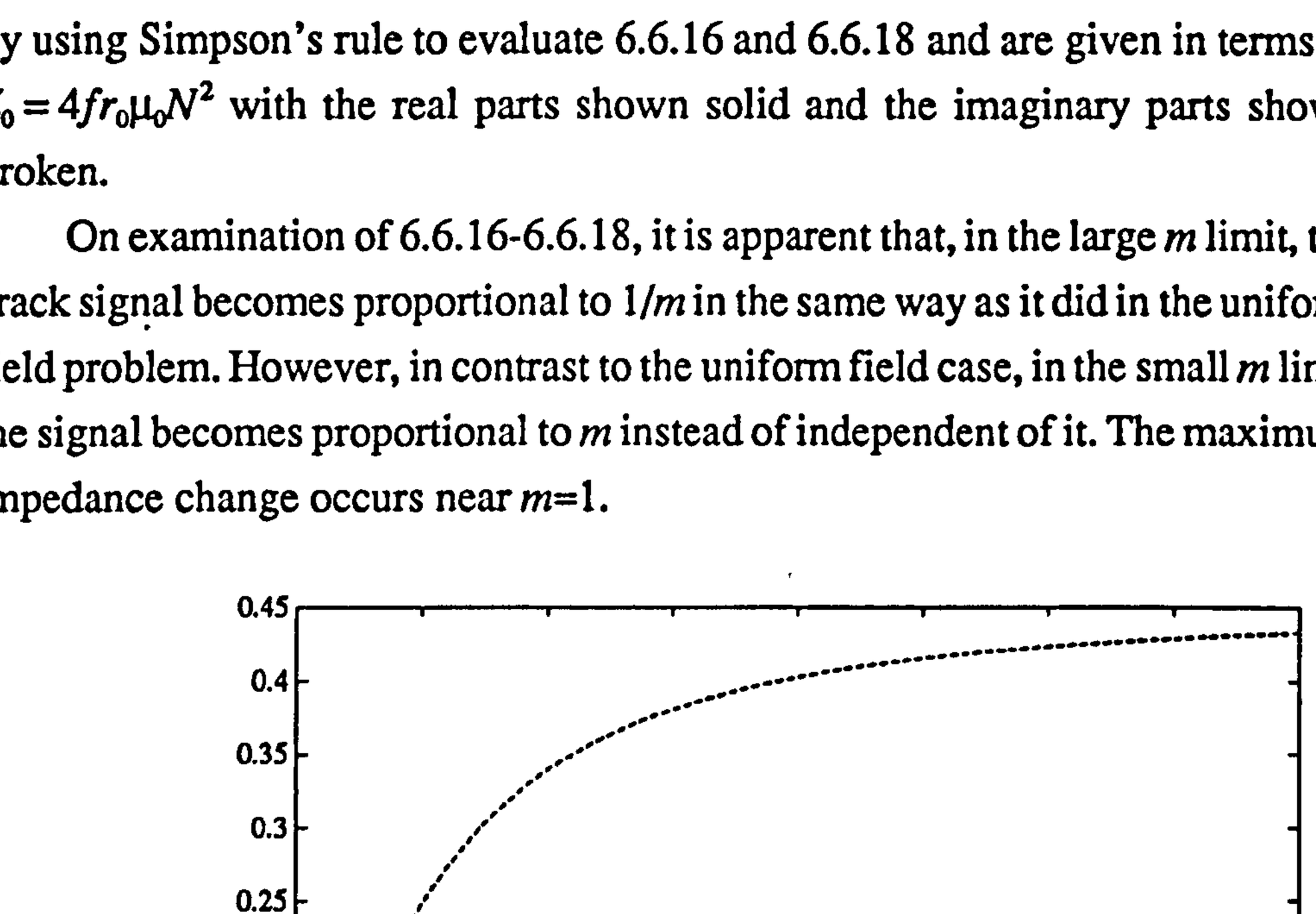

Fig.6.2 Variation of impedance change with depth
(z/r_0=0.1, y=0, m=1)

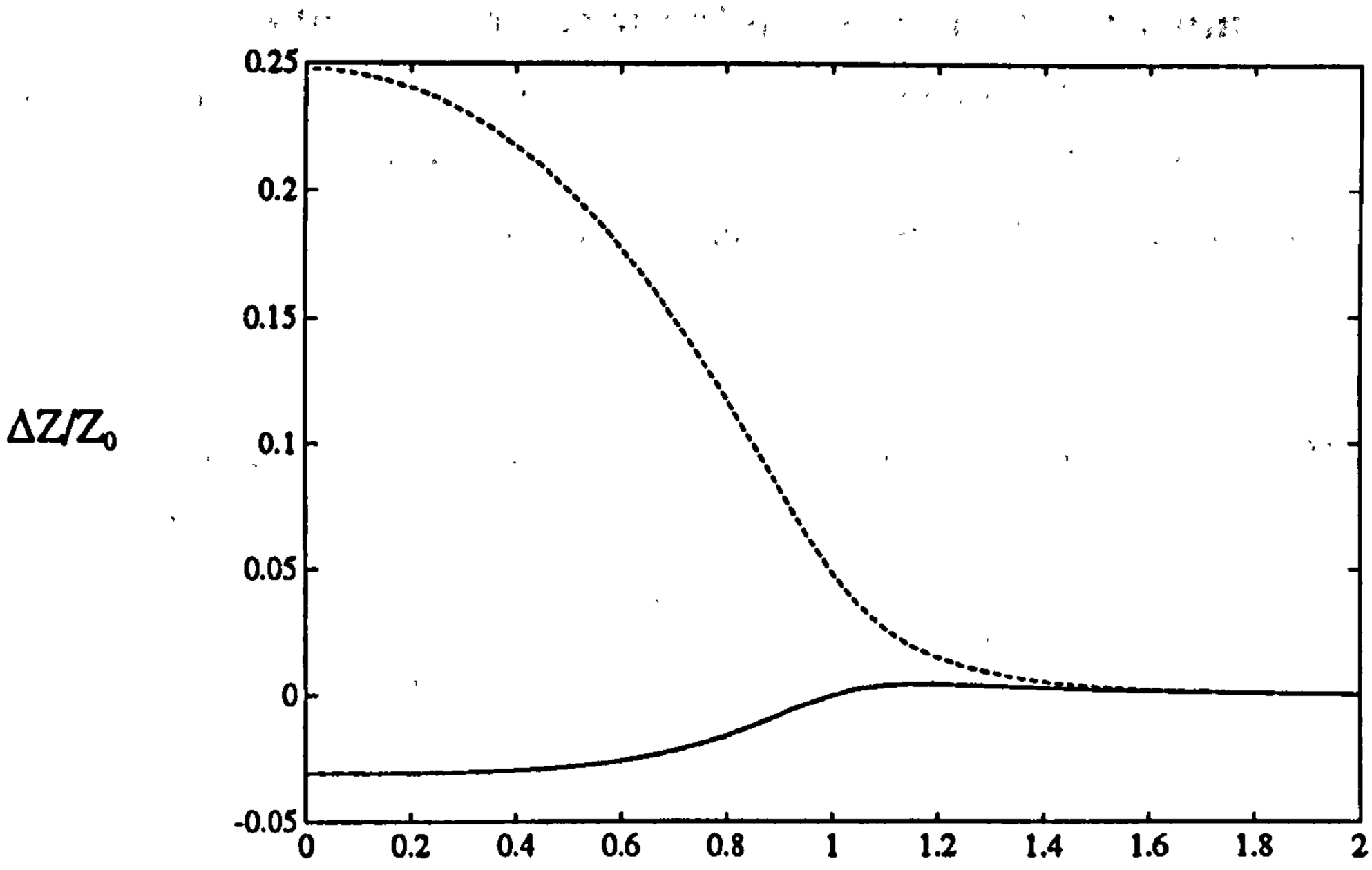

Fig.6.3 Variation of impedance change with offset
(z/r_0=0.1, b/r_0=0.5, m=1)

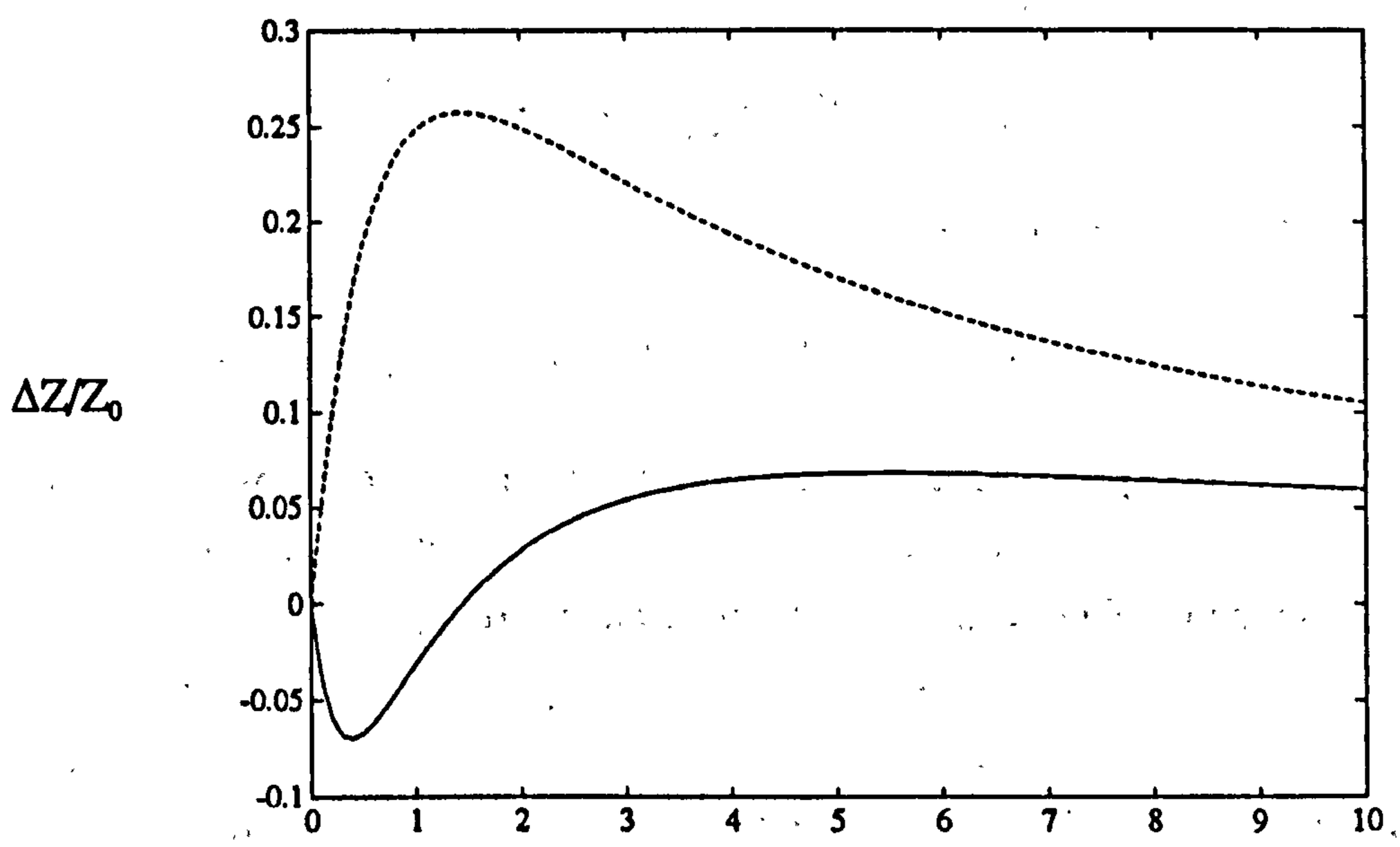

Fig.6.4 Variation of impedance change with m
(z/r_0=0.1, b/r_0=0.5, y=0)

6.7 Impedance change due to the uncracked plate

For the sake of completeness, the calculation of the impedance change on bringing the coil from free-space up to the uncracked plate will now be explained. In equation 6.2.10, the relevant perturbation is

$$\tilde{\psi}_p(z_0) = \frac{\gamma - k_z}{\gamma + k_z} \tilde{\psi}_f(z_0) \exp(-2k_z z_0). \tag{6.7.1}$$

The measured voltage due to this perturbation is obtained by substituting 6.7.1 into 6.5.6 to give

$$\tilde{V}(k_z) = N\pi r_0^2 i\omega\mu_0 \frac{2J_1(k_z r_0)}{k_z r_0} k_z e^{-2k_z z_0} \frac{\gamma - k_z}{\gamma + k_z} \tilde{\psi}_f(z_0) . \tag{6.7.2}$$

As before, the free-space potential is substituted in from 6.4.8 to give

$$\tilde{V}(k_z) = 2N^2\pi^2 r_0^4 I_c i\omega\mu_0 \left(\frac{J_1(k_z r_0)}{k_z r_0} \right)^2 k_z e^{-2k_z z_0} \frac{\gamma - k_z}{\gamma + k_z} \quad . \tag{6.7.3}$$

The impedance change follows, by inversion

$$\Delta Z = \frac{1}{4\pi^2 I_c} \int_{-\infty}^{\infty} \int_{-\infty}^{\infty} \tilde{V}(k_z) dk_x dk_y, \tag{6.7.4}$$

$$\Delta Z = \frac{1}{2\pi I_c} \int_0^{\infty} k_z \tilde{V}(k_z) dk_z \quad . \tag{6.7.5}$$

Finally, substitution of 6.7.3 into 6.7.5 gives

$$\Delta Z = N^2 \pi r_0^2 i\omega\mu_0 \int_0^{\infty} [J_1(k_z r_0)]^2 e^{-2k_z z_0} \frac{\gamma - k_z}{\gamma + k_z} dk_z \quad . \tag{6.7.6}$$

Cheng [118] derived an expression for the impedance change caused by a flat plate for arbitrary skin-depth, using the vector potential, and his formula becomes equal to 6.7.6 in the thin-skin limit, as expected.

7 Some extensions to other geometries

7.1 Introduction

All of the systems discussed so far had in common that there was only one crack in each test-piece, that the test-pieces were flat plates and that the receiver coils were air-cored. In this chapter, three examples are given where each of these restrictions is relaxed, without altering the basis of the modelling. In the first example, the flaw is a pair of identical overlapping fatigue cracks in a flat plate. In the second example, the crack is situated in the interior corner of an angled test-piece. In the final example, a semi-empirical analysis is given for crack depth measurement in mild steel plates using a ferrite-cored measuring probe.

7.2 Overlapping cracks

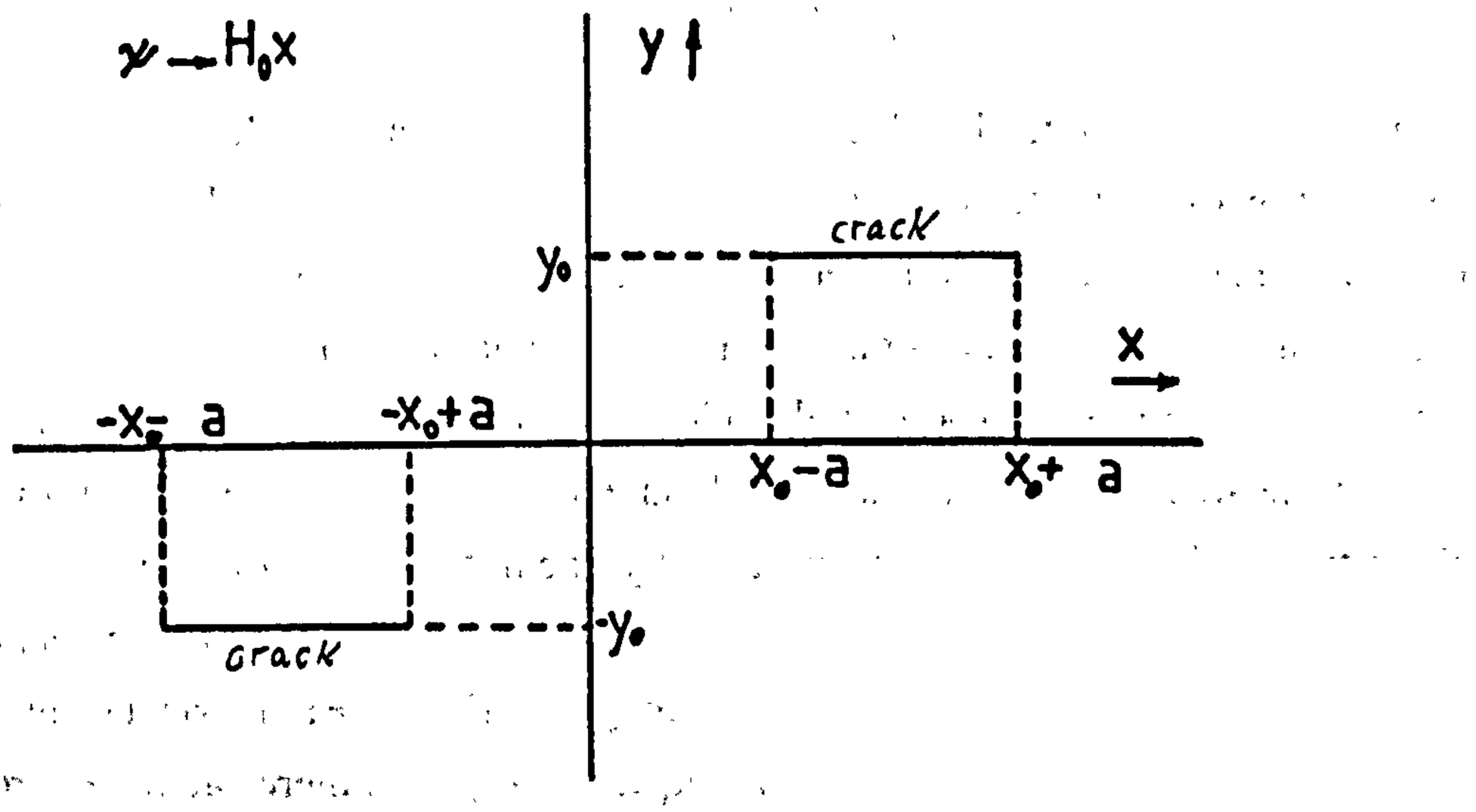

Fig. 7.1 ~~Overlapping crack parameters~~ Parameters for overlapping or offset cracks

The crack separation is $2y_0$ and the offset is $2x_0$, as shown in fig. 7.1. The same analysis applies for truly overlapping cracks ($x_0<a$) and offset cracks ($x_0>a$). For the sake of simplicity, it will be assumed that the applied field is uniform. The contributions of both the cross-crack potential differences, $2\phi_1$ and $2\phi_2$, must be included, so the surface impedance boundary condition is

$$\frac{\partial^2\psi}{\partial x^2}+\frac{\partial^2\psi}{\partial y^2}+\gamma\frac{\partial\psi}{\partial z}=2\frac{\partial\phi_1}{\partial x}\delta(y+y_0)+2\frac{\partial\phi_2}{\partial x}\delta(y-y_0). \qquad (7.2.1)$$

If the two cracks have identical profiles then the flawed test-piece has rotational symmetry of order two about the z axis. The two potentials $2\phi_1$ and $2\phi_2$ can therefore be written in terms of a common potential ϕ,

$$\phi_1 = \phi(x + x_0) \tag{7.2.2}$$

and

$$\phi_2 = \phi(-x + x_0). \tag{7.2.3}$$

The boundary condition 7.2.1 becomes

$$\frac{\partial^2\psi}{\partial x^2} + \frac{\partial^2\psi}{\partial y^2} + \gamma\frac{\partial\psi}{\partial z} = 2\frac{\partial\phi(x + x_0)}{\partial x}\delta(y + y_0) + 2\frac{\partial\phi(-x + x_0)}{\partial x}\delta(y - y_0). \tag{7.2.4}$$

The Fourier transform solution of Laplace's equation, subject to this boundary condition, is

$$\tilde{\psi}(k_x, k_y) = \frac{-2ik_x e^{-k_z z}}{k_z^2 + \gamma k_z}\left(\tilde{\phi}(k_x)e^{ik_x x_0 + ik_y y_0} + \tilde{\phi}(-k_x)e^{-ik_x x_0 - ik_y y_0}\right). \tag{7.2.5}$$

In the large m limit, the Born approximation remains valid because the perturbation of the uniform field by the two-crack system is of order $1/m$, just as it is for the single crack. To generate the scalar potential it is simply necessary to solve the usual two-dimensional Born approximation problem and incorporate the additional complex exponentials of 7.2.5 before inverting the transform.

In the small m limit, the unfolded plane does not have lines of symmetry along the crack bottom edges. Consequently, the unfolding algorithm predicts a discontinuity in the scalar potential across each crack. This is forbidden because it would imply non-zero divergence of the magnetic flux. The numerical solutions of the unfolded problem published by Haq et al. [90] must therefore be regarded as approximate only.

A solution for general m, including both limits, can be obtained by the method of chapter 3. The appropriate boundary condition for the two-dimensional problem is found by inversion of 7.2.5 along one of the crack mouths,

$$\psi(x, y_0, 0) = \frac{1}{2\pi}\int_{-\infty}^{\infty} 2ik_x[\tilde{\phi}(k_x)\tilde{F}(k_x) + \tilde{\phi}(-k_x)\tilde{L}(k_x)]e^{ik_x x}\,dk_x + H_0 x, \quad (7.2.6)$$

where

$$\tilde{L}(k_x) = -\frac{1}{\pi}\int_{-\infty}^{\infty} \frac{\exp(2ik_y y_0)}{k_z^2 + \gamma k_z}\,dk_y. \quad (7.2.7)$$

Although this frequency domain boundary condition is slightly different from the previous one, methods similar to those of chapter 3 could, in principle, be used to find the potential ϕ and hence the whole field. The space domain form of 7.2.7 is

$$\psi(x, y_0, 0) = H_0 x + \int_{-\infty}^{\infty} F(x - x')\phi(x')dx' + \int_{-\infty}^{\infty} L(x + x')\phi(x')dx'. \quad (7.2.8)$$

The first integral is the same *convolution* as before; the second integral is called a *correlation* and corresponds to the scattering of the field between the two cracks, i.e. the effect that the presence of one crack has on the internal field of the other one. In the small m limit, $\tilde{L}(k_x)$ can be found analytically,

$$\tilde{L}(k_x) = -\frac{1}{\pi}\int_{-\infty}^{\infty} \frac{\exp(2ik_y y_0)}{k_z^2}\,dk_y = -\exp(-|2k_x y_0|)/|k_x|. \quad (7.2.9)$$

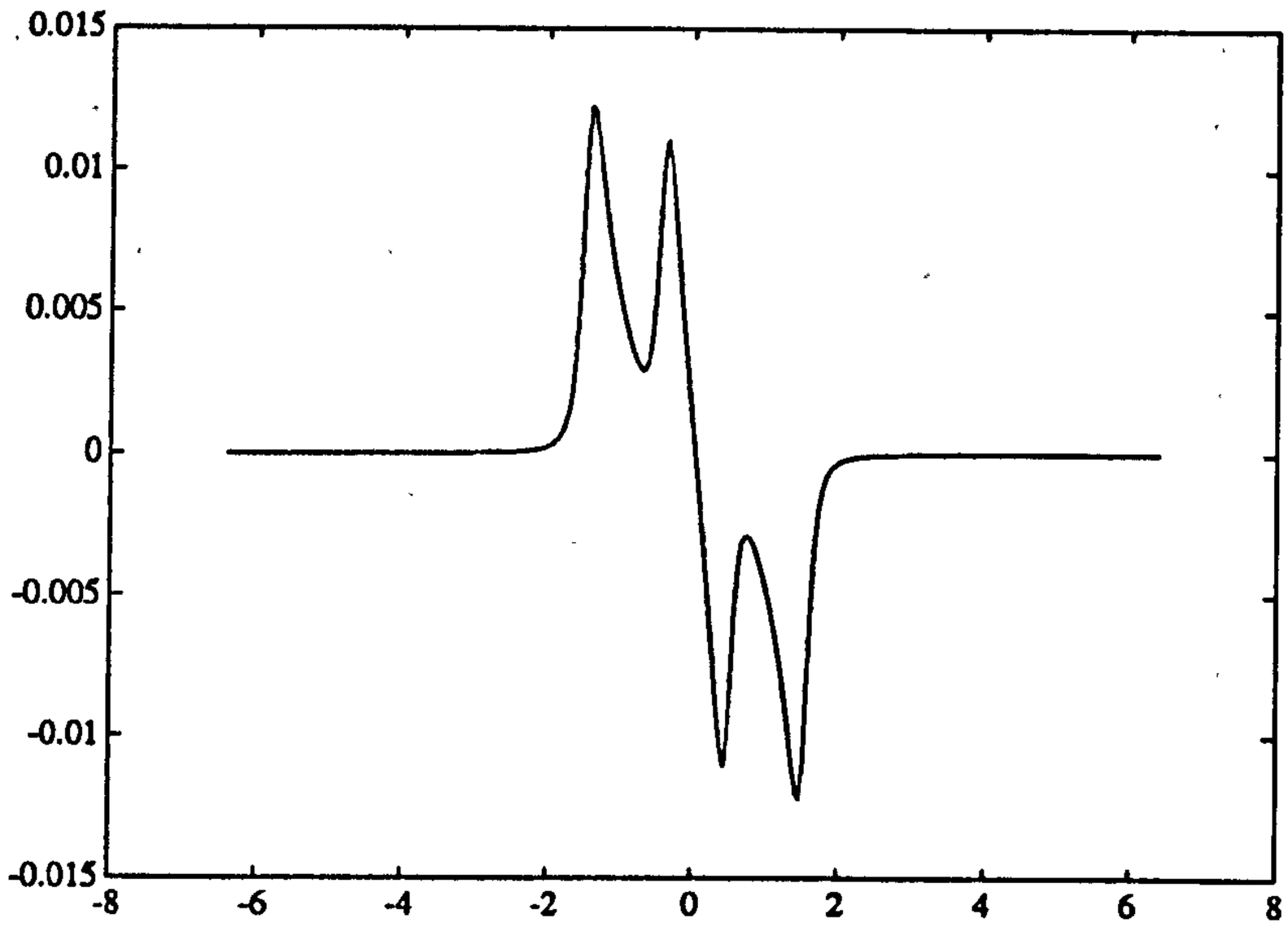

Fig. 7.2 Overlapping cracks in the large m limit

Fig. 7.2 shows H_z, calculated by the Born approximation, for a pair of identical overlapping semi-elliptical fatigue cracks with m=100, a=1, b=0.5, $2x_0$=0.5, $2y_0$=0.1, y=0, z=0.1.

7.3 Crack in an interior corner

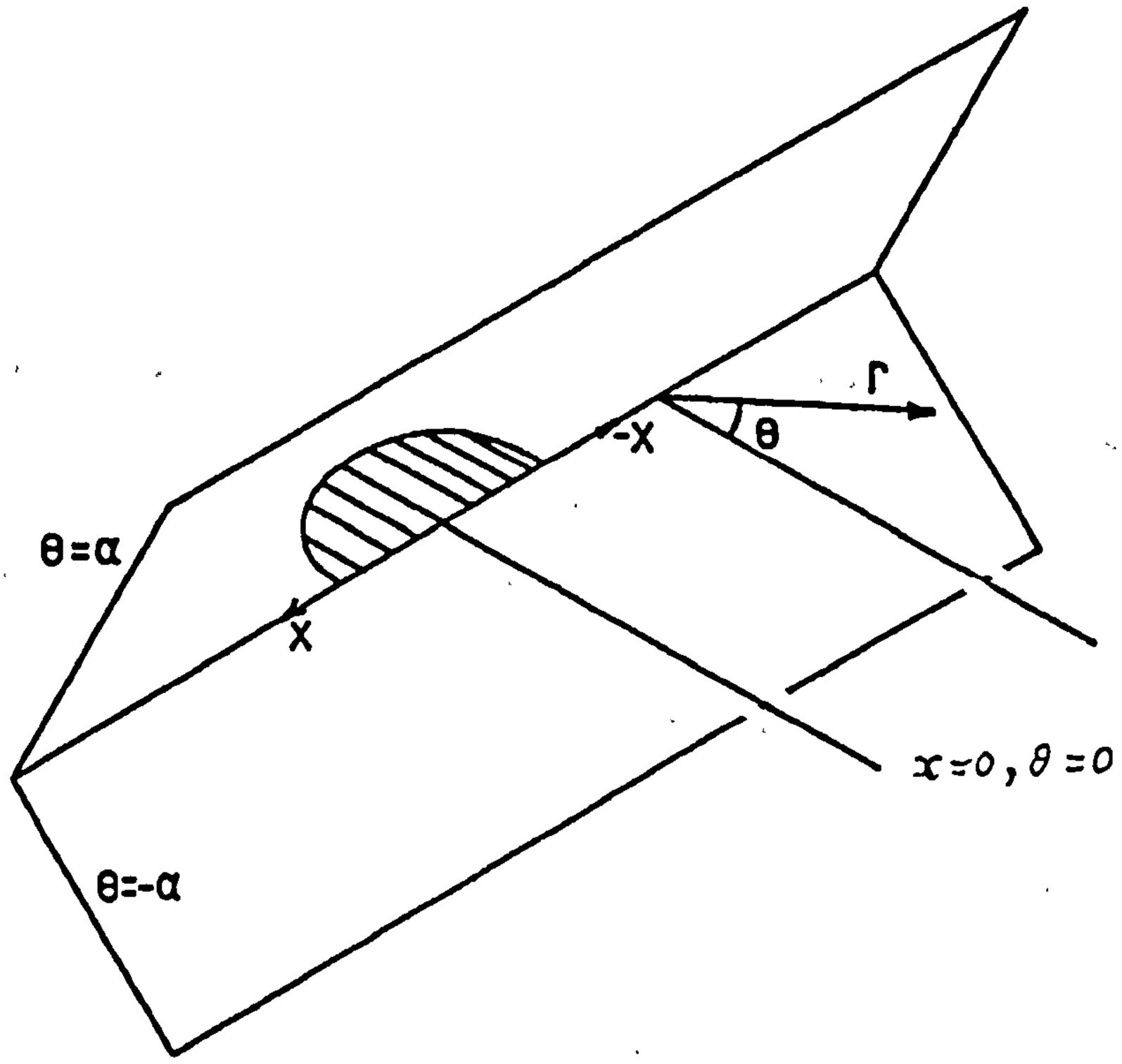

Fig. 7.3 Crack in an interior corner

A serious practical limitation of the flat plate theory is that fatigue cracks usually grow in a region where the local stress is much higher than the global stress of the test-piece. The centre of a large flat plate is not a likely site for such a stress concentration. Unfortunately, the sort of irregular geometric features that are often the cause of high stress concentration factors are also the ones that may be expected to be least amenable to analytic solution. The best strategy for overcoming this problem may well be to combine the extended surface impedance boundary condition of chapter 3 with boundary element or finite element methods. However, limiting case solutions can be found analytically for one quite realistic case: the interior corner of an angled test-piece.

The problem can be written in cylindrical polar coordinates as shown in fig.7.3. Laplace's equation in this coordinate system is

$$\frac{1}{r}\frac{\partial}{\partial r}\left(r\frac{\partial \psi}{\partial r}\right)+\frac{1}{r^2}\frac{\partial^2 \psi}{\partial \theta^2}+\frac{\partial^2 \psi}{\partial x^2}=0. \qquad (7.3.1)$$

By the method of separation of variables, a solution for 7.3.1 that is symmetric in θ as required may be shown to be

$$\psi = \cos(n\theta)e^{ik_x x}[A_n \mathrm{I}_n(k_x r) + B_n \mathrm{K}_n(k_x r)], \tag{7.3.2}$$

where I_n and K_n are modified Bessel functions. To find the potential of the field near a crack it is necessary to combine solutions of this form, with coefficients A_n and B_n chosen to satisfy the surface impedance boundary condition.

In the small m limit, the external field does not influence the surface field at all, so the potential on $\theta = \pm\alpha$ is given by the same unfolding model that was used for the flat plate, but with z=0 and y replaced by r. A suitable Fourier transform solution can be found by putting m=0 in the general solution of chapter 3, which gives

$$\psi = H_0 x - \frac{1}{2\pi}\int_{-\infty}^{\infty} \frac{ik_x}{|k_x|}\tilde{\phi}(k_x)e^{-|k_x r|}e^{ik_x x}\,dk_x. \tag{7.3.3}$$

It may easily be verified that the two-dimensional Laplace equation

$$\frac{\partial^2\psi}{\partial r^2} + \frac{\partial^2\psi}{\partial x^2} = 0 \tag{7.3.4}$$

is obeyed and the normal and tangential field components are continuous at the crack mouth, as required in the unfolding model.

Now the exponential decay function can be written as a sum of modified Bessel functions (equation 9.6.38 in reference [119]),

$$e^{-k_x r} = \mathrm{I}_0(k_x r) + 2\sum_{n=1}^{\infty} \mathrm{I}_n(k_x r)(-1)^n. \tag{7.3.5}$$

A combination of solutions of the form 7.3.2 which reduces to 7.3.3 on $\theta = \pm\alpha$ is therefore

$$\psi = H_0 x - \frac{1}{2\pi}\int_{-\infty}^{\infty} \frac{ik_x}{|k_x|}\tilde{\phi}(k_x)\left[\mathrm{I}_0(|k_x r|) + 2\sum_{n=1}^{\infty} \mathrm{I}_n(|k_x r|)(-1)^n \frac{\cos n\theta}{\cos n\alpha}\right]e^{ik_x x}\,dk_x. \tag{7.3.6}$$

The modified Bessel functions $\mathrm{I}_n(k_x r)$ become infinite as $k_x r$ becomes infinite and the series itself only decays to zero because the terms alternate. It would be very difficult to evaluate 7.3.6 because the results would tend to be dominated by rounding errors.

In the large m limit, the correct combination of solutions is determined from the behaviour of the magnetic flux. On the metal surfaces $\theta = \pm\alpha$, the normal component of flux is zero so that $H_\theta = 0$ for all r (at the crack itself, the flux coming out is directed radially). This condition can be satisfied, for all q, by allowing only the terms with $n=0$ in 7.3.2. All of the terms of the form 7.3.2 are therefore zero except the lowest order. The term in $I_0(k_x r)$ must be zero to keep the field bounded as r becomes infinite, so the solution is

$$\psi = H_0 x + \int_{-\infty}^{\infty} B_0(k_x) K_0(|k_x r|) e^{ik_x x} dk_x. \tag{7.3.7}$$

Note that this solution is independent of θ. The coefficient B_0 may be inferred by conservation of flux. Since $H_\theta = 0$ on $\theta = \pm\alpha$, no flux enters or leaves the test-piece except at the crack, so all the flux that leaves the crack mouth from one side of the plane $x = x_0$ must enter into the crack on the other side. As explained in chapter 3, the flux per unit length coming out of the crack is $2H_x(x,0)/\gamma$ so that

$$2i\alpha \int_{-\infty}^{\infty} \int_{0}^{\infty} B_0(k_x) r k_x K_0(|k_x r|) e^{ik_x} dr\, dk_x = 2/\gamma \int_{-a}^{x_0} H_x(x,0) dx = 2\phi(x_0)/\gamma. \tag{7.3.8}$$

Taking the Fourier transform on x gives

$$2\pi i \alpha k_x B_0(k_x) \int_{0}^{\infty} r K_0(|k_x r|) dr = \tilde{\phi}(k_x)/\gamma \tag{7.3.9}$$

and the integral on r is equal to $1/k_x^2$ (standard form (5.52.2 in reference [116]) so that

$$B_0(k_x) = -\frac{i k_x \tilde{\phi}(k_x)}{2\pi\alpha\gamma}. \tag{7.3.10}$$

The final form for the potential is therefore

$$\psi = H_0 x - \frac{1}{2\pi\alpha\gamma} \int_{-\infty}^{\infty} i k_x \tilde{\phi}(k_x) K_0(|k_x r|) e^{ik_x x} dk_x \tag{7.3.11}$$

The flat plate is a special case of the interior corner with $\alpha = \pi/2$ so that the flat plate solution given in section 3.6 should reproduce formula 7.3.11 for this angle. The large m limit of 3.6.13 substituted into 3.6.8 is

$$\psi = H_0 x - \frac{1}{2\pi^2} \int_{-\infty}^{\infty} \int_{-\infty}^{\infty} \frac{i k_x \tilde{\phi}(k_x)}{k_z \gamma} e^{ik_x x} e^{ik_y y} e^{-k_z z} dk_x dk_y. \tag{7.3.12}$$

Another standard integral (3.961.2 in [116]) gives

$$\psi = H_0 x - \frac{1}{\pi^2 \gamma} \int_{-\infty}^{\infty} i k_x \tilde{\phi}(k_x) \mathrm{K}_0\left(k_x \sqrt{y^2+z^2}\right) e^{ik_x x} \mathrm{d}k_x, \qquad (7.3.13)$$

which corresponds to 7.3.11 for $\alpha = \pi/2$, as expected.

7.4 Ferrite-cored probe

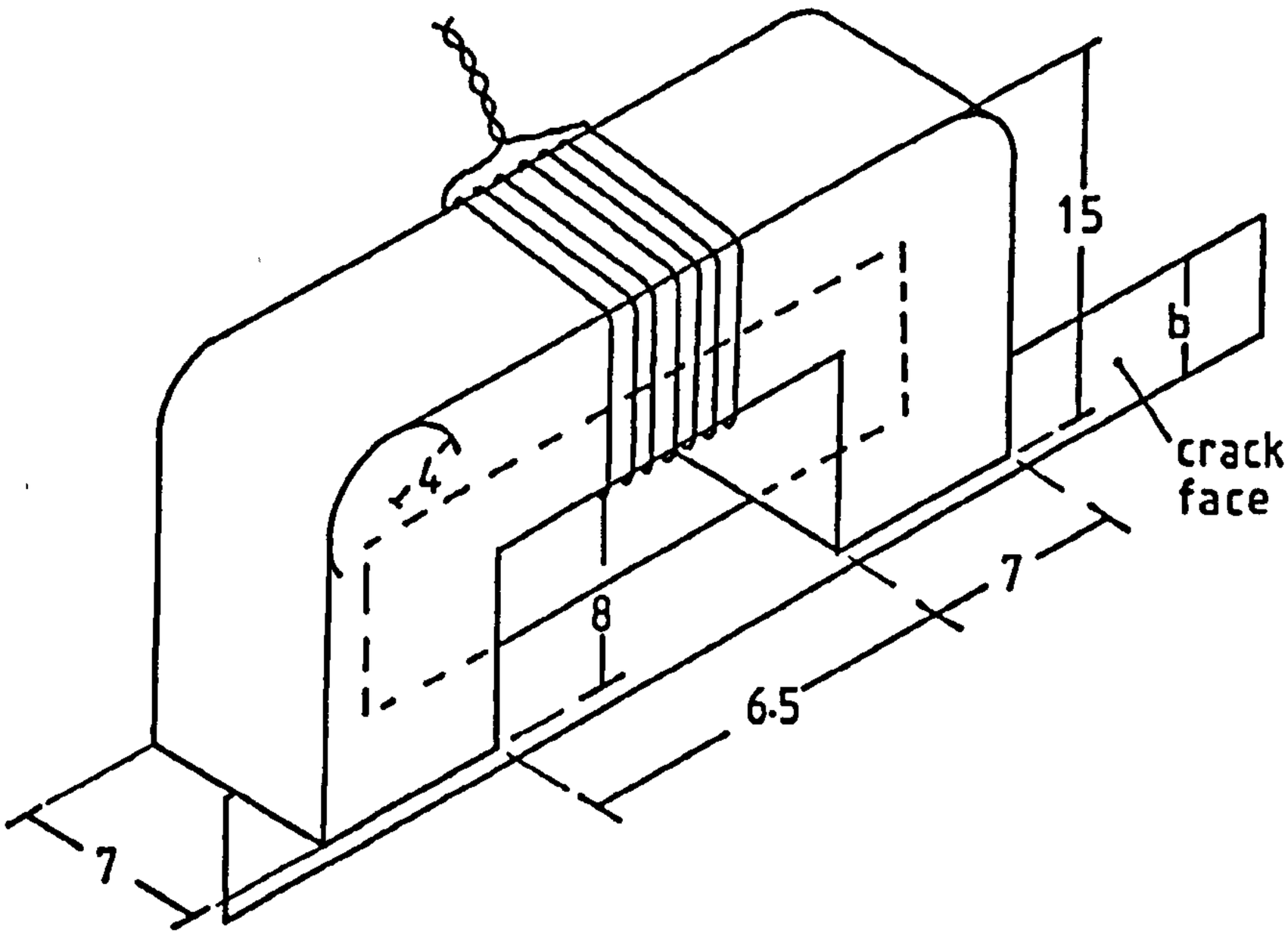

Fig. 7.4 Dimensions of the ferrite cored probe (mm)

Unlike a small air-cored search coil, a ferrite-cored coil changes the field that it is measuring. In general, to find the fields in the presence of a ferrite-core, a new three-dimensional solution is required, for example using finite element or volume integral methods. However, the unfolding model can still provide a useful approximation for the fields on the surface of a ferromagnetic test-piece with a ferrite-cored measuring probe. Fig.7.4 shows a U-shaped ferrite-cored coil measuring the field on the surface of a uniformly deep crack.

The flux coupling with the coil will be partly from the surface of the test-piece and partly from the surrounding air. If the probe is well shielded, then the flux comes from the test-piece only and this is, presumably, the optimum mode for inspection. In the small m limit it may be assumed, as before, that no flux leaves the metal surface except directly underneath the probe. The skin depth in a ferromagnetic metal at reasonable frequencies will typically be of the order

of 0.1mm so the cross-sectional area of the ferrite core is much greater than the cross-sectional area of the thin-skin near the crack. Therefore, since the permeabilities of the ferrite and the test-piece are comparable, the reluctance of the magnetic circuit shown in fig. 7.4 as a broken line is dominated by the reluctance of the thin-skin layer within the test-piece. That is to say, the magnetic field inside the test-piece is much higher than the field in the core, so the line integral of H around the broken line is dominated by the section inside the test-piece. Let ψ_1 be the potential under one end of the U core and ψ_2 be the potential under the other end then

$$\oint \mathbf{H} \cdot \mathrm{ds} = \psi_1 - \psi_2. \tag{7.4.1}$$

If the coil current is I_c and there are N turns then, by Ampère's law,

$$\psi_1 - \psi_2 = NI_c. \tag{7.4.2}$$

In particular, if the current in the coil is zero, the scalar potentials under the two core ends are equal, that is to say , the ferrite core acts as a magnetic short circuit.

$$\psi_1 = \psi_2. \tag{7.4.3}$$

The ferrite-cored coil can be used as a conventional eddy-current probe or it can be used as measuring coil with an externally applied uniform field. In both cases it should be possible to calculate the crack signal by using the unfolding model and imposing the condition 7.4.2 on the regions immediately under the core ends. The arbitrary constant in ψ is most conveniently chosen so that ψ is antisymmetric in x. The unfolded problem for a uniform applied field is shown in fig.7.5.

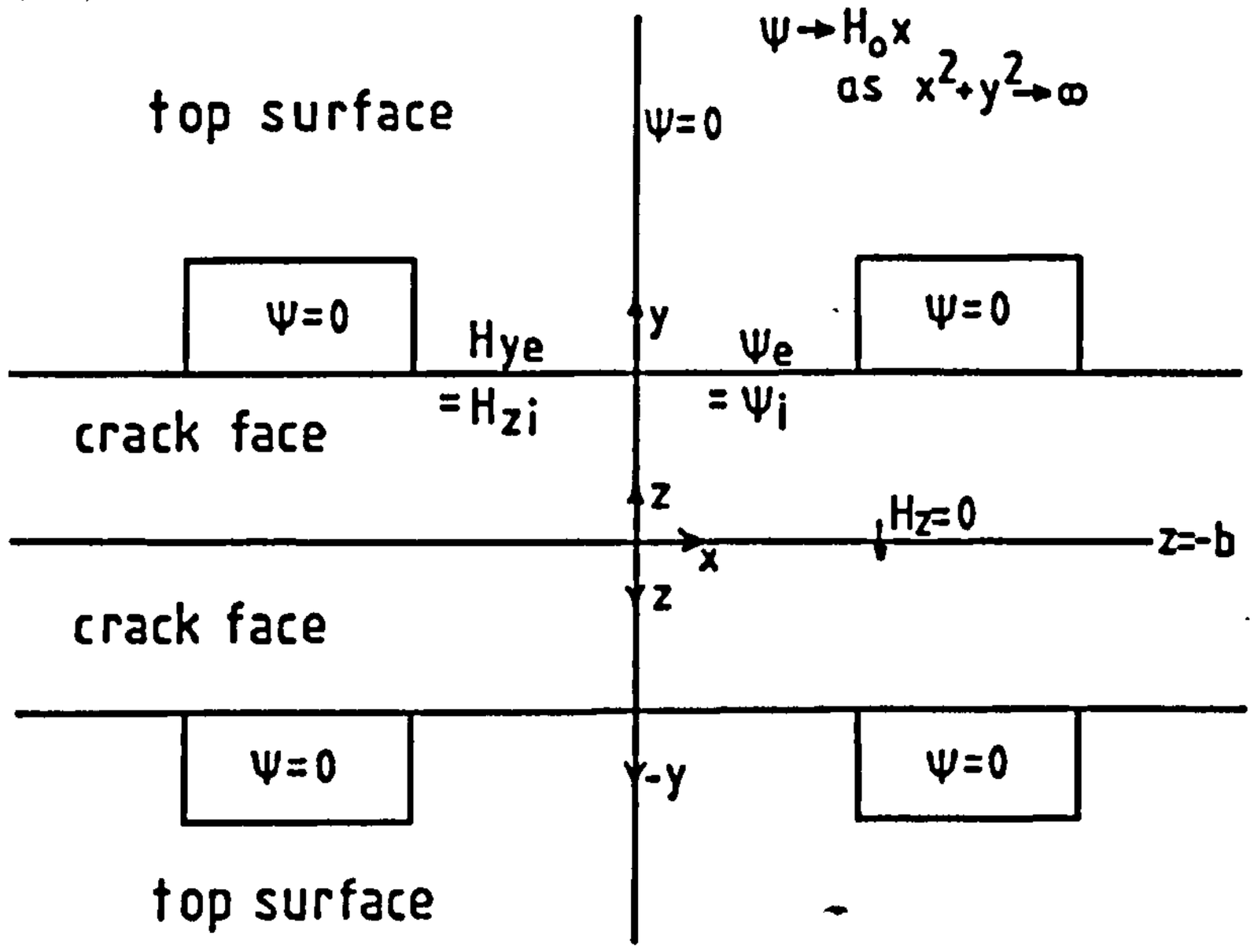

Fig. 7.5 Unfolded problem for the ferrite-cored probe for $I_c = 0$.

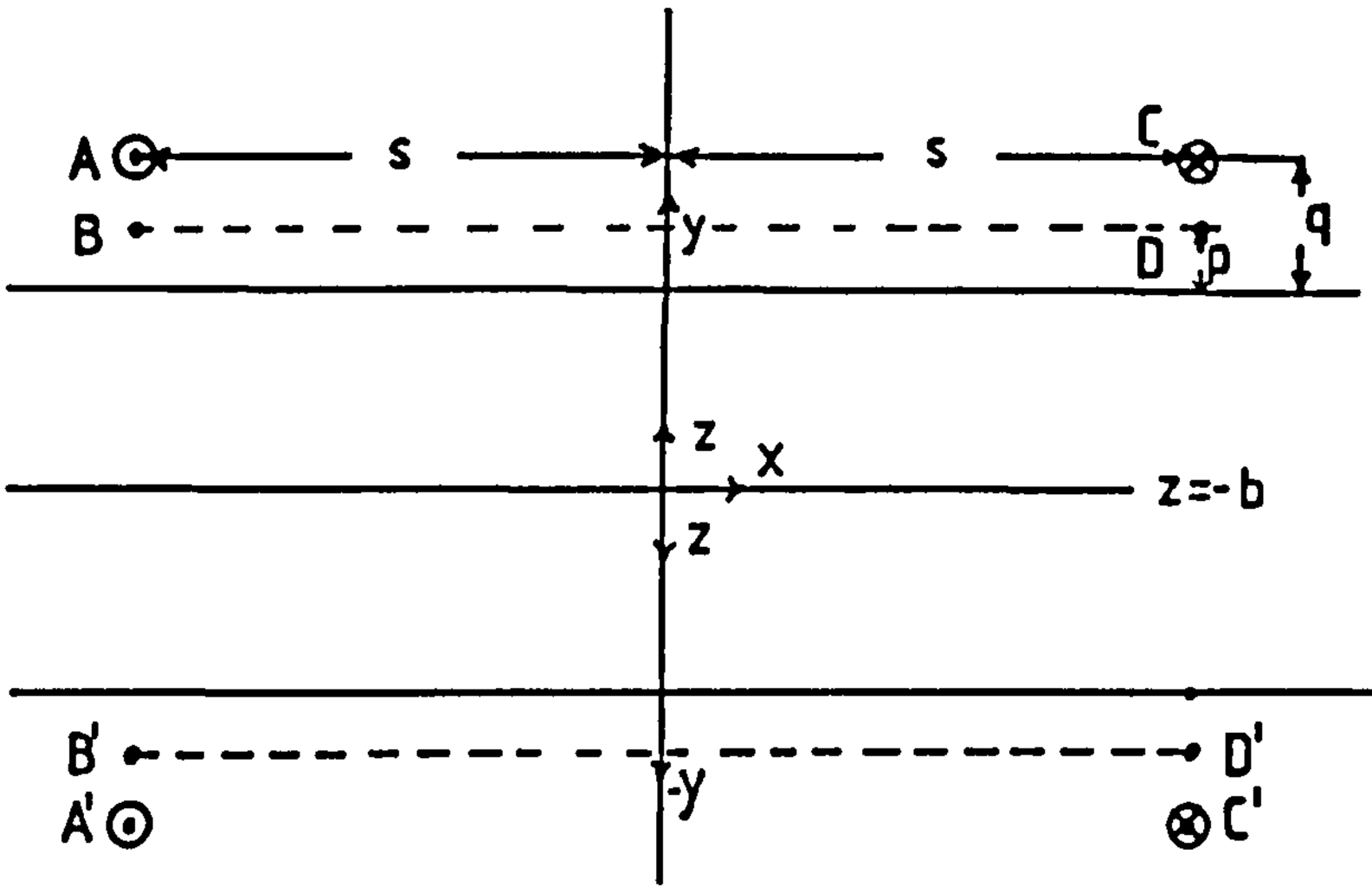

Fig. 7.6 Approximate model for the ferrite-cored probe

As a general guide to the feasibility of this method, a semi-empirical model (fig.7.6) was proposed in which one end of the core is considered to act like two point-sources of flux at points A(-*s*,*q*) and A′(-*s*,-*q*) on either side of the crack and the other end of the core to act like two corresponding sinks at points C(*s*,*q*) and C′(*s*,-*q*) where *s* and *q* are empirically adjustable distances. Since the potential at each point source is infinite, the potential under the negative *x* core-end was

considered to be equal to the potential at the points B(-s,p) adjacent to A and B′(-s,-p) adjacent to A′ where p was also chosen empirically. The corresponding points on the positive x side are D(s,p) and D′(s,-p).

By symmetry, all four sources must be of equal strength Φ so that the flux coupling with the coil is $2N\Phi$.The magnetic scalar potential due to one of the point sources is

$$\psi = \frac{\gamma\Phi}{2\pi}\ln r, \tag{7.4.4}$$

at distance r from the source. The voltage measured across the coil is

$$V = -2i\omega\Phi N. \tag{7.4.5}$$

Equation 7.4.2 becomes

$$\psi_1 - \psi_2 = \psi_B - \psi_D = \psi_{B'} - \psi_{D'} = NI_c. \tag{7.4.6}$$

For symmetric problems, 7.4.6 implies that

$$2\psi_B = 2\psi_{B'} = -2\psi_D = -2\psi_{D'} = NI_c. \tag{7.4.7}$$

In principle, the model can be applied either if the probe is used in the single-coil eddy-current mode or if there is a separate applied field. Consider first the case where there is a separate uniform applied field H_0 and the coil current I_c is zero. The potential at the reference points B, B′, D and D′ consists of contributions from the four sources and from the uniform applied field. Equation 7.4.7 gives

$$\psi = H_o s + \frac{\gamma\Phi}{2\pi}\left\{\ln|q-p| + \ln(q+p+2b) - \frac{1}{2}\ln[(p-q)^2+4s^2] - \frac{1}{2}\ln[(p+q+2b)^2+4s^2]\right\}. \tag{7.4.8}$$

Let V_c be the voltage with the probe placed evenly across the crack and V_r be the voltage with the probe far from the crack, equivalent to b=0 then, from 7.4.5

$$\frac{V_r}{V_c} = \frac{\ln\left\{\left[1+\frac{4s^2}{(q-p)^2}\right]\left[1+\frac{4s^2}{(q+p+2b)^2}\right]\right\}}{\ln\left\{\left[1+\frac{4s^2}{(q-p)^2}\right]\left[1+\frac{4s^2}{(q+p)^2}\right]\right\}} \tag{7.4.9}$$

The eddy-current case is very similar, except that the uniform field term $H_0 s$ must be removed from 7.4.8 and the left-hand side must have a term from the driving current. From 7.4.2 and 7.4.6 with ψ antisymmetric,

$$\psi = NI_c/2 = \frac{\gamma\Phi}{2\pi}\left\{\ln|q-p| + \ln(q+p+2b) - \frac{1}{2}\ln[(p-q)^2+4s^2] - \frac{1}{2}\ln[(p+q+2b)^2+4s^2]\right\}. \tag{7.4.10}$$

Formula 7.4.9 therefore applies equally well to the eddy current case if V_c and V_r are replaced with Z_c and Z_r. An appealing feature of this simple model is that 7.4.9 can be rearranged to give an explicit formula for the crack depth

$$b = \frac{s}{\sqrt{\left[1+\frac{4s^2}{(q-p)^2}\right]^{V_r/V_c-1}\left[1+\frac{4s^2}{(q+p)^2}\right]^{V_r/V_c}-1}} - (q+p)/2. \qquad (7.4.11)$$

The response to shallow cracks can be found from a Taylor expansion about b=0

$$\frac{V_c}{V_r}-1 \approx \frac{4b}{(q+p)\left[1+\frac{(q+p)^2}{4s^2}\right]\ln\left\{\left[1+\frac{4s^2}{(q+p)^2}\right]\left[1+\frac{4s^2}{(q-p)^2}\right]\right\}}, \qquad (7.4.12)$$

which is equivalent to the response of an ACPD probe of length

$$l = \frac{(q+p)}{2}\left[1+\frac{(q+p)^2}{4s^2}\right]\ln\left\{\left[1+\frac{4s^2}{(q+p)^2}\right]\left[1+\frac{4s^2}{(q-p)^2}\right]\right\} . \qquad (7.4.13)$$

As the crack depth increases the sensitivity becomes progressively weaker until no further increase in coil voltage is seen. The maximum coil voltage may easily be found by allowing b to become infinite in 7.4.9,

$$V_c/V_r - 1 = \frac{\ln\left[1+\frac{4s^2}{(q+p)^2}\right]}{\ln\left[1+\frac{4s^2}{(q-p)^2}\right]}. \qquad (7.4.14)$$

Fig. 7.7 shows a least-squares fit of the theoretically predicted signal $V_c/V_r - 1$ to experimentally measured data on notches in mild steel plates with a uniform applied field at 1kHz. Shielding the probe with multiple layers of aluminium foil had only a very small effect on the signal. The best values for the adjustable constants are p=2.71mm, q=5.52mm and s=7.24mm, which are reasonable for the probe dimensions shown in figure 7.4. The equivalent ACPD probe length for shallow cracks is 25.7mm and the maximum signal as the crack depth becomes infinite is $V_c/V_r - 1$=0.425. The response of the ferrite-cored coil as a single-coil eddy-current probe was not well modelled by the approximate theory because it was found to be much more sensitive to notch opening than the response with a uniform applied field. A more theoretical model of the ferrite-cored probe could be based on a solution of the unfolded problem shown in fig 7.5, for example

using finite-difference, finite element or boundary element methods. An important question to investigate is the validity of the unfolding model for shielded and unshielded probes over a range of frequencies.

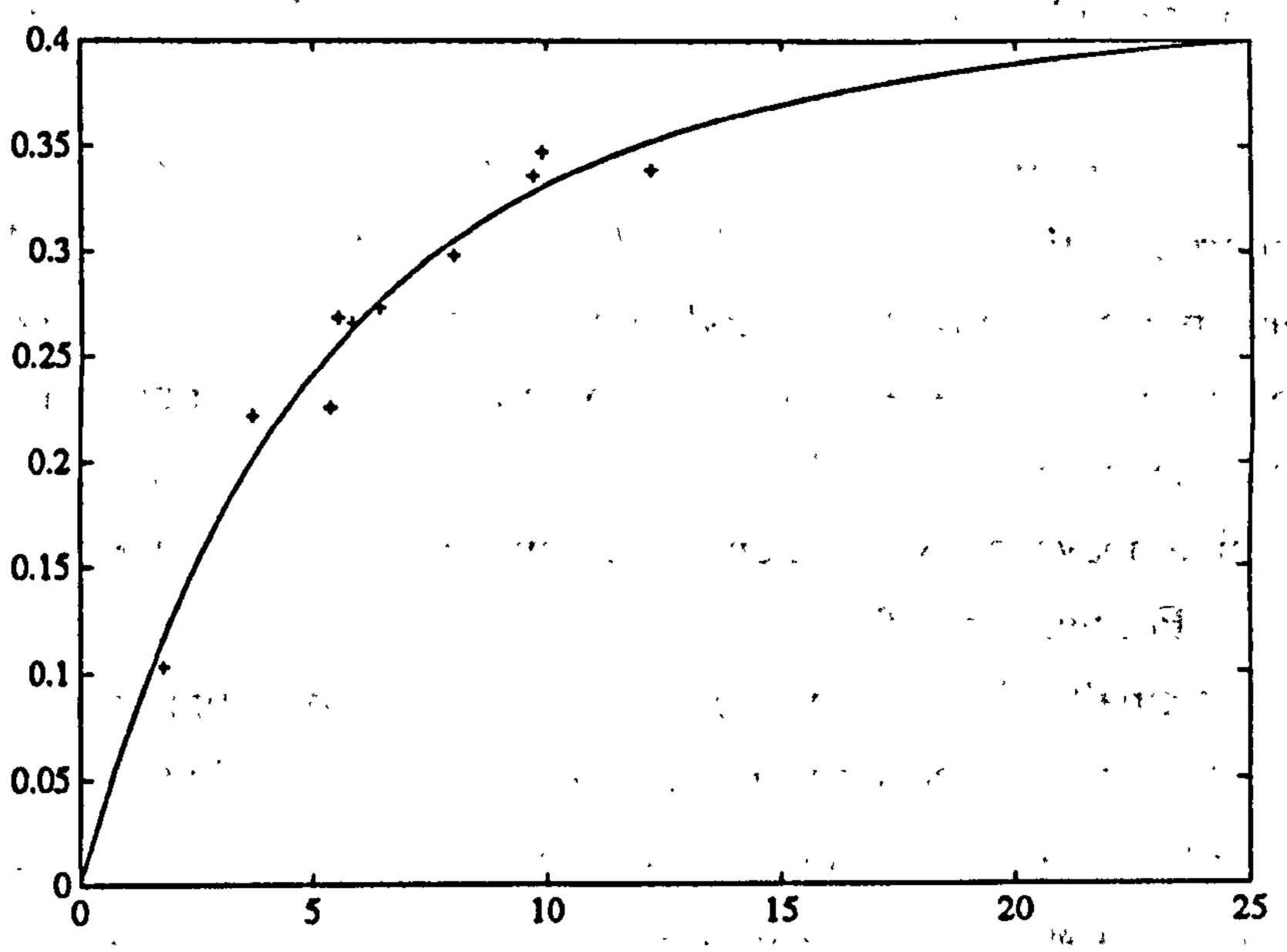

Fig. 7.7 Response of the ferrite-cored probe

8 Concluding remarks

A variety of electromagnetic methods of non-destructive testing can be used to find and measure metal fatigue cracks. High frequency methods, where the skin-depth is small compared to the crack depth, have been examined in detail. The behaviour of the electromagnetic field can be modelled mathematically without a detailed analysis of the region inside the metal by using the surface impedance approximation. Although this method is not immediately applicable to a cracked test-piece it is possible to modify it to take account of the source of flux represented by the crack. In general this leads to a coupled system consisting of a potential which obeys the three-dimensional Laplace equation outside the test-piece and a potential which obeys the two-dimensional Laplace equation on the crack faces.

For very high frequencies or non-magnetic test-pieces the flux from the crack has a small effect on the exterior field and the Born approximation, previously used by Auld and his co-workers, is valid. In ferromagnetic test-pieces, if the frequency is not too high, the flux in the exterior region is small compared with the flux inside the metal so that the two-dimensional potential on the crack face is effectively coupled with a two-dimensional potential on the unflawed surface of the test-piece. It is then possible to "unfold" the problem and find the fields by solving a standard two-dimensional potential problem, an algorithm previously used by Collins, Michael and co-workers. The transition between these two limiting cases is governed by a dimensionless parameter $m=a/\mu_r\delta$. When m is very small the unfolding theory is valid and when m is very large the Born approximation is valid.

For a flat plate test-piece a solution of the three-dimensional problem for general m can be found using Fourier transforms and this solution has been used to develop models of the response of air-cored measuring coils to fatigue cracks for both uniform and non-uniform applied fields. It is possible to extend the models to cases where there is more than one crack. Crack depth can be calculated by tabulating results from the models for a range of parameters and interpolating. This method has already undergone trials for two petroleum industry applications: drill-string threaded connections and welded tubular joints.

The methods developed for flat plates and air-cored coils have limited scope for extension to other geometries but it should still be possible to use the surface impedance boundary condition, modified to take account of the fatigue crack, for irregular test-pieces and ferrite-cored probes. For example, the finite element and boundary element methods could be applied if special elements were used to take account of the boundary conditions on the cracked test-piece surface. The flat-plate solutions are useful as tests of the accuracy of such numerical models.

Appendix A The Boundary Condition Function for a Flat Plate

The boundary condition function is defined in equation 3.6.16 as

$$\bar{F}(k_x) = -\frac{1}{\pi}\int_{-\infty}^{\infty} \frac{dk_y}{k_z^2 + k_z\gamma} \tag{A1}$$

where

$$k_z^2 = k_x^2 + k_y^2 \tag{A2}$$

and the sign of k_z is positive. It may be integrated using the substitution

$$\frac{k_y}{|k_x|} = \frac{2t}{1-t^2} \tag{A3}$$

which transforms the integral into an elementary arctangent form

$$\bar{F}(k_x) = -\frac{4}{\pi}\int_0^1 \frac{dt}{(|k_x| - \gamma)t^2 + |k_x| + \gamma} \quad , \tag{A4}$$

$$\bar{F}(k_x) = \frac{-4\tan^{-1}\sqrt{\frac{|k_x| - \gamma}{|k_x| + \gamma}}}{\pi\sqrt{k_x^2 - \gamma^2}} \quad . \tag{A5}$$

No difficulties are caused by the complex constant γ because the definite integral is evaluated directly from the indefinite integral without the assumption that the constant is real. For the purpose of computation it is convenient to rewrite A5 in logarithmic form because complex arctangents are not supported by most compilers. Let the complex number w be defined so that

$$\sin w = \sqrt{\frac{1 - \gamma/|k_x|}{2}} \tag{A6}$$

and

$$\cos w = \sqrt{\frac{1 + \gamma/|k_x|}{2}} \quad , \tag{A7}$$

then

$$\tan w = \sqrt{\frac{|k_x| - \gamma}{|k_x| + \gamma}} \quad . \tag{A8}$$

From A6 and A7

$$\sin 2w = \sqrt{1-(\gamma/k_x)^2} \tag{A9}$$

and

$$\cos 2w = \gamma/|k_x| \quad , \tag{A10}$$

so that

$$2iw = \ln\left(\gamma/|k_x| + \sqrt{(\gamma/k_x)^2-1}\right) \quad . \tag{A11}$$

Therefore, the final form of the boundary condition function for a flat plate is

$$\bar{F}(k_x) = -\frac{2\ln\left(\gamma/|k_x| + \sqrt{(\gamma/k_x)^2-1}\right)}{|k_x|\,\pi\sqrt{(\gamma/k_x)^2-1}} \quad . \tag{A12}$$

It is possible to obtain this expression directly from A4 using the method of partial fractions. The asymptotic forms are

$$\text{In the Born limit} \quad \bar{F}(k_x) \to 0 \ \text{ as } \ |\gamma/k_x| \to \infty,$$

$$\text{In the Laplace limit } \bar{F}(k_x) \to -1/|k_x| \ \text{ as } \ |\gamma/k_x| \to 0. \tag{A13}$$

Whilst the transform of F is useful in its own right, it is also possible to find an analytic form for the function itself by inverting 3.6.16

$$F(x) = -\frac{1}{2\pi^2}\int_{-\infty}^{\infty}\int_{-\infty}^{\infty}\frac{e^{ik_x x}\,dk_x dk_y}{k_z^2+\gamma k_z} \quad , \tag{A14}$$

$$F(x) = -\frac{1}{2\pi^2}\int_{0}^{\infty}\int_{0}^{2\pi}\frac{\cos(xk_z\cos\theta)\,d\theta\,dk_z}{k_z+\gamma} \quad , \tag{A15}$$

$$F(x) = -\frac{1}{\pi}\int_{0}^{\infty}\frac{J_0(xk_z)\,dk_z}{k_z+\gamma} \quad , \tag{A16}$$

$$F(x) = -\frac{1}{2}[H_0(\gamma|x|) - Y_0(\gamma|x|)] \tag{A17}$$

where J_0 is the Bessel function of order zero, H_0 is the Struve function of order zero and Y_0 is the Neumann function of order zero. The integrals in A16 and A17 are given in reference [116] formulae 8.411.1 and 6.562.2 respectively. For numerical purposes, the function F may be evaluated by numerical integration, e.g. of A16 or of the Fourier inversion integral. Finally, it should be pointed out that when the flaw is not tightly closed, F must be multiplied by the notch-opening correction factor described in section 3.5.

Appendix B Comparison between the general *m* model and the Schwarz-Christoffel model

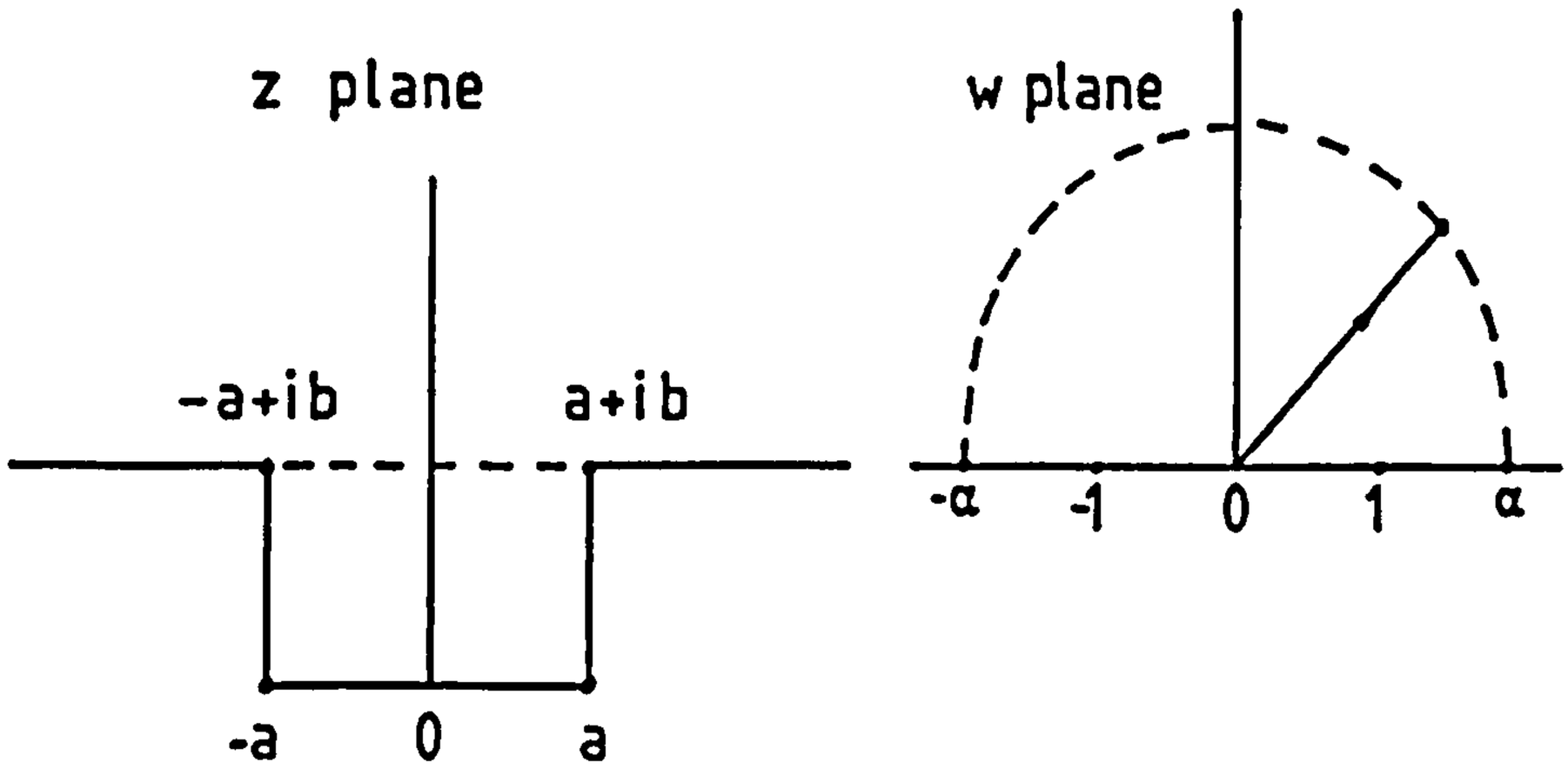

Fig. B Schwarz-Christoffel transformation for a rectangular crack

The Schwarz-Christoffel mapping [82] is defined by the complex differential equation

$$\frac{dz}{dw} = (w - w_0)^{n_0} (w - w_1)^{n_1} (w - w_2)^{n_2} \ldots\ldots \tag{B1}$$

and has the effect of mapping the interior of a polygon onto a half plane. It may be understood as being built from the basic mapping

$$\frac{dz}{dw} = (w - w_l)^{n_l} \tag{B2}$$

which is trivially analytic except at the pole $w = w_l$, where an angle of $-n_l\pi$ in the z plane is mapped onto a straight line in the w plane. Repeated applications simply follow the chain rule of ordinary differentiation. The angles generated in previous applications are unaffected by repeating the transformation because of the angle-preserving or conformal property of analytic mappings. It is possible to map open polygonal shapes (those with corners at infinity) if the sum of the n_l is not equal to 2.

The unfolded plane for a rectangular crack (fig.B) may be mapped onto a half-plane by the Schwarz-Christoffel transformation [87]

$$z = K \int_0^w \left(\frac{w^2 - \alpha^2}{w^2 - 1} \right)^{\frac{1}{2}} dw \tag{B3}$$

The constant K has been taken outside the integral in order to fix two of the poles at $w = \pm 1$. For a uniform incident field of unit strength, the potentials ϕ and ψ are the real and imaginary parts of Kw respectively. That is to say, i is used here with a different significance from its meaning in the general m problem, where imaginary numbers are used to represent quantities in quadrature with the applied field. However, in the m=0 limit all the fields are in phase, so no confusion arises.

From B3, the lengths of the crack axes are

$$a = K\int_0^1 \left(\frac{\alpha^2-u^2}{1-u^2}\right)^{\frac{1}{2}} du = K\int_0^{\pi/2} (\alpha^2-\sin^2 v)^{\frac{1}{2}} dv, \tag{B4}$$

$$b = K\int_1^{\alpha} \left(\frac{\alpha^2-u^2}{u^2-1}\right)^{\frac{1}{2}} du = K\int_0^{\operatorname{arcosh}\alpha} (\alpha^2-\cosh^2 v)^{\frac{1}{2}} dv. \tag{B5}$$

The unknown constant α is determined by the aspect ratio b/a and in this work it was found numerically using binary splitting and Romberg integration [108]. Once α was known, K was found from B4.

The crack mouth potential ϕ_o, corresponding to the imaginary part of Kw, was found by integrating numerically along the path indicated in the figure by the diagonal line in the w plane. Binary splitting was used to pick the correct upper limit so that Im(z)=b. The process was repeated for the range of angles

$$0 < \theta < \frac{\pi}{2} \tag{B6}$$

to scan over one half of the crack mouth. A minor disadvantage of this method is that it produces values of ϕ_o at irregular values of x, so that it is necessary to use linear interpolation when comparing with the results of the general m model, evaluated at $m = 0$ (see Table B overleaf).

Table B Comparison of predicted ϕ_0 values

b/a	*x/a*	General *m* (at *m*=0)	Schwarz-Christoffel transformation	percentage difference
1	0	0.4035550	0.3995636	0.99
1	0.25	0.3890130	0.3851734	0.99
1	0.5	0.3420294	0.3386706	0.98
1	0.75	0.2482318	0.2458875	0.94
0.5	0	0.3198386	0.3172663	0.81
0.5	0.25	0.3107702	0.3082848	0.80
0.5	0.5	0.2787881	0.2775653	0.79
0.5	0.75	0.2111717	0.2095802	0.75
0.25	0	0.2044294	0.2033342	0.54
0.25	0.25	0.2011250	0.2000567	0.53
0.25	0.5	0.1886389	0.1876464	0.53
0.25	0.75	0.1541072	0.1533639	0.48

Appendix C Conversion from Plane Elliptical Coordinates to Plane Cartesian Coordinates

When the harmonic functions are rewritten in Cartesian coordinates on the line $z=0$ they simply become polynomials. The basic formula is

$$x = \cosh\xi \cos\eta. \tag{C1}$$

On the line segment $\xi=0$, corresponding to the portion of the crack lip that lies between the foci, 3.8.15 and 3.8.16 give

$$\phi = \sum_{n=1}^{\infty} A_n \frac{\cos(2n-2)\eta}{\cosh(2n-2)\alpha}, \tag{C2}$$

$$\psi = \sum_{n=1}^{\infty} B_n \frac{\cos(2n-1)\eta}{\sinh(2n-1)\alpha}. \tag{C3}$$

From C1

$$x = c\cos\eta, \tag{C4}$$

so that

$$\sqrt{c^2-x^2} = c\sin\eta. \tag{C5}$$

Therefore

$$x \pm \sqrt{x^2-c^2} = c(\cos\eta \pm i\sin\eta) = ce^{\pm i\eta}. \tag{C6}$$

The terms in the numerator in 3.8.21 are therefore

$$(x+\sqrt{x^2-c^2})^r + (x-\sqrt{x^2-c^2})^r = 2c^r\cos r\eta, \tag{C7}$$

which are equal to the terms in the numerators of C2 and C3, multiplied by c^r. Between the positive focus and the positive end of the crack, $\eta=0$ and 3.8.15 and 3.8.16 become

$$\phi = \sum_{n=1}^{\infty} A_n \frac{\cosh(2n-2)\xi}{\cosh(2n-2)\alpha}, \tag{C8}$$

$$\psi = \sum_{n=1}^{\infty} B_n \frac{\cosh(2n-1)\xi}{\sinh(2n-1)\alpha}. \tag{C9}$$

Equation C1 gives

$$x = c\cosh\xi, \tag{C10}$$

$$\sqrt{x^2-c^2} = c\sinh\xi, \tag{C11}$$

so the analogue of C7 is

$$(x+\sqrt{x^2-c^2})^r + (x-\sqrt{x^2-c^2})^r = 2c^r\cosh r\xi, \tag{C12}$$

which gives the correct numerators for C8 and C9. When C12 is evaluated at $\xi=\alpha$, it gives the correct denominators for C2 and C8

$$(a+b)^r+(a-b)^r=2c^r\cosh r\alpha. \tag{C13}$$

Similarly, C10 and C11 also imply that

$$(a+b)^r-(a-b)^r=2c^r\sinh r\alpha \tag{C14}$$

which gives the correct denominators for C3 and C9 and completes the coordinate conversion. The formula in 3.8.21 is therefore valid on both sides of the positive focus. It is clear by inspection that 3.8.19, 3.8.20 and 3.8.21 give symmetric ϕ and antisymmetric ψ as required. Although the polynomials P_r are real, they require the use of complex numbers to be evaluated directly, for points between the foci.

Appendix D Comparison of Semi-Elliptical Model with Born and Unfolding Limits

Table D1 Comparison of predicted ϕ_0 for m=0

b/a	*x/a*	General *m*	Unfolding Solution	percentage difference
1	0	0.3863492	0.3850032	0.35
1	0.25	0.3716095	0.3705495	0.29
1	0.5	0.3244538	0.3244090	0.01
1	0.75	0.2315703	0.2342941	-1.2
0.5	0	0.3036140	0.3017056	0.63
0.5	0.25	0.2927256	0.2909374	0.61
0.5	0.5	0.2577421	0.2563680	0.53
0.5	0.75	0.1882142	0.1878694	0.18
0.25	0	0.1951917	0.1942280	0.49
0.25	0.25	0.1886791	0.1877479	0.49
0.25	0.5	0.1676824	0.1668580	0.49
0.25	0.75	0.1255118	0.1249190	0.47

Table D2 Comparison of predicted ϕ_0 values for $m = 10^{10}$

b/a	*x/a*	General *m*	Born Approximation	percentage difference
1	0	0.6367425	0.6366197	0.019
1	0.25	0.6098922	0.6097532	0.023
1	0.5	0.5247533	0.5245487	0.039
1	0.75	0.3617571	0.3613181	0.12
0.5	0	0.4374709	0.4374566	0.0033
0.5	0.25	0.4206926	0.4206730	0.0047
0.5	0.5	0.3668869	0.3668444	0.012
0.5	0.75	0.2608730	0.2607368	0.052
0.25	0	0.2420679	0.2420679	0
0.25	0.25	0.2338703	0.2338703	0
0.25	0.5	0.2073801	0.2073796	0.00024
0.25	0.75	0.1538450	0.1538409	0.0027

References

[1] Electromagnetic Fields and Waves (3rd ed.)
P Lorrain, D P Corson and F Lorrain
W H Freeman and Co. (1988)

[2] G W C Kaye and T H Laby
Tables of Physical and Chemical Constants (15th ed.)
Longman's (1986)

[3] D. Broek
Elementary Engineering Fracture Mechanics (4th ed.)
Martinus Nijhoff (1986)

[4] Non-destructive Testing
R Halmshaw
Edward Arnold (1987)

[5] V S Cecco and C R Bax
Eddy current in-situ inspection of ferromagnetic monel tubes
Mater. Eval. **33** 1 (1975)

[6] S A Schelkunoff
Bell Systems Technical Journal **17** 17 (1938)

[7] D E Hughes
Induction-balance and Experimental Researches therewith
Phil. Mag. **8** 50 (1879)

[8] I Vigness, J E Dinger and R Gunn
Eddy current type flaw detectors for non-magnetic materials
J. Appl. Phys. **13** 377 (1942)

[9] F Förster and H Breitfeld
Z. Metall. **45**(4) 188 (1954)

[10] H L Libby
Introduction to Electromagnetic Nondestructive Test Methods
Wiley (1971)

[11] B A Auld, J C Moulder, S Jefferies, P J Schull, S Ayter and J Kenney
Eddy-Current Reflection Probes: Theory and Experiment
Res. Nondestr. Eval. **1** 1 (1989)

[12] T R Schmidt
The Casing Inspection Tool-An Instrument for the In-situ Detection of External Corrosion in Oil Wells
Corrosion **17**(7) 329t (1961)

[13] D L Atherton, C J Toal and T R Schmidt
Investigations of the Remote Field Eddy Current Technique In Large Diameter Pipeline
Brit. J. NDT **31**(9) 485 (September 1989)

[14] B M Thornton and W M Thornton
The measurement of the thickness of metal walls from one surface only, by an electrical method
Proc. Inst. Mech. Eng. **140** 349 (1938)

[15] A Trost
Ermittlung von Rissen and Messung der Risstiefen in Metallischen Werkstoffen durch elektrische Spannungsmessung
Metallwirtschaft **23** 308 (1944)

[16] R O Ritchie, G G Garrett and J F Knott
Intl. J. Fracture Mech. **7** 462 (1971)

[17] M D Halliday and C J Beevers
The d.c. electrical potential method for crack length measurement
In *The measurement of crack length and shape during fracture and fatigue*
C J Beevers (ed.)
Engineering Materials Advisory Services(1980)

[18] R P Wei and R L Brazill
An a.c. Potential System for Crack Length Measurement
In *The measurement of crack length and shape during fracture and fatigue*
C J Beevers (ed.)
Engineering Materials Advisory Services(1980)

[19] G Gille
The electrical potential method and its application to nondestructive testing
Nondestructive testing 4 36 (1971)

[20] U Betz
Fatigue crack growth measurements using the electrical potential method
Materialprüfung 14 73 (1972)

[21] W D Dover, F D W Charlesworth, K A Taylor, R Collins and D H Michael
A. C. Field Measurements: Theory and Practice
In *The measurement of crack length and shape during fracture and fatigue*
C J Beevers (ed.)
Engineering Materials Advisory Services(1980)

[22] W D Dover and R Collins
Recent Advances in the Detection and Sizing of Cracks Using Alternating Current Field Measurements
Brit. J. NDT 22(6) 291 (1980)

[23] W D Dover, F D W Charlesworth, K A Taylor, R Collins and D H Michael
The Use of A. C. Field Measurements to Determine the Shape and Size of a Crack in a Metal
In *Eddy-Current Characterisation of Materials and Structures*
ASTM STP 722
G Birnbaum and G Free (eds.)
American Society for Testing and Materials (1981)

[24] British Standards Institution BS 6072:1981
Method for Magnetic Particle Flaw Detection

[25] B C Adhikari
A new concept of crack depth measurement
Brit. J. NDT 29(2) 96 (1987)

[26] R W E Shannon, D W Hamlyn and D White
Experience with on-line inspection
Institution of Gas Engineers Communication 1155
IGE Autumn Research Meeting (1981)

[27] C N Owston
On-site examination of ferritic steel tubes in heat exchangers using an internal probe and an electro-magnetic technique
Brit. J. NDT **27**(4) 227 (1985)

[28] M Klein
Mathematical Thought from Ancient to Modern Times P.698
Oxford (1972)

[29] W Lord and R Palanisamy
Development of Theoretical Models for Nondestructive Testing Eddy-current Phenomena
In *Eddy-Current Characterisation of Materials and Structures*
ASTM STP 722
G Birnbaum and G Free (eds.)
American Society for Testing and Materials (1981)

[30] F Förster and K Stambke
Z. Metal. **45**(4) 166 (1954)

[31] D L Waidelich and C J Renken
Proc. Nat. Electronics Conf. **12** 188 (1956)

[32] M L Burrows
A Theory of Eddy-Current Flaw Detection
Ph.D. Thesis University of Michigan
University Microfilms Inc., Ann Arbor (1964)

[33] C V Dodd and W E Deeds
Analytical Solutions to Eddy-Current Probe-Coil Problems
J. Appl. Phys. **39**(6) 2829 (1968)

[34] A H Kahn, R Spal and A Feldman
Eddy-current losses due to a surface crack in a conducting material
J. Appl. Phys. **48**(11) 4454 (1977)

[35] R Spal and A H Kahn
Eddy currents in a conducting cylinder with a crack
J. Appl. Phys. **50**(10) 6135 (1979)

[36] A H Kahn and R Spal
A Boundary Integral Equation Method for Calculating the Eddy-Current Distribution in a Long Cylindrical Bar with a Crack
In *Eddy-Current Characterisation of Materials and Structures*
ASTM STP 722
G Birnbaum and G Free (eds.)
American Society for Testing and Materials (1981)

[37] N F Mott and H S W Massey
The Theory of Atomic Collisions (3rd ed.) p.86
O.U.P. (1965)

[38] F Muennemann, B A Auld, C M Fortunko and S A Padget
Inversion of Eddy Current Signals in a Non-uniform Probe Field
Review of Progress in Quantitative Nondestructive Evaluation
D O Thompson and D E Chimenti (eds.)
2B 1501 Plenum Press (1983)

[39] B A Auld, S Jefferies, J C Moulder and J C Gerlitz
Semi-elliptical surface flaw EC interaction and inversion: theory
Rev. Prog. QNDE 5A 383 (1986)

[40] J C Moulder, J C Gerlitz, B A Auld and S Jefferies
Semi-elliptical surface flaw EC interaction and inversion: experiment
Rev. Prog. QNDE 5A 395 (1986)

[41] J C Moulder, P J Schull and T E Capobianco
Uniform Field Eddy Current Probe: Experiments and Inversion for Realistic Flaws
Rev. Prog. QNDE 6A 601 (1987)

[42] R Palanisamy and W Lord
Finite element modelling of electromagnetic NDT phenomenon
IEEE Trans. MAG-15(6) 1479 (1979)

[43] D L Atherton, B Szpunar and S Sullivan
The application of finite element calculations to the remote field eddy current technique
Mater. Eval. 45 1083 (1987)

[44] W Lord, Y S Sun, S S Udpa and S Nath
A finite element study of the remote field phenomenon
IEEE Trans. **MAG-24**(1) 435 (1988)

[45] P C French and L J Bond
Finite element modelling of eddy current NDE
J. NDE 7(1) 55 (1988)

[46] R E Beissner
Boundary element model of flaw detection in three dimensions
J. Appl. Phys. **60**(1) 352 (1986)

[47] S K Burke
Eddy current induction by a coil near a conducting edge in 2d
Rev. Prog. QNDE **6A** 169 (1987)

[48] S K Burke
A perturbation method for calculating coil impedance in eddy current testing
J. Phys. D:Appl. Phys. **18** 1745 (1985)

[49] L D Sabbagh and H A Sabbagh
Development of a system to invert eddy-current data and reconstruct flaws
Rev. Prog. QNDE **2B** 1555 (1983)

[50] H A Sabbagh, L D Sabbagh and S N Vernon
Verification of an Eddy-Current Flaw Inversion Algorithm
IEEE Trans. **MAG-22**(6) 1881 (1987)

[51] W S Dunbar
The Volume Integral Method of Eddy Current Modeling
J. NDE **5**(1) 9 (1985)

[52] D. McA. McKirdy
Recent Improvements to the Application of the Volume Integral Method of Eddy Current Modelling
J. NDE 8(1) 45 (1989)

[53] S K Burke
A Benchmark Problem for Computation of ΔZ in eddy-current NDE
J. NDE 7(1/2) 35 (1988)

[54] H A Sabbagh
A model of Eddy-Current Probes with Ferrite Cores
IEEE Trans. **MAG-23**(2) 1888 (1987)

[55] H A Sabbagh, J R Bowler and L D Sabbagh
A Model of Eddy-Current Probes with Ferrite Cores
Nondestructive Testing and Evaluation **5** 67 (1989)

[56] J R Bowler, L D Sabbagh and H A Sabbagh
A Theoretical and Computational Model of Eddy-Current Probes Incorporating Volume Integral and Conjugate Gradient Methods
IEEE Trans. **MAG-25**(3) 2650 (1989)

[57] S A Jenkins and J R Bowler
Calculations of the flaw signal generated by a differential eddy-current probe
Rev. Prog. QNDE **9A** 829 (1990)

[58] T B A Senior
Impedance Boundary Conditions for Imperfectly Conducting Surfaces
Appl. Sci. Res. B **8** 418 (1960)

[59] T H Fawzi, M Taher Ahmed, P E Burke
On the Use of the Impedance Boundary Conditions in Eddy Current Problems
IEEE Trans. **MAG-21**(5) 1835 (1985)

[60] M Taher Ahmed, J D Lavers, P E Burke
Direct BIE Formulation for Skin and Proximity Effect Calculation With and Without the Use of the Surface Impedance Approximation
IEEE Trans. **MAG-25**(5) 3937 (1989)

[61] A Nicolas
3D Eddy Current Solution by BIE Techniques
IEEE Trans **MAG-24**(1) 130 (1988)

[62] K Davey and L Turner
Steady-state and transient eddy current predictions using surface impedances in shell structures
J. Appl. Phys. **66**(6) 2501 (1989)

[63] R E Beissner
A three-dimensional boundary element model for eddy current NDE
Rev. Prog. QNDE **8A** 229 (1989)

[64] R E Beissner
Scalar potential model of eddy-current interactions with three-dimensional flaws
J. NDE **7** 15 (1988)

[65] R E Beissner
Approximate model of eddy-current probe impedance for surface breaking flaws
J. NDE **7** 25 (1988)

[66] R E Beissner and J S Graves
Computer modeling of eddy current probability of crack detection
Rev. Prog. QNDE **9A** 885 (1990)

[67] J A Ogilvy, C C Holt and D J Mackeith
Eddy current NDE: Theory and experiment
To be published in : Rev. Prog. QNDE **10** (1991)

[68] S R Oaten and J Blitz
The touch method of eddy-current testing
Nondestructive testing communications **3** 139 (1987)

[69] S K Burke and L R F Rose
Eddy-current NDI of cracks in thin plates
J. Phys. D:Appl. Phys. **20** 797 (1987)

[70] S K Burke and L R F Rose
Interaction of induced currents with cracks in thin plates
Proc. R. Soc. Lond. A **418** 229 (1988)

[71] S K Burke and L R F Rose
Eddy current detection of short cracks in sheets
Rev. Prog. QNDE **8A** 251 (1989)

[72] S K Burke
Eddy-current inspection of cracks in a multilayer conductor
J. Appl. Phys. **67**(1) 465 (1990)

[73] D Rodger
Computer modelling of eddy current NDT by using 3D finite elements
In *Electromagnetic Inspection*
Institute of Physics Short Meetings Series, No. 12
(IOP Publishing 1988)

[74] S H H Sadeghi and D Mirshekar-Syahkal
A method for sizing long surface cracks in metals based on the measurement of the surface magnetic field
Rev. Prog. QNDE **9A** 351 (1990)

[75] S H H Sadeghi and D Mirshekar-Syahkal
A new technique for sizing cracks in metals, utilizing an induced surface magnetic field
Rev. Prog. QNDE **9A** 593 (1990)

[76] J F Knott
The Use of Analogue and Mapping Techniques with Particular Reference to Detection of Short Cracks
In *The measurement of crack length and shape during fracture and fatigue*
C J Beevers (ed.)
Engineering Materials Advisory Services(1980)

[77] H H Johnson
Calibrating the Electric Potential Method for Studying Slow Crack Growth
Materials Research and Standards **5**(9) 442 (September 1965)

[78] K H Schwalbe and D Hellmann
Application of the Electrical Potential Method to Crack Length Measurements Using Johnson's Formula
J. Testing and Evaluation **9**(3) 218 (1981)

[79] R O Ritchie and K J Bathe
On the Calibration of the Electrical Potential Method for the Measurement of Crack Growth Using Finite Element Methods
Int. J. Fracture **15** 47 (1979)

[80] G H Aronson and R O Ritchie
Optimization of the Electrical Potential Technique for Crack Growth Monitoring in Compact Test Pieces Using Finite Element Analysis
J. Testing and Evaluation 7(4) 208 (1974)

[81] S Nath, Y K Shin, W Lord and T J Rudolphi
Boundary integral and finite element simulation of electromagnetic NDE phenomena
Rev. Prog. QNDE 9A 303 (1990)

[82] G Arfken
Mathematical Methods for Physicists
Second Edition, Academic Press (1970)

[83] D H Michael, R T Waechter and R Collins
The measurement of surface cracks in metals by using a.c. electric fields
Proc. R. Soc. Lond. A 381 139 (1982)

[84] H M Shang, R Haq, R Collins and D H Michael
The Detection and Measurement of Symmetric Corner Cracks by the a.c. Field Method
J. NDE 5(3/4) 169 (1986)

[85] M P Connolly, D H Michael and R Collins
The inversion of surface potential measurements to determine crack size and shape
J. Appl. Phys. 64(5) 2638 (1988)

[86] D H Michael and R Collins
Recent studies in modelling for the a.c. field measurement technique
Rev. Prog. QNDE 6A 193 Plenum Press (1987)

[87] D H Michael, R Collins, M McIver, A Niemiro and D Parramore
A study of the leakage field through holes and cracks in metal plates
Proc. R. Soc. Lond. A 421 55 (1989)

[88] R Collins, D H Michael and K B Ranger
The a.c. field around a plane semi-elliptical crack in a metal surface
Proc. 13th NDE Symposium San Antonio, Texas, 21-23 April 1981

[89] A M Lewis, D H Michael, M C Lugg and R Collins
Thin-skin electromagnetic fields around surface-breaking cracks in metals
J. Appl. Phys. **64**(8) 3777 (1988)

[90] R Haq, D H Michael and R Collins
The detection and measurement of overlapping fatigue cracks at welded joints by thin-skin electromagnetic fields
Proc. R. Soc. Lond. A **419**, 69 (1988)

[91] M McIver
Characterisation of surface-breaking cracks in metals by using a.c. electric fields
Proc. R. Soc. Lond. A **421**, 179 (1989)

[92] D H Michael, R Collins and W D Dover
Detection and measurement of cracks in threaded bolts with an a.c. potential difference method
Proc. R. Soc. Lond. A **385**, 145 (1983)

[93] M C Lugg, H M Shang, R Collins and D H Michael
The measurement of surface crack inclination in metals using a.c. electric fields
J. Phys. D:Appl. Phys. **21** 1814 (1988)

[94] M G Silk
Sizing crack-like defects by ultrasonic means
Research Techniques in NDT Vol. III Chapter 2
R S Sharpe (ed.)
Academic Press (1977)

[95] D Mirshekar-Syahkal, D H Michael and R Collins
Parasitic voltages induced by artificial flaws when measured using the a.c. field technique
J. NDE 2(3/4) 195 (1981)

[96] D C Jiles
Review of Magnetic methods for nondestructive evaluation (Part 2)
NDT International **23** 83 (1990)

[97] N N Zatsepin and V E Shcherbinin
Calculation of the magnetic field of surface defects
I. Field topography of defect models
Sov. J. NDT 2 50 (1966)

[98] N N Zatsepin and V E Shcherbinin
Calculation of the magnetic field of surface defects
II.Experimental verification of the principal theoretical relationships
Sov. J. NDT 2 59 (1966)

[99] V E Shcherbinin and A I Pashagin
Influence of the extension of a defect on the magnitude of its magnetic field
Sov. J. NDT 8 441 (1972)

[100] J H Hwang and W Lord
Finite element modelling of magnetic field-defect interactions
J Test. and Eval. 3 21 (1975)

[101] W Lord, J M Bridges, W Yen and R Palanisamy
Residual and active leakage fields around defects in ferromagnetic materials
Mater. Eval. 36 47 (1978)

[102] D L Atherton and M G Daly
Finite element calculation of magnetic flux leakage detector signals
NDT International 20 235 (1987)

[103] D L Atherton and W Czura
Finite element calculations on the effect of permeability variation on magnetic flux leakage signals
N D T International 20 239 (1987)

[104] F Förster
New findings in the field of non-destructive magnetic leakage field inspection
NDT International 19(1) 3 (1986)

[105] C Edwards and S B Palmer
The magnetic leakage field of surface breaking cracks
J. Phys. D:Appl. Phys. **19** 657 (1986)

[106] K Goebbels
Surface crack detection by magnetic particle inspection (*in German*)
Materialprüfung **30**(10) 327 (1988)

[107] J M McCoy and B K Tanner
Simulation of particle trajectories in magnetic particle inspection
IEEE Trans. **MAG-24**(2) 1665 (1988)

[108] W H Press, B P Flannery, S A Teukolsky, W T Vetterling
Numerical Recipes
The Art of Scientific Computing
C.U.P. 1986

[109] The NAG FORTRAN Library Manual, Mark 12
The Numerical Algorithms Group Limited (1987)

[110] D H Michael, A M Lewis, M McIver and R Collins
Thin-skin electromagnetic fields in the neighbourhood of surface breaking cracks in metals
Accepted for publication in Proc. R. Soc. Lond. A

[111] P Horowitz and W Hill
The Art of Electronics p.307 C.U.P. 1980
(p.455 2nd. Ed. 1989)

[112] S M Thompson, P J Allen and B K Turner
Magnetic Properties of Welds in High-Strength Pearlitic Steels
IEEE Trans. **MAG-26**(5) p.1984 (1990)

[113] B A Dale and M C Moyer
Sensitivity and Reliability of Commercial Drill-String Inspection Services
7th Offshore South East Asia Conference
Singapore 1988

[114] D A Topp, J D McGugan and W D Dover
Automated inspection system for drillstring threaded connections using ACFM techniques
Offshore Drilling Technology Conference
Aberdeen 28 November 1990

[115] M Riaziat
Analytical methods in electromagnetic nondestructive evaluation
Ph.D Thesis
Stanford University (1984)

[116] I S Gradshteyn and I M Ryzhik
Table of integrals, series and products
Academic Press (1980)

[117] S G Lipson and H Lipson
Optical Physics
C.U.P. (1981)

[118] D H S Cheng
The reflected impedance of a circular coil in the proximity of a semi-infinite medium
IEEE Trans. **IM-14**(3) 107 (1965)

[119] M Abramowitz and I A Stegun
Handbook of Mathematical Functions
Dover Pub. (1965)